Brunel University London

Non-invasive wave intensity analysis in common carotid artery of healthy humans

A thesis submitted to Brunel University London

For the Degree of

Doctor of Philosophy

By

Nicola Pomella

Institute of Environment, Health and Societies

Biomedical Engineering Research Theme

April 2017

Declaration of Authenticity

I hereby declare that the work presented in this thesis is my own.

Nicola Pomella

Abstract

The study of arterial wave propagation is essential to understand the physiopathology of the cardiovascular system, as waves carry clinically relevant information. Impedance analysis was used for such type of studies, where results were presented in the frequency domain, but it was difficult to relate specific events to time points within the cardiac cycle. Therefore, a mathematical tool called wave intensity analysis was developed, initially using measurements of pressure and velocity (PU approach). However, the need to acquire such measurements in a non-invasive, direct and simultaneous fashion led to the development of the DU approach, a type of wave intensity analysis carried out using vessel diameter and flow velocity waveforms, thus giving up the pressure measurement. It is the only available technique, at present, able to extract wave intensity information without relying on distally recorded pressure measurements and on non-simultaneous recordings. Due to its non-invasive nature for collecting the required measurements, this technique has a potential use in clinical and research settings to investigate physiological changes under rapid perturbations, such as the ones introduced by exercise. In this thesis, the DU approach is performed by only using an ultrasound device and to extract information about cardio-arterial interaction in the human common carotid artery.

In the first experimental chapter of this thesis, a reproducibility study of common carotid DU-derived wave intensity parameters was conducted on a healthy young cohort, both at rest and during exercise (semi-recumbent cycling). Carotid diameter and blood flow velocity features, as well as wave intensity parameters such as forward compression, backward compression and forward expansion wave peaks and energies, were overall fairly reproducible. In particular, diameter variables exhibited higher reproducibility and lower dispersion than corresponding velocity variables, whereas wave intensity energy variables exhibited higher reproducibility and lower dispersion than corresponding peaks. Local wave speed, calculated via lnDU-loop, a technique based only on local measurements of diameter and velocity and often associated with the DU approach, was also reproducible. It is possible to conclude that the DU-derived wave intensity analysis is reliable both at rest and during exercise.

In a subsequent study, DU-derived wave intensity analysis was performed on a young trained cohort to investigate the contribution of cardiac and peripheral vascular alterations to common carotid wave intensity parameters, under rapid physiological perturbations, such as

semi-recumbent cycling at incremental workrates, and subsequent recovery. Judging by the increase in local wave speed, the common carotid artery stiffened substantially as workrate increased whilst peak and energy of the forward and backward compression waves also increased, due to enhanced ventricular contractility, which was associated with larger reflections from the cerebral microcirculation and other vascular beds in the head. However, the reflection indices remained unchanged during exercise, highlighting that the increased magnitude of reflections is mainly due to the enhanced contractility, rather than changes in vascular resistance, at least at the carotid artery in young healthy individuals. The forward expansion wave increased during exercise, as the left ventricle actively decelerated blood flow in late systole, potentially improving filling time during diastole. In the early recovery, the magnitude of all waves returned to baseline value. Finally, the X wave, attributed to the reflection of the backward compression wave, had a tendency to increase during exercise and to return to baseline value in early recovery.

A further development of wave intensity analysis came with the reservoir-wave approach, able to separate, from the pressure and velocity waveforms, the component solely due to the reservoir volume, for the correct evaluation of backward- and forward-travelling waves. A number of issues, however, still remains, involving specifically the lack of consensus over the fitting technique and over the value of the asymptotic pressure value (P_∞), used for the determination of the reservoir waveform. Therefore, to give a contribution to the debate involving the more correct model for the pressure and velocity reservoir-wave approach, a study aimed to investigate various common carotid hemodynamic and wave intensity parameters, using different fitting techniques and values of P_∞ currently available in literature, was performed and described in the last chapter of this thesis. The study demonstrated that different fitting method and values of P_∞ could bring significant variations in values and trends of hemodynamic and wave intensity parameters. However, despite the changes in the shape of the reservoir pressure waveform, its peak and integral with respect to time tended to remain constant. This is an important feature, because both reservoir peak pressure and its integral have been used in clinical settings for the calculation of diagnostic indicators. The reservoir and excess velocity peaks, instead, changed more significantly. This outcome, together with the concomitant substantial change in excess pressure peak and integral, may greatly affect wave intensity parameters. Wave intensity parameters were, in fact, significantly more sensitive to fitting techniques and values of P_∞ than pressure parameters. Finally, the wave speed did not substantially change, leading to the conclusion that the calculation of local vessel distensibility and/or compliance, when calculated from the excess components of the waveforms, seemed insensitive to fitting techniques and values of P_∞.

Acknowledgements

I would like to thank all the people that helped me in this journey, from the very beginning to the end.

First and foremost, I would like to thank my principal supervisor, Prof. Ashraf Khir, who guided me through those years, giving me precious advice and being always available. Thanks to him, I had the opportunity to take part in important conferences, both in UK and abroad, and publish on journals. I also would like to thank my second supervisor, Dr. Christina Kolyva, who guided me step by step through the research journey, especially in the first period, when I was less experienced.

Prof José Gonzalez-Alonso, Dr. Mark Rakobowchuk and Dr. Eurico Wilhelm were also a big part of this thesis project, and their valuable help, especially on physiological issues and on the organisation of the journal papers, was very important to me. Eurico is more a friend than a colleague and his support during the long experimental days was very appreciated.

During those years, I always felt very welcome in BIB, becoming my second home. I am deeply grateful to all staff and students, with whom I enjoyed basically all my working days and nights out. In particular, John Louis, June, Shima, Vincent, Robin, Gianpaolo, Markella, Diego, Christoph, Nikolay, Masoud, Aihua, Gijs, Nas, Yasaman and Robbin. I spent an amazing time with all of you, running or cycling together, watching movies and having dinners together, or just sharing working time with you. The peculiar international community in BIB, and in Brunel in general, helped me in opening my mind and discovering new realities and new cultures. I will never stop to be grateful to BIB and to Brunel for that. I also would like to thank Miss Jenny Kume and Mister Roger Paton who helped me, with their professional experience, with any bureaucratic and technical issue during my journey and made it less difficult.

Last but not least, I would like to thank my family and Shav, to whom this thesis is dedicated, for their constant support in every day of my life.

Table of Contents

LIST OF FIGURES IX

LIST OF TABLES XVII

NOMENCLATURE XIX

CHAPTER 1: BACKGROUND 1
1.1 THE CARDIOVASCULAR SYSTEM 1
1.1.1 The heart cycle 3
1.1.2 The arterial system 6
1.2 WAVE PROPAGATION IN THE CARDIOVASCULAR SYSTEM 8
1.2.1 Impedance analysis 10
1.2.2 Wave Intensity Analysis 11
1.3 DETERMINATION OF WAVE SPEED 12
1.3.1 Local techniques for the determination of the wave speed 14
1.4 INVASIVE AND NON-INVASIVE MEASUREMENTS OF PRESSURE AND VELOCITY 16
1.5 THE DU APPROACH 17
1.6 THE RESERVOIR-WAVE APPROACH 17
1.6.1 The Reservoir-Wave approach at any arbitrary location 19
1.7 CLINICAL VALUE OF WAVE INTENSITY ANALYSIS 20
1.8 CAROTID WAVE INTENSITY ANALYSIS 21
1.9 OBJECTIVES 26
1.10 THESIS OUTLINE 27

CHAPTER 2: THEORETICAL BACKGROUND 29
2.1 DEVELOPMENT OF THE BASIC EQUATIONS 29
2.2 THE METHOD OF CHARACTERISTICS 32
2.3 WAVE INTENSITY SEPARATION 35
2.4 THE DU THEORY 37
2.5 THE RESERVOIR-WAVE THEORY 42
2.5.1 The Reservoir-Wave theory at any arbitrary location 44
2.5.2 Extension to reservoir velocity 47

CHAPTER 3: A REPRODUCIBILITY STUDY OF NON-INVASIVE WAVE INTENSITY ANALYSIS IN COMMON CAROTID ARTERY 48
3.1 INTRODUCTION 48
3.2 MATERIAL AND METHODS 49
3.2.1 Study group 49
3.2.2 Instrumentation and measurements 49
3.2.3 Protocol 50
3.2.4 Data analysis 51
3.2.5 Statistical analysis 53
3.3 RESULTS 55
3.3.1 Hemodynamic parameters 55
3.3.2 Wave parameters 59
3.3.3 Inter-observer reproducibility 63
3.4 DISCUSSION 68

3.4.1 Reproducibility of parameters 70
3.4.2 Implications for future work 71
3.4.3 Experimental considerations and limitations 72
3.4.4 Conclusions 72

CHAPTER 4: NON-INVASIVE ASSESSMENT OF WAVE INTENSITY ANALYSIS DURING EXERCISE 73
4.1 INTRODUCTION 73
4.2 MATERIAL AND METHODS 74
4.2.1 Study Group 74
4.2.2 Experimental design 74
4.2.3 Instrumentation 75
4.2.4 Ultrasound measurements 76
4.2.5 Data Analysis 76
4.2.6 Statistical Analysis 78
4.3 RESULTS 79
4.3.1 Hemodynamic parameters 79
4.3.2 Wave speed and distensibility 81
4.3.3 Wave intensity parameters 83
4.3.4 Reflection Indices 89
4.4 DISCUSSION 90
4.4.1 Relative contributions of diameter and velocity to blood flow 91
4.4.2 Distensibility and wave speed with increasing exercise intensity 91
4.4.3 Wave intensity parameters 92
4.4.3.1 Forward, backward compression waves and reflection indices 92
4.4.3.2 The X-wave 93
4.4.3.3 Forward expansion wave with increasing exercise intensities 94
4.4.4 Methodological considerations 95
4.4.5 Limitations 96
4.5 CONCLUSIONS 96

CHAPTER 5: IMPLICATIONS OF VARYING FITTING TECHNIQUE AND ASYMPTOTIC DIASTOLIC PRESSURE ON WAVE INTENSITY PARAMETERS 97
5.1 INTRODUCTION 97
5.2 MATERIAL AND METHODS 99
5.2.1 The Asklepios population 99
5.2.1.1 Study Group 99
5.2.2 Protocol 99
5.2.2.1 Blood pressure measurements 100
5.2.2.2 Blood flow velocity measurements 101
5.2.3 Data analysis 101
5.2.3.1 Fitting algorithm settings 102
5.2.3.2 Wave intensity analysis 107
5.2.4 Statistical analysis 108
5.3 RESULTS 109
5.3.1 Effects of algorithm settings on results 109
5.3.1.1 Tolerance value 109
5.3.1.2 Performance of different least-squares algorithms 110
5.3.2 DOF-Window analysis 111
5.3.3 P_{∞}-Variation analysis 117
5.3.4 Age-gender analysis 121

5.4 DISCUSSION 125
5.4.1 Limitations 130
5.5 CONCLUSIONS 130
CHAPTER 6: GENERAL DISCUSSIONS AND CONCLUSIONS 132
6.1 ADVANTAGES AND LIMITATIONS OF THE DU APPROACH 134
6.1.1 Advantages 135
6.1.2 Limitations 135
6.2 CONCLUSIONS 136
6.3 LIMITATIONS OF THE THESIS 136
6.4 FUTURE PERSPECTIVE 138
LIST OF REFERENCES 139
LIST OF PUBLICATIONS RELATED TO THIS THESIS 153

List of Figures

Figure 1.1: Schematic representation of the cardiovascular system. Taken from Hall (2015). ……3

Figure 1.2: Schematic diagram of the heart, picturing the four cavities and the main vessels. Taken from Hall (2015). ……..4

Figure 1.3: Wiggers diagrams for the left side of the heart. Taken from Hall (2015)……6

Figure 1.4: Schematic representation of the microcirculation. Taken from Hall (2015)……7

Figure 1.5: First measurement of WIA in man. P: pressure, U: velocity, dI: wave intensity. The dotted lines represent the separated beats. Taken from Parker et al. (1988), as modified by Parker (2009b). ……..12

Figure 1.6: Comparison between lnDU-loop (a) and PU-loop (b) in vitro (measurements taken from a latex tube being filled with water and receiving a half-sinusoidal pressure pulse at the inlet). Dashed lines indicate linear portions in both loops and arrows indicate linear portions in both loops and arrows indicate the direction of the loops. Taken from Feng & Khir (2010). ……..15

Figure 1.7: Visual explanation of the Windkessel effect. Schematic working principle of a fire-engine pumps (top) and arterial reservoir (bottom). Taken from: Kurzon. Licence: CC BY-SA 3.0…….…..17

Figure 1.8: Common carotid artery and its bifurcation. Modified from: Blausen, Medical gallery of Blausen Medical 2014. WikiJournal of Medicine. License: CC BY 3.0……...21

Figure 1.9: Measured pressure and flow velocity waveforms (top) and wave intensity (bottom) from human carotid artery. S,R,D stand for FCW, BCW and FEW peaks, respectively. X indicates the X mid-systolic wave. Taken from Zambanini et al. (2005)…….23

Figure 2.1: Separated D waveforms (a), U waveforms (b) and non-invasive wave intensity ($_n$dI) (c) from human carotid artery. Green lines show measured waveforms, blue lines indicate forward components and red lines are associated with backward components. Taken from Feng & Khir (2010)……41

Figure 2.2: Schematic representation of the arterial system. Modified from http://www.bg.ic.ac.uk/research/k.parker/res_press_web/rp_definition.html……... 42

Figure 2.3: Diagrams of blood pressure and its separated components, the reservoir and the excess ones. Top: Canine measured aortic pressure (P_{aorta}), separated reservoir component ($P_{reservoir}$), left ventricular measured pressure (P_{LV}) and asymptotical value of pressure (P_{∞}). Bottom: Measured inflow (Q_{in}), outflow (Q_{out}) and excess component of the pressure ($P_{wave} \equiv P_{ex}$). The scales are adjusted to highlight the qualitative similarity between P_{wave} and Q_{in}. The two vertical dashed lines indicate $Q_{in} = Q_{out}$: $P_{reservoir}$ neither increases or decreases. Taken from Wang et al. (2003) as modified by Tyberg et al. (2009)……46

Figure 3.1: Experimental setup. (A) Monitoring of ultrasound system while acquiring carotid images and Doppler information. In the frozen image on the monitor is the common carotid artery, together with the diameter waveform (*pink*) and blood velocity contour (*blue*) on the right side of the screen. (B) Semi-recumbent cycle ergometer and control box: (1) ergometer, (2) control box, (3) handle for the left arm…….…..….50

Figure 3.2: Comparison between raw and Savitzky–Golay smoothed signals. Top: *D* and *dD* waveforms; Bottom: *U* and *dU* waveforms.....52

Figure 3.3: Example of waveforms. Top: Carotid diameter and blood flow velocity. D_{max}, U_{max}, ΔD and ΔU are shown. Bottom: Corresponding wave intensity. The *dark blue areas* represent, from left to right, the forward compression (FCW) and forward expansion (FEW) waves; the *red areas* represent the backward compression (BCW) and backward expansion (BEW) waves, as reflections of FCW and FEW, respectively; the *green areas* represent, from left to right, the reflections of BCW and BEW. Only FCW, BCW and FEW are labelled……..….54

Figure 3.4: Example of lnDU loop at rest for one subject. The regression line of the early systolic linear part is shown. ……...…...….55

Figure 3.5: Vector plots of measurements performed at rest and during exercise on both days. (A) Δ*D*. (B) Δ*U*. (C) Wave speed. (D) Forward compression wave (FCW) area. (E) Backward compression wave (BCW) area. (F) Forward expansion wave (FEW) area….....57

Figure 3.6: Comparison of Δ*D* (A,B), Δ*U* (C,D) and wave speed (E,F) values between the two days of testing, during rest and exercise for the whole cohort…….....58

Figure 3.7: Bland–Altman plots of Δ*D* (A,B), Δ*U* (C,D) and wave speed (E,F) values for the 2 d of testing during rest and exercise for the whole cohort. (A,C,E) Rest condition. (B,D,F)

Exercise. The *dark thick line* represents the mean difference; the grey lines, ±2 standard deviations. ……59

Figure 3.8: Comparison of forward compression wave (FCW) (A,B), backward compression wave (BCW) (C,D) and forward expansion wave (FEW) (E,F) area values between the two days of testing during rest and exercise for the whole cohort……..…62

Figure 3.9: Bland–Altman plots of forward compression wave (FCW) (A,B), backward compression wave (BCW) (C,D) and forward expansion wave (FEW) (E,F) area values between the 2 d of testing during rest and exercise for the whole cohort. (A,C,E) Rest condition. (B,D,F) Exercise. The *dark thick line* represents the mean difference; the grey lines, ±2 standard deviations……63

Figure 3.10: Comparison of ΔD (A,B), ΔU (C,D) and wave speed (c) (E,F) values between the two observers during rest (A,C,E) and exercise (Exe; B,D,F) for the whole cohort. Data from both days of testing are pooled……65

Figure 3.11: Bland–Altman plots of ΔD (A,B), ΔU (C,D) and wave speed (c) (E,F) values between the two observers during rest (A,C,E) and exercise (Exe; B,D,F) for the whole cohort. Data from both days of testing are pooled. The *dark thick line* represents the mean difference; the grey lines, ±2 standard deviations. ……..……66

Figure 3.12: Comparison of forward compression wave (FCW) (A,B), backward compression wave (BCW) (C,D) and forward expansion wave (FEW) (E,F) area values between the two observers during rest (A,C,E) and exercise (Exe; B,D,F) for the whole cohort. Data from both days of testing are pooled. ……..……67

Figure 3.13: Bland–Altman plots of forward compression wave (FCW) (A,B), backward compression wave (BCW) (C,D) and forward expansion wave (FEW) (E,F) area values between the two observers during rest (A,C,E) and exercise (*Exe*; B,D,F) for the whole cohort. Data from both days of testing are pooled. The *dark thick line* represents the mean difference; the grey lines, ±2 standard deviations. ……..……68

Figure 4.1: Experimental protocol. Arrows designate ultrasound measurements and blood pressure recordings. Percentages indicate the corresponding fraction of the maximal workrate. 0%: unloaded. ……....….75

Figure 4.2: Bar chart displaying mean and standard deviation of ΔD (A) and ΔU (B) for each working condition of the protocol (n=8). W_{max}: maximal workrate; C: control (rest); [*,●,◊,□]: ANOVA p-values. Statistical significance against the control condition was labelled with (*) and against 0% condition was labelled with (□); 40, 60, 70% maximal workrate conditions were labelled with (◊) if significantly different from the corresponding

previous exercise step (20, 40, 60%, respectively); recovery conditions that were significantly different from 70% condition were labelled with (●)……..……81

Figure 4.3: Bar chart displaying mean and standard deviation of wave speed (A) and distensibility (B) for each working condition of the protocol (n=8). W_{max}: maximal workrate; C: control (rest); [*,●,◊,□]: ANOVA p-values. Statistical significance against the control condition was labelled with (*) and against 0% condition was labelled with (□); 40, 60, 70% maximal workrate conditions were labelled with (◊) if significantly different from the corresponding previous exercise step (20, 40, 60%, respectively); recovery conditions that were significantly different from 70% condition were labelled with (●)……..…82

Figure 4.4: Distensibility plotted against mean arterial pressure values at rest, during exercise and in the recovery (n=8). Values are averages across all participants for each condition. ……..….83

Figure 4.5: Bar chart displaying mean and standard deviation of FCW peak (A), BCW peak (B) and RI_I (C) for each working condition of the protocol (n=8). W_{max}: maximal workrate; C: control (rest); [*,●,◊,□]: ANOVA p-values. Statistical significance against the control condition was labelled with (*) and against 0% condition was labelled with (□); 40, 60, 70% maximal workrate conditions were labelled with (◊) if significantly different from the corresponding previous exercise step (20, 40, 60%, respectively); recovery conditions that were significantly different from 70% condition were labelled with (●)……..…..…..84

Figure 4.6: Bar chart displaying mean and standard deviation of FCW area (A), BCW area (B) and RI_E (C) for each working condition of the protocol (n=8). W_{max}: maximal workrate; C: control (rest); [*,●,◊,□]: ANOVA p-values. Statistical significance against the control condition was labelled with (*) and against 0% condition was labelled with (□); 40, 60, 70% maximal workrate conditions were labelled with (◊) if significantly different from the corresponding previous exercise step (20, 40, 60%, respectively); recovery conditions that were significantly different from 70% condition were labelled with (●)…….85

Figure 4.7: Bar chart displaying mean and standard deviation of WD1 index, for each working condition of the protocol (n=8). W_{max}: maximal workrate; C: control (rest); [*,●,◊,□]: ANOVA p-values. Statistical significance against the control condition was labelled with (*) and against 0% condition was labelled with (□); 40, 60, 70% maximal workrate conditions were labelled with (◊) if significantly different from the corresponding previous exercise step (20, 40, 60%, respectively); recovery conditions that were significantly different from 70% condition were labelled with (●)…….……..….86

Figure 4.8: Bar chart displaying mean and standard deviation of FEW peak (A) and FEW area (B), for each working condition of the protocol (n=8). W_{max}: maximal workrate; C: control (rest); [*,●,◊,□]: ANOVA p-values. Statistical significance against the control condition was labelled with (*) and against 0% condition was labelled with (□); 40, 60, 70% maximal workrate conditions were labelled with (◊) if significantly different from the corresponding previous exercise step (20, 40, 60%, respectively); recovery conditions that were significantly different from 70% condition were labelled with (●)……87

Figure 4.9: Bar chart displaying mean and standard deviation of X peak (A) and X area (B), for each working condition of the protocol (n=8). W_{max}: maximal workrate; C: control (rest); [*,●,◊,□]: ANOVA p-values. Statistical significance against the control condition was labelled with (*) and against 0% condition was labelled with (□); 40, 60, 70% maximal workrate conditions were labelled with (◊) if significantly different from the corresponding previous exercise step (20, 40, 60%, respectively); recovery conditions that were significantly different from 70% condition were labelled with (●)……..….88

Figure 4.10: Bar chart displaying mean and standard deviation of CCA resistance for each working condition of the protocol (n=8). C: control (rest). None of the working condition was statistically significantly different from C or between each other……..89

Figure 4.11: Correlation graphs for RI_I vs. RI_E (A) and for RI_I and RI_E vs. CCA resistance (B), for all working conditions (n=8). The lines with unitary slope are also displayed…….90

Figure 4.12: Test power curve for the reflection coefficient RI_E (n=8) at control, during exercise and recovery. Values obtained during exercise and recovery are taken as means for the alternative hypothesis. H_a, alternative hypothesis. ……..95

Figure 5.1: Comparison of pressure waveforms between 3 DOF and 2 DOF settings with full window (Left) and between 3 DOF and 2 DOF with 23 window (Right) for one patient. The measured pressure is depicted in blue. The top waveforms depicted along with the measured pressure represent the reservoir components, whereas the bottom waveforms the excess components. 23: 23 window, full: full window, meas: measured waveform…….…104

Figure 5.2: Comparison of pressure waveforms between full and 23 window with 3 DOF (Left) and between full and 23 window with 2 DOF (Right) settings for one patient. The measured pressure is depicted in blue. The top waveforms depicted along with the measured pressure represent the reservoir components, whereas the bottom waveforms the excess components. 23: 23 window, full: full window, meas: measured waveform…….....105

Figure 5.3: Comparison of velocity waveforms between 3 DOF and 2 DOF settings with full window (Left) and between 3 DOF and 2 DOF with 23 window (Right) for one patient. The measured velocity is depicted in blue. The top waveforms depicted along with the measured velocity represent the reservoir components, whereas the bottom waveforms the excess components. 23: 23 window, full: full window, meas: measured waveform……...….105

Figure 5.4: Comparison of velocity waveforms between full and 23 window with 3 DOF (Left) and between full and 23 window with 2 DOF (Right) settings for one patient. The measured velocity is depicted in blue. The top waveforms depicted along with the measured velocity represent the reservoir components, whereas the bottom waveforms the excess components. 23: 23 window, full: full window, meas: measured waveform……...…106

Figure 5.5: Examples of P_{ex} (green) and U (blue) waveforms for one patient. The pressure waveforms have been scaled down. Top Left: 3 DOF setting; Top Right: 2 DOF setting; Bottom Left: 3 DOF 23 setting; Bottom Left: 2 DOF 23 setting. ……..…….106

Figure 5.6: Example of $P_{ex}U_{ex}$ loop (Top Left), P_{ex} contour (Top Right), U_{ex} contour (Bottom Left) and corresponding wave intensity (Bottom Left) for one patient. A straight line highlighting the slope of the linear portion is superimposed on the $P_{ex}U_{ex}$ loop. Forward compression (FCW), backward compression (BCW) and forward expansion (FEW) waves are labelled in the wave intensity plot. dI+: forward wave intensity component, dI-: backward wave intensity component. ……..……108

Figure 5.7: Comparisons of $P_r\ max$ and $P_{ex}\ max$ (Top Left), $U_r\ max$ and $U_{ex}\ max$ (Top Right), P_∞ (Bottom Left) and b (Bottom Right) values among all fitting settings. *: significant difference between 3 DOF and 2 DOF in full window ($p<0.05$), *23: significant difference between 3 DOF and 2 DOF in 23 window, *2: significant difference between 2 DOF and 2 DOF 23, *3: significant difference between 3 DOF and 3 DOF 23. Y-axis units are reported in each figure title. Values are reported as mean $\pm$ SD……...…113

Figure 5.8: Comparisons of PRI (Left) and PEI (Right) values among all fitting settings. *: significant difference between 3 DOF and 2 DOF in full window ($p<0.05$), *23: significant difference between 3 DOF and 2 DOF in 23 window, *2: significant difference between 2 DOF and 2 DOF 23, *3: significant difference between 3 DOF and 3 DOF 23. Y-axis units are reported in each figure title. Values are reported as mean $\pm$ SD……...…114

Figure 5.9: Comparisons of PP_r index values among all fitting settings. *: significant difference between 3 DOF and 2 DOF in full window ($p<0.05$), *23: significant difference between 3 DOF and 2 DOF in 23 window, *2: significant difference between 2 DOF and 2

DOF 23, *3: significant difference between 3 DOF and 3 DOF 23. Y-axis units are reported in each figure title. Values are reported as mean ± SD……114

Figure 5.10: Comparisons of wave speed c (Top Left), FEW area (Top Right), FCW area (Bottom Left) and BCW area (Bottom Right) values among all fitting settings. *: significant difference between 3 DOF and 2 DOF in full window ($p<0.05$), *23: significant difference between 3 DOF and 2 DOF in 23 window, *2: significant difference between 2 DOF and 2 DOF 23, *3: significant difference between 3 DOF and 3 DOF 23. Y-axis units are reported in each figure title. Values are reported as mean ± SD……..…116

Figure 5.11: Comparison of b values among positive (+25%, +50%, +75%, +100%) and negative (-25%, -50%, -75%) variations of P_∞, with respect to the reference value (R) extracted from 2 DOF full window setting. *: significant difference with respect to R ($p<0.05$). Y-axis units are reported in each figure title. Values are reported as mean ± SD……..…...117

Figure 5.12: Comparisons of $P_{ex}\ max$ (Top Left), $P_r\ max$ (Top Right), $U_r\ max$ (Bottom Left) and $U_{ex}\ max$ (Bottom Right) values among positive (+25%, +50%, +75%, +100%) and negative (-25%, -50%, -75%) variations of P_∞, with respect to the reference value (R) extracted from 2 DOF full window setting. *: significant difference with respect to R ($p<0.05$). Y-axis units are reported in each figure title. Values are reported as mean ± SD……..118

Figure 5.13: Comparisons of PEI (Left) and PRI (Right) values among positive (+25%, +50%, +75%, +100%) and negative (-25%, -50%, -75%) variations of P_∞, with respect to the reference value (R) extracted from 2 DOF full window setting. *: significant difference with respect to R ($p<0.05$). Y-axis units are reported in each figure title. Values are reported as mean ± SD. ……119

Figure 5.14: Comparisons of PP_r index values among positive (+25%, +50%, +75%, +100%) and negative (-25%, -50%, -75%) variations of P_∞, with respect to the reference value (R) extracted from 2 DOF full window setting. *: significant difference with respect to R ($p<0.05$). Y-axis units are reported in each figure title. Values are reported as mean ± SD……120

Figure 5.15: Comparisons of wave speed c (Top Left), FCW area (Top Right), FEW area (Bottom Left) and BCW area (Bottom Right) values among positive (+25%, +50%, +75%, +100%) and negative (-25%, -50%, -75%) variations of P_∞, with respect to the reference value (R) extracted from 2 DOF full window setting. *: significant difference with respect to

R (p<0.05). Y-axis units are reported in each figure title. Values are reported as mean ± SD……..…121

Figure 5.16: Comparison of $P_r\ max$ (Top Left), $P_{ex}\ max$ (Top Right), $U_r\ max$ (Bottom Left) and $U_{ex}\ max$ (Bottom Right), among half-decades (1st: 35-40, 2nd: 41-45, 3rd: 46-50, 4th: 51-55 yr) in all fitting settings. HD: half-decade. *: significant difference between 2nd HD and 1st HD, †: significant difference between 3rd HD and 1st HD, ‡: significant difference between 4th HD and 1st HD. Y-axis units are reported in each figure title. Values are reported as mean ± SD. ……122

Figure 5.17: Comparisons of $P_r\ max$ (Top Left), $P_{ex}\ max$ (Top Right), $U_r\ max$ (Bottom Left) and $U_{ex}\ max$ (Bottom Right), between genders in all fitting settings. *: significant difference (p<0.05). Y-axis units are reported in each figure title. Values are reported as mean ± SD……..……124

Figure 5.18: Comparison of $\bar{P}_n$ values among all fitting settings. *: significant difference between 3 DOF and 2 DOF in full window (p<0.05), *23: significant difference between 3 DOF and 2 DOF in 23 window, *2: significant difference between 2 DOF and 2 DOF 23, *3: significant difference between 3 DOF and 3 DOF 23. Y-axis units are reported in each figure title. Values are reported as mean ± SD. ……..126

Figure 5.19: Comparison of a values among all fitting settings. *: significant difference between 3 DOF and 2 DOF in full window (p<0.05), *23: significant difference between 3 DOF and 2 DOF in 23 window, *2: significant difference between 2 DOF and 2 DOF 23, *3: significant difference between 3 DOF and 3 DOF 23. Y-axis units are reported in each figure title. Values are reported as mean ± SD. ……..……..127

Figure 5.20: Comparison of a values among positive (+25%, +50%, +75%, +100%) and negative (-25%, -50%, -75%) variations of P_∞, with respect to the reference value (R) extracted from 2 DOF full window setting. *: significant difference with respect to R (p<0.05). Y-axis units are reported in each figure title. Values are reported as mean ± SD……..……..…128

List of Tables

Table 2.1: Properties of the separated pressure, velocity and intensity waves……..……37

Table 2.2: Properties of the separated diameter, velocity and intensity waves. ……...……38

Table 3.1: Hemodynamic parameters at rest and during submaximal cycling. Data are averaged among 12 participants. D_{max}: peak diameter; U_{max}: peak velocity; ΔD: diameter pulse; ΔU: velocity pulse; $\sigma^2{}_{\mathrm{dD}}$: variance of dD; $\sigma^2{}_{\mathrm{dU}}$: variance of dU; ICC abs. agree Si/Me: absolute agreement intraclass correlation coefficients, Si: single, Me: mean; CV: within-subjects coefficient of variation Details in the text. ……..……56

Table 3.2: Wave parameters at rest and during submaximal cycling. Data are averaged among 12 participants. c: wave speed; FCW: forward compression wave; BCW: backward compression wave; FEW: forward expansion wave; ICC abs. agree Si/Me: absolute agreement intraclass correlation coefficients, Si: single, Me: mean; CV: within-subjects coefficient of variation. ……..60

Table 3.3: Assessment of inter-observer reproducibility for the hemodynamic and wave parameters, at rest and during submaximal cycling. Data are from 12 participants. D_{max}: peak diameter; U_{max}: peak velocity; ΔD: diameter pulse; ΔU: velocity pulse; $\sigma^2{}_{\mathrm{dD}}$: variance of dD; $\sigma^2{}_{\mathrm{dU}}$: variance of dU; c: wave speed; FCW: forward compression wave; BCW: backward compression wave; FEW: forward expansion wave; ICC: intraclass correlation coefficient. ……..64

Table 4.1: Hemodynamic parameters at selected workrates (n=8). Data are mean ± SD. W_{max}, maximal workrate; HR, heart rate; SBP, systolic blood pressure; DBP, diastolic blood pressure; MAP, mean arterial pressure; MBF: mean CCA blood flow; CO, cardiac output; CCA/CO, mean CCA blood flow to cardiac output ratio = 2 x MBF/CO; D_{max}, peak of diameter waveform; U_{max}, peak of velocity waveform; Womersley, Womersley number; Re, Reynolds number. [*,●,◊,□]: ANOVA p-values. Statistical significance against the control condition was labelled with (*) and against 0% condition was labelled with (□); 40, 60, 70% maximal workrate conditions were labelled with (◊) if significantly different from the corresponding previous exercise step (20, 40, 60%, respectively); recovery conditions that were significantly different from 70% condition were labelled with (●)……..……80

Table 4.2: Regression analysis for reflection indices and CCA resistance (n=8). CCA Res, common carotid artery resistance; RI_I, reflection index calculated from peaks; RI_E, reflection index calculated from areas; * Significant regression ($p<0.05$)……...…..90

Table 5.1: Basic characteristics of subjects (n=1037). bpm: beats per minute, DBP: brachial diastolic blood pressure, F: female, HD: half-decade, HR: heart rate, M: male, MAP: brachial mean blood pressure, n: number of subjects, SBP: brachial systolic blood pressure, T: total. Values are reported as mean ± SD. ……...…100

Table 5.2: Properties of the analyses performed. *b*: diastolic time constant; P_∞: asymptotical pressure value; $\bar{P}_n$: reservoir pressure value at the dicrotic notch. *: simulations are performed with different fixed P_∞ values, ranging from -75% to +100% of the reference value obtained from 2 DOF full analysis. ……103

Table 5.3: Effect of tolerance value on hemodynamic and wave intensity parameters. ΔTol%: relative difference in tolerance value; ^: the relative difference is displayed with the sign for clarity. More details in the text. ……..…110

Table 5.4: Effect of type of algorithm on hemodynamic and wave intensity parameters. LM: Levenberg-Marquardt; fmin: fminsearch. % refers to relative difference in value with respect to the corresponding reference algorithm "lsqcurvefit"; ^: the relative difference is displayed with the sign for clarity. More details in the text. ……111

Table 5.5: Percentage (%) variations of wave intensity parameters obtained with PU loop (measured waveforms), with respect to corresponding parameters obtained with excess components P_{ex} and U_{ex}. †: not significant ($p>0.05$). As indicated, only one variation was not significant (FEW area in 2 DOF full setting). ……116

Table 5.6: Percentage (%) variations of 2nd, 3rd and 4th half-decade values with respect to corresponding 1st half-decade values, for $P_r\ max, P_{ex}\ max, U_r\ max$ and $U_{ex}\ max$, in all settings. Female and male values are pooled together. HD: half-decade. ……...…123

Table 5.7: Correlation and regression analysis for $P_r\ max, P_{ex}\ max, U_r\ max$ and $U_{ex}\ max$ with age, in all fitting settings. R^2: Pearson's correlation coefficient……..…….123

Table 5.8: Percentage (%) variations of male values with respect to corresponding female values, for $P_r\ max, P_{ex}\ max, U_r\ max$ and $U_{ex}\ max$ in all settings……..…124

Table 5.9: Actual asymptotical pressure values corresponding to P_∞ percentage variations used in the P_∞-Variation analysis (n=1037). w.r.t.R: with respect to the reference (R). Values are reported as mean ± SD……..…….128

Nomenclature

$\Delta \boldsymbol{D}$: vessel diameter pulse;

$\Delta \boldsymbol{U}$: blood flow velocity pulse;

$\boldsymbol{\rho}$: blood density;

$\boldsymbol{\sigma_{dD}^2}$, $\boldsymbol{\sigma_{dU}^2}$: variances of dD and dU, respectively;

$\boldsymbol{A}$: cross-sectional area;

$\boldsymbol{a}$: systolic time constant of the reservoir waveform;

$\boldsymbol{b}$: diastolic time constant of the reservoir waveform;

BCW: backward compression wave;

C: control condition;

CCA: common carotid artery;

CO: cardiac output;

CV: coefficient of variation;

$\boldsymbol{D}$: vessel diameter waveform;

$\boldsymbol{dA}$: differential of A;

DBP: diastolic blood pressure;

$\boldsymbol{dD}, \boldsymbol{dD_+}, \boldsymbol{dD\_}$: differential of D, its forward (+) and backward (-) components;

$\boldsymbol{dI}, \boldsymbol{dI_+}, \boldsymbol{dI\_}$: wave intensity, its forward (+) and backward (-) components;

$\boldsymbol{D_{max}}$: peak of diameter waveform;

DOF: degrees of freedom;

$\boldsymbol{dP}, \boldsymbol{dP_+}, \boldsymbol{dP\_}$: differential of P, its forward (+) and backward (-) components;

$\boldsymbol{D_s}$: vessel distensibility;

$\boldsymbol{dU}, \boldsymbol{dU_+}, \boldsymbol{dU\_}$: differential of U, its forward (+) and backward (-) components;

FCW: forward compression wave;

FEW: forward expansion wave;

HD: half-decade;

HR: heart rate;

ICC: intra-class correlation coefficient;

$\boldsymbol{lnD}$: logarihmic diameter waveform;

MAP: mean arterial blood pressure;

MBF: common carotid artery mean blood flow;

$\boldsymbol{P}$: blood pressure waveform;

$\boldsymbol{P_{\infty}}$: asymptotical pressure value;

$\boldsymbol{PEI}$: integral of P_{ex};

$\boldsymbol{P_{ex}}$: excess pressure waveform;

$\boldsymbol{P_n}$: measured pressure value at the dicrotic notch;

$\boldsymbol{\overline{P}_n}$: reservoir pressure value at the dicrotic notch;

$\boldsymbol{P_r}$: reservoir pressure waveform;

$\boldsymbol{PRI}$: integral of P_r;

R: reference value;

$\boldsymbol{\overline{R}}$: mean flow resistance;

$\mathbf{RI_I}$: reflection index calculated from peak values;

$\mathbf{RI_E}$: reflection index calculated from area values;

SBP: systolic blood pressure;

SD: standard deviation;

$\boldsymbol{T_N}$: dicrotic notch time;

$\boldsymbol{U}$: blood flow velocity waveform;

$\boldsymbol{U_{ex}}$: excess velocity waveform;

$\boldsymbol{U_{max}}$: peak of velocity waveform;

$\boldsymbol{U_r}$: reservoir velocity waveform;

WD: wave intensity as defined by Tanaka et al. (2015);

WD1: first peak of WD;

WI: wave intensity;

WIA: wave intensity analysis;

$\mathbf{W_{max}}$: maximal workrate;

w.r.t.R: "with respect to Reference";

X: mid-systolic X wave.

Chapter 1: Background

Cardiovascular diseases (CVDs) represent the global leading causes of death. They include: coronary heart pathologies, such as forms of angina pectoris and myocardial infarction; cerebrovascular pathologies, such as strokes; peripheral arterial pathologies; rheumatic heart disease; congenital heart diseases, such as hypoplasia and forms of cyanotic, septal or obstruction defects; deep vein thrombosis and pulmonary embolism.

According to the World Health Organization Report 2014 (WHO 2014), a total of 56 million deaths occurred in the world in 2012, 38 million of which due to non-communicable diseases (NCDs), a class of pathologies which are non-infectious and non-transmissible. CVDs, in particular, represented 46.2% of all NCD-related deaths, followed by cancers (21.7%), respiratory diseases and diabetes. Over three quarters of deaths caused by CVDs occurred in low- to middle income countries. Premature deaths (<70 years) globally involved 52% of NCDs, 37% of which were CVDs, followed by malignant neoplasm (27%).

There were statistically significant causal relationships between CVDs and some behavioural risk factors, such as unhealthy diet (high sodium intake), physical inactivity, tobacco use and harmful use of alcohol. Among all the CVDs, heart attack and stroke counted for 80% of the deceases. According to the WHO projections, the estimated total number of NCD deaths (and proportionally of CVD deaths) will increase from 38 million to 52 million by 2030. For successful prevention and treatment of CVDs, a profound understanding of the hemodynamics of the cardiovascular system, in both physiological and pathological conditions, is essential.

1.1 The cardiovascular system

The cardiovascular system (schematically depicted in Figure 1.1) counts three main components: the blood, the heart and the vessels. The blood transports O_2 and nutrients to all cells of the body, CO_2 to the lungs and cell waste products to specific organs to be eliminated, such as kidneys and liver; it also acts as first defence line in the immune system and is important for the thermoregulation of the organism. The second component is the heart, which acts as a pump, able to spontaneously initiate rhythmic contractions and whose force delivery and frequency are regulated by neuronal and hormonal factors. The vessels, finally, carry the blood around the body and are categorised into arteries, which carry the blood from the heart to the periphery and the lungs, and veins, which carry the blood from the periphery and lungs toward the heart.

From a hydraulic point of view, the cardiovascular system can be thought as a hydraulic closed circuit, divided into two sub-systems connected in series: a small or pulmonary circulation, starting from the right side of the heart, which pumps the blood toward the pulmonary capillary system, and a systemic circulation, starting from the left side of the heart and delivering the blood to all other organs. The oxygenated blood coming from the lungs exits the small circulation through the pulmonary veins and enters the systemic circulation through the left side of the heart and the aorta. In the capillary beds, gas exchange between the blood and the body cells takes place: O_2 diffuses to the cells and CO_2, one of the main waste products, dilutes into the blood. The de-oxygenated blood is gathered by the systemic veins, which deliver it to the right side of the heart through the superior and inferior venae cavae. In this way, the blood exits the systemic circulation and enters the small circulation, guided to the lungs by the pulmonary arteries. In the lungs another gas exchange occurs, in which O_2 diffuses to the blood and CO_2 is eliminated by respiration. The oxygenated blood is ready to be delivered to the heart and all organs again and the loop closes. The fundamental action of the heart will be described in the next sub-section.

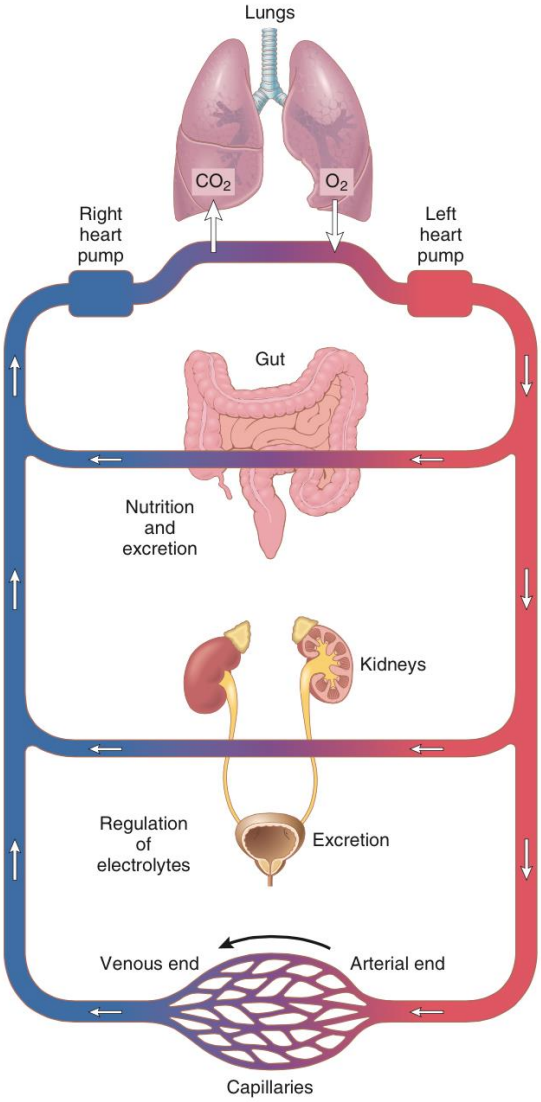

Figure 1.1: Schematic representation of the cardiovascular system. Taken from Hall (2015).

1.1.1 The heart cycle

The heart is a hollow organ divided into four cavities, two atria and two ventricles (Figure 1.2), grouped into two pumps, each of them formed of a combination of an atrium and a ventricle: the right pump pushes the blood into the pulmonary circulation and the left pump in turn pushes the blood into the systemic circulation.

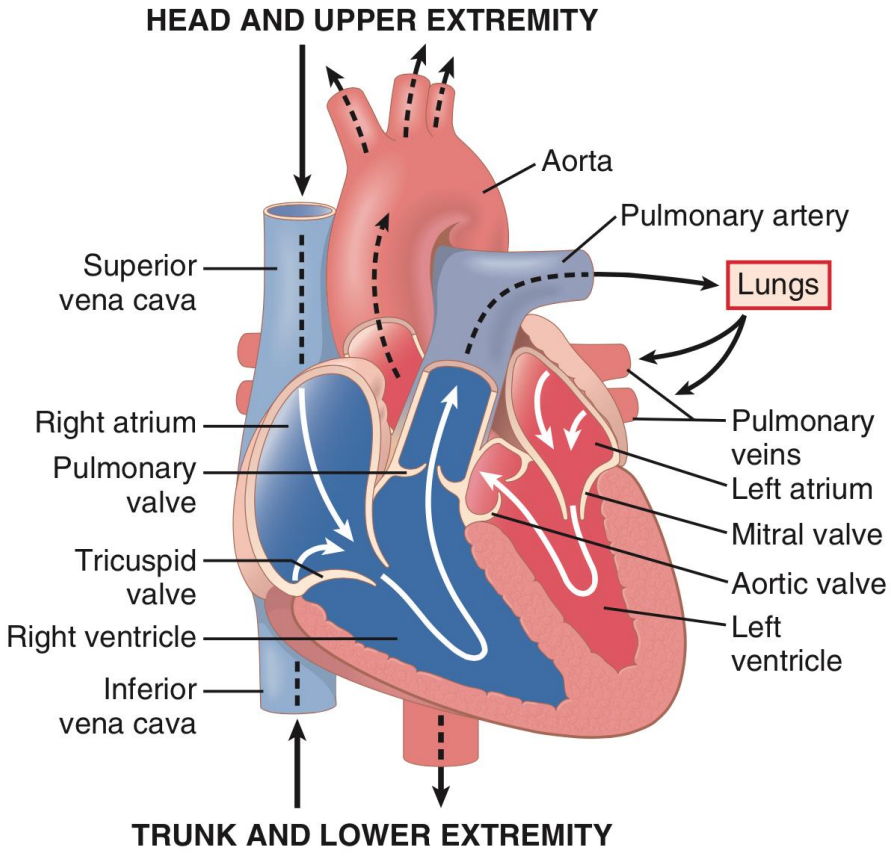

Figure 1.2: Schematic diagram of the heart, picturing the four cavities and the main vessels. Taken from Hall (2015).

A group of pacemaker cells located in the sinoatrial node (near the right atrium) is responsible for the generation of the rhythmic pulses that lead the whole organ to perform synchronized contractions. The pulses travel along the fibres of the conduction system, which includes the Bachmann's bundle (connecting the two atria), the atrioventricular node (which delivers the signals to the ventricles, through the bundle of His and its branches, and could also work as a pacemaker) and the Purkinje fibres (which transmit the electric pulses to the contracting cells of the ventricles). A characteristic periodic pattern of atrial, ventricular blood pressure and volume, and aortic pressure and volume, can be recorded. Its traces are plotted in the so-called Wiggers diagrams in Figure 1.3. The period of the heart cycles can vary according to the organism demands: the cardiovascular centre that controls the heart functions is located in the brainstem, it receives input signals from different sets of baroreceptors and chemoreceptors in the body and transmits the output through the parasympathetic (vague) and sympathetic nerves.

The heart cycle is substantially divided into systole and diastole, the latter being longer than, or at most equal (in some cases during high intensity exercise) to the systole. A description of the heart cycle in the left side of the heart follows:

- **Systole**: it begins when the mitral valve (between atrium and ventricle) closes. At this stage the ventricle is filled with blood, and in absence of inflow and outflow, as the aortic valve is also closed, the chamber experiences a rapid increment of pressure due to the myocardial contraction. This stage is called isovolumic contraction, as the ventricle's volume is unchanged. When the pressure gradient across the aortic valve becomes positive, in so far as the ventricular pressure becomes greater than the aortic pressure, the valve opens and the blood is discharged into the aorta. This phase is called ejection. During ejection, myocardial contraction still takes place and the ventricular pressure rises up to a maximum (around 120 mmHg). The aortic pressure "follows", with a slight inertial delay, the ventricular pressure until it reaches a maximum, which is lower than the aforementioned ventricular pressure peak. The ventricular volume rapidly decreases after the aortic valve opening, while in the late stage of ejection the volumic decrement is more gradual. When the aortic valve closes, because its pressure gradient becomes negative, the diastole begins. At the end of systole, a T-wave is registered in the electrocardiogram, due to ventricular repolarization.
- **Diastole**: the first stage of diastole is called isovolumic relaxation: both valves are closed, the ventricular volume does not change and a rapid decrement of pressure within the ventricle is brought by a rapid myocardial relaxation, up to the point when the ventricular pressure falls below the atrial pressure, which experienced, meanwhile, a substantial increment due to blood filling (through the pulmonary veins). The pressure gradient opens the mitral valve and the blood flows from the atrium to the ventricle whose volume rapidly, then gradually, rises, without a corresponding rise in pressure. The two stages described are called rapid inflow and diastasis, the latter being characterised by a plateau in both atrial and ventricular pressures and ventricular volume. At the end of diastasis, the P-wave is registered in the ECG, the atrial contraction takes place and a slight increment of atrial pressure, followed by a delayed increment in ventricular pressure of the same order of magnitude, is recorded, during the phase called atrial systole. During diastole, the pressure inside the aorta follows an exponential decay, due to the discharge of the aortic blood into the circulatory system. At the end of the atrial systole, the QRS-complex is registered, which triggers the ventricular contraction. As soon as the ventricular pressure rises above the atrial pressure, the mitral valve closes and systole begins again.

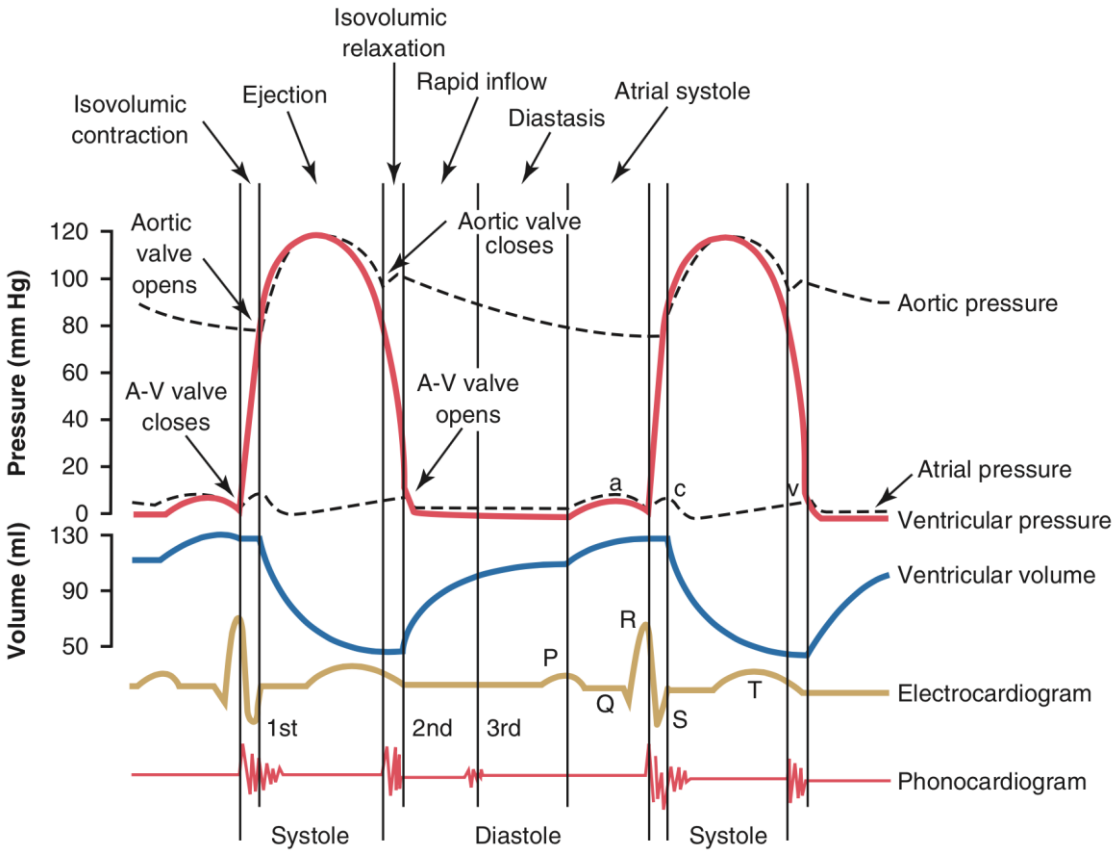

Figure 1.3: Wiggers diagrams for the left side of the heart. Taken from Hall (2015).

1.1.2 The arterial system

Three types of blood vessels are found in the body: arteries, veins and capillaries. The arteries deliver the blood away from the heart, whereas the veins carry the blood back toward the heart. Capillaries constitute a net of vessels surrounding organs where the exchange of nutrients and waste products takes place. The arteries and veins are substantially made of three layers: the innermost (tunica intima) has a polysaccharide intercellular matrix surrounded by endothelial cells, wrapped into a lamina of connective tissue; the tunica media is made of connective tissue, elastic fibres (surrounded by smooth muscles to control the lumen diameter), and another elastic lamina; the tunica adventitia, the outermost layer, is composed of connective tissue and contains nerves and nutrient capillaries in the larger arteries (the so-called vasa vasorum). The media is the thickest layer in the arteries, while the adventitia is the thickest layer in the veins.

The capillaries are constituted of endothelium and in some cases of connective tissue. Their internal diameter can range between 4 and 9 micrometres (Hall 2015).

Arterioles and venules are smaller arteries and veins, with internal diameter from 10 to 15 micrometres (Hall 2015) and surrounded by muscular layers, that bridge the large vessels to the capillary nets. The arterioles, because of their small diameter, constitute the primary site of vascular resistance. A schematic representation of the vessels is given in Figure 1.4.

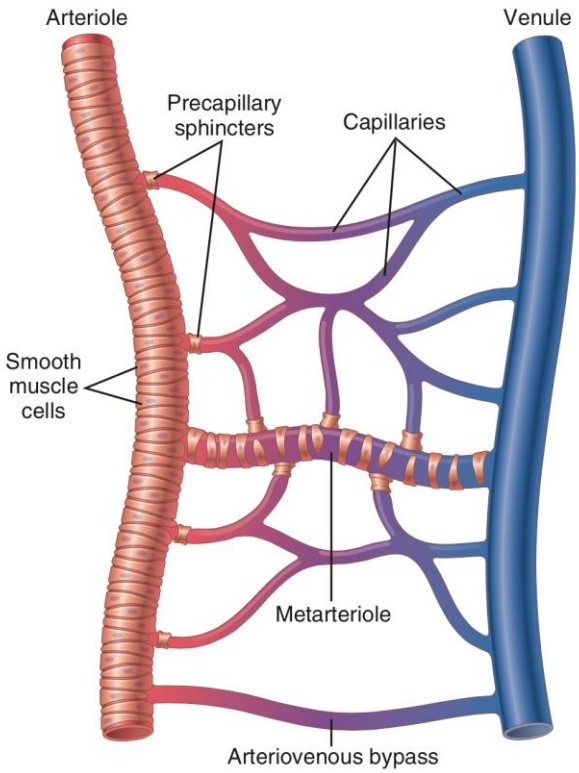

Figure 1.4: Schematic representation of the microcirculation. Taken from Hall (2015).

Different types of arteries exist, based on the proportional amount of elastic and collagenous fibres (Saladin 2007):

- **Elastic (or conducting) arteries**, the largest vessels in the body, such as the aorta, the pulmonary arteries, the common carotid, the subclavian and common iliac; they have a large amount of elastin and collagen in the tunica media, and proportionally a lesser amount of muscular fibres. This anatomical structure gives them the possibility of stretching under pressure, storing and releasing elastic energy to the blood, through the windkessel effect, thus contributing to transform the heart pulsatile outflow into a continuous flow in smaller vessels;

- **Muscular (or distributing) arteries**, smaller-sized than elastic arteries; they contain thick layers of smooth muscle and a lesser amount of elastin and collagen than elastic arteries. The windkessel effect is less pronounced and their controlled diameter, through local and central mechanisms, is essential to vascular resistance changes. Brachial, femoral, renal and splenic arteries are example of such type.

An important mechanical parameter related to the vessels, especially arteries, is the compliance C, defined as the ratio between the change in volume brought by a specific change in blood pressure. In differential notation $C = dV/dP$, where V is the reference volume of the vessel at a specific blood pressure P and $V + dV$ is the volume at $P + dP$. The compliance can also be written in terms of changes of cross-sectional area A, assuming that the length of the vessel does not change. Therefore, in differential notation it becomes: $C_A = dA/dP$. A related parameter is the distensibility D_s, defined as the ratio between the change in normalized volume, or cross-sectional area, brought by a specific change in blood pressure. In differential notation, the definition involving the areas reads: $D_s = (1/A)(dA/dP)$[1]. Distensibility and compliance are related, as $D_s = C_A/A$ for a specific reference area value (a similar identity holds if volumes are used), but the distensibility allows physicians to compare mechanical properties of different vessels with different sizes. The loss of elasticity leads to arterial stiffening and decrease of distensibility. Arterial stiffening is a natural process occurring with age (Franklin et al. 2001) and is linked to hypertension and related cardiovascular diseases (Benetos et al. 1997; Arnett et al. 2000; Franklin et al. 2005).

The understanding of cardiovascular physiology was a gradual historical process (that still goes on) that borrowed theoretical frameworks from different disciplines, for example fluid mechanics. A brief overview of the breakthroughs is given in the next section, with a major focus on wave propagation in the arterial system.

1.2 Wave propagation in the cardiovascular system

A wave is a form of transfer of energy in space and time, which may happen through a medium. This is specifically the case of mechanical waves and involves, therefore, oscillation of matter. Mechanical waves travel as a disturbance of a given physical quantity originating from the balance of deforming and restoring forces in the medium. In the cardiovascular system the physical quantities propagating as waves are blood pressure,

[1] The units of distensibility do not change if either the volumes or the areas are used for the definition: [Pa^{-1}] in SI.

blood flow velocity, vessel diameter and other related / derived parameters. The media involved in this process are the vessel tissues and the blood mass, which have different densities.

The modern foundations of fluid mechanics, the broad framework which includes the mechanical wave theory in fluids, have been posed during the 17^{th} – 18^{th} centuries. As Tokaty (1971) stated: *"Newton was the first to cement the foundation of the edifice, Euler to erect its walls and floor, and Lagrange to add all, or almost all, those other major parts which make an edifice a safe and rather enjoyable house"*. The successful theoretical framework developed in those years helped many investigators to pose the basis of the arterial fluid mechanics and quantitative physiology. Ancient civilisations reached a strikingly good body of anatomical knowledge about the cardiovascular system (Parker 2009a). For example, Galen, the Greek physician, studied the arteries, including the coronaries, the veins and the capillaries and worked on the propagation of pulse (Karamanou et al. 2015). However, he did not understand the circulation and the prominent role of the heart. His work influenced all the Medieval medicine, until the Renaissance period. The first modern observations and studies on the circulation were made by Harvey (1628) who first understood that the cardiovascular system is a closed system. Borelli (1680) first described the capacitive behaviour of the elastic arteries, and Hales (1733) provided for the first time an in-vivo measurement of blood pressure[2], but was Euler that in 1775 published a paper entitled *Principia pro motu sanguinis per arteria determinando* (literally: the principles for determining the flow of the blood through arteries) (Euler 1775) in which he derived the one-dimensional equations for the wave propagations in the elastic arteries. However, he could not fully solve them for the lack of techniques available at that time. He also posed some constitutive laws (usually called "tube laws" in modern jargon), that were corrected almost a century later by Hagen (1839) and Poiseuille (1846). Further studies by Hagenbach (1860) and other investigators refined the equations; an account of these discoveries can be found in Sutera & Skalak (1993).

Frank was one of the most successful physiologists, and his contribution led to the body of knowledge available nowadays (Parker 2009a). He developed the Windkessel formulation accounting for the arterial compliance (Frank 1899) and developed the theory of waves in arteries. Frank's theory of waves constituted the background from which McDonald and Womersley developed the impedance analysis, discussed in the following section.

[2] Hales cannulated a horse's neck to quantitatively visualize the movements of the blood in the cannula during the cardiac cycles.

1.2.1 Impedance analysis

Considerations about the nature of flow in the arteries led to the development of the impedance analysis. McDonald (1952) studied the rabbit aortic flow and discovered that during systole turbulences occur, despite the experimental studies of Hess (1917), who studied dogs' aortic flow, and Ralston et al. (1947) who studied cats' arterial flow. He also found backflow in the rabbit aorta and eddies at its bifurcation, and further investigations led to the analysis of phasic changes in the arterial flow and pressure oscillations in the canine femoral artery (Mcdonald 1955), reaching the conclusions that the blood flow and the pressure gradient are oscillatory in nature. They are, therefore, amenable of decomposition in the frequency domain by Fourier analysis. Encouraged by these discoveries, Womersley (1955; 1958) developed a theoretical framework for the description of the blood flow, "borrowing" the mathematics behind the distribution of alternate currents in conductors, in which currents and voltages have their direct analogies with flows and pressure gradients in the arterial system, respectively. Womersley's theory, in particular, recalls the Poiseuille's law only in steady-state condition and it represents its generalisation. The new technique, called impedance analysis and originated by both McDonald's and Womersley's works, was advanced by some other investigators, such as Taylor (1966a; 1966b) O'Rourke (O'Rourke and Taylor 1967; O'Rourke 1982) and Westerhof et al. (1969; 1971; 1972) who separated pressure and flow into forward and backward (reflected) components.

Assuming the cardiovascular system in a steady state oscillation, driven by the cardiac repeated beats, arterial pressure and flow waveforms can be decomposed using the Fourier analysis. In this way, both waveforms will be equal to the summation of a time-averaged value and a (theoretical) infinite set of sinusoidal components with specific amplitudes, frequencies and phase shifts. The ratio between the Fourier transforms of pressure, $\tilde{P}(f)$, and flow, $\tilde{Q}(f)$, measured at the inlet of an artery is called input impedance $Z_{in} = \tilde{P}(f)/\tilde{Q}(f)$, and it includes contributions of reflected waves. The characteristic impedance Z_0 of the artery is defined as the ratio of forward components of pressure and flow transforms, thus eliminating the effect of reflections. It is practically calculated by neglecting the lower harmonics of the input impedance, as higher frequencies correspond to higher dissipation of reflected waves (Westerhof et al. 1972). The characteristic impedance is then related to the wave speed c, the speed at which the pulse propagates (essential for the wave separation), through the formula: $Z_0 = \rho c/A$, where A is the cross-sectional area of the vessel and ρ the blood's density.

However, Fourier analysis is not able to give any information about location of events associated to each frequency component in the time domain; therefore, it is not

possible to use it in case of transient or non-periodic flow. The two main assumptions behind the impedance analysis are the linearity (in so far as the waves interact additively) and steady-state oscillatory mode of the cardiovascular system, although Parker (2009b) suggested that the cardiovascular system is over-damped and each heart beat should be considered as an isolated event, that happens to occur periodically because of the regularity of the cardiac functions. For these reasons, a new mathematical analysis called Wave Intensity Analysis (WIA) was developed, which will be the object of the next section.

1.2.2 Wave Intensity Analysis

The German mathematician Riemann (1860) was able to develop a theoretical tool, the so-called method of characteristics, to solve hyperbolic partial differential equations, such as the ones developed by Euler for the arterial mechanics. Anliker et al. (1971) used this method for the first time to explain the arterial wave propagation and this work led Parker & Jones (1990) to develop wave intensity analysis (WIA), which does not assume periodicity and linearity and it is totally carried out in the time domain. A derivation of the fundamental equations of WIA from general principles, such as the laws of momentum conservation and mass conservation, and of the method of characteristics, will be discussed in the Chapter 2.

The wave intensity dI (sometimes labelled as WI) is calculated as the product of changes in pressure and velocity, as $dI = dPdU$, and has S.I. units of W/m^2, representing the energy flux carried by the wave. The wave energy carried in a specific time interval $T = t_2 - t_1$ can be found as the integral of the wave intensity over T: $I = \int_{t_1}^{t_2} dIdt$.

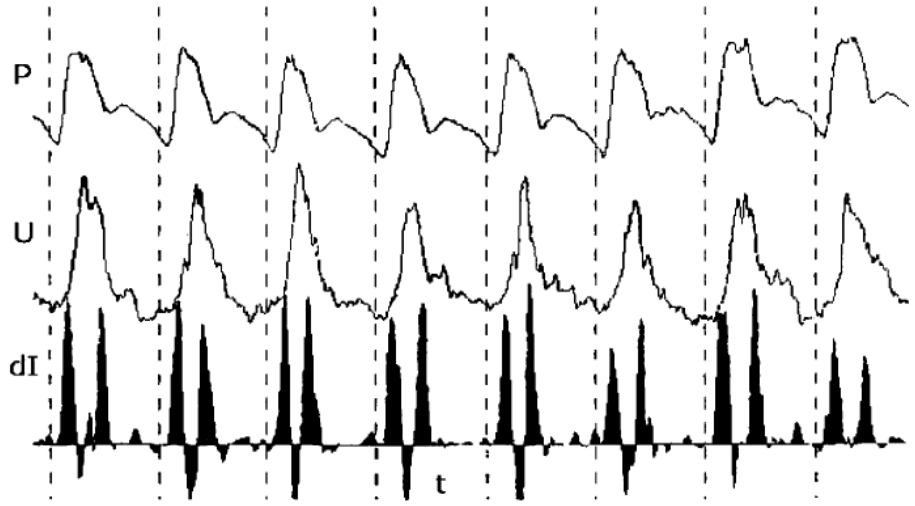

Figure 1.5: First measurement of WIA in man. P: pressure, U: velocity, dI: wave intensity. The dotted lines represent the separated beats. Taken from Parker et al. (1988), as modified by Parker (2009b).

In Figure 1.5 the first measurement of dI in a man is shown. Three main features are visible: the first two positive peaks, namely the forward compression wave (FCW) and the forward expansion wave (FEW), and a prominent negative peak, the backward compression wave (BCW). These three waves, found in systole, are related to specific events of the cardiac cycle, as will be discussed in the following sections: the FCW is related to the contractility of the left ventricle at the beginning of systole; the FEW is linked to the decrease of shortening velocity of the ventricle in late systole, before the relaxation takes place; the BCW is attributed to the reflection of FCW at a downstream vascular bed.

1.3 Determination of wave speed

The estimation of the wave speed value, also called pulse wave velocity (PWV) in the clinical environment, is crucial for the wave separation. Wave speed is a measure of arterial stiffness, which has a prognostic and diagnostic value, as it is an independent predictor of stroke and cardiovascular mortality in hypertensive patients (Laurent et al. 2001; 2003). First theoretical calculations of the wave speed in an artery were given by Thomas Young (1808), followed by the theoretical and experimental work of the Weber brothers (Weber and Weber 1825; Weber 1866). In all these studies, the wave speed was associated with the elastic properties of the artery and the density of the blood. Moens (1877) and Korteweg (1878) later developed another equation for the wave speed in thin-walled tubes after a theoretical and experimental work. It is interesting to note that both Young-Weber and Moens-Korteweg formulations define the wave speed as a square root of a ratio;

however, the latter has the elasticity contribution (Young's modulus of the vessel wall) plugged into the numerator and the radius of the vessel into the denominator, whereas the former includes the elasticity contribution (radial distensibility) into the denominator and radius into the numerator.

Frank (1920) derived the wave speed by only taking account of the distensibility D_s of the vessel and the density of the blood: $c = \sqrt{(\rho D_s)^{-1}}$. Bramwell & Hill (1922) developed the same equation, with a slight change in the definition of distensibility: while Frank defined it as a change in normalized cross-sectional area of the vessel driven by an elementary change in pressure, Bramwell and Hill defined it as a change in normalized volume driven by an elementary change in pressure: $D_s = dV/(VdP)$. However, the length of the vessel is assumed not to change during physiological pressure perturbations; then the two formulations are substantially the same.

By considering the following assumptions:

- Isotropic elastic arterial wall;
- Incompressible inviscid (ideal) fluid;
- Thin wall ($\frac{h}{2R} \leq 0.1$, where h is the wall thickness and R the radius of the vessel);

the Moens-Korteweg equation can be derived: $c = \sqrt{\frac{E_{circ}\, h}{2R\rho}}$, where E_{circ} is the Young modulus in the circumferential direction. Further refinements of this equation, especially by dropping the thin wall hypothesis, led Bergel (1960; 1961a; 1961b) to formulate an equation including the Poisson's ratio σ of the vessel: $c = \sqrt{\frac{E_{circ}\, h}{2R\rho}(1 - \sigma^2)}$, whereas Hughes et al. (1979) showed that the elastic modulus of the aorta increases exponentially with the pressure, so that $E_{circ} = E_0 e^{\varphi P}$, with φ depending on the particular vessel and animal species and E_0 being a reference elastic modulus. Bramwell-Hill and Moens-Korteweg equations can be useful to determine the elastic properties of the vessel by knowing the local wave speed, or vice versa, although the direct estimation of mechanical properties in vivo is rather challenging.

The most common method to calculate the wave speed in clinical environment is the foot-to-foot method, which only requires the measurement of the pressure waveform in two different locations, usually carotid and femoral arteries. The foot of a wave is defined as the point, at the end of diastole, where the steep rise of the wavefront begins. Although it is easy to quantify the foot-to-foot wave speed, it can be only an unrefined estimation, as it represents an average over all the intermediate vessels between the chosen points, therefore a surrogate of the stiffness of the large arteries.

Local techniques suitable for wave intensity have been recently developed, and they are based on the simultaneous measurements of blood pressure and velocity, or vessel diameter and blood velocity, at the same location. This set of measurements is not difficult anymore, even in a clinical environment. An overview of these local techniques will be given in the next section.

1.3.1 Local techniques for the determination of the wave speed

The most important techniques are the PU-loop, the $lnDU$-loop, the sum of squares, the QA-loop and the D^2P-loop.

PU-loop: It was first developed by Khir et al. (2001) and assumes only forward waves travelling in the artery in early systole. Its mathematical formulation is associated to the water-hammer equation, that will be discussed in Chapter 2, and reads: $dP_{\pm} = \pm\rho c\, dU_{\pm}$. The wave speed c can be calculated by plotting the pressure against the velocity over the whole cardiac cycle and estimating the slope of the linear part, associated to the early systolic period. The blood density ρ is assumed constant. Figure 1.6b shows an example of PU-loop.

lnDU-loop: this technique is based on diameter and velocity measurements. It allows the calculation of the wave speed by computing the ratio between the change in forward (or backward) velocity occurring for a given change in logarithmic forward (or backward) diameter: $c = \frac{1}{2}\frac{dU_{\pm}}{d\ln D_{\pm}}$. Its formulation recalls the PU-loop. Assuming a reflection-free early systolic period, the slope of the linear part of the $lnDU$-loop can be related to the wave speed. Figure 1.6a shows an example of $lnDU$-loop. Chapter 2 will focus more in detail on this technique.

Sum of squares: In short arterial segments, such as coronary arteries, reflected waves become prominent, therefore Davies et al. (2006) developed a method, called sum of squares, to minimise the net wave energy for a specific value of ρc. By applying the water-hammer equation, they assumed that the product $\sum dU_+ dU_-$ is small compared to $\sum[(dU_+)^2 + (dU_-)^2]$, in which the sums extend over the whole cardiac cycle, and obtained the following equation for the wave speed: $c = \frac{1}{\rho}\sqrt{\frac{\sum dP^2}{\sum dU^2}}$.

QA-loop: Rabben et al. (2004) found an equation for c without the need of a pressure waveform. Given a reflection-free period in the cardiac cycle, the wave speed can be estimated as the ratio between the change in flow and the corresponding change in luminal area. A loop can be drawn by plotting the flow against the luminal area, in order to calculate

the slope of the linear portion, which corresponds to c. This technique is therefore called QA-loop.

<u>D^2P *loop:*</u> The slope of the linear part of D^2P-loop, corresponding to the late diastolic period, can be used to calculate the wave speed, assuming the arterial wall to be a Voigt type visco-elastic material (Alastruey et al. 2011): $c = D_0\sqrt{dP/\rho \cdot d(D^2)}$, where D_0 is the mean arterial diameter.

Validation of these so-called one-point techniques has been performed numerically (Alastruey et al. 2011; Swillens et al. 2013) showing that the sum of squares only performs well close to reflection sites and that, although PU-loop, QA-loop, $lnDU$-loop and D^2P-loop perform well and uniformly in elastic tubes, they significantly differ in realistic geometries, because of the presence of the reflections. The D^2P-loop gave the smallest difference between estimates and theoretical values, although it has only been tested using a Voigt-type model for the arterial wall (Alastruey et al. 2011). Moreover, the PU-loop tends to overestimate the wave speed, whereas QA-loop and $lnDU$-loop to underestimate it. In fact, an in-vitro study by Borlotti et al. (2014) showed that the PU-loop overestimated the wave speed close to a positive reflection site and underestimated it close to a negative reflection site, with the opposite holding true for the QA- and $lnDU$-loops. Based on these observations, Segers et al. (2014) developed a method based on three simultaneously acquired waveforms (P, U, D) to compensate the reflections and showed that the "corrected" wave speed, calculated by neglecting the higher harmonics of the signals, produced better results than any other technique, both numerically and in-vivo, against reference values obtained from the Bramwell-Hill equation. However, the need of direct and simultaneous measurements of P, U and D at the same location makes the application of this new methodology quite challenging in the clinical environment.

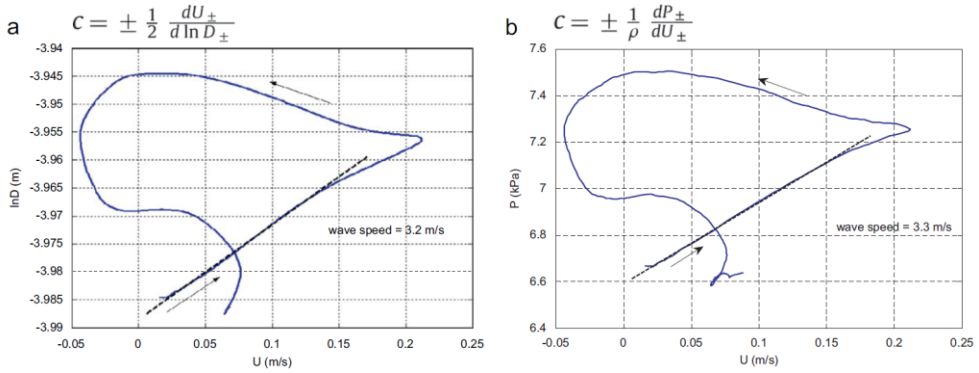

Figure 1.6: Comparison between lnDU-loop (a) and PU-loop (b) in vitro (measurements taken from a latex tube being filled with water and receiving a half-sinusoidal pressure pulse at the inlet). Dashed lines indicate linear portions in both loops and arrows indicate the direction of the loops. Taken from Feng & Khir (2010).

1.4 Invasive and non-invasive measurements of pressure and velocity

Measures of blood pressure and flow velocity waveforms are needed to perform WIA. The first studies were inherently invasive, performed on humans (Parker et al. 1988; Parker & Jones 1990; Jones et al. 1992) and dogs (Jones et al. 2002) through catheter-mounted pressure and velocity transducers. However, non-invasive methodology was required for WIA to become a clinical tool. The relationship between pressure and diameter was already established to be linear in animal experiments with dogs (Barnett, Mallos and Shapiro 1961; Patel et al. 1963). In a small cohort of patients with cardiovascular disease, Sugawara et al. (2000) found out that the pressure-diameter relationship in the human carotid artery is relatively linear throughout the whole cardiac cycle, with slight differences in systole, a small delay in diastole and a slight degree of hysteresis. They concluded that the relationship could be regarded as linear for practical purposes. Thus, a surrogate of the blood pressure waveform started to be used, obtained by echo-tracking the vessel diameter and scaling the waveform against systolic and diastolic brachial pressure values recorded via cuff-type manometer. The measurements of blood velocity were straightforward because of the development of clinical Doppler system, mounted on ultrasound machines. Niki et al. (2002) tested the new non-invasive methodology and found out that the overall reproducibility was clinically acceptable, although FCW and FEW showed too high variability. The authors also suggested to let the subjects rest in the supine position before recording, in order to obtain stable data. The main problem of this approach is that the carotid waveforms are calibrated with brachial pressure data. Because every vessel experiences different pressure and diameter change patterns during the cardiac cycle, the calibration of a diameter waveform over pressure values recorded from a different artery brings a substantial inaccuracy.

To overcome this problem, arterial applanation tonometry for the measurement of blood pressure started to be used in WIA studies. This methodology consists of applanating (flattening) the corresponding artery to get the intraluminal pressure by a strain gauge-tipped pencil probe (Matthys & Verdonck, 2002; Matthys et al. 2002), and its accuracy and reproducibility have been increasing since its first development (Drzewiecki et al. 1983). Zambanini et al. (2002) applied for the first time the applanation tonometry to perform non-invasive WIA. They established reproducibility of WI parameters of carotid, brachial and radial arteries in a cohort of treated hypertensives and found that, although FCW, BCW and FEW waves were reproducible, the mid-systolic X-wave had high variability. Later, Zambanini et al. (2005) quantified WI parameters in carotid, brachial and radial arteries of healthy volunteers, and Curtis et al. (2007) applied the same technique to assess the

differences in carotid WI parameters between healthy subjects and patients who had chronic heart failure. They discovered that FCW was reduced in magnitude in the patients' cohort, and BCW was increased, thus maintaining the systolic blood pressure but placing an additional load on the heart. Despite the use in the research and clinical fields, this methodology has an important shortcoming that limits its range of applications: the flow velocity is not recorded simultaneously with the pressure waveform. In rapid physiological perturbations, such as the ones introduced by exercise conditions, the concurrent recording of pressure and velocity cannot be given up.

1.5 The DU approach

Feng & Khir (2010) developed the DU approach to overcome those problems, related to the non-simultaneity of the measurements and the scaling of the diameter waveform. The DU approach is based on direct measurements of vessel diameter and blood flow velocity and the "non-invasive" wave intensity (often labelled as dI_n) is defined as $dI_n = dDdU$, dD and dU being the derivatives of the diameter and velocity, respectively. Wave intensity dI_n retains the same advantages as the original wave intensity $dPdU$, being positive for forward waves and negative for backward waves. This technique has been validated in vitro (Feng & Khir, 2010; Li & Khir, 2011) and in vivo (Borlotti et al. 2012).

1.6 The Reservoir-Wave approach

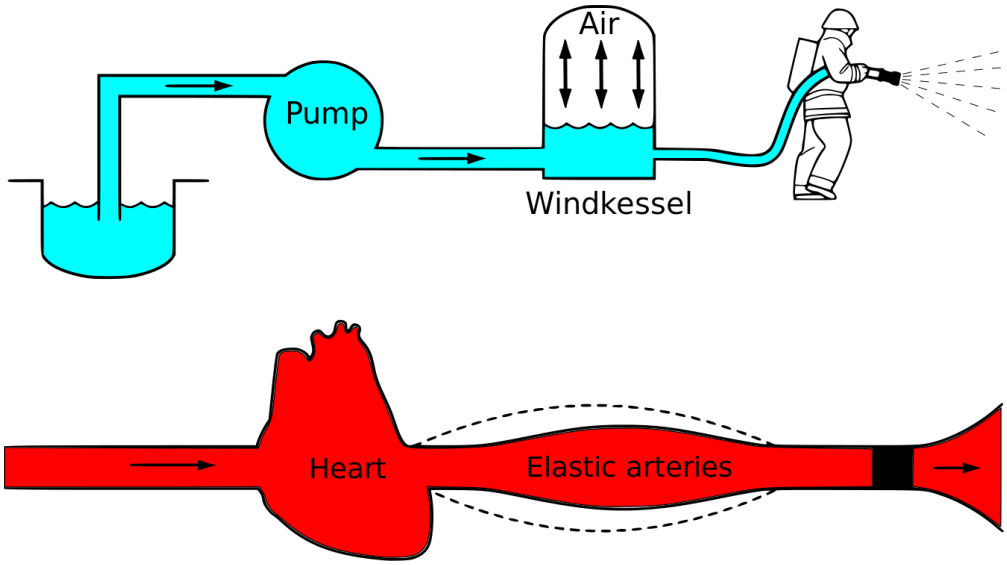

Figure 1.7: Visual explanation of the Windkessel effect. Schematic working principle of a fire-engine pumps (top) and arterial reservoir (bottom). Taken from: Kurzon. Licence: CC BY-SA 3.0.

Otto Frank was the first scientist to describe the Windkessel effect (Frank 1899) inspired by the experimental results of Hales and the work of Borelli. The Windkessel effect (air chamber, in German) is a "pushing action" in diastole, due to the (visco)elastic recoil of the artery, after being radially stretched by the blood in systole (see Figure 1.7). In diastole, shortly after the aortic valve closes, the proximal aortic flow falls to zero, while pressure remains high. The "wave-only" approach can explain this phenomenon only by considering a set of self-cancelling diastolic forward and backward waves, which don't have a realistic biological cause (Davies et al. 2007). Almost 40% of the stroke volume ejected during systole is stored in the arterial "reservoir" (Wang et al. 2003): this happens because the blood flow at the inlet of the arterial system is greater than the flow at the outlet, due to peripheral downstream resistance. During diastole, when the heart's pumping ceases, the artery releases the stored energy, which is transferred to the blood flow.

The Windkessel effect, also called "arterial reservoir effect" or "arterial cushioning", contributes to convert the pulsatile flow into a continuous flow in the arterial tree and helps the perfusion of organs. One of this organ is the heart itself, as most of all coronary flow happens during diastole [partly attributed to the arterial reservoir and partly attributed to a local suction effect triggered by the myocardial relaxation (Spaan, Breuls and Laird 1981; Justin E. Davies et al. 2006)].

Frank considered the artery as a compliant chamber, inspired by the working principles of the early fire-engine pumps (Parker, 2009a), as depicted in Figure 1.7. The equation of mass conservation for all the arterial system in diastole (when no flow comes from the heart) reads: $dV/dt = Q_{in} - Q_{out} = -(P - P_{\infty})/R$, in which R is the arterial resistance to the flow, Q_{in} and Q_{out} the incoming and outgoing flows, respectively (with $Q_{in} = 0$ in diastole), P the pressure at the inlet and P_{∞} the pressure level at the microcirculation. In particular, although R is the resistance of the overall arterial system, it mainly represents the resistance of the microcirculation: in fact, according to the Poiseuille's law, the resistance depends on the fourth power of the vessel radius at the denominator, making the contribution of the small vessels very high. By recalling the compliance $C = dV/dP$, the equation for the exponential decay of pressure in diastole can be obtained: $P(t) = (P_0 - P_{\infty})exp(-t/\tau) + P_{\infty}$, where τ is the time constant, equal to RC, and P_0 is the pressure at the beginning of diastole ($t = 0$). In the first models, P_{∞} was assumed to be null. While the resistance is lumped into the microcirculation, the compliance is more concentrated into the large elastic arteries, in particular the proximal aorta.

Despite the successful description of the behaviour of pressure in diastole, the Windkessel model could not explain the pressure waveform in systole and assumed all the arterial system acting as a single chamber, without wave propagation. Frank was aware of

this dichotomy but could not explain it, although he tried to solve the model by incorporating an incoming constant or sinusoidal flow from the heart during systole (Parker 2009a). After the development of electromagnetic flowmeters and the application of impedance analysis to the arterial flow, Westerhof (1972) introduced a new element in Frank's model, the aortic impedance Z_0, which is defined as the ratio between forward aortic pressure and flow for each harmonic component, and is equal to $\rho c/A$, A being the aortic cross-sectional area. When reflected waves are absent, the ratio between measured pressure and flow for each harmonic (input impedance Z_{in}) is equal to Z_0 (Westerhof et al. 1972). The so-called three-element windkessel model took account of wave aspects through the wave speed c, included in the aortic impedance, and was able to predict the pressure waveform throughout all the cardiac cycle; however, some high-frequency components, such as the inflection point and the second peak[3], could not be described (Westerhof, Lankhaar and Westerhof 2009). Further development led to a four-element Windkessel, by Burattini & Gnudi (1982) and Stergiopulos et al. (1999), by introducing the arterial inertance L, which modifies the low-frequency components of the pressure waveform, although its difficult estimation in the arterial system prevented the model to become successful in practice (Westerhof, Lankhaar and Westerhof 2009).

The first hybrid theory which modelled both the arterial cushioning and the wave propagation in the time domain was due to Wang et al. (2003). Following Lighthill (1978), it assumed that aortic pressure P_{ao} is an instantaneous summation of a reservoir pressure P_r and wave pressure (or "excess" pressure) P_{ex}, so that $P_{ao}(x,t) = P_r(x,t) + P_{ex}(x,t)$ at any time during the cardiac cycle and at any location along the aorta[4]. The investigators found that P_r was proportional to the aortic volume and P_{ex} resembled the aortic flow waveform.

1.6.1 The Reservoir-Wave approach at any arbitrary location

The generalisation of the reservoir-wave approach to any location in the arterial tree was made by Aguado-Sierra, Alastruey, et al. (2008). They assumed that the pressure diastolic decay at all locations in the arterial tree is very similar and the linear relationship between P_{ex} and Q_{in} holds in all arteries, considering that the arterial bifurcations should be close to well-matched for forward waves. The same investigators also developed the reservoir-wave approach for the velocity U, defining reservoir and excess velocities. It is

[3] The second peak of pressure is used to calculate the augmentation index, which has a clinical value.
[4] In literature the reservoir/windkessel pressure is labelled as P_{wk} or P_r, whereas the excess/wave pressure is labelled as P_{ex} or P_e.

important to consider that the reservoir pressure is generally obtained through a fitting procedure and there is currently no consensus over the fitting method that should be used. Several investigators used, in fact, different fitting windows, such as the whole diastolic period (Aguado-Sierra, Alastruey, et al. 2008), its last two thirds (Wang et al. 2003; Davies et al. 2010) or its last third (Bia et al. 2011; Wang et al. 2011), as well as a different number of free-fitted parameters (Wang et al. 2003; Aguado-Sierra, Alastruey, et al. 2008). In some cases, the asymptotical pressure value was fixed to a specific value (Aguado-Sierra, Alastruey, et al. 2008; Aguado-Sierra, Davies, et al. 2008; Vermeersch et al. 2009).

1.7 Clinical value of wave intensity analysis

Parker et al. (1988) applied WIA for the first time on pressure and velocity waveforms recorded in a human ascending aorta and suggested that the heart actively decelerates the blood flow in late systole, against the generally accepted idea, at that time, that the reflected waves are important determinants of the flow deceleration. They discovered the forward expansion wave in late systole, generated by the left ventricle, suggesting that it was the primary cause of blood deceleration and aortic valve closure. Later, Jones et al. (1992) showed that WIA in humans has a quantitative meaning, as the peaking and steepening of the forward compression wave, as well as the broadening of the forward expansion wave, are the main contributors to the pressure wave amplification seen in the arterial tree, running toward the periphery. Jones et al. (2002) performed pharmacological experiments on anesthetized dogs to find that the peak of forward compression wave is quantitatively related to the inotropic state of the ventricle, hence to the ventricle contractility, and is reduced during vasoconstriction, while the forward expansion wave is insensitive to the inotropic state of the ventricle but is reduced during vasodilation. A theoretical explanation was given by Ramsey & Sugawara (1997): the forward compression peak is linearly proportional to $\rho^{-1}c^{-1}\max(dP_v/dt)^2$, where dP_v/dt is the rate of left ventricular pressure increase, while the forward expansion peak is linearly proportional to $\rho c\max(dU_a/dt)^2$, dU_a/dt being the aortic deceleration toward the end of ejection. Therefore, the forward compression wave is related to the cardiac contractility and the arterial compliance (through c), while the forward expansion wave is related to the arterial compliance, the inertia of the blood flow towards the end of ejection and the cardiac relaxation. WIA has also been extensively applied to other locations rather than aorta, such as coronary, femoral, and carotid arteries (which is the topic of the next section), to explore various physio-pathological conditions.

1.8 Carotid wave intensity analysis

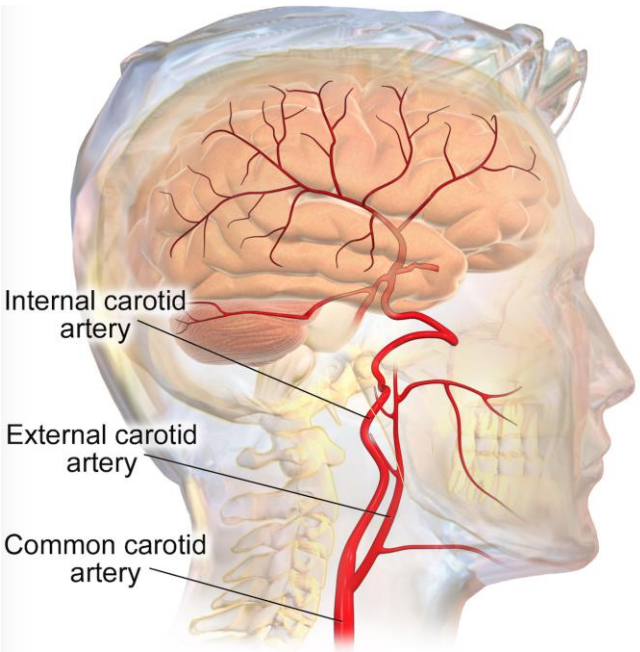

Figure 1.8: Common carotid artery and its bifurcation. Modified from: Blausen, Medical gallery of Blausen Medical 2014. WikiJournal of Medicine. License: CC BY 3.0.

The common carotid artery (schematically depicted in Figure 1.8) is anatomically more accessible than the aorta or the coronaries, therefore it was used for physiological investigation since the beginning of the development of WIA. Forward waves detected in the carotid artery are generated by the left ventricle and travel along the aortic arch before reaching the left and right common carotid arteries. Backward waves are generated from the head vasculature, consisting of the cerebral microvasculature and the vessels of other head tissues and organs, such as skin, meninges, eyes, tongue and salivary glands.

The first WIA study in the carotid artery was performed by Niki et al. (1999) in patients suffering from mitral regurgitation, a condition in which the mitral valve leaks and allows blood flow towards the left atrium. They found that peak of FEW significantly decreases before patients undergo surgery, but it increases to the values in the range of the healthy group after surgery. This suggests that the left ventricle can recover the ability to actively stop aortic blood flow by decelerating myocardial shortening, possibly due to the absence of leakage in the left atrium after surgery.

In dilated cardiomyopathy (DCM) the systolic cardiac performance is impaired. Siniawski et al. (2002) and Sugawara et al. (2009) found that there is a significant lowering of peak of FCW in patients suffering from DCM. Siniawski et al. (2002) found there is also a significant decrease of FEW peak, which was not observed by Sugawara et al. (2009). The

same investigators also demonstrated that DCM patients are less tolerant of orthostatic stress than healthy and transplanted patients, and that the values of FCW peak significantly decreases with age in those patients (Sugawara et al. 2009). In hypertrophic cardiomyopathy (HCM) the diastolic function is impaired. The peak of FEW is significantly smaller in patients with HCM, while the FCW peak is not significantly different, although it shows a decrease with age, which suggests deterioration of cardiac performance in those patients.

In hypertensive (HT) patients, Sugawara et al. (2009) showed that BCW energy is greater than in a control group, although reflections from the head do not augment aortic pressure, suggesting an enhanced cerebral vasomotor tone. Also, BCW energy is related to maximum flow velocity in the carotid artery (which indicates a more sensitive autoregulation in HT patients).

Ohte et al. (2003) demonstrated that the amplitude of FCW in the carotid artery strongly correlates with left ventricle contractility, awhile patients with chronic heart failure have a significantly decreased FCW (Wen et al. 2010) as well as decreased FEW. Fujimoto et al. (2004) also found that the magnitude of FCW is related to the vascular tone: HT patients treated with doxazosin (an antihypertensive pharmacological agent able to decrease peripheral vascular resistance), showed a significant increment of FCW and FEW and a decrement of BCW, which also correlates with the change in mean blood pressure before and after the treatment.

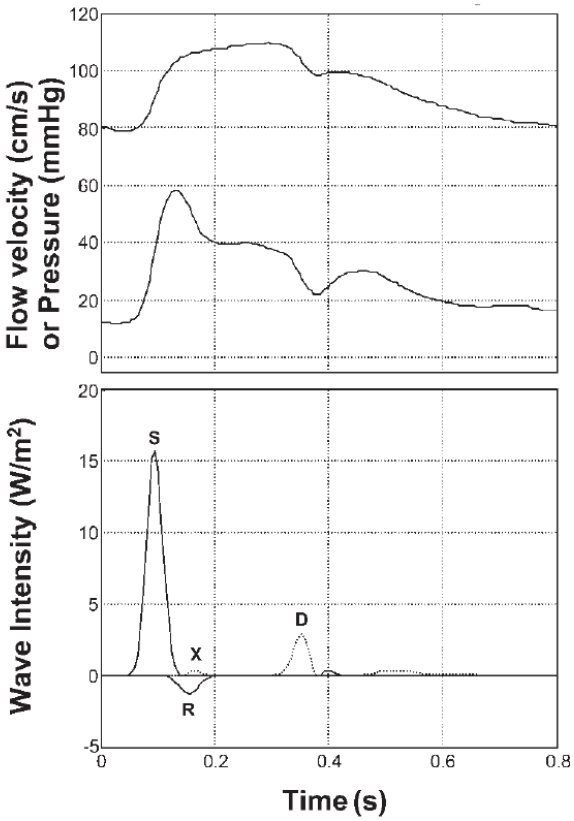

Figure 1.9: Measured pressure and flow velocity waveforms (top) and wave intensity (bottom) from human carotid artery. S,R,D stand for FCW, BCW and FEW peaks, respectively. X indicates the X mid-systolic wave. Taken from Zambanini et al. (2005).

Peripheral arteries in general exhibit a pattern of mid-systolic waves, with magnitudes and peaks substantially smaller than those of FCW and FEW (Zambanini et al. 2005; C. H. Manisty et al. 2009; C. Manisty et al. 2009). This mid-systolic sequence was paid little attention by the first investigators (Niki et al. 1999; 2002; Bleasdale et al. 2003; Ohte et al. 2003), allegedly due to the importance of studying the main peaks at that time and to the small size of the mid-systolic waves that could be ignored as artefacts. Zambanini et al. (2005) first described and quantified the X-wave at many locations including the carotid artery (see Figure 1.9). The X-wave is generated as reflection of BCW at the inlet of the aortic arch. As the X-wave is not seen in the ascending aorta, it is unlikely generated by the ventricle. The change in cross-section between the common carotid and the aortic arch is considerable[5], therefore the "open-end" type reflection of BCW produces a forward expansion wave. Also, its peak increases towards the periphery (Zambanini et al. 2005). Other types of wave, such as backward expansion waves (BEW), were studied in the pulmonary artery (Hollander et al. 2001) and the coronary arteries (Sun et al. 2000), and

[5] The right common carotid artery, before reaching the aortic arch, meets the right subclavian artery to form the brachiocephalic artery, which connects to the aortic arch. The left common carotid artery, instead, is directly connected to the aortic arch.

quantified in the carotid in control and pharmacologically treated groups by Manisty et al. (C. H. Manisty et al. 2009; C. Manisty et al. 2009).

Bleasdale et al. (2003) demonstrated that the BCW measured from carotid artery reflects changes in cerebral vasomotor tone, through a study involving healthy volunteers under hypercapnia condition, which causes cerebral vasodilation. Cerebral vasodilation is therefore related to a decrease in magnitude of carotid BCW and a decrease in the reflection coefficient, calculated as the ratio between the magnitude of BCW over the magnitude of FCW. However, the forward compression seems to be not significantly affected by the hypercapnia condition.

Swampillai et al. (2006) studied the effects of caffeine and nicotine on left ventricular function through carotid WIA and found an increase in wave speed and magnitude of the FCW, while BCW and FEW remained unchanged, after caffeine consumption. This suggested sympathetic effects on the left ventricular function. Smoking did not affect the wave intensity, but it acutely increased local arterial stiffness, suggesting an increase in systolic loading on the left ventricle.

Yan et al. (2012) conducted a study aiming to investigate changes in wave intensity parameters during fire-fighting duty, in the context of analysing possible grounds for sudden cardiac events, the leading cause of death for line-of-duty firefighters. They found a reduction in both magnitudes of the FCW and BCW after firefighting activities, not accompanied by a significant increment in arterial stiffness, which could indicate a deterioration of systolic left ventricular function, as well as concomitant changes in cerebral vasomotor tone, allegedly resulting from psychological stress, as elucidated by Webb et al. (2010). FEW instead remained unchanged.

The effect of hot water bathing on wave intensity has been studied by Hatano et al. (2002), who discovered that systolic function and reflections might decrease in magnitude during the bathing phase (immersion in hot water). A delay in the arrival of the BCW with respect to the FCW after bath, driven by vasodilatation, suggests that hot hydrotherapy decreases the afterload and improves the circulation.

Zhang et al. (2010) proved that FCW, BCW and FEW, measured from carotid artery in hyperthyroid patients without any cardiovascular dysfunction, are considerably greater in magnitude compared to a control healthy group. Interestingly, no echocardiographic differences were found between groups in left ventricular ejection fraction and fraction shortening. These findings suggested that WI indices are more sensitive than echocardiographic indices in detecting substantial changes of cardiac performance in hyperthyroid patients, who usually undergo abnormal hemodynamic and cardiovascular states. Zhang et al. (2010) also revealed that in some of the tested patients mid-systolic

abnormal waves were present, suggesting that excessive energy is delivered from the heart into the arterial system, creating a characteristic pattern of reflected and re-reflected waves.

Carotid WIA was also tested in patients with Fontan physiology, to understand the cerebral perfusion. Saiki et al. (2014) demonstrated that FCW is significantly smaller in those patients compared to a control group, and that the ratio between BCW and FCW was greater in magnitude. They also found increased carotid arterial stiffness and central venous pressure, thought as independent determinants of the decreased FCW, because of their role as inflow and outflow resistance to the cerebral circulation, respectively.

A study by Manisty et al. (2010) demonstrated that WRI, a reflection index accounting for re-reflections from the body and calculated through wave intensity analysis, is able to predict future cardiovascular events, independently of blood pressure and other cardiovascular risk factors. The ratio of backward and forward components of the pressure, P_b/P_f, and the carotid augmentation index, did not perform as well as WRI. A clinical study performed by Li & Guo (2013) suggested that FEW and BCW measured at the carotid artery could be used to differentiate non-obstructive hypertrophic cardiomyopathy from left ventricular hypertrophy secondary to hypertension. Higher degree of sensitivity and specificity was found with the use of FEW to distinguish the two pathologies, compared to the use of BCW. Li & Guo (2013) also stated that femoral WIA is less reliable than carotid WIA in performing these comparisons.

Miao et al. (2011) demonstrated that different geometries of hypertensive remodelled hearts produced different patterns of FCW and FEW. C. H. Manisty et al. (2009) also performed a comparison between amlodipine and atenolol in hypertensive patients through carotid WIA and showed that carotid systolic blood pressure, WRI and P_b/P_f were smaller in patients treated with amlodipine; this difference was associated with a likely lesser degree of wave reflection associated with amlodipine-based therapy, probably resulting from the vasodilator action of amlodipine. Palombo et al. (2009) showed that, in patients with previously untreated hypertension, who underwent 6 months of vasodilator therapy with barnidipine, central blood pressure and augmentation index were reduced, but wave intensity, reflection indices and intrinsic arterial stiffness did not significantly change. Vriz et al. (2015) demonstrated that WI can be a useful index for the stratification of patients with heart failure and reduced ejection fraction, together with traditional echocardiographic parameters. FEW, in fact, was significantly lower in non-survivors, and specific threshold of FCW and FEW helped to assess patients' risk of cardiovascular mortality.

Carotid WIA has demonstrated a great diagnostic and prognostic potential so far, and its usage in clinical settings could offer a deeper insight into the physiological and pathological conditions of the cardiovascular system.

1.9 Objectives

The DU approach is a technique with a great potential in the clinical setting, because it relies upon the measurement of the diameter waveform. This circumvents the need of measuring the blood pressure, which can be done in-situ invasively or via non-invasive methodologies that are neither direct or simultaneous, as discussed in previous sections. The technique has been tested in vitro and in-vivo, although a reproducibility study under physiological perturbations is lacking[6]. Because of its potential, the DU approach can be a valid and competitive technique to assess vascular and cardiac performance changes under rapid physiological perturbations, but such a study has not been performed yet. In fact, all the current typologies of pressure-based WIA cannot guarantee direct and simultaneous measurements of two variables at a given location.

Moreover, the reservoir-wave approach has been demonstrated effective in the analysis of cardiovascular waves, but such a formulation for the diameter waveform is lacking; therefore, it is not currently possible to couple the DU approach with a reservoir-wave analysis. Before the development of such a theory, the current hybrid approach for the reservoir pressure lacks consensus on the method to find the fitting parameters and on the value of the asymptotical pressure value.

Therefore, the specific objectives of the thesis are:

1) To investigate whether non-invasive wave intensity analysis based on measurements of diameter and velocity is a reproducible technique, under physiological perturbations, such as exercise, in humans;

2) To examine the contribution of cardiac and peripheral vascular alterations to common carotid DU-derived wave intensity parameters, under incremental workrates and subsequent recovery in humans;

3) To give a contribution to the debate involving the more correct model for the pressure reservoir-wave approach, testing and comparing different fitting techniques currently available in literature and examining the effect of varying the pressure asymptotical value on hemodynamic and wave intensity parameters.

[6] More precisely, such study was lacking at the thesis initiation. The reproducibility study performed in this thesis has been published and is now available in literature (more details in Chapter 3).

1.10 Thesis outline

In order to meet the aforementioned objectives, the thesis has been structured in the following chapters:

- Chapter 2: entitled "Theoretical background", contains the theoretical formulations of wave intensity analysis, method of characteristics, DU approach and reservoir-wave theory. All are derived from fundamental principles;

- Chapter 3: entitled "A reproducibility Study of Non-invasive Wave Intensity Analysis in Common Carotid Artery". Inter-session and inter-observer reproducibility studies of DU-derived wave speed and wave intensity parameters were performed on a young healthy cohort. Measurements were taken from the common carotid artery, both at rest and during exercise (mild semi-recumbent cycling). Having established WIA was reproducible, a subsequent study was performed, to investigate the effects of exercise on DU-derived wave speed and wave intensity parameters;

- Chapter 4: entitled "Non-invasive Assessment of Wave Intensity Analysis during Exercise". A DU-derived wave intensity study was performed on a selected young and trained cohort, under baseline conditions, different degrees of physiological perturbations (semi-recumbent cycling) and subsequent recovery. The aim was to examine the effect of cardiac and peripheral vascular alterations induced by incremental exercise on common carotid wave intensity parameters. The magnitudes of incident and reflected waves, of reflection indices (as indicators to response of the head circulation) and of the local wave speed were calculated and compared among the different conditions;

- Chapter 5: entitled "Implications of Varying Fitting Technique and Asymptotic Diastolic Pressure on Wave Intensity Parameters". The reservoir-wave technique was performed on both pressure and velocity data collected from healthy humans, using two different methodologies: a) applying different fitting techniques available in literature to obtain the pressure asymptotical value and the time constants for the reservoir pressure waveform, b) fixing the pressure asymptotical value and calculating the time constants for the determination of the reservoir waveform. The

separated reservoir and excess pressure and velocity components were subsequently used to perform quantitative analyses, in order to compare relevant hemodynamic and wave intensity parameters;

- Chapter 6: entitled “General Discussions and Conclusions”; it summarizes the findings of the previous chapters, putting them in a perspective of possible future works, and highlights the limitations of the studies.

Chapter 2: Theoretical Background

The fundamental equations of wave intensity analysis are derived in the following sections, from the basic principles of momentum conservation and mass conservation, by applying the method of characteristics. The main features of wave intensity, focusing on both PU- and DU approaches, will be illustrated, together with a description of the hybrid reservoir-wave approach.

2.1 Development of the basic equations

Momentum conservation law: The conservation of linear momentum requires that the rate of change of momentum of a differential element must equal the sum of two contributions: the net momentum flux into the element and the "rate of production" of momentum, given by the external force per unit mass (also called "body forces") acting on it. The mathematical layout of this principle can be derived from Newton's second law of motion for a fluid particle of mass ρdV: $\rho dV \cdot (acceleration) = (force\ acting\ on\ \rho dV)$. The mass density is denoted by ρ and the elementary volume by dV. The equation reads:

$$\frac{\partial \rho \boldsymbol{v}}{\partial t} + \text{div}\,\mathbf{P} = \rho \boldsymbol{b} \tag{2.1}$$

Where $\rho \boldsymbol{v}$ represents the momentum density vector, **P** a comprehensive momentum flux second-order tensor, which may include pressure fields and viscous stresses as well as the advection term, div is the divergence operator and $\boldsymbol{b}$ the external body forces per unit volume. Therefore, the first term of (2.1) represents the momentum rate change, the second one the net momentum flux into the mass element and the last term the external body forces.

Coupled with this general principle, a so-called constitutive model for the fluid behaviour under consideration is needed. The constitutive equation for an isotropic Newtonian fluid, for which the viscous stress is linearly proportional to the strain rate (the rate of change of its deformation) and in which there is no preferential direction of stress, is the following:

$$\sigma_{ij} = \mu\left(\frac{\partial v_j}{\partial x_i} + \frac{\partial v_i}{\partial x_j} - \frac{2}{3}D\delta_{ij}\right) + \varsigma D\delta_{ij} \tag{2.2}$$

Where μ is called shear or dynamic viscosity and ς bulk viscosity, σ_{ij} denotes the second-order viscous stress tensor, δ_{ij} the Kronecker's delta, D the trace of the second-order rate-of-strain tensor, equal to div $\boldsymbol{v}$. The velocity vector field $\boldsymbol{v}$ has components (v_1, v_2, v_3) along the coordinate axes (x_1, x_2, x_3) and indices i, j can assume values 1,2,3. By coupling the Newtonian constitutive law with the conservation of linear momentum and rearranging the terms, one gets the so-called Navier-Stokes equation for Newtonian viscous fluids:

$$\rho \frac{\partial \boldsymbol{v}}{\partial t} + \rho(\boldsymbol{v} \cdot \nabla)\boldsymbol{v} = -\nabla p + \mu \Delta \boldsymbol{v} + \left(\frac{1}{3}\mu + \varsigma\right) \nabla(\text{div}\, \boldsymbol{v}) + \boldsymbol{b} \tag{2.3}$$

In which ∇ represents the nabla operator, Δ the laplacian operator (∇^2) and p the pressure field. The following assumptions for the blood arterial flow are made:

- Body forces such as gravity are negligible ($\boldsymbol{b} = \boldsymbol{0}$);
- The blood is assumed to be an incompressible fluid because its compressibility is minor compared to the vessel wall distensibility (Lighthill 1978; Pedley 1980). This assumption implies that ρ is regarded as uniform and constant and div $\boldsymbol{v} = 0$;
- Viscous losses are considered locally negligible away from branches and arterial discontinuities (Parker & Jones 1990). This implies that the blood is considered an inviscid fluid with $\mu = 0$;
- The longitudinal fluid motion is an order of magnitude greater than the radial motion (Lighthill, 1978). This implies that flow can be considered as one-dimensional along the vessel axial coordinate x. Therefore the velocity vector field becomes $\boldsymbol{v} = (U, 0, 0)$ where U denotes the x-component of velocity averaged over the cross-sectional area of the vessel, and $p = (P, 0, 0)$, where P indicates the spatially averaged pressure acting along the x coordinate.

Under these assumptions, Navier-Stokes equation (2.3) reads:

$$U_t + UU_x = -\frac{P_x}{\rho} \tag{2.4}$$

where subscripts indicate corresponding partial derivatives.

Mass conservation law: The conservation of mass law states that the change of mass of a differential element dV must equal the net mass flow rate crossing the boundary dA of dV with unit normal $\boldsymbol{n}$:

$$\rho \frac{dV}{dt} = \rho \boldsymbol{v} \cdot \boldsymbol{n} dA \tag{2.5}$$

It is assumed the mass density ρ to be constant (incompressible fluid).
In a vessel, one can consider dV being an elementary disc-shaped volume parallel to the major axis of the vessel and assume that the change in dV is solely due to the change in cross-sectional area dA. In the same one-dimensional framework as for the momentum law, it is considered $\boldsymbol{v} = (U, 0,0)$ being anti-parallel to the unit normal $\boldsymbol{n}$. Then equation (2.5) can be restated as:

$$A_t + (UA)_x = 0 \tag{2.6}$$

By introducing a general constitutive model for the vessel regarded as a "tube" ("tube law"), in which the cross-sectional area of the tube depends only upon the instantaneous local pressure, i.e. $A = f(P(x,t);\ x)$, the conservation equations can be restated in terms of P and U only, by applying the chain rule of partial derivatives:

$$\left.\frac{\partial A}{\partial t}\right|_x = A_P P_t \tag{2.7}$$

$$\left.\frac{\partial A}{\partial x}\right|_t = A_x + A_P P_x \tag{2.8}$$

Where $A_P = (\partial A/\partial P)|_x$ is the local compliance of the vessel (at location x), namely the local change in area driven by the change in pressure, and $A_x = (\partial A/\partial x)|_P$. Equations (2.4) and (2.6) then become:

$$P_t + UP_x + \frac{A}{A_P} U_x + \frac{UA_x}{A_P} = 0 \tag{2.9}$$

$$U_t + \frac{P_x}{\rho} + UU_x = 0 \tag{2.10}$$

Written in matrix form, it reads:

$$\begin{bmatrix} U & \frac{A}{A_P} \\ \frac{1}{\rho} & U \end{bmatrix} \begin{bmatrix} P_x \\ U_x \end{bmatrix} = \begin{bmatrix} -P_t - \frac{UA_x}{A_P} \\ -U_t \end{bmatrix} \tag{2.11}$$

The matrix of coefficients has eigenvalues:

$$\begin{cases} \gamma_f = U + \left(\frac{A}{\rho A_P}\right)^{\frac{1}{2}} \\ \gamma_b = U - \left(\frac{A}{\rho A_P}\right)^{\frac{1}{2}} \end{cases} \tag{2.12}$$

Where subscripts f and b stand for forward and backward direction, respectively, as will be clearer in the next paragraph. The solutions of the system (2.11) can be found via the method of characteristics, discussed in the following section.

2.2 The method of characteristics

Partial differential equations (PDE) can be grouped in different categories, based on the order of their derivatives and the nature of their coefficients. In particular, second-order PDE written in the canonical form, $Au_{xx} + Bu_{xy} + Cu_{yy} + \cdots = 0$, where subscripts indicate partial derivatives and only the highest-order terms are accounted, can be classified upon the value of the discriminant ($\Delta = B^2 - AC$). Hyperbolic ($\Delta > 0$), parabolic ($\Delta = 0$), and elliptic ($\Delta < 0$) equations are associated to different physical phenomena, in particular the hyperbolic ones are usually called "wave equations" because they describe wave-like behaviours.

The method of characteristics is a mathematical tool to find solutions of hyperbolic PDEs, based on a technique that finds parametrised curves (the so-called characteristic directions) along which the PDE behaves as a system of ordinary differential equations (ODEs). Wave intensity analysis was developed by applying the method of characteristics to the one-dimensional Euler's equations for arterial vessels derived in the previous sections (Parker et al. 1988; Parker & Jones 1990).

The following discussion mainly follows Parker & Jones (1990) and Parker (2009b). The first-order partial differential equations (2.9) and (2.10) constitute a hyperbolic system, which is therefore suitable to be solved by the method of characteristics. The characteristic

directions are defined as the eigenvalues of the system, from equation (2.12): $\frac{dx}{dt} \coloneqq \gamma_f = U + c$, or $\frac{dx}{dt} \coloneqq \gamma_b = U - c$ where $c = \sqrt{A/(\rho A_P)}$. The total derivative with respect to time can be written as:

$$\frac{d}{dt} = \frac{\partial}{\partial t} + \frac{dx}{dt}\frac{\partial}{\partial x} = \frac{\partial}{\partial t} + (U \pm c)\frac{\partial}{\partial x} \tag{2.13}$$

By applying (2.13), the system of equations (2.9) and (2.10) reduces to:

$$\frac{dP}{dt} - (U \pm c)P_x + UP_x + \rho c^2 U_x = -\frac{UA_x}{A_P} \tag{2.14}$$

$$\frac{dU}{dt} - (U \pm c)U_x + \frac{P_x}{\rho} + UU_x = 0 \tag{2.15}$$

Multiplying equation (2.14) by $\frac{1}{\rho c}$ and adding it to the equation (2.15), one gets:

$$\frac{dU}{dt} + \frac{1}{\rho c}\frac{dP}{dt} = -\frac{UcA_x}{A} \tag{2.16a}$$

Similarly, multiplying equation (2.14) by $\frac{1}{\rho c}$ and subtracting it from equation (2.15), one obtains:

$$\frac{dU}{dt} - \frac{1}{\rho c}\frac{dP}{dt} = +\frac{UcA_x}{A} \tag{2.16b}$$

By introducing the Riemann variables R_f and R_b one can restate equations (2.16a) and (2.16b) in a simpler way:

$$\begin{cases} R_f \coloneqq U + \int \frac{dP}{\rho c} \xrightarrow{yields} \frac{dR_f}{dt} = -\frac{UcA_x}{A} \\ R_b \coloneqq U - \int \frac{dP}{\rho c} \xrightarrow{yields} \frac{dR_b}{dt} = +\frac{UcA_x}{A} \end{cases} \tag{2.17}$$

Therefore, the waves are convected with the flowing fluid, and if blood velocity $U \neq 0$ in the vessel, the waves propagate downstream with velocity $U + c$ and upstream with velocity $U - c$. As in the arterial system $U < c$, there will be always waves traveling in both directions.

The Riemann variables are generally given by the boundary conditions applied at the inlet and outlet of the vessel, and by assuming c constant it is possible to solve for P and U at a specific location (x, t). In particular, one can write the equations (2.17) as differences:

$$\begin{cases} dR_f = dU + \dfrac{dP}{\rho c} \\ dR_b = dU - \dfrac{dP}{\rho c} \end{cases} \xrightarrow{yields} \begin{cases} dP = \dfrac{\rho c}{2}(dR_f - dR_b) \\ dU = \dfrac{1}{2}(dR_f + dR_b) \end{cases} \tag{2.18}$$

and define the wave intensity as the product of the incremental differences dP and dU at a given time t: $dI(t) = dP(t)dU(t)$, which has the property that forward waves always make a positive contribution to dI and backward waves always a negative contribution.

The water-hammer equation can be derived from the method of characteristics. In fact, by considering a change in pressure dP or velocity dU along the forward characteristic (dP_f, dU_f, respectively), the backward characteristic R_b must remain unchanged ($dR_b = 0 = dP_b = dU_b$), and vice-versa for a change in pressure or velocity along the backward characteristic:

$$\begin{cases} dR_b = 0 = dU_f - \dfrac{dP_f}{\rho c} \\ dR_f = 0 = dU_b + \dfrac{dP_b}{\rho c} \end{cases} \xrightarrow{yields} \begin{cases} dP_f = +\rho c\, dU_f \\ dP_b = -\rho c\, dU_b \end{cases} \tag{2.19}$$

The latter set of equations constitutes the water-hammer equation and gives the relationship between the change of forward (f) and backward (b) pressure and velocity occurring across a wavefront. In developing the water-hammer equation, the linear additivity of forward and backward components of pressure and velocity is assumed: $dP = dP_f + dP_b$ and $dU = dU_f + dU_b$.

Assuming a reflection-free early systolic period (Khir et al. 2001), $dP = dP_f$ and $dU = dU_f$; therefore, the water-hammer equation (2.19) can be integrated over the linear part of the PU-loop, giving $\Delta P_{lin} = \rho c \Delta U_{lin}$, which allows the calculation of the wave speed.

2.3 Wave Intensity Separation

As already seen, the wave intensity dI has S.I. units of W/m^2 and represents the energy flux carried by the wave. The wave energy carried in a specific time interval $T = t_2 - t_1$ can be found as the integral of the wave intensity over that time interval: $I = \int_{t_1}^{t_2} dIdt$. Although the method of characteristics does not require any assumption about linearity, it would be possible to extract more information from the measurements if the assumption of linear additivity of the incremental forward and backward "wavelets" were made. Parker & Jones (1990) and Parker (2009b) concluded that a linearized theory is not significantly different from the non-linear theory in the context of arterial hemodynamics, and that it is possible to make the amplitude of the wavelets dP and dU as small as desired with a proper choice of sampling frequency, which makes the linearized theory more accurate.

The assumption of additivity for the change in pressure and velocity, $dP = dP_+ + dP_-$ and $dU = dU_+ + dU_-$, respectively, led to the water-hammer equation and allows now the separation of the measured waves and intensity into forward and backward components. From equation (2.19):

$$\begin{cases} dP_f = \frac{1}{2}(dP + \rho c dU) \\ dP_b = \frac{1}{2}(dP - \rho c dU) \end{cases} \tag{2.20}$$

$$\begin{cases} dU_f = \frac{1}{2}\left(dU + \frac{dP}{\rho c}\right) \\ dU_b = \frac{1}{2}\left(dU - \frac{dP}{\rho c}\right) \end{cases} \tag{2.21}$$

The separated wave intensity becomes, after little algebra:

$$\begin{cases} dI_f := dP_f dU_f = +\frac{1}{4\rho c}(dP + \rho c dU)^2 \\ dI_b := dP_b dU_b = -\frac{1}{4\rho c}(dP - \rho c dU)^2 \end{cases} \tag{2.22}$$

This yields additivity of wave intensity:

$$dI_f + dI_b = \frac{1}{4\rho c}[(dP + \rho c dU)^2 - (dP - \rho c dU)^2] = dP dU = dI. \tag{2.23}$$

The separated pressure and velocity waves can be reconstructed by summing the incremental changes:

$$\begin{cases} P_f(t) = \sum_{\tau=0}^{t} dP_f(\tau) + P_0 \\ P_b(t) = \sum_{\tau=0}^{t} dP_b(\tau) + P_0 \end{cases} \tag{2.24}$$

$$\begin{cases} U_f(t) = \sum_{\tau=0}^{t} dU_f(\tau) + U_0 \\ U_b(t) = \sum_{\tau=0}^{t} dU_b(\tau) + U_0 \end{cases} \tag{2.25}$$

Where P_0 and U_0 are integration constants (P and U at $t = 0$).

Forward waves are usually originated by the pumping action of the heart. Backward waves, which travel toward the heart, are the reflections of forward waves, which met a reflection site in the arterial tree during their passage. At the reflection site, the incident (forward) wave is partly reflected in the opposite direction (becoming a backward wave) and partly transmitted downstream the reflection site. When a backward wave reaches the heart, it can be reflected again, becoming a forward wave which travels toward the periphery. Changes in magnitude and phase of the waves happen at every reflection site.

If the wave is a compression wave, $dP > 0$, while if it is an expansion wave, $dP < 0$. The heart generates, for example, a compression wave in early systole, "pushing" the blood into the aorta and into the pulmonary artery, and an expansion wave in late systole, when the ventricular contraction rate decreases, causing a "suction" effect on the blood that propagates into the vessels. A wave can accelerate the blood ($dU > 0$) or decelerate it ($dU < 0$), considering as a reference direction the one travelling toward the periphery. A forward compression wave then accelerates the blood, giving a positive change in velocity, as well as a backward expansion wave. Forward expansion and backward compression waves decelerate the blood, instead. By the definition of dI, it is easy to determine the sign of wave intensity. Forward compression and expansion waves have positive intensity, while

backward compression and expansion waves have negative intensity. Table 2.1 recaps the signs and the properties of the waves:

Direction	Pressure	Velocity	Wave Intensity
Forward	Compression (dP>0)	Acceleration (dU>0)	Positive (dI>0)
Forward	Expansion (dP<0)	Deceleration (dU<0)	Positive (dI>0)
Backward	Compression (dP>0)	Deceleration (dU<0)	Negative (dI<0)
Backward	Expansion (dP<0)	Acceleration (dU>0)	Negative (dI<0)

Table 2.1: Properties of the separated pressure, velocity and intensity waves.

2.4 The DU theory

Feng & Khir (2010) introduced a method to perform a DU wave intensity analysis from direct and simultaneous measurements of diameter and velocity, in order to overcome the problems introduced by both the pressure-diameter calibration and the tonometry. Starting from the Bramwell-Hill equation $c^2 = 1/\rho D_s$ and taking account for the definition of distensibility $D_s = (1/A)(dA/dP)$[7], one can re-define the wave speed in terms of changes in diameter dD:

$$\frac{dA}{A} = \frac{2dD}{D} \xrightarrow{yields} dP = \rho c^2 \frac{2dD}{D} \tag{2.26}$$

With dD representing the incremental change in diameter of the cross-sectional area of the vessel. A forward compression wave $(dP > 0,\ dU > 0)$ causes an increase of diameter $(dD > 0)$ as well as a backward compression wave $(dP > 0,\ dU < 0)$. Oppositely, a forward expansion $(dP < 0,\ dU < 0)$ and a backward expansion wave $(dP < 0,\ dU > 0)$ cause a decrement of diameter $(dD < 0)$. This follows from the equation (2.26), which in turn follows from the definition of compliance: as it is always a positive number, for a positive incremental change in pressure a positive incremental change in diameter occurs, and vice versa[8]. Table 2.1 can be therefore updated in the following Table 2.2:

[7] It is assumed that the length of the vessel / tube does not change.

[8] The term "expansion" can be misleading regarding the change in diameter, as an expansion wave actually decreases the cross-sectional area rather than "expand" it, so Parker suggested to use "decompression" instead (Sugawara et al. 2009).

Direction	Diameter	Velocity	Wave Intensity
Forward	Compression (dD>0)	Acceleration (dU>0)	Positive (dI>0)
Forward	Expansion (dD<0)	Deceleration (dU<0)	Positive (dI>0)
Backward	Compression (dD>0)	Deceleration (dU<0)	Negative (dI<0)
Backward	Expansion (dD<0)	Acceleration (dU>0)	Negative (dI<0)

Table 2.2: Properties of the separated diameter, velocity and intensity waves.

By assuming the linear additivity $dD = dD_f + dD_b$, as for the PU-formulation of WI, one can restate the equation (2.26):

$$dP_f + dP_b = \frac{2\rho c^2}{D}(dD_f + dD_b) \tag{2.27}$$

and aim to substitute the pressure components with velocity components, by means of the water-hammer equation (2.19). In fact, by only considering forward components ($dP_b = dD_b = 0$), it is possible to calculate the wave speed from diameter and velocity changes:

$$\rho c\, dU_f = \frac{2\rho c^2}{D} dD_f \xrightarrow{yields} c = \frac{dU_f \cdot D}{2dD_f} \xrightarrow{yields} c = \frac{1}{2}\frac{dU_f}{d\ln D_f} \tag{2.28}$$

By considering $dD/D = d\ln D$. In the case of ($dP_f = dD_f = 0$), one obtains a similar equation, valid for backward components:

$$\rho c\, dU_b = -\frac{2\rho c^2}{D} dD_b \xrightarrow{yields} c = -\frac{dU_b \cdot D}{2dD_b} \xrightarrow{yields} c = -\frac{1}{2}\frac{dU_b}{d\ln D_b} \tag{2.29}$$

These formulas are similar to the ones obtained for the PU-loop method. A linear portion is expected plotting the $\ln DU$-loop, during the early part of systole, when backward reflected waves are absent, so that $dD = dD_f$ and $dU = dU_f$. By integrating dU and dD over the linear part of the loop, $c = 0.5\,\Delta U_{lin}/\Delta \ln D_{lin}$. An important thing to mention is that this ratio is actually the *inverse* of the slope of the linear part of the $\ln DU$-loop.

The separation of the waves is straightforward, and follows from similar calculations as for $dI = dPdU$. In fact, by only considering unidirectional waves (only forward or only backward components), one obtains the "non-invasive counterpart" of the water-hammer equation:

$$\begin{cases} dD_f = +\dfrac{D}{2c}dU_f \\ dD_b = -\dfrac{D}{2c}dU_b \end{cases} \tag{2.30}$$

through which one can calculate the separated components of changes in diameter and velocity from the measured waves:

$$\begin{cases} dD_f = \dfrac{1}{2}\left(dD + \dfrac{D}{2c}dU\right) \\ dD_b = \dfrac{1}{2}\left(dD - \dfrac{D}{2c}dU\right) \end{cases} \tag{2.31}$$

$$\begin{cases} dU_f = \dfrac{1}{2}\left(dU + \dfrac{2c}{D}dD\right) \\ dU_b = \dfrac{1}{2}\left(dU - \dfrac{2c}{D}dD\right) \end{cases} \tag{2.32}$$

and finally obtain the separated waveforms through summations of the corresponding wavelets:

$$\begin{cases} D_f(t) = \displaystyle\sum_{\tau=0}^{t} dD_f(\tau) + D_0 \\ D_b(t) = \displaystyle\sum_{\tau=0}^{t} dD_b(\tau) + D_0 \end{cases} \tag{2.33}$$

$$\begin{cases} U_f(t) = \displaystyle\sum_{\tau=0}^{t} dU_f(\tau) + U_0 \\ U_b(t) = \displaystyle\sum_{\tau=0}^{t} dU_b(\tau) + U_0 \end{cases} \tag{2.34}$$

D_0 and U_0 being the end-diastolic diameter and velocity values, respectively (at $t = 0$).

Non-invasive wave intensity dI_n is defined as $dI_n = dDdU$ and its separated contributions are given by $dI_{nf} = dD_f dU_f$ and $dI_{nb} = dD_b dU_b$. By using the equations

(2.31) and (2.32), it is possible to explicitly restate dI_n components in terms of measured changes:

$$\begin{cases} dI_{nf} = +\dfrac{c}{2D}\left(dD + \dfrac{D}{2c}dU\right)^2 \\ dI_{nb} = -\dfrac{c}{2D}\left(dD - \dfrac{D}{2c}dU\right)^2 \end{cases} \tag{2.35}$$

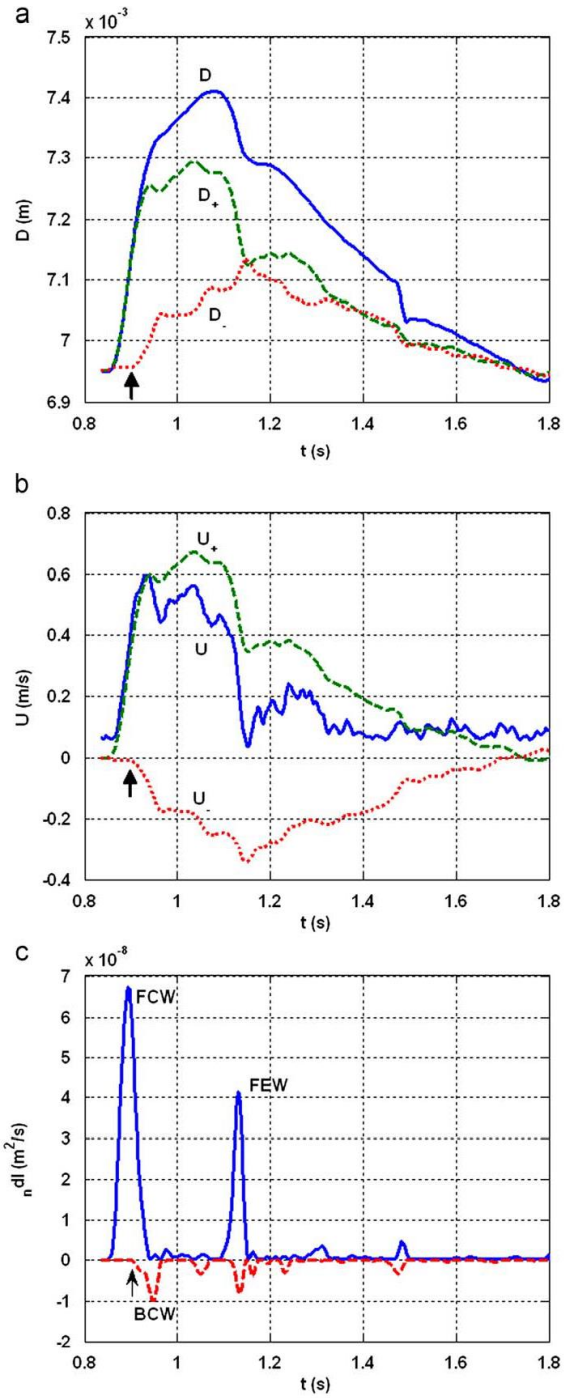

Figure 2.1: Separated D waveforms (a), U waveforms (b) and non-invasive wave intensity ($_n$dI) (c) from human carotid artery. Green lines show measured waveforms, blue lines indicate forward components and red lines are associated with backward components. Taken from Feng & Khir (2010).

dI_n is always positive in the forward and always negative in the backward direction (Feng & Khir 2010). The technique was validated in vitro using elastic tubes, against PU-loop and wave intensity $dPdU$. It also performed well under change of fluid density (Li & Khir 2011)

and in vivo (Borlotti et al. 2012). An example of its application in vivo can be seen in Figure 2.1.

Recently, another similar technique has been developed for the estimation of left ventricular force-frequency relationship, and has been validated in exercise condition among healthy humans (Tanaka et al. 2015). In this context, wave intensity WD is defined as:

$$WD = \frac{1}{D}\frac{dD}{dt}\frac{dU}{dt} \tag{2.36}$$

It is interestingly correlated to the original wave intensity $WI = dPdU$ through the stiffness index β:

$$WD = \frac{1}{\beta P}\, WI \tag{2.37}$$

at a specific pressure P and diameter D. However, no wave separation technique has been developed at present.

2.5 The Reservoir-Wave theory

The derivation of the reservoir-wave equations by Wang et al. (2003) mainly followed the Frank's windkessel model, but extended to systole.

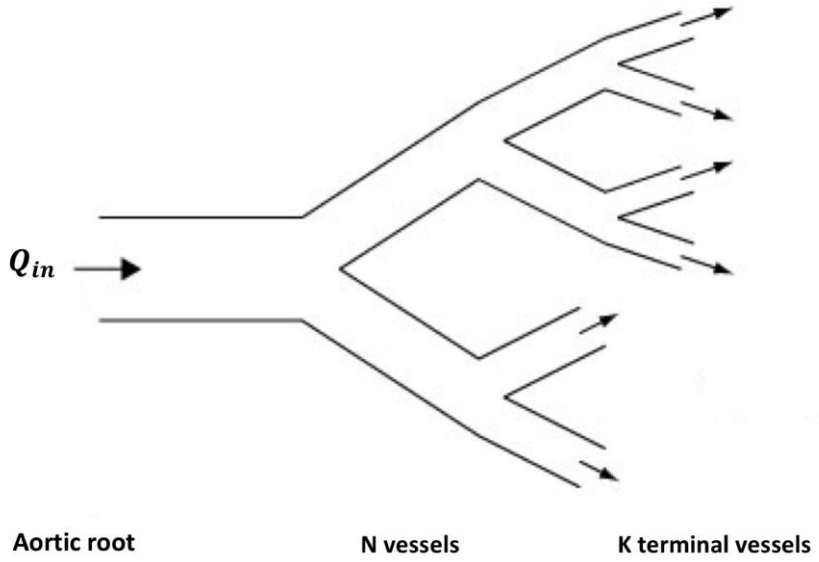

Figure 2.2: Schematic representation of the arterial system. Modified from http://www.bg.ic.ac.uk/research/k.parker/res_press_web/rp_definition.html

Assuming that the measured pressure is the summation of reservoir and excess waveforms, $P(x,t) = P_r(t) + P_{ex}(x,t)$, $P_r(t)$ is defined as the pressure component that follows the conservation of mass equation in the arterial system: the temporal variation of $P_r(t)$, in a given time interval, can be obtained by considering the temporal variation of the arterial reservoir volume V_r, being the difference of the aortic blood inflow and outflow, in the same time interval. In differential terms it reads:

$$\frac{dP_r(t)}{dt} = \frac{dP_r}{dV_r}\frac{dV_r}{dt} = \frac{dP_r}{dV_r}[Q_{in}(t) - Q_{out}(t)] \tag{2.39}$$

In Figure 2.2 a schematic representation of the arterial tree is given, consisting of an aortic root fed by Q_{in}, a total number of N vessels, and K<N terminal vessels feeding the microcirculation. By defining P_i as the pressure level in the ith vessel and C_i its compliance ($i \in 1{:}N$), R_j the vascular resistance of the jth terminal vessel ($j \in 1{:}K$), P_∞ the pressure at the microcirculation, the equation (2.39) becomes:

$$\sum_N \frac{C_i dP_i}{dt} = Q_{in} - \sum_K \frac{P_j - P_\infty}{R_j} \tag{2.40}$$

The original windkessel formulation (Frank 1899) did not account for the wave propagation, so that P_r was the same throughout all the system, propagating at infinite speed. In this case equation (2.40) reads:

$$C_T \frac{dP_r}{dt} = Q_{in} - \frac{P_r - P_\infty}{R_T} \tag{2.41}$$

Where $C_T = \sum C_n$ is the total compliance of the arterial system (practically equal to the compliance of the large arteries), and ${R_T}^{-1} = \sum R_j^{-1}$ the total resistance of the terminal vessels (practically equal to the total resistance of the arterial system).

By considering P_r propagating at finite speed, but uniformly, in the arterial system [as it is assumed that the measured pressure at any arterial location has very similar diastolic decay, from Aguado-Sierra, Alastruey, et al. (2008)], P_r takes the form:

$$P_r(x,t) = P_r(t - T_x(x)) \tag{2.42}$$

where T_x is the time delay, which is dependent on the location. Considering T_x small (order of magnitude of tens of ms), as the wave speed in the arterial tree has an order of magnitude up to tens of m/s:

$$P_r(t - T_x) = P_r(t) + O(T_x) \approx P_r(t) \tag{2.43}$$

It is possible, therefore, to neglect the delay and write the solution in a simpler way. In particular, the Wang's formulation takes the same form as the Frank's windkessel equation, and in diastole, when $Q_{in} = 0$, the solution of equation (2.41) is a simple exponential decay:

$$P_r(t) = (P_0 - P_\infty)e^{-bt} + P_\infty \tag{2.44}$$

where $b = 1/\tau = 1/R_T C_T$ and it is the same in any arterial location. During systole, $Q_{in} \neq 0$ and the solution reads:

$$P_r(t) = P_\infty + (P_0 - P_\infty)e^{-bt} + e^{-bt}\int_{t_0}^{t} \frac{Q_{in}(t')}{C} e^{bt'} dt' \tag{2.45}$$

where t_0 and P_0 mark the beginning of ejection.

Q_{in} was experimentally calculated in canine aortas. By assuming no waves in the last two-thirds of diastole (Stergiopulos, Segers and Westerhof 1999) and no flow from the heart, the parameters R, C and P_∞ were estimated by fitting the model against the measured waveform. Wang et al. (2003) found that the measured flow Q_{in} is qualitatively identical to P_{ex} (as shown in Figure 2.3), indicating that forward waves dominate in the diastole, and their ratio suggesting a resistive phenomenon; moreover the quantitative estimation of this proximal resistance is similar to the characteristic impedance proposed by Westerhof et al. (1972).

2.5.1 The Reservoir-Wave theory at any arbitrary location

The generalisation of the reservoir-wave theory in the arterial tree was made by Aguado-Sierra, Alastruey, et al. (2008). They assumed that the pressure diastolic decay at all locations in the arterial tree is very similar and the linear relationship between P_{ex} and Q_{in} holds in all arteries, considering that the arterial bifurcations should be close to well-

matched for forward waves. Consequently, P_{ex} is qualitatively unchanged. This assumption can fail in the arterioles and smaller vessels, but it holds in the large arteries (Aguado-Sierra, Alastruey, et al. 2008). The equation (2.41) of mass conservation in terms of pressure then becomes:

$$\frac{dP_r}{dt} = \frac{\gamma}{C_T}(P - P_r) - \frac{P_r - P_\infty}{R_T C_T} \tag{2.46}$$

Where $Q_{in} = \gamma(P - P_r)$ and γ is a proportionality constant. By defining $a = \gamma / C_T$, one obtains:

$$\frac{dP_r}{dt} = a(P - P_r) - b(P_r - P_\infty) \tag{2.47}$$

It is important to specify which term depends on x or t in the equation (2.47):

$$\frac{dP_r(t)}{dt} = a(x)(P(x,t) - P_r(t)) - b(P_r(t) - P_\infty) \tag{2.48}$$

with b and P_∞ constant (and uniform) values and a depending on the location, because of γ. Again, in diastole $Q_{in} = 0$ and $P = P_r$, so that the equation (2.47) reduces to a simple exponential decay with time constant $1/b$. By multiplying equation (2.47) by $e^{(a+b)t}$ and integrating by parts, it is possible to find the general solution, valid for the whole cycle:

$$P_r(x,t) = \frac{b}{a+b} P_\infty + e^{-(a+b)t}\left[\int_0^t aP(t')e^{(a+b)t'}dt' + P_0 - \frac{b}{a+b}P_\infty\right] \tag{2.49}$$

It is important to consider that the diastolic decay of the reservoir pressure is independent of the arterial location, by assumption. In fact, the only parameters involved are b and P_∞.

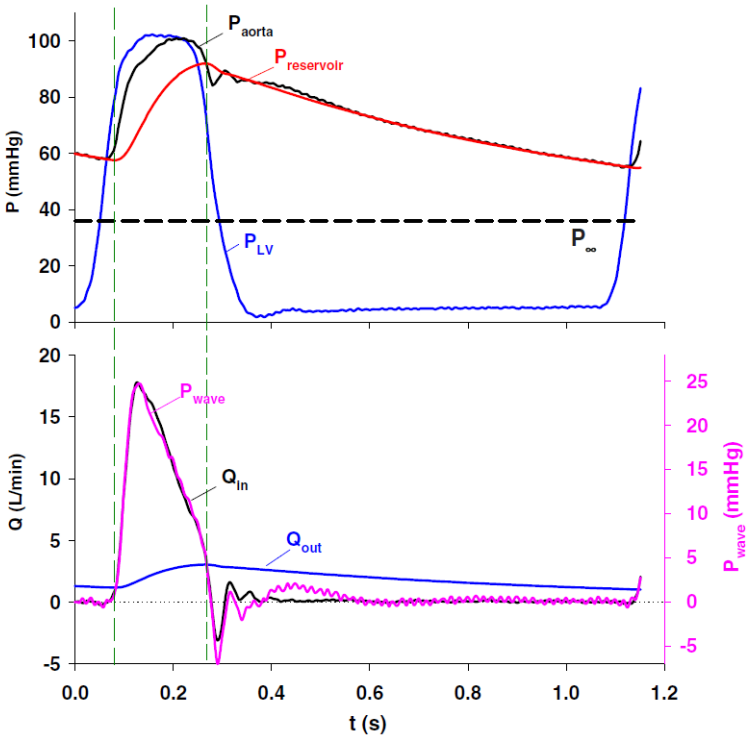

Figure 2.3: Diagrams of blood pressure and its separated components, the reservoir and the excess ones. Top: Canine measured aortic pressure (P_{aorta}), separated reservoir component ($P_{reservoir}$), left ventricular measured pressure (P_{LV}) and asymptotical value of pressure (P_{∞}). Bottom: Measured inflow (Q_{in}), outflow (Q_{out}) and excess component of the pressure ($P_{wave} \equiv P_{ex}$). The scales are adjusted to highlight the qualitative similarity between P_{wave} and Q_{in}. The two vertical dashed lines indicate $Q_{in} = Q_{out}$: $P_{reservoir}$ neither increases or decreases. Taken from Wang et al. (2003) as modified by Tyberg et al. (2009).

However, during systole, a plays a significant role and P_r depends on the arterial location. The constant a and b are found by fitting, P_{∞} is either assumed to be a specific value or found by fitting, and P_0 corresponds to the starting point of the onset of P. In particular, for finding a, the continuity of P_r at the ending point of systole T_N is enforced:

$$P_r(T_N) = \frac{b}{a+b}P_{\infty} + e^{-(a+b)T_N}\left[\int_0^{T_N} a\,P(t')e^{(a+b)t'}dt' + P_0 - \frac{b}{a+b}P_{\infty}\right] \quad (2.50)$$

Whereas $P_r(T_N)$ is either assumed to be a specific value or found by fitting. T_N is the time when the aortic valve shuts and corresponds to the dicrotic notch in the measured pressure waveform, or the first zero crossing of the second derivative of the pressure, in case the dicrotic notch is not present (Aguado-Sierra, Alastruey, et al. 2008).

2.5.2 Extension to reservoir velocity

Aguado-Sierra, Alastruey, et al. (2008) also developed a reservoir velocity theory, given that the blood velocity may not be null in the late diastole in more distal vessels than aorta. It is assumed that the reservoir and the wave component interact additively, so that $U = U_r + U_{ex}$, where U_r is the reservoir velocity, U the measured waveform and U_{ex} the wave component. U_r is established to be directly proportional to $P - P_\infty$ at the end of diastole when the reservoir effect is dominant. By defining $\bar{R}$ as the downstream resistance and calculating it as $\bar{R} = (\langle P \rangle - P_\infty)/\langle U \rangle$, where $\langle P \rangle$ and $\langle U \rangle$ are the time-averaged measured pressure and velocity in diastole, respectively, the reservoir velocity becomes:

$$U_r = \frac{P - P_\infty}{\bar{R}} \tag{2.51}$$

As can be seen, the calculation of reservoir velocity needs simultaneous measurements of pressure and velocity, specifically for the determination of the downstream resistance. It is demonstrated that the wave components of velocity are minimal during diastole, if the wave separation is performed by using $P_{ex}U_{ex}$-loop instead of PU-loop. In fact, without performing any reservoir subtraction a significant wave activity emerges during diastole, consisting of self-cancelling waves with equal forward and backward pressures and opposite velocities (Aguado-Sierra, Alastruey, et al. 2008).

The pressure reservoir theory has been successfully extended to the venous system (Wang et al. 2006), in particular to the vena cava, and the left ventricular filling (Flewitt et al. 2007). Davies et al. (2010) analysed the clinical relevance of the reservoir approach and demonstrated that the magnitude of the reservoir pressure increases with age and is related to the aortic augmentation index, while the excess pressure is a predictor of cardiovascular events.

Chapter 3: A reproducibility Study of Non-invasive Wave Intensity Analysis in Common Carotid Artery*

3.1 Introduction

The aim of the study presented in this Chapter was to assess the reproducibility of non-invasive, ultrasound-derived wave intensity (WI) parameters in humans at the common carotid artery (CCA). The temporal changes in pressure and flow generated during every cardiac cycle are inextricably linked and propagate as waves along the vascular tree. Waves contain embedded information about both their origin and the tissue through which they propagate or are reflected, thereby providing insight into the dynamic interactions among the various components of the cardiovascular system. As explained in Chapter 1, since antiquity the study of the arterial pulse has played a key role in the understanding of human circulation (Karamanou et al. 2015), but recent mathematical and computational developments have opened new windows for advancing our knowledge and understanding of cardiovascular mechanics and hemodynamics. In particular, wave propagation along the vascular tree can be studied with wave intensity analysis (WIA), a powerful tool first developed by Parker & Jones (1990), involving the decomposition of pulsatile flow into its wave components. Several carotid WIA studies have been conducted based on non-invasive CCA blood pressure and flow velocity (U) measurements, with the former derived from either CCA diameter (D) measurements (Niki et al. 2002; Rakebrandt et al. 2009; Carbone et al. 2010) or applanation tonometry (Curtis et al. 2007). However, these surrogate signals are computed by the analysis of distally recorded, usually non-simultaneous blood pressure waves, giving rise to inaccuracies (Meinders & Hoeks 2004; Zambanini et al. 2005, Van Bortel et al. 2001) especially with rapid physiological perturbations. To circumvent this problem, recent theoretical work yielded an algorithm incorporating non-invasive D (instead of arterial blood pressure) and U measurements when determining local wave speeds and implementing WIA (Feng & Khir 2010). This progress paralleled technological developments that led to a new generation of ultrasound machines with the capacity for

* Article published as: Pomella N, Wilhelm EN, Kolyva C, González-Alonso J, Rakobowchuk M, Khir AW. Common Carotid Artery Diameter, Blood Flow Velocity and Wave Intensity Responses at Rest and during Exercise in Young Healthy Humans: A Reproducibility Study. Ultrasound in Medicine & Biology, 2017; 43(5): 943-57.

direct and simultaneous non- invasive measurements of arterial *D* and *U*, through echo-tracking and Doppler ultrasound, respectively.

A simple physiologic perturbation that may provide a substantial challenge to the implementation of this methodology is exercise. Moreover, unlike other techniques, WIA applied in the CCA may be uniquely qualified to investigate the cardiac–cerebrovascular interaction under this complex physiologic perturbation. For this endeavour to be successful, the ability to obtain reproducible CCA *D* and *U* measurements during rest and exercise is vital. Therefore, the aim of this study was to assess the reproducibility of non-invasive ultrasound measurements of CCA *D* and *U*, and of derived wave intensity parameters, obtained from young healthy participants at rest and during submaximal exercise. To the best of our knowledge, no studies existed on WIA reproducibility when derived from arterial diameter and velocity waveforms. Establishing WIA reproducibility will pave the way for more detailed exploration of the cardiac–cerebrovascular interaction and cerebral vascular resistance responses during exercise in humans.

3.2 Material and Methods

3.2.1 Study group

The study was approved by the Brunel University London Research Ethics Committee and complied with the guidelines of the Declaration of Helsinki. Twelve healthy volunteers (aged 27 ± 2 y, 6 females, body mass: 66.9 ± 5.7 kg, height: 1.69 ± 0.1 m, body mass index: 23.3 ± 1.2 kg/m^2) participated in the study after providing informed written consent. All participants were familiar with cycling, but none was a trained athlete. The participants' average daily physical activity levels were within the normal range for a sedentary to moderately active population (Sallis et al. 1985).

3.2.2 Instrumentation and measurements

An SSD-5500 ultrasound system (Aloka, Tokyo, Japan) equipped with a 7.5-MHz linear array vascular probe was used. The ultrasound echo tracking subsystem measured *D* with a resolution of 0.013 mm, whereas the Doppler subsystem measured *U* with a resolution of 0.012 m/s. The scans were performed in the longitudinal view, obtaining therefore images of the longitudinal section of the artery, approximately 2 cm proximal to the bifurcation. The images were optimised to ensure that its depth was as shallow as

possible and the vessel walls well delineated (clear discrimination amongst the lumen, media–intima and adventitia). The gates were positioned manually in B-mode between the media and intima of the anterior and posterior walls, and parallel to them. The Doppler gate was positioned at the centre of the vessel, parallel to the walls, ensuring that the insonation angle was always between 58° and 60°. The B- and M-modes were then simultaneously displayed on a split screen, and the *D* waveform was calculated as the distance between the two walls over time obtained from the M-mode tracing. The *U* waveform was obtained from the pulsed-wave Doppler mode. Both *D* and *U* were sampled at 1000 Hz (Figure 3.1A). Every measurement consisted of the simultaneous recording of *D* and *U* signals for at least 6 s. A supine bicycle ergometer, mounted on a bed and equipped with a power control box, was used to perform the exercise protocol (Angio, Lode, Groningen, Netherlands) (Figure 3.1B).

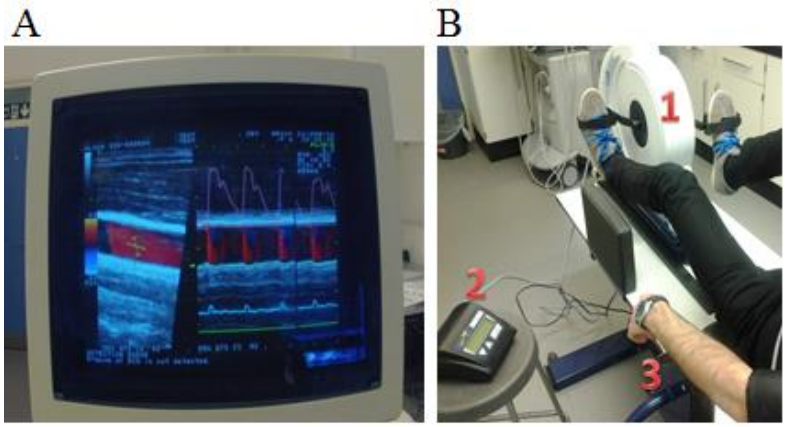

Figure 3.1: Experimental setup. (A) Monitoring of ultrasound system while acquiring carotid images and Doppler information. In the frozen image on the monitor is the common carotid artery, together with the diameter waveform (*pink*) and blood velocity contour (*blue*) on the right side of the screen. (B) Semi-recumbent cycle ergometer and control box: (1) ergometer, (2) control box, (3) handle for the left arm.

3.2.3 Protocol

The participants were tested twice over two consecutive days and at the same time of the day. Temperature and humidity in the laboratory did not differ between the two days (i.e., ~20°C and ~40%, respectively). Volunteers were asked to refrain from vigorous exercise and caffeine consumption for 24 h and 12 h, respectively, before the laboratory visits and to maintain the same diet on the two days of testing. The tests were conducted

with the participants in a reclined position and their upper bodies in the semi- recumbent position (angle 32°). The participants were not restrained, but they were asked to minimize head movements and maintain a stable position by holding the bed's handles, especially during exercise (Figure 3.1B).

A total of 12 measurements were taken during each day of testing, 6 at rest and 6 during exercise. Exercise measurements involved participants cycling for 2–3 min at a low cadence (30–50 rpm) and low workrate (20–40 W) (warmup period), before increasing to a cadence of 60 rpm and workrates of 80 W for males and 50 W for females (exercise period), corresponding to ≈30%–35% of the participants' maximal workrate on a bicycle ergometer and consistent with the classification of participants as sedentary to moderately active (Sallis et al. 1985; Fletcher et al. 2013). The recording of the 6 exercise measurements started 3 min into the exercise period, while the participant continued cycling. The whole protocol (warmup and exercise) lasted approximately 20 min. After completion of the measurements, the workrate was decreased and the subject continued cycling for 1 min (cool-down period). Volunteers had visual feedback to maintain a constant cadence.

3.2.4 Data analysis

Data analysis was performed in MATLAB (Version R2010b, The MathWorks, Natick, Massachusetts, USA). A second-degree Savitzky–Golay filter (Savitzky & Golay, 1964) with a 16-point half-width window was applied to both *D* and *U* waveforms to eliminate high-frequency noise (Figure 3.2). For every participant, six measurements were recorded during four conditions: rest and exercise during the first day (Rest 1 and Exercise 1, respectively) and rest and exercise during the second day (Rest 2 and Exercise 2, respectively). For each measurement, the best-quality consecutive heart cycles were selected for further analysis (at least three), based on whether they retained typical physiologic features (such as the dicrotic notch) and presented no obvious drift or dampening. For the cardiac cycles selected from each measurement, *dD* and *dU* were calculated as the incremental differences between adjacent elements (in the sense of finite differences) of *D* and *U*, respectively. The following features were extracted from *D* and *U* each cardiac cycle: (i) peak (systolic) diameter (D_{max}); (ii) change in diameter or pulse (ΔD), defined as the difference between peak (systolic) and trough (diastolic) values; (iii) peak (systolic) velocity (U_{max}); (iv) change in velocity or pulse (ΔU), derived similarly to ΔD (Figure 3.3).

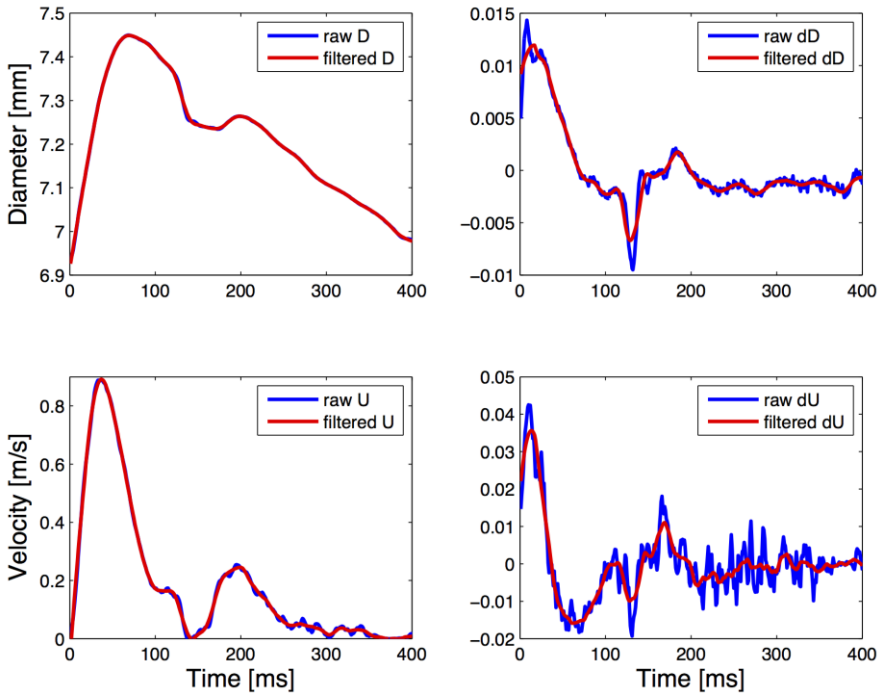

Figure 3.2: Comparison between raw and Savitzky–Golay smoothed signals. Top: *D* and *dD* waveforms; Bottom: *U* and *dU* waveforms.

The variances of dD and dU were calculated by subtracting the mean ($\bar{\cdot}$) from the instantaneous signal ($\cdot_k$), where k represents the kth element of the temporal series:

$$\sigma^2_{dD} = \frac{1}{N}\sum_{k=1}^{N}\left(dD_k - \overline{dD}\right)^2 \tag{3.1}$$

$$\sigma^2_{dU} = \frac{1}{N}\sum_{k=1}^{N}\left(dU_k - \overline{dU}\right)^2 \tag{3.2}$$

where *N* is the total number of data points along time included in the segment selected from each measurement. Variable σ^2_{dD} has units of mm^2 and σ^2_{dU} units of m^2/s^2.

Assuming that reflected waves are absent during the early-systolic portion of each cardiac cycle, wave speed c (m/s) for each analysed beat was calculated from the initial slope of the lnDU loop as in Feng & Khir (2010); see Figure 3.4:

$$c = \frac{1}{2}\frac{dU_f}{d\ln D_f} \tag{3.3}$$

Wave intensity (m^2/s) was computed as the product $dI = dD \cdot dU$ and was separated into forward (dI_f) and backward (dI_b) components using the calculated c (Feng & Khir 2010). The peak (m^2/s) and area (m^2) of the forward compression wave, which is generated by the contraction of the left ventricle, were derived for each cardiac cycle from the amplitude and area, respectively, of the early-systolic peak observed in dI_f (Figure 3.3). Similarly, the peak and area of the backward compression wave, which is attributed to reflections from the cerebral circulation, were determined for each cardiac cycle from the amplitude and area, respectively, of the mid-systolic peak that was present in dI_b. Finally, the peak and the area of the forward expansion wave (FEW), which is generated by the deceleration of the heart's contraction, were determined for each cardiac cycle from the amplitude and area, respectively, of the late-systolic peak in dI_f. The area parameters are associated with the energy of the waves, in comparison with similar parameters obtained with PU-WIA having units of J m^{-2}. Mean values for all parameters were derived at each measurement, and further averaging yielded mean values for each day at rest and during exercise.

3.2.5 Statistical analysis

All values are expressed as mean ± standard deviation (SD). The statistical analyses were performed using SPSS Statistics (Version 20, IBM, Armonk, New York, USA). Tukey's test was performed for the detection of outliers (Tukey 1977; Hoaglin, Iglewicz and Tukey 1986; Hoaglin & Iglewicz 1987). All variables were tested for normality using the Shapiro–Wilk test (Shapiro & Wilk 1965). Subsequently, a two-tailed Student *t*-test determined whether the data differed between testing days. The intra-class correlation coefficients (ICCs), as absolute agreement between single measures or between data set means, were calculated between the two days of testing, separately for rest and exercise, to provide a measure of inter-session reproducibility. The within-patient coefficient of variation (CV) between testing days was also calculated for each participant, separately for rest and exercise, and then averaged across all participants to provide a measure of the dispersion of the data around the mean during rest and exercise. Inter-observer reproducibility was assessed via ICCs between data set means by taking into account all measurement sessions for both testers, separating the rest and exercise data.

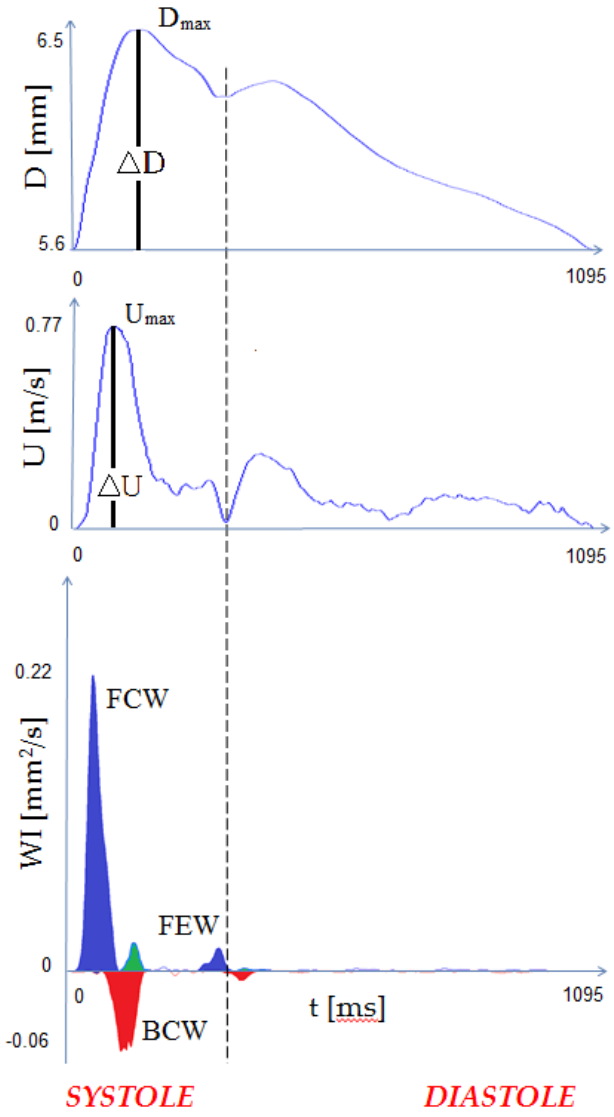

Figure 3.3: Example of waveforms. Top: Carotid diameter and blood flow velocity. D_{max}, U_{max}, ΔD and ΔU are shown. Bottom: Corresponding wave intensity. The *dark blue areas* represent, from left to right, the forward compression (FCW) and forward expansion (FEW) waves; the *red areas* represent the backward compression (BCW) and backward expansion (BEW) waves, as reflections of FCW and FEW, respectively; the *green areas* represent, from left to right, the reflections of BCW and BEW. Only FCW, BCW and FEW are labelled.

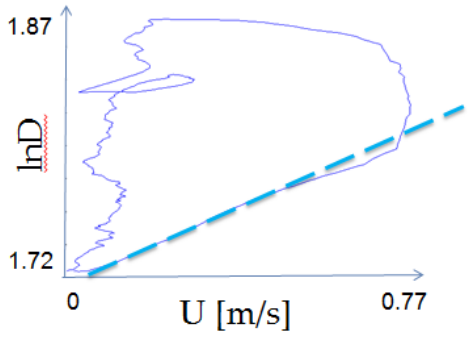

Figure 3.4: Example of lnDU loop at rest for one subject. The regression line of the early systolic linear part is shown.

An ICC > 0.7 was classified as "high reproducibility," an ICC < 0.5 as "low reproducibility" and an ICC between the two as "moderate reproducibility" (Portney & Watkins 2000). A CV ≥ 20% was considered "high dispersion," a CV ≤ 10% was considered "low dispersion," and the range between the two was considered "moderate dispersion." Implementing Bland–Altman analysis, the differences between two values (day 1 minus day 2) were plotted against their mean value, and the limits of agreement were defined as the mean difference ± 2SD (Bland and Altman, 1986). Statistical significance was assumed for $p < 0.05$.

3.3 Results

3.3.1 Hemodynamic parameters

Table 3.1 summarises the mean values across all participants of the hemodynamic parameters under each condition. All variables were normally distributed apart from D_{max} at the first testing session (Rest 1 and Exercise 1) and $\sigma^2{}_{\mathrm{dD}}$ at several testing sessions and conditions (Rest 2, Exercise 1, and Exercise 2). Two outliers were observed in the same participant for the parameters D_{max} and $\sigma^2{}_{\mathrm{dD}}$ and were not excluded from the data sets. The *t*-tests revealed no statistically significant differences between testing days for any of the hemodynamic parameters ($p > 0.05$ for all).

Hemodynamic parameters		Rest 1	Rest 2	Exercise 1	Exercise 2
$\mathbf{D_{max}}$	mean ± SD [mm]	6.91 ± 0.54	7.07 ± 0.48	7.33 ± 0.72	7.21 ± 0.49
	ICC abs. agree. Si/Me	0.67 / 0.80		0.65 / 0.79	
	CV (%)	3.4		3.9	
$\mathbf{U_{max}}$	mean ± SD [m/s]	0.75 ± 0.13	0.74 ± 0.15	0.91 ± 0.19	0.90 ± 0.21
	ICC abs. agree. Si/Me	0.64 / 0.78		0.76 / 0.86	
	CV (%)	9.4		8.9	
ΔD	mean ± SD [mm]	0.59 ± 0.15	0.60 ± 0.14	0.71 ± 0.16	0.74 ± 0.16
	ICC abs. agree. Si/Me	0.93 / 0.96		0.92 / 0.96	
	CV (%)	6.0		5.3	
ΔU	mean ± SD [m/s]	0.69 ± 0.16	0.69 ± 0.17	0.90 ± 0.20	0.90 ± 0.22
	ICC abs. agree. Si/Me	0.74 / 0.85		0.78 / 0.88	
	CV (%)	10.4		9.2	
$\boldsymbol{\sigma^2_{dD}}$	mean ± SD [mm^2]	0.56 ± 0.23	0.53 ± 0.27	2.03 ± 1.16	1.97 ± 1.02
	ICC abs. agree. Si/Me	0.82 / 0.90		0.91 / 0.96	
	CV (%)	17.1		12.0	
$\boldsymbol{\sigma^2_{dU}}$	mean ± SD [m^2/s^2]	2.00 ± 0.85	1.74 ± 0.79	6.42 ± 2.70	6.16 ± 2.82
	ICC abs. agree. Si/Me	0.39 / 0.56		0.60 / 0.75	
	CV (%)	29.3		22.5	

Table 3.1: Hemodynamic parameters at rest and during submaximal cycling. Data are averaged among 12 participants. D_{max}: peak diameter; U_{max}: peak velocity; ΔD: diameter pulse; ΔU: velocity pulse; $\sigma^2{}_{\mathrm{dD}}$: variance of dD; $\sigma^2{}_{\mathrm{dU}}$: variance of dU; ICC abs. agree Si/Me: absolute agreement intraclass correlation coefficients, Si: single, Me: mean; CV: within-subjects coefficient of variation. Details in the text.

The pulse values (ΔD and ΔU) had high reproducibility, whereas the corresponding peak values (D_{max} and U_{max}) were less reproducible, both at rest and during exercise, despite the low CV values that accompanied them. Furthermore, among these four parameters, the diameter variables exhibited generally higher reproducibility than the corresponding velocity variables at rest as well as during exercise; these findings were complemented by the CV values, which indicated higher dispersion for the velocity parameters.

In terms of derivatives, ICCs were high, supporting reproducibility of both at rest

and during exercise (Table 3.1). There was low (single absolute agreement) and moderate (mean absolute agreement) reproducibility of $\sigma^2{}_{\mathrm{dU}}$ at rest and moderate (single absolute agreement) or high (mean absolute agreement) reproducibility of $\sigma^2{}_{\mathrm{dU}}$ during exercise. CV magnitudes suggested lower dispersion for $\sigma^2{}_{\mathrm{dD}}$ compared to $\sigma^2{}_{\mathrm{dU}}$.

The majority of the hemodynamic parameters had higher ICC values and lower CV values during exercise compared with rest. Only D_{max} exhibited the opposite behaviour, with lower ICC and higher CV during exercise. Figure 3.5A and B illustrates the individual variations within participants in mean ΔD and ΔU, respectively, across testing days and conditions. Although the values for ΔD and ΔU over the whole cohort indicate that they did not vary substantially between testing days (Table 3.1), the individual data show that for some participants the variation observed between different days was considerable, both at rest and during exercise. The comparisons between day 1 and day 2 in Figure 3.6 and the Bland–Altman graphs in Figure 3.7 illustrate that the majority of data points for the hemodynamic parameters fall within the limits of agreement, without any obvious trend or inconsistency in variability across the graph.

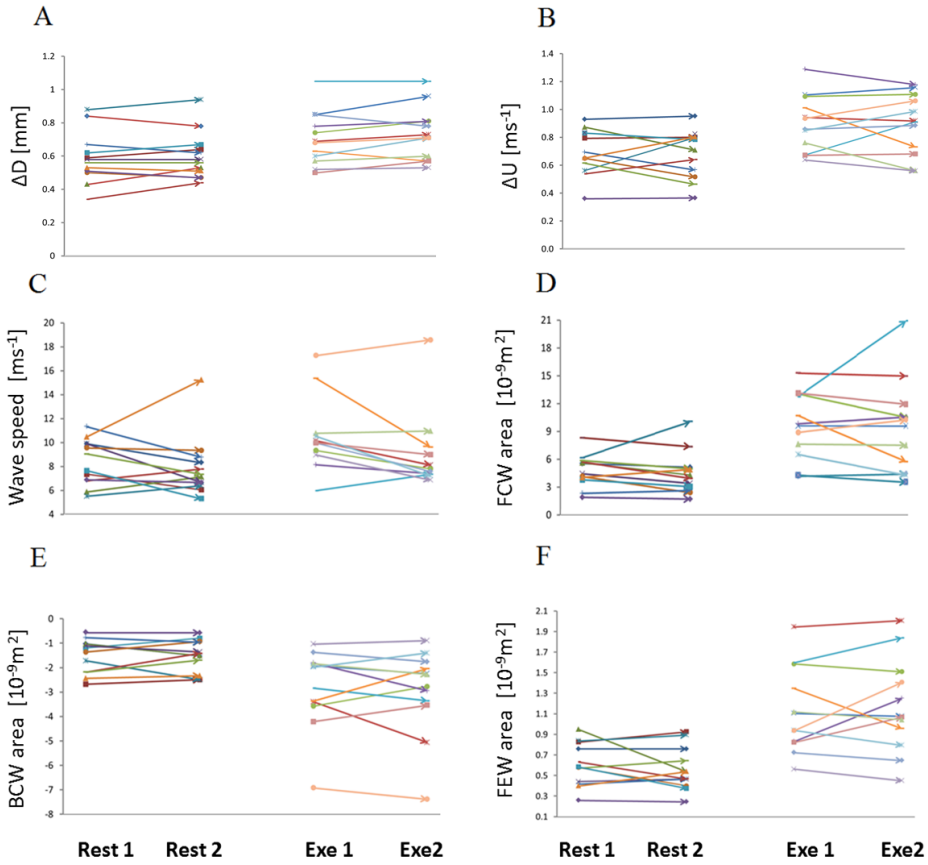

Figure 3.5: Vector plots of measurements performed at rest and during exercise on both days. (A) ΔD. (B) ΔU. (C) Wave speed. (D) Forward compression wave (FCW) area. (E) Backward compression wave (BCW) area. (F) Forward expansion wave (FEW) area.

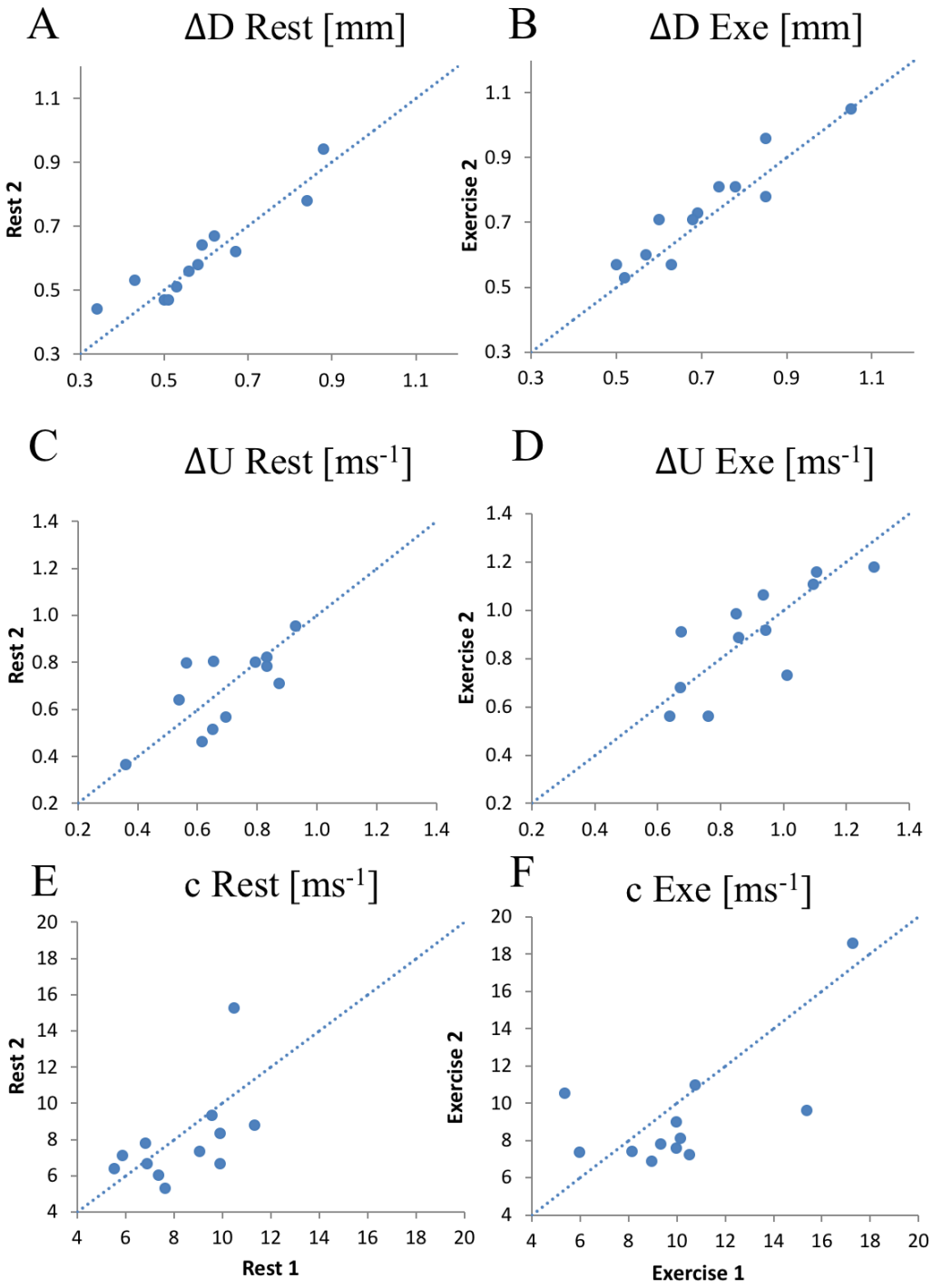

Figure 3.6: Comparison of Δ*D* (A,B), Δ*U* (C,D) and wave speed (E,F) values between the two days of testing, during rest and exercise (Exe) for the whole cohort.

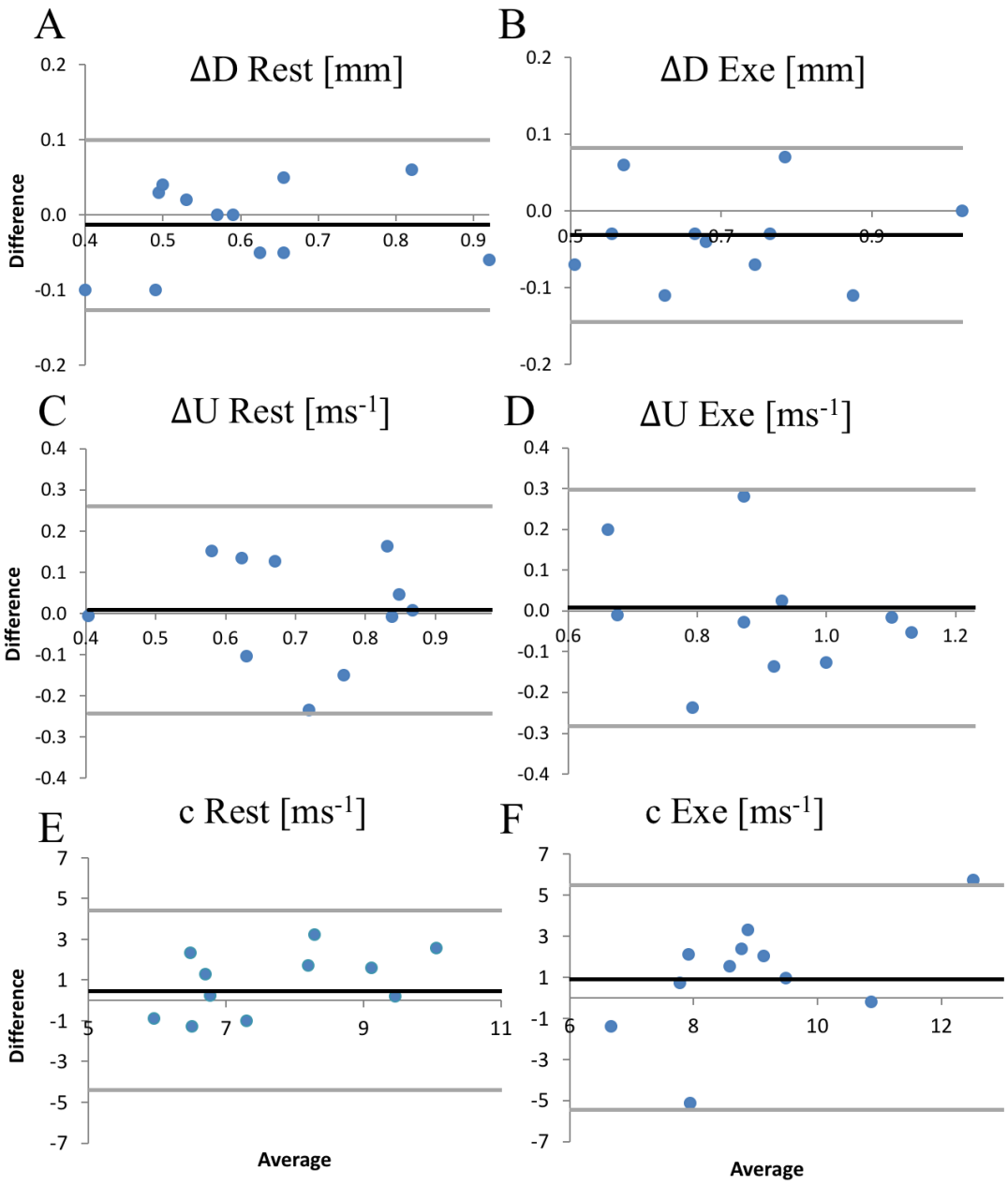

Figure 3.7: Bland–Altman plots of Δ*D* (A,B), Δ*U* (C,D) and wave speed (E,F) values for the two days of testing during rest and exercise for the whole cohort. (A,C,E) Rest condition. (B,D,F) Exercise (Exe). The *dark thick line* represents the mean difference; the grey lines, ±2 standard deviations.

3.3.2 Wave parameters

The mean values of the wave parameters that were investigated are provided, under each condition, in Table 3.2, together with the results of the statistical analysis. Wave speed

values were normally distributed, except at Rest 2 and during Exercise 2. FCW peak values displayed similar behaviour and were not normally distributed at Rest 2 and Exercise 2. The outlier for FCW peak was observed in the same participant as for the hemodynamic parameters, whereas the outlier for the wave speed was observed in a different participant. They were not excluded from the data sets. All other wave parameters, BCW and FEW peaks, FCW, BCW and FEW areas, were normally distributed. No significant differences between testing days were evident for any of the wave parameters ($p > 0.05$ for all).

Wave parameters		Rest 1	Rest 2	Exercise 1	Exercise 2
c	mean ± SD [m/s]	8.36 ± 1.92	7.92 ± 2.58	10.15 ± 3.37	9.26 ± 3.23
	ICC abs. agree. Si/Me	0.54 / 0.70		0.65 / 0.79	
	CV (%)	14.6		17.1	
FCW peak	mean ± SD [10^{-6} m^2/s]	0.16 ± 0.06	0.15 ± 0.10	0.39 ± 0.16	0.39 ± 0.23
	ICC abs. agree. Si/Me	0.65 / 0.79		0.72 / 0.84	
	CV (%)	21.8		15.3	
FCW area	mean ± SD [10^{-9} m^2]	4.83 ± 1.76	4.50 ± 2.32	9.66 ± 3.56	9.53 ± 5
	ICC abs. agree. Si/Me	0.73 / 0.84		0.76 / 0.86	
	CV (%)	17.1		13.7	
BCW peak	mean ± SD [10^{-6} m^2/s]	-0.05 ± 0.02	-0.05 ± 0.02	-0.13 ± 0.08	-0.13 ± 0.07
	ICC abs. agree. Si/Me	0.69 / 0.82		0.80 / 0.89	
	CV (%)	18.5		22.3	
BCW area	mean ± SD [10^{-9} m^2]	-1.52 ± 0.70	-1.50 ± 0.65	2.85 ± 1.61	2.97 ± 1.77
	ICC abs. agree. Si/Me	0.78 / 0.87		0.88 / 0.94	
	CV (%)	18.6		18.4	
FEW peak	mean ± SD [10^{-6} m^2/s]	0.04 ± 0.01	0.03 ± 0.01	0.06 ± 0.02	0.06 ± 0.02
	ICC abs. agree. Si/Me	0.77 / 0.87		0.81 / 0.89	
	CV (%)	12.5		15.0	
FEW area	mean ± SD [10^{-9} m^2]	0.60 ± 0.21	0.56 ± 0.21	1.13 ± 0.41	1.17 ± 0.46
	ICC abs. agree. Si/Me	0.70 / 0.82		0.84 / 0.91	
	CV (%)	14.6		13.1	

Table 3.2: Wave parameters at rest and during submaximal cycling. Data are averaged among 12 participants. *c*: wave speed; FCW: forward compression wave; BCW: backward compression wave; FEW: forward expansion wave; ICC abs. agree Si/Me: absolute agreement intraclass correlation coefficients, Si: single, Me: mean; CV: within-subjects coefficient of variation.

The ICC values for wave speed exhibited moderate (single absolute agreement) or high (mean absolute agreement) reproducibility, both at rest and during exercise. FCW and BCW peaks exhibited moderate reproducibility at rest and high reproducibility during exercise, whereas the FEW peak displayed high reproducibility in both conditions. ICC mean absolute agreement coefficients were high for all parameters and both conditions. FCW, BCW and FEW areas exhibited high reproducibility at rest and during exercise.

Coefficient of variation values for wave speed exhibited low dispersion at rest and moderate dispersion during exercise. The FCW peak values had high dispersion at rest and moderate dispersion during exercise. The BCW peak exhibited moderate dispersion at rest and high dispersion during exercise, whereas FEW peak values had low dispersion both at rest and during exercise. FCW, BCW and FEW areas exhibited low or moderate dispersion under both conditions. Overall, wave speed, BCW peak and FEW peak dispersions increased from rest to exercise, whereas FCW peak and FCW area dispersion substantially decreased. BCW and FEW areas did not exhibit a substantial change in dispersion. The ICC values increased from rest to exercise condition for all parameters. Figure 3.5C–F illustrates the changes among individual participants between testing days in mean wave speed, mean FCW, mean BCW and mean FEW areas, respectively, separately into rest and exercise. The averages of the whole cohort suggest neither parameter varied substantially between testing days (Table 3.2). The comparisons between day 1 and day 2 (Figure 3.8) and the Bland–Altman graphs (Figure 3.9) indicate that the majority of data points for the wave parameters fall within the limits of agreement.

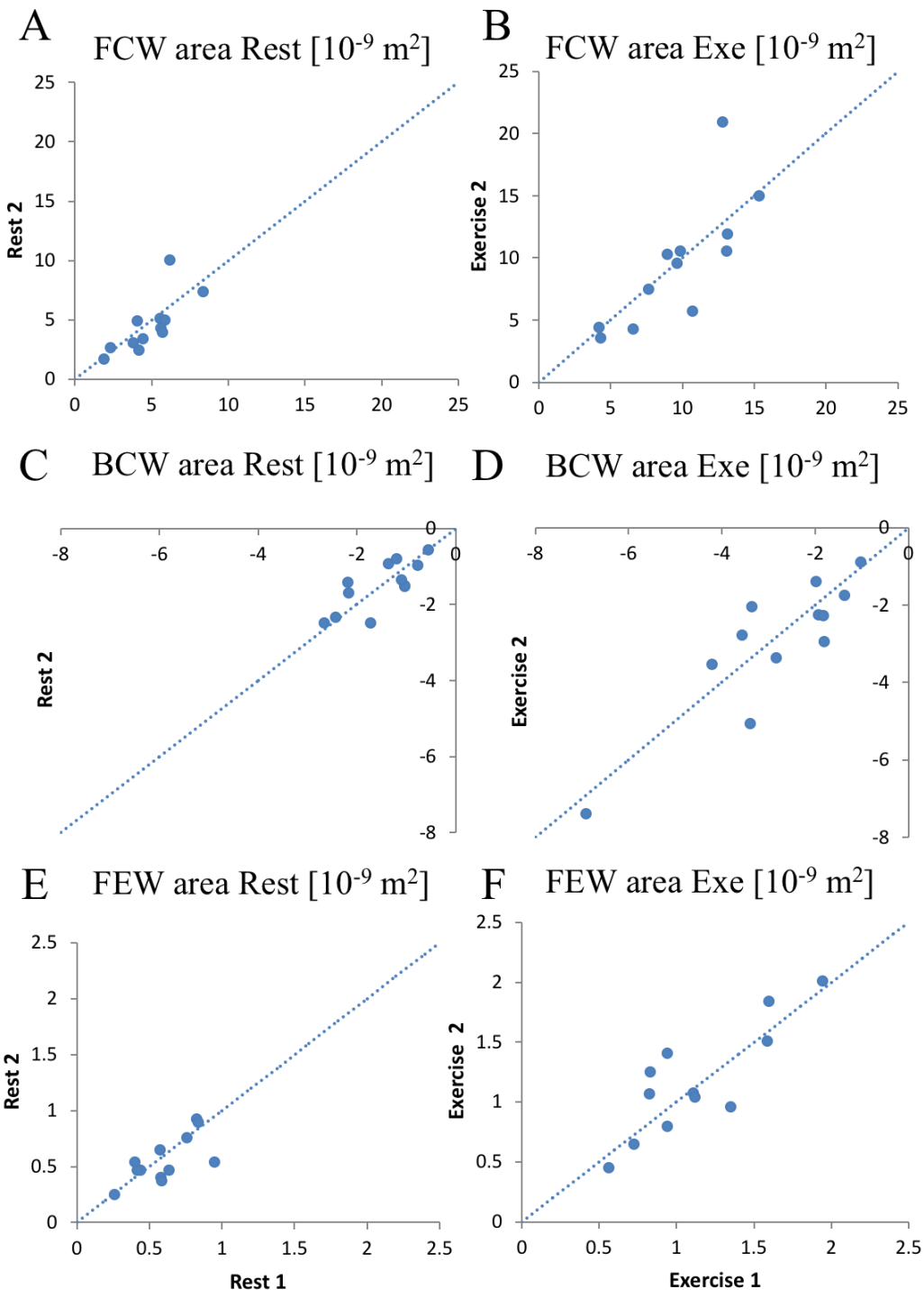

Figure 3.8: Comparison of forward compression wave (FCW) (A,B), backward compression wave (BCW) (C,D) and forward expansion wave (FEW) (E,F) area values between the two days of testing during rest and exercise (Exe) for the whole cohort.

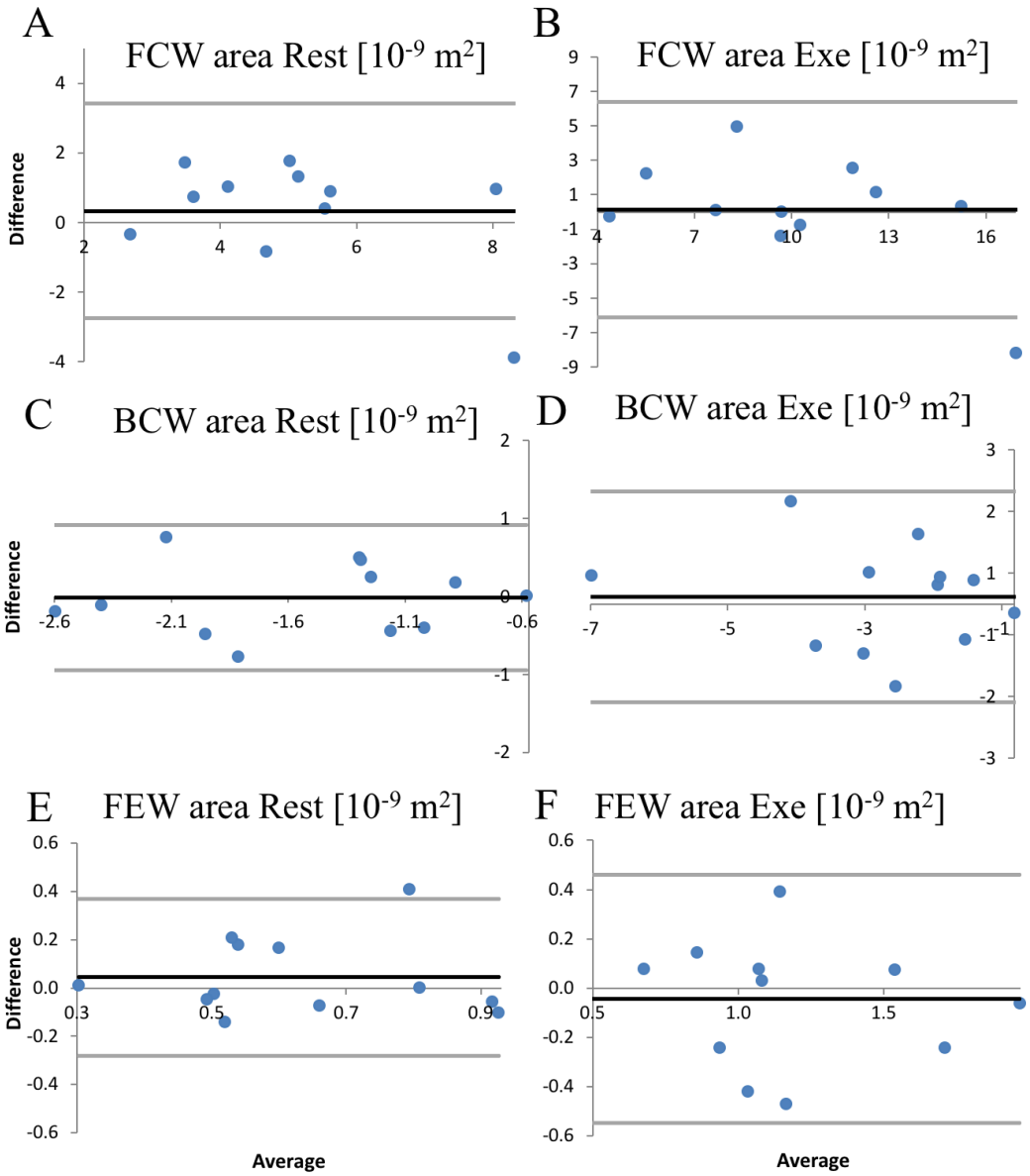

Figure 3.9: Bland–Altman plots of forward compression wave (FCW) (A,B), backward compression wave (BCW) (C,D) and forward expansion wave (FEW) (E,F) area values between the two days of testing during rest and exercise for the whole cohort. (A,C,E) Rest condition. (B,D,F) Exercise (Exe). The *dark thick line* represents the mean difference; the grey lines, ±2 standard deviations.

3.3.3 Inter-observer reproducibility

Table 3.3 and Figures 3.10 to 3.13 display the mean ICC values for inter-observer reproducibility for relevant hemodynamic and wave intensity parameters, across all participants, separating rest and exercise conditions. Most of the parameters exhibited a

lower ICC value during exercise (ΔU and BCW area showing the most significant difference between the two conditions), although still exhibiting high reproducibility. Only the wave speed and BCW peak didn't have high, but moderate reproducibility during exercise. The presence of one outlier was recorded for ΔU (during exercise) and wave speed (both at rest and during exercise) as well as for BCW area (at rest and during exercise) and FCW area (only at rest). Overall, both hemodynamic and wave intensity parameters were fairly inter-observer reproducible.

Parameters	**ICC Rest**	**ICC Exercise**
D_{max}	0.76	0.81
U_{max}	0.94	0.72
ΔD	0.94	0.95
ΔU	0.97	0.72
$\sigma^2{}_{dD}$	0.91	0.91
$\sigma^2{}_{dU}$	0.85	0.81
c	0.84	0.56
FCW peak	0.96	0.90
FCW area	0.94	0.83
BCW peak	0.77	0.67
BCW area	0.87	0.71
FEW peak	0.72	0.79
FEW area	0.88	0.73

Table 3.3: Assessment of inter-observer reproducibility for the hemodynamic and wave parameters, at rest and during submaximal cycling. Data are from 12 participants. D_{max}: peak diameter; U_{max}: peak velocity; ΔD: diameter pulse; ΔU: velocity pulse; $\sigma^2{}_{dD}$: variance of dD; $\sigma^2{}_{dU}$: variance of dU; c: wave speed; FCW: forward compression wave; BCW: backward compression wave; FEW: forward expansion wave; ICC: intraclass correlation coefficient.

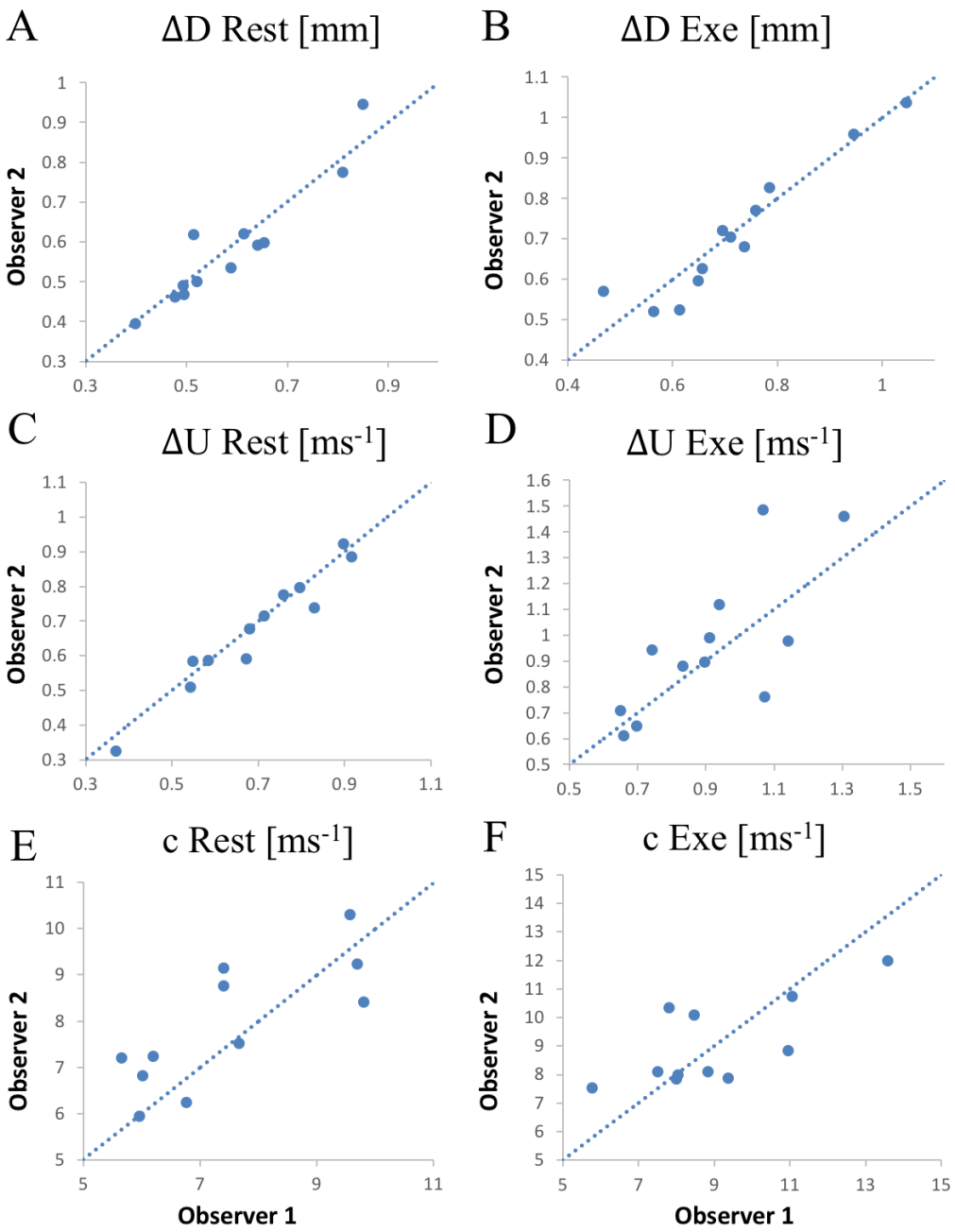

Figure 3.10: Comparison of ΔD (A,B), ΔU (C,D) and wave speed (c) (E,F) values between the two observers during rest (A,C,E) and exercise (Exe; B,D,F) for the whole cohort. Data from both days of testing are pooled.

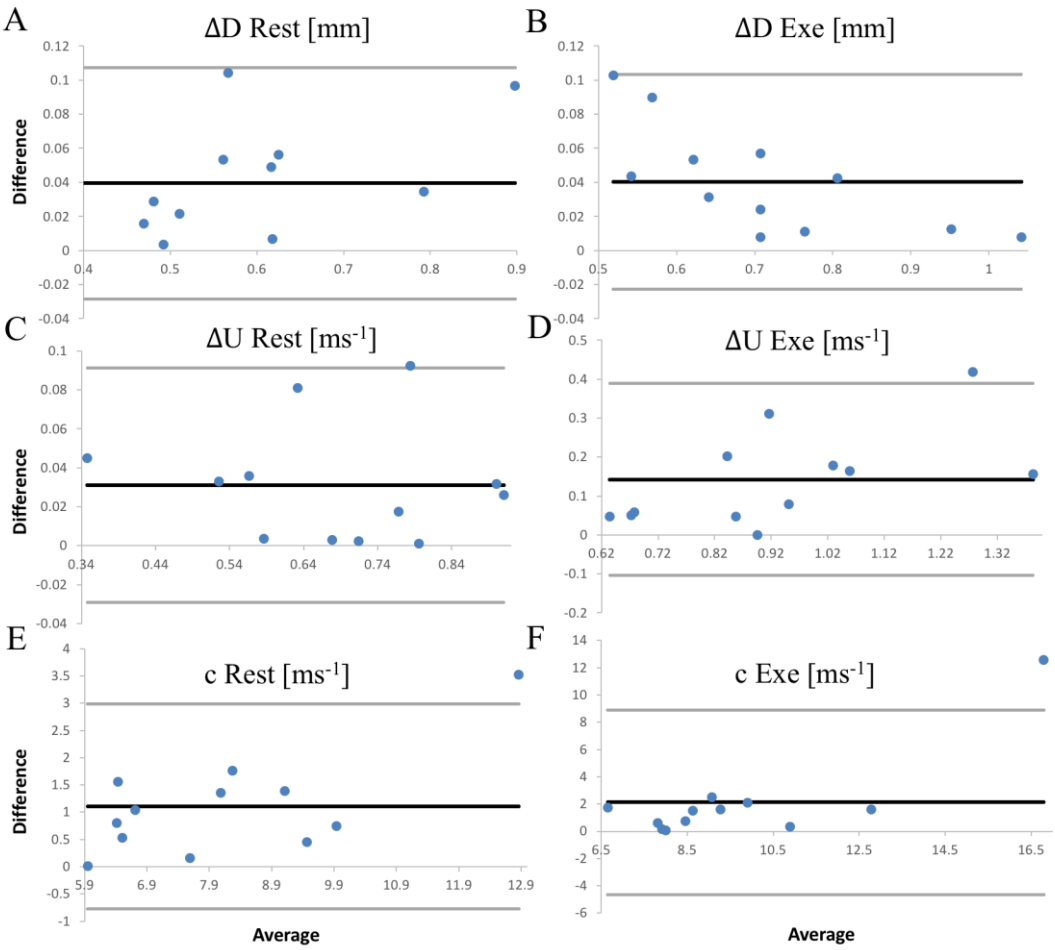

Figure 3.11: Bland–Altman plots of ΔD (A,B), ΔU (C,D) and wave speed (c) (E,F) values between the two observers during rest (A,C,E) and exercise (Exe; B,D,F) for the whole cohort. Data from both days of testing are pooled. The *dark thick line* represents the mean difference; the grey lines, ±2 standard deviations.

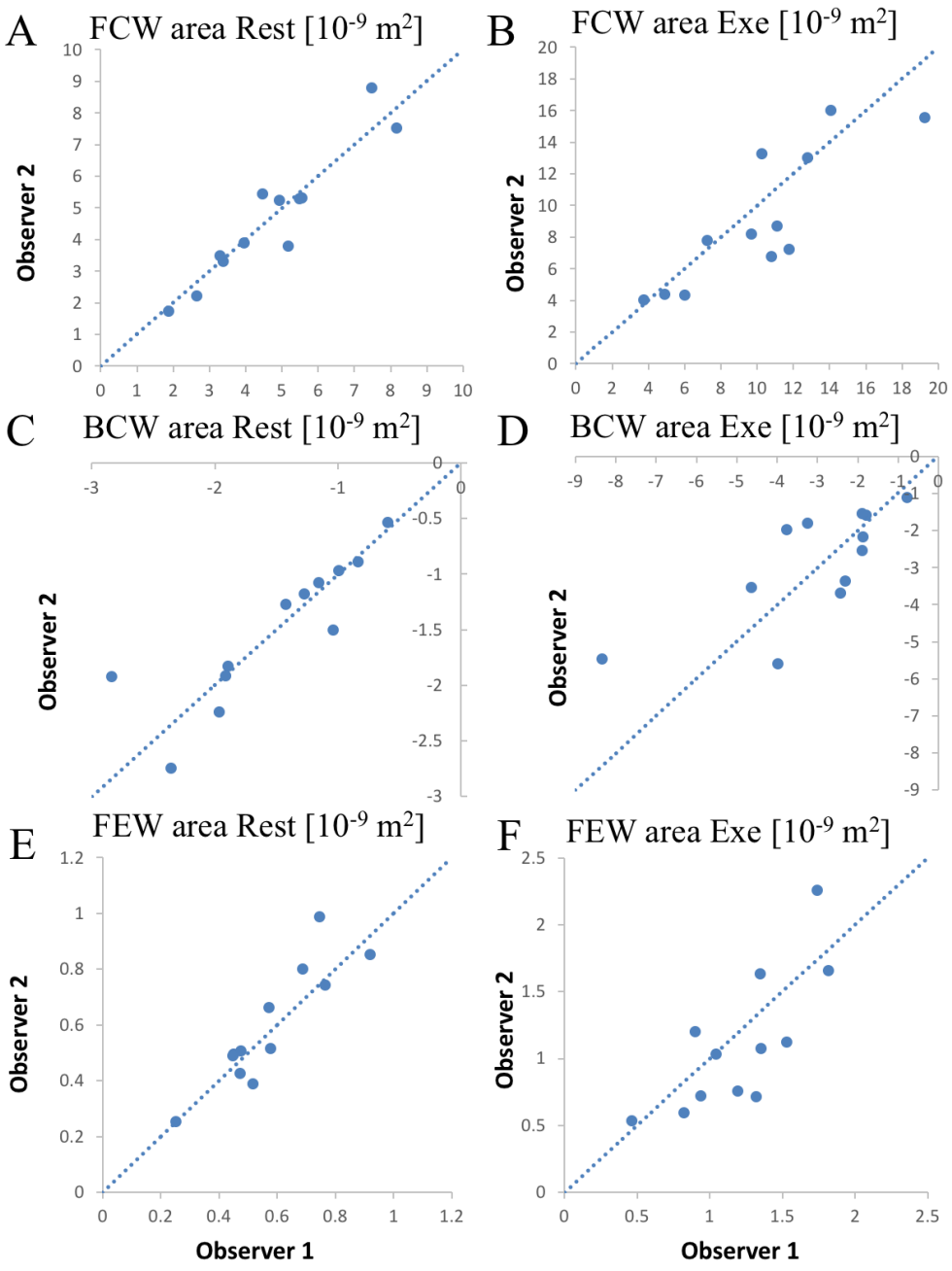

Figure 3.12: Comparison of forward compression wave (FCW) (A,B), backward compression wave (BCW) (C,D) and forward expansion wave (FEW) (E,F) area values between the two observers during rest (A,C,E) and exercise (Exe; B,D,F) for the whole cohort. Data from both days of testing are pooled.

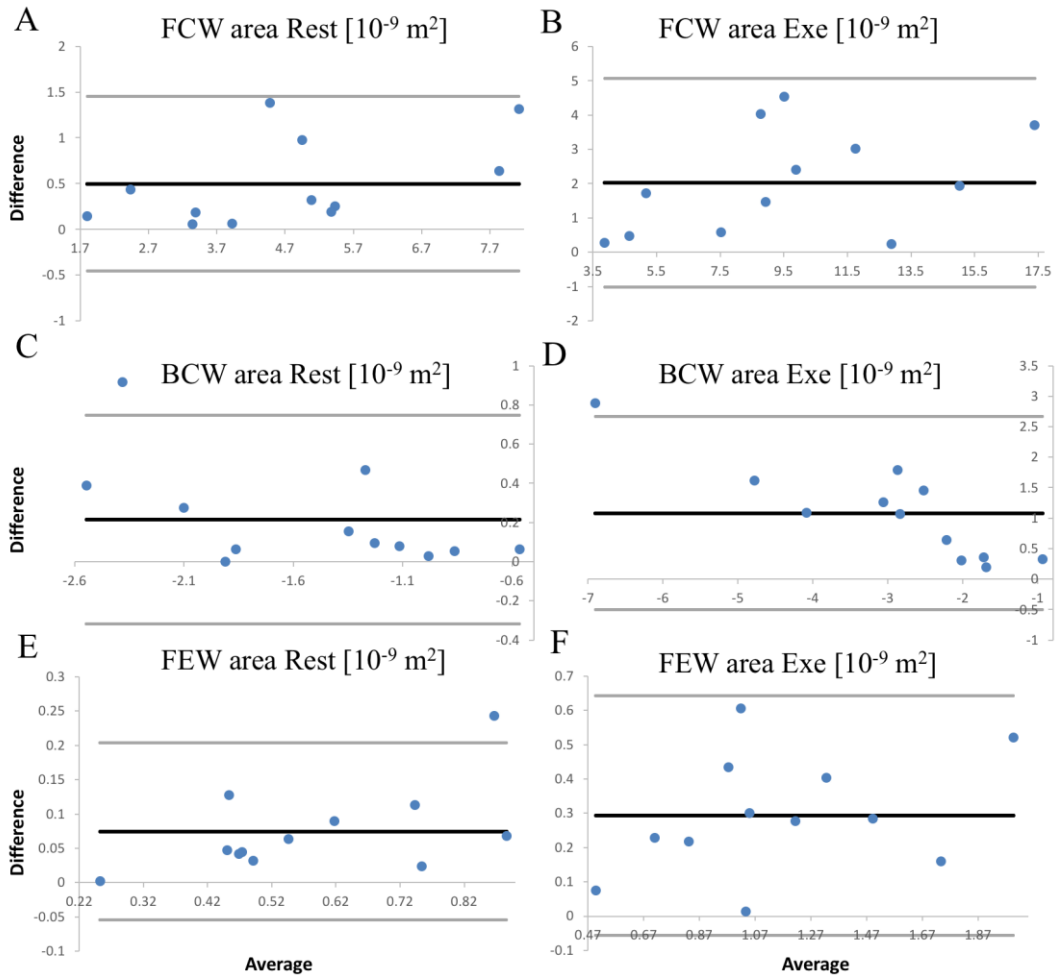

Figure 3.13: Bland–Altman plots of forward compression wave (FCW) (A,B), backward compression wave (BCW) (C,D) and forward expansion wave (FEW) (E,F) area values between the two observers during rest (A,C,E) and exercise (*Exe*; B,D,F) for the whole cohort. Data from both days of testing are pooled. The *dark thick line* represents the mean difference; the grey lines, ±2 standard deviations.

3.4 Discussion

This study illustrates that variables used to derive direct and simultaneous non-invasive wave intensity parameters are reproducible when performed at rest and during semi-recumbent cycling at moderate intensities (30%–40% of maximal workrate). The non-invasive measurements of blood pressure and flow velocity to perform WIA were first suggested by Sugawara et al. (2000), who found a linear relationship between pressure and diameter waveforms throughout the whole cardiac cycle. Thus, the analysis relied upon measuring diameter and velocity from the carotid artery and obtaining a surrogate of

pressure waveform by scaling the diameter to brachial pressure values recorded via a cuff-type manometer (Niki et al. 2002). The reproducibility of this methodology was found clinically acceptable, although FCW and FEW showed high variability (Niki et al. 2002). The shortcoming was that pressure contours quantitatively and qualitatively change along the arterial tree because of wave reflections (Esper, Pinsky and Care 2014); therefore, the process of scaling the diameter waveform, recorded from a specific artery, to pressure data recorded from a different artery, inevitably led to errors. To overcome this problem, applanation tonometry for non-invasive measurements of blood pressure, introduced by Matthys & Verdonck (2002), was applied to WIA (Zambanini et al. 2002; Curtis et al. 2007). With this technique, simultaneous measurements of pressure and velocity at the same location are not possible, thus limiting its application when rapid physiologic perturbations, such as those introduced by exercise conditions, must be taken into account. Further development led to a direct and simultaneous non-invasive methodology, which does not need pressure recordings, but only D and U (Feng & Khir 2010). To the best of our knowledge, the present study is the first to test this methodology in vivo under acute physiologic perturbations.

In this study, pulse variables (ΔD and ΔU) were more reproducible than the corresponding peak variables (D_{max}, U_{max}), and, generally, variables related to diameter measures exhibited higher reproducibility and lower dispersion than the velocity variables at rest and during exercise. The majority of the hemodynamic parameters had greater reproducibility and lower dispersion during exercise compared with rest. Overall, reproducibility increased from rest to exercise for all wave parameters. The dispersion increased from rest to exercise for the wave speed, BCW peak and FEW peak, whereas it substantially decreased for FCW peak and FCW area. BCW and FEW areas did not exhibit a substantial change in dispersion from rest to exercise. Almost all the hemodynamic and wave parameters were normally distributed.

In relation to previous studies examining dynamic parameters of the carotid arteries, these findings are consistent with those of Studinger et al. (2003), who examined arterial diameters in high resolution, and Hellstrom et al. (1996), who examined blood velocities. Previous studies have pointed out several factors affecting the reproducibility of parameters that can be used to derive WIA variables. Specifically, Peters et al. (2001) supported the notion that reproducibility is mostly affected by the velocity measurement, rather than the diameter. Furthermore, Deane & Markus (1997) found that, although the posterior-lateral approach offers optimal results compared with the anterior approach, both methods give reproducible data sets for the CCA. An anterior approach to insonate the CCA was used in the present study for technical reasons, mainly because of the experimental setup. In addition to inherent variabilities in the signals obtained from humans, Beales et al. (2011) suggested

that the main reason for a poor overall reproducibility relates to operator variability. They also suggested that using the trailing edge to leading edge borders to delineate arterial diameters improves image reproducibility alongside the use of high-resolution machines (>5 MHz). In the present study these suggestions were followed to limit the impact of these issues.

3.4.1 Reproducibility of parameters

The variability in D_{max} and U_{max} values may be due to superimposed respiration patterns, which can shift the waveform with the breathing cycle both at rest and during exercise. D_{max} and U_{max} are substantially affected by this type of drift, whereas the calculation of pulse tends to eliminate it. In agreement with this reasoning, ΔD and ΔU exhibit better reproducibility than D_{max} and U_{max}, both inter-session and inter-observer; nonetheless, all four parameters have good reproducibility.

Factors related to the computation of the derivatives could be affecting the reproducibility of *dD* and *dU*. The filtering of the raw data preceded any other form of data processing. One of the most commonly used filters for WIA is the Savitzky–Golay filter (Savitzky & Golay 1964), but, as was recently reported (Rivolo et al. 2014), the derivatives of the smoothed signals seem to be more affected by the filter parameters than the smoothed signals themselves. In addition, the noise level superimposed over any waveform increases when calculating its derivative, as well as the average error. Considering a measurement error of *D* and *U* equal to their respective resolutions (0.013 mm and 0.012 m/s) can lead to propagation errors equal to 0.026 mm and 0.024 m/s for the *D* and *U* derivatives, respectively, as well as for ΔD and ΔU (Jcgm 2008). The propagation errors are small compared to ΔD and ΔU values (5% and 3%, respectively) and are not expected to affect the results significantly. It could thus be anticipated that *D* and *U* would exhibit better reproducibility than *dD* and *dU*, respectively, merely because of the higher levels of noise present in the latter signals; therefore, ΔD and ΔU exhibiting better reproducibility than ${\sigma^2}_{\mathrm{dD}}$ and ${\sigma^2}_{\mathrm{dU}}$, respectively, is not unexpected.

For the assessment of *dD* and *dU* reproducibility, comprehensive parameters were used, calculated using every single element of the signals, whereas for the assessment of *D* and *U* reproducibility, only two elements (peak and trough) of the corresponding waveforms were used. Even though the latter method is inherently more vulnerable to noise and artefact interference, it appears that the added noise present in the derivative signals results in ${\sigma^2}_{\mathrm{dD}}$ and ${\sigma^2}_{\mathrm{dU}}$ being less reproducible than ΔD and ΔU. Although *D* and *U* are measured simultaneously and by the same probe, the manual adjustments of gates and angles may

affect each signal differently, and this may be more evident among derivatives, especially *dU*. Regardless, there were no substantial differences, neither for $\sigma^2{}_{\mathrm{dD}}$ nor for $\sigma^2{}_{\mathrm{dU}}$, between the days of testing, neither at rest nor during exercise, suggesting that with an adequate sample size this inconsistency may be overcome.

Analysis of wave speed ICC values revealed overall moderate and high reproducibility, both inter-session and inter-observer. The calculation of wave speed is intimately connected to the ratio of pulse variables (ΔU and ΔD), as highlighted by equation (3.3), and it is mainly affected by the reproducibility of velocity variables. The inaccuracies in measuring velocity are inherent to the methodology itself. In fact, the actual ultrasound measurement of velocity is a combined signal of all the red blood cells that are causing the Doppler frequency shift. This is not uniform from beat to beat, because the blood flow and the red blood cells entering the sample volume (region of interest) and making up the shift inherently change from beat to beat, whereas the diameter is determined by tracking the same sample volume throughout. What the ultrasound probe records is only an average over the cross-sectional area of the vessel. Therefore, the wave speed reproducibility cannot be higher than or similar to the reproducibility of diameter variables. Nevertheless, the lnDU loop technique may have played (and may play, in general) an important role in affecting the reproducibility, as addressed under 'Experimental Considerations and Limitations', because of the linearity threshold settings.

Finally, wave energy (area) reproducibility was more consistent than wave intensity peak reproducibility, both inter-session and inter-observer. This is probably due to the area calculation, taking into account a whole segment of the waveform, rather than just a single point. The latter is more susceptible to noise and artefact interference than the former. Nevertheless, both areas and peaks exhibited a generally high degree of reproducibility.

3.4.2 Implications for future work

Despite a number of potential error sources, it is possible to obtain *D* and *U* measurements and perform direct and simultaneous non-invasive WIA reliably both at rest and during exercise. Unlike other local techniques, such as near- infrared spectroscopy, non-invasive WIA is uniquely qualified to investigate the coupling of the heart with the cerebral vasculature. Furthermore, contrary to magnetic resonance imaging-based techniques, non-invasive WIA can provide results at sub-beat temporal resolution, using lower cost equipment.

3.4.3 Experimental considerations and limitations

Data from two participants (one male) produced outliers in some, but not all, data sets (D_{max}, $\sigma^2{}_{\mathrm{dD}}$, FCW peak, c). Further investigation did not highlight any qualitatively nonphysiological waveform or error in the analysis. Therefore, the corresponding data points represent real variation and cannot be dismissed.

Although the ensemble averaging process is more common in the analysis of ultrasound measurements, it could lead to miscalculations of wave speed values, which are strictly dependent on the early upstroke of the waveforms; consequently, erroneous estimates of WI parameters could be created in this study. Therefore, it was chosen to calculate all parameters from individual cardiac cycles and then average the results. This method may have contributed to lower theoretical reproducibility values and must be considered in relation to previous work. On the other hand, the wave speed obtained from the lnDU loop has been derived visually from the optimal linear fit over the early systolic part of the loop. Although repeating the calculations manually gave very similar results, the possibility exists that the use of an automatic linear regression algorithm would reduce the inter-observer variability. However, a drawback associated with the use of an automatic linear regression algorithm could be the assessment of a proper "linearity threshold", which may in turn be data set dependent (Khir et al. 2007).

Finally, the lack of electrocardiogram and breath frequency monitoring to assess the impact of heart rate and breathing frequency on the variability of the data in the present study is a limitation that warrants further investigation in future studies.

3.4.4 Conclusions

Arterial diameter and blood flow velocity waveforms, obtained from ultrasound measurements of the CCA of young healthy participants, are fairly reproducible, together with all derived parameters, including wave intensity, both at rest and during submaximal semi-recumbent exercise. This outcome opens up new possibilities for non-invasive investigation of cardiovascular properties under physiologic perturbations.

Chapter 4: Non-invasive Assessment of Wave Intensity Analysis during Exercise*

4.1 Introduction

This Chapter focuses on the non-invasive determination of local wave speed and wave intensity-derived parameters in response to physiological perturbations. As highlighted in Chapter 1, an important extension of the original WIA was the development of non-invasive WIA, using direct and simultaneous measurements of diameter (D) and blood flow velocity (U), which can be acquired using Doppler ultrasound (Feng & Khir 2010). This approach produces wave intensity curves that are almost identical to those produced using arterial pressure, without relying on the calibration of pressure waveforms to brachial blood pressure and circumventing the problem of non-simultaneous measurements via applanation tonometry. This temporally dispersed acquisition becomes especially erroneous when rapid physiological perturbations, such as physical activity at different workrates, are involved. The lnDU-loop (Feng & Khir 2010) also enables the determination of local wave speed non-invasively, offering a useful tool to investigate local stiffness under different conditions, like exercise.

Exercise is a complex and substantial physiological stress that involves alterations in autonomic nervous system activity, which affect both the frequency and contractility of cardiac dynamics (Stöhr, González-Alonso and Shave 2011; Munch et al. 2014) whilst selectively altering peripheral vascular resistance in different vascular beds, depending on their active or inactive status (Saltin et al. 1998). For example, vascular resistance decreases substantially in contracting skeletal muscle as local factors override the systemic elevations in sympathetic activity, which induces vasoconstriction and increases downstream resistance in non-active tissues (Mortensen et al. 2008). Within the cerebral vasculature, however, incremental exercise induces unique responses, with cerebrovascular resistance (CvR) normally decreasing up to moderate workrates (~60% of maximal aerobic power output) and increasing thereafter as the workrate rises to maximal levels (Ide & Secher 2000; Sato et al. 2011; Trangmar et al. 2014); this is due to differential redistribution of the blood flow, obtained by centrally and locally controlling the diameter of the vessels. Initial work addressing whether alterations in CvR can be monitored by WIA were first performed by Bleasdale et al. (2003), who demonstrated that CO_2-rebreathing-induced cerebrovascular

* Article accepted for publication in the American Journal of Physiology, Heart and Circulatory Physiology (2018).

dilation reduced the magnitude of CCA reflected waves. Conversely, Sato et al. (2011) reported that exercise-induced physiological perturbations differentially altered vascular resistances in various head tissues, in relation to the complex interaction of thermoregulatory adjustments to the facial vasculature and alterations in cerebral vascular resistance, induced by changing CO_2 and pH. These divergent responses combine to alter reflected waves arriving at the CCA, thus the imputed values at this vessel are complex. However, the impact of those alterations on left ventricular performance remains unexplored. Wave intensity analysis is a unique tool with the potential to examine this cardiac-cerebrovascular interaction.

Therefore, the aim of this study was to examine the contribution of cardiac and peripheral vascular alterations, at different exercise workrates and throughout subsequent recovery, upon CCA wave intensity parameters. The magnitude of incident and reflected waves was examined, as well as of reflection indices as responses originating from the cerebral circulation and other microcirculatory beds in the head. It is hypothesized that indices of left ventricular contractility and late-systolic active blood flow deceleration would parallel increases in exercise intensity, up to moderate-to-high workrates (60% of maximal workrate) and that reflection indices would change concomitantly with changes in CCA vascular resistance during exercise and recovery.

4.2 Material and Methods

4.2.1 Study Group

Eight healthy endurance trained males (triathletes and cyclists, aged 27 ± 4 y, body mass: 68.1 ± 4.3 kg, height: 1.76 ± 0.1 m, body mass index: 22.0 ± 0.6 kg/m^2) participated in the study. Participants completed a health questionnaire to exclude those with overt cardiovascular or metabolic diseases, smokers and participants taking any medication. The experimental procedures and potential risks were explained prior to testing and written informed consent was obtained. The study was approved by the Brunel University London Research Ethics Committee and conformed to the guidelines of the Declaration of Helsinki.

4.2.2 Experimental design

Participants attended a temperature and humidity controlled (20-24°C, 40%) laboratory on two occasions separated by at least 48 hours. A ramp incremental step exercise

test to volitional fatigue was performed (Rossiter, Kowalchuk and Whipp 2006) using a semi-recumbent cycling ergometer (Angio, Lode B.V., Groningen, The Netherlands) mounted on an examination table and equipped with a power control box. The results obtained during this session were used to determine the individual maximal workrate (W_{max}) defined as the power at which the participant was no longer able to maintain the required cadence (60 rpm). Average W_{max} for all eight participants was 362 $\pm$ 36 W. In the second experimental session participants rested for 30 min and then performed an incremental exercise trial based on their W_{max}, and monitored throughout 1 hour of post-exercise recovery (Figure 4.1). Hemodynamic measurements to determine carotid artery WIA were obtained throughout the experimental trial during this second session (details in the "Ultrasound Measurements" section).

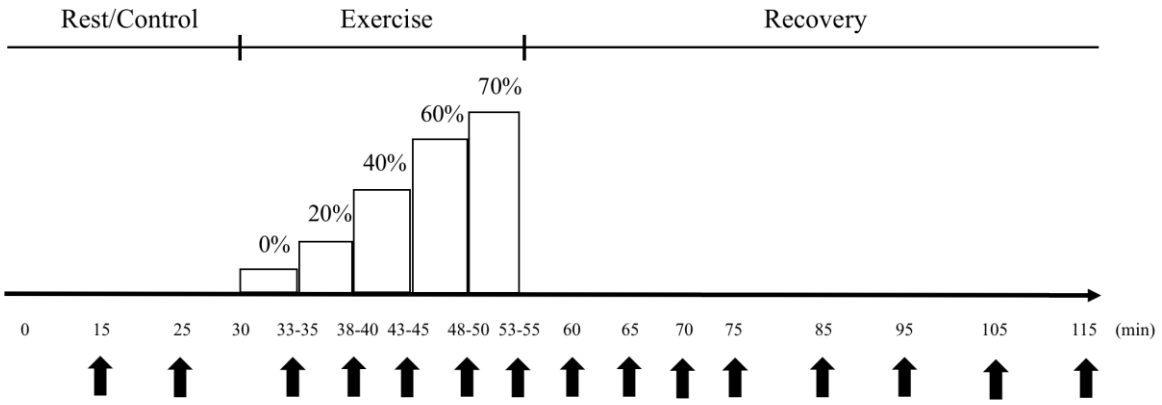

Figure 4.1: Experimental protocol. Arrows designate ultrasound measurements and blood pressure recordings. Percentages indicate the corresponding fraction of the maximal workrate. 0%: unloaded.

4.2.3 Instrumentation

A SSD – 5500 ultrasound system (Aloka, Tokyo, Japan) equipped with a 7.5 MHz linear array probe and a three electrode ECG system (V5 configuration) was used to insonate the right common carotid artery. Scans were performed in the longitudinal view approximately 2 cm proximal to the bifurcation. The ultrasound echo tracking sub-system measured D with a resolution of 0.013 mm. The gates were positioned manually between the borders of media and intima of the superficial and deep walls, and parallel to them. The D waveform was tracked automatically as the distance between the two gates over time and obtained from the M-mode tracing. The pulse-wave Doppler sub-system measured U with a resolution of 0.012 m/s and the Doppler gate was positioned manually in B-mode at the

centre of the vessel, parallel to the walls, ensuring that the insonation angle was always between 58° and 60°. Both D and U were simultaneously sampled at 1000 Hz. Continuous non-invasive blood pressure was obtained using a photo-plethysmography based system from the left middle finger that was calibrated to oscillometrically measured brachial blood pressure (Finometer® Pro, Finapres Medical Systems BV, Amsterdam, The Netherlands). The monitoring device estimated systolic blood pressure (SBP), diastolic blood pressure (DBP) and cardiac output (CO) (model flow method: Allen 2007; Harms et al. 1999). Mean arterial pressure (MAP) was calculated as: MAP = 1/3 SBP + 2/3 DBP. At high workrates, the finger plethysmorgraphy device was unable to reliable obtain a signal and cuff pressures were recorded instead. The experimental exercise protocol was performed on the same semi-recumbent cycling ergometer described above.

4.2.4 Ultrasound measurements

Measurements were acquired before exercise, during each stage of exercise and at selected time points during post-exercise recovery. D and U were obtained simultaneously and spanned a window of 8 to 25 heart cycles, depending on the heart rate of the participant.

Participants arrived at the laboratory at least 2 h post prandial, having not performed strenuous exercise or consumed caffeine for 24 h and 12 h, respectively. They assumed a semi-recumbent position (32°) and were asked to minimize head movement and maintain a stable position by holding the table handles, especially during exercise. Prior to any acquisition of carotid artery parameters, participants were instrumented and rested for 30 min. D and U were acquired twice in this period to determine baseline values. Participants then cycled continuously for 25 min with workrate increasing every 5 min (20, 40, 60, and 70% of each subject's W_{max}), and D and U were acquired during the last 2 min of each exercise stage. After the incremental test, participants cycled for 30 s with no resistance and finally rested in the semi-recumbent position throughout the next 60 min of recovery. Carotid imaging and wave recordings also took place at 5, 10, 15, 20, 30, 40, 50, 60 min post-exercise. For every participant, two measurements were recorded at each of the aforementioned conditions.

4.2.5 Data Analysis

Data were analysed using custom designed algorithms in Matlab (version R2010b, The MathWorks, Inc., Natick, Massachusetts, USA), based upon previous work (Khir et al. 2007) and adapted for non-invasive determination of wave parameters (Feng & Khir 2010).

D and U waveforms were post-processed using a Savitzky-Golay filter (Savitzky & Golay 1964) with a second-degree polynomial and a 16-point half-width window, to eliminate high-frequency noise.

For each measurement, at least 3 consecutive heart cycles presenting no obvious drift (due to low-frequency respiratory cycles) or dampening and retaining typical normal physiological features were selected for the analysis; the hemodynamic and wave parameters were calculated on a beat-by-beat basis for each selected segment and averaged to produce a single measure for each participant at each time point (working condition). To define a single control (baseline) condition, the four measurements taken at the pre-exercise stages (two at 15 min- and two at 25 min time points) were averaged.

The hemodynamic parameters extracted from D and U were: i) peak (systolic) diameter (D_{max}) ii) change in diameter or pulse (ΔD), defined as the difference between peak (systolic) and trough (diastolic) values; iii) peak (systolic) velocity (U_{max}); iv) change in velocity or pulse (ΔU), derived similarly to ΔD; v) common carotid artery mean blood flow (MBF) calculated as the product of mean blood velocity and mean carotid artery cross-sectional area (πr^2) over the heart cycle; vi) CCA resistance, calculated as the ratio of MAP to MBF (Sato et al. 2011). A circular common carotid artery cross-section was assumed throughout the protocol.

Further considerations about the nature of the blood flow can be elucidated from the Womersley and the Reynolds numbers, whose values are reported in Table 4.1. During exercise, frequency of waves and blood viscosity significantly change, affecting the Womersley number and the velocity profile. The frequency of oscillations was derived from the HR, the blood density was assumed to be constant, the mean radius was measured and the blood viscosity was assumed to linearly increase up to 15% at W_{max}; a value obtained by averaging results of Connes et al. (2004), who determined the increases in blood viscosity in athletes with different levels of hemoglobin saturation. During recovery, the blood viscosity was assumed to fall to baseline values (Vandewalle et al. 1988).

Considering that reflected waves were absent during the early systolic portion of each cardiac cycle, the slope of the linear part of lnDU-loop (Feng & Khir 2010) was used to calculate c (m/s) using the following equation:

$$c = \frac{1}{2}\frac{dU_f}{d\ln D_f} \tag{4.1}$$

The subscripts "+" indicate the forward components of the waves. Further, carotid artery distensibility (D_s) was calculated using c in the Bramwell-Hill equation (Bramwell & Hill 1922):

$$D_s = \rho^{-1} \cdot c^{-2} \tag{4.2}$$

where blood density ρ was assumed equal to 1050 kg/m^3.

The non-invasive wave intensity waveform (dI) (m^2/s) was calculated as the product of dD and dU: $dI = dD \cdot dU$, and separated into the forward and backward components, dI_f and dI_b respectively, through the equations:

$$\begin{cases} dI_f = +\dfrac{1}{4(D/2c)}\left(dD + \dfrac{D}{2c}dU\right)^2 \\ dI_b = -\dfrac{1}{4(D/2c)}\left(dD - \dfrac{D}{2c}dU\right)^2 \end{cases} \tag{4.3}$$

The peak (m^2/s) and area (m^2) of the FCW, which is generated by the contraction of the left ventricle, were derived for each cardiac cycle from the amplitude and area, respectively, of the early-systolic peak observed in dI_f. Similarly, the peak and area of BCW, which is attributed to reflections from the cerebral circulation and other microcirculatory beds in the head, were determined for each cardiac cycle from the amplitude and area, respectively, of the mid-systolic peak present in dI_b. Also, the peak and area of the forward X wave, which is attributed to the reflection of BCW, were determined from the amplitude and area of the mid-systolic peak present in dI_f. Finally, the peak and the area of FEW, which is generated by the decrease in shortening velocity of the left ventricle during late systole, were determined from the amplitude and area of the late-systolic peak seen in dI_f. The area parameters are associated with the energy of the waves, in comparison with similar parameters obtained with PU-WIA having units of J m^{-2}.

Two different types of reflection indices were computed: the modulus of the ratio of peak BCW to peak FCW (RI_I) as in Borlotti et al. (2012), and the modulus of the ratio between energies of BCW and FCW (RI_E). Also, wave intensity peak WD1 was calculated, as in Tanaka et al. (2015), as another index of contractility. Mean values for all parameters were derived at each measurement.

4.2.6 Statistical Analysis

All values are reported as mean ± SD. The statistical analyses were performed using SPSS Statistics (v 20, IBM, Armonk, NY, USA). The mean values derived per each condition were tested via repeated measures one-way ANOVA and post-hoc Tukey's test.

Regression analyses were performed within subjects (Bland, Altman 1995a) and between subjects (Bland, Altman, 1995b) accounting for repeated measures. Statistical significance was assumed for p-value < 0. 05.

4.3 Results

4.3.1 Hemodynamic parameters

Table 4.1 and Figure 4.2 show the variation of hemodynamic parameters in different conditions. ΔD and ΔU increased during the latter more intense stages of exercise, by up to 58% and 93%, respectively ($p<0.05$) and significantly decreased at the beginning of recovery, returning to baseline values (Figure 4.2). The same trend occurred with MBF, which increased by 62% from baseline during the last stage of exercise (non significantly, $p>0.05$), then decreased to values that were not different from baseline in recovery. D_{max} and U_{max} showed similar patterns, increasing by 11% and 75%, respectively, throughout exercise and decreasing back to baseline values in the recovery period, however only U_{max} reached statistical significance ($p<0.05$). The Womersley number almost doubled, from 4.4 at baseline value to 8.1 at 70% W_{max}. Therefore, the velocity profile in the CCA at rest and during recovery could be considered parabolic whereas it became prominently flat during exercise. Values of Reynolds number (using D_{max} and U_{max}) ranged from 1693 ± 470 at baseline to 2946 ± 733 at 70% W_{max}, whereas during recovery they were similar to the baseline (the average among all measurements in recovery being 1703 ± 526). Thus the flow became turbulent and inertial forces more prominent during exercise whereas adjusted to control values within 5 min post-exercise.

Variable	Rest	40% W_{max}	70% W_{max}	5-min recovery
HR (bpm)	53 ± 5	120 ± 5*◊□	164 ± 12*□	80 ± 10*●
SBP (mmHg)	125 ± 12	159 ± 19*	188 ± 15*□	123 ± 13●
DBP (mmHg)	65 ± 5	73 ± 8	81 ± 9*	71 ± 10
MAP (mmHg)	85 ± 6	102 ± 11	117 ± 11*□	88 ± 10●
MBF (mL min^{-1})	442 ± 143	468 ± 170	717 ± 50	391 ± 283●
CO (L min^{-1})	5.8 ± 0.5	15.1 ± 2.2*□	21.9 ± 5.7*□	8.0 ± 0.6●
CCA/CO (%)	16 ± 6	7 ± 3*	8 ± 3	14 ± 8
D_{max} (mm)	7.3 ± 0.6	7.8 ± 0.4	8.1 ± 0.6	7.3 ± 0.5
U_{max} (m s^{-1})	0.8 ± 0.2	1.1 ± 0.3	1.4 ± 0.4*	0.8 ± 0.3●
Womersley (1)	4.4 ± 0.4	6.9 ± 0.6*□◊	8.2 ± 0.6*□	5.4 ± 0.4*●
Re (1)	1693 ± 470	2424 ± 674	2946 ± 733*	1795±634●

Table 4.1: Hemodynamic parameters at selected workrates (n=8). Data are mean ± SD. W_{max}, maximal workrate; HR, heart rate; SBP, systolic blood pressure; DBP, diastolic blood pressure; MAP, mean arterial pressure; MBF, mean CCA blood flow; CO, cardiac output; CCA/CO, mean CCA blood flow to cardiac output ratio = 2 x MBF/CO; D_{max}, peak of diameter waveform; U_{max}, peak of velocity waveform; Womersley, Womersley number; Re, Reynolds number. [*,●,◊,□]: ANOVA p-values. Statistical significance against the control condition was labelled with (*) and against 0% condition was labelled with (□); 40, 60, 70% maximal workrate conditions were labelled with (◊) if significantly different from the corresponding previous exercise step (20, 40, 60%, respectively); recovery conditions that were significantly different from 70% condition were labelled with (●).

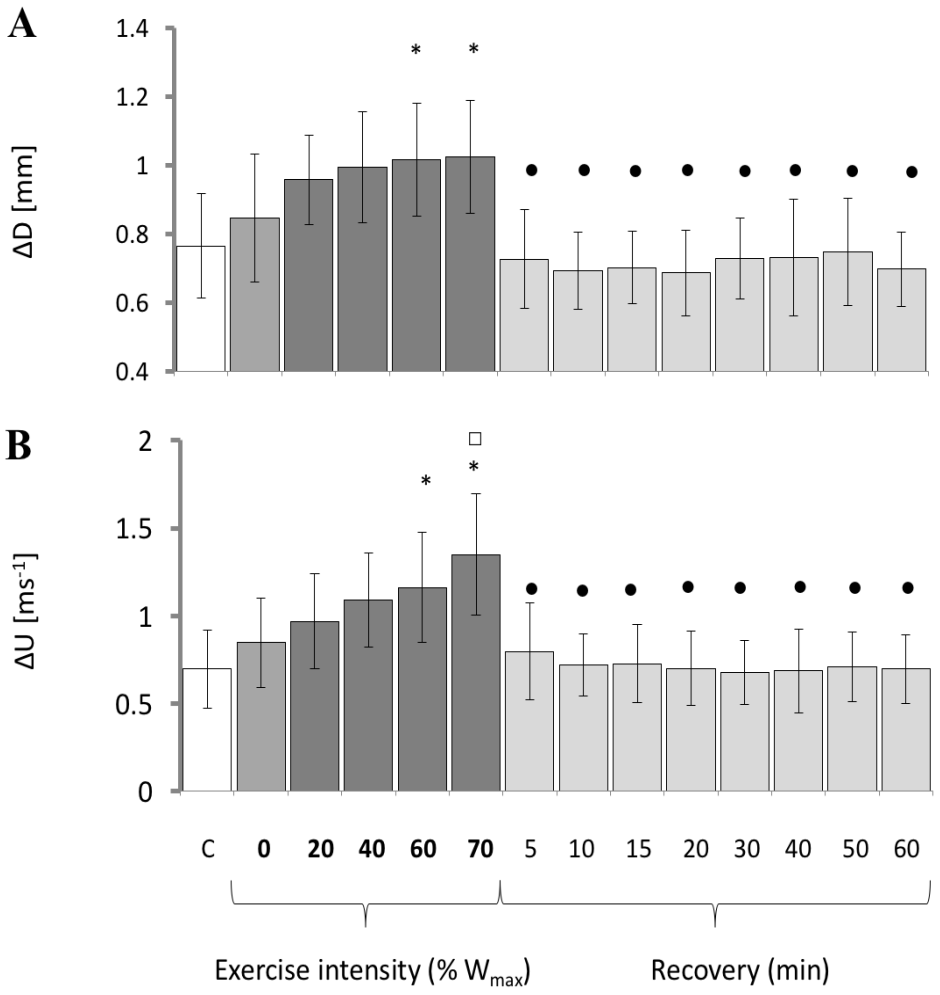

Figure 4.2: Bar chart displaying mean and standard deviation of ΔD (A) and ΔU (B) for each working condition of the protocol (n=8). W_{max}: maximal workrate; C: control (rest); [*,●,◊,□]: ANOVA p-values. Statistical significance against the control condition was labelled with (*) and against 0% condition was labelled with (□); 40, 60, 70% maximal workrate conditions were labelled with (◊) if significantly different from the corresponding previous exercise step (20, 40, 60%, respectively); recovery conditions that were significantly different from 70% condition were labelled with (●).

4.3.2 Wave speed and distensibility

Changes of c and D_s during incremental exercise are shown in Figures 4.3-4.4. Wave speed significantly increased during incremental exercise by up to 136% compared to baseline (Figure 4.3A, $p<0.05$), and returned to baseline values early in recovery. D_s

followed an inverse pattern, decreased during incremental exercise by as much as 79% (Figure 4.3B, $p<0.05$) then slowly stabilized near baseline values in recovery.

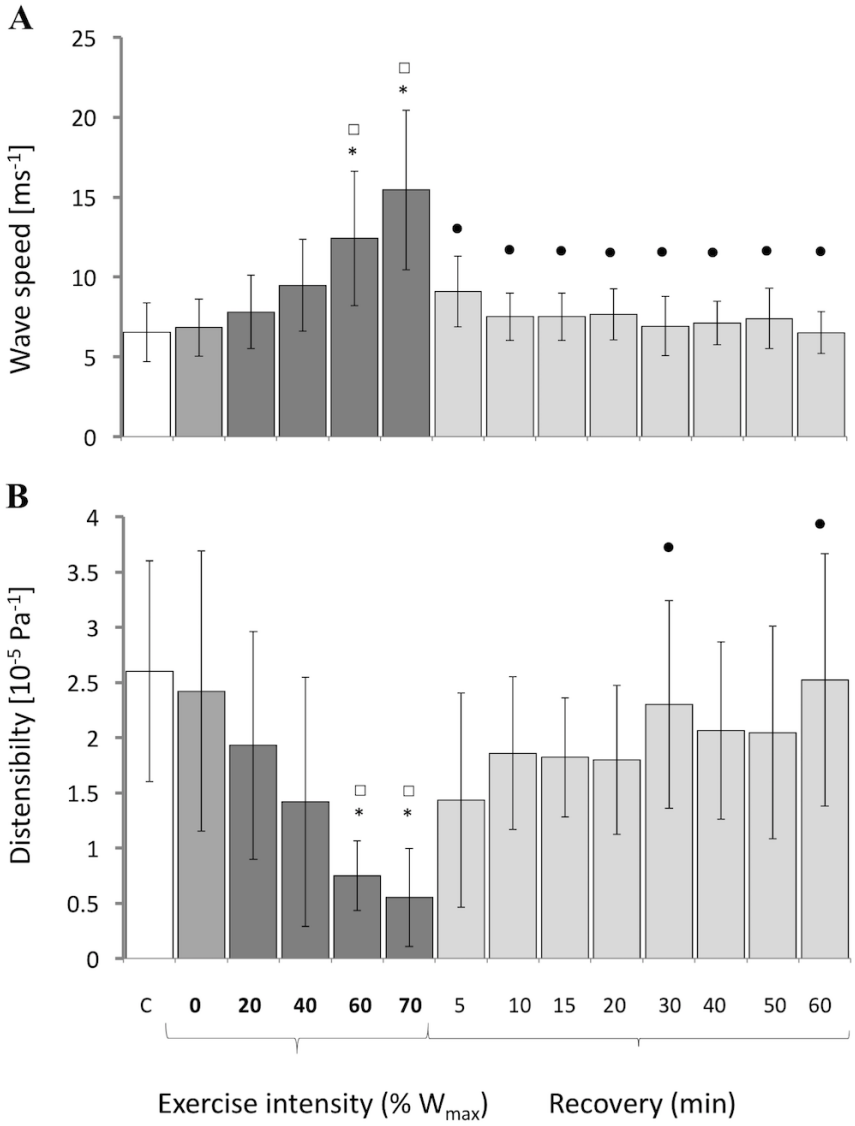

Figure 4.3: Bar chart displaying mean and standard deviation of wave speed (A) and distensibility (B) for each working condition of the protocol (n=8). W_{max}: maximal workrate; C: control (rest); [*,●,◊,□]: ANOVA p-values. Statistical significance against the control condition was labelled with (*) and against 0% condition was labelled with (□); 40, 60, 70% maximal workrate conditions were labelled with (◊) if significantly different from the corresponding previous exercise step (20, 40, 60%, respectively); recovery conditions that were significantly different from 70% condition were labelled with (●).

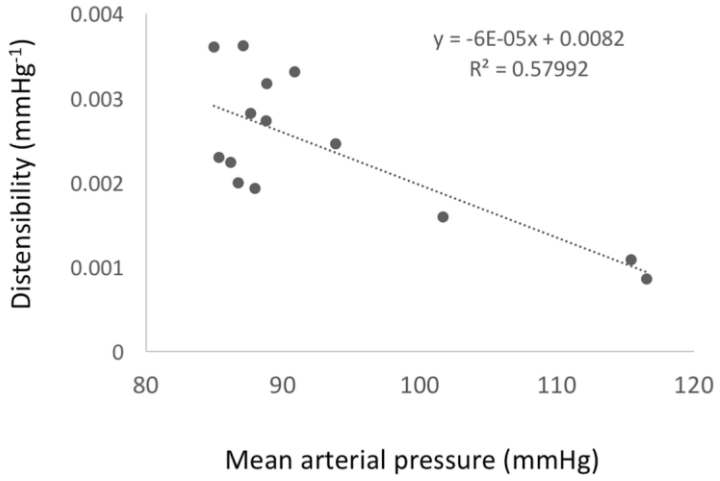

Figure 4.4: Distensibility plotted against mean arterial pressure values at rest, during exercise and in the recovery (n=8). Values are averages across all participants for each condition.

4.3.3 Wave intensity parameters

Wave intensity parameters are displayed in Figures 4.5-4.10. The peak and energy of the FCW followed similar trends, with values continuously increasing significantly during incremental exercise, up to 452% and 316% in relation to baseline values, respectively (Figures 4.5A, 4.6A, $p<0.05$), then returned rapidly during recovery. The peak and energy of the BCW followed an inverse trend compared to FCW variables (Figures 4.5B, 4.6B, $p<0.05$). These reductions with exercise were up to 700% and 390%, for the peak and energy values, respectively, and they quickly returned to baseline during recovery.

The peak and energy of the FEW followed a similar pattern as that of FCW, with an increase during exercise that reached 718% and 900% above baseline (both $p<0.05$), respectively, and returned towards baseline values in recovery (Figure 4.8A, B). X peak and energy increased during exercise by 360% and 240% (both $p<0.05$), respectively, and returned to baseline values during recovery (Figure 4.9A, B). However, there was a decrease of 9% and 12%, respectively for the peak and energy during the last stage of exercise (70% W_{max}) indicating there was no longer a difference compared to baseline ($p>0.05$). WD1 followed the same pattern as FCW and FEW, significantly increasing by 377% ($p<0.05$) during maximal exercise and quickly returning towards baseline values in recovery (Figure 4.7).

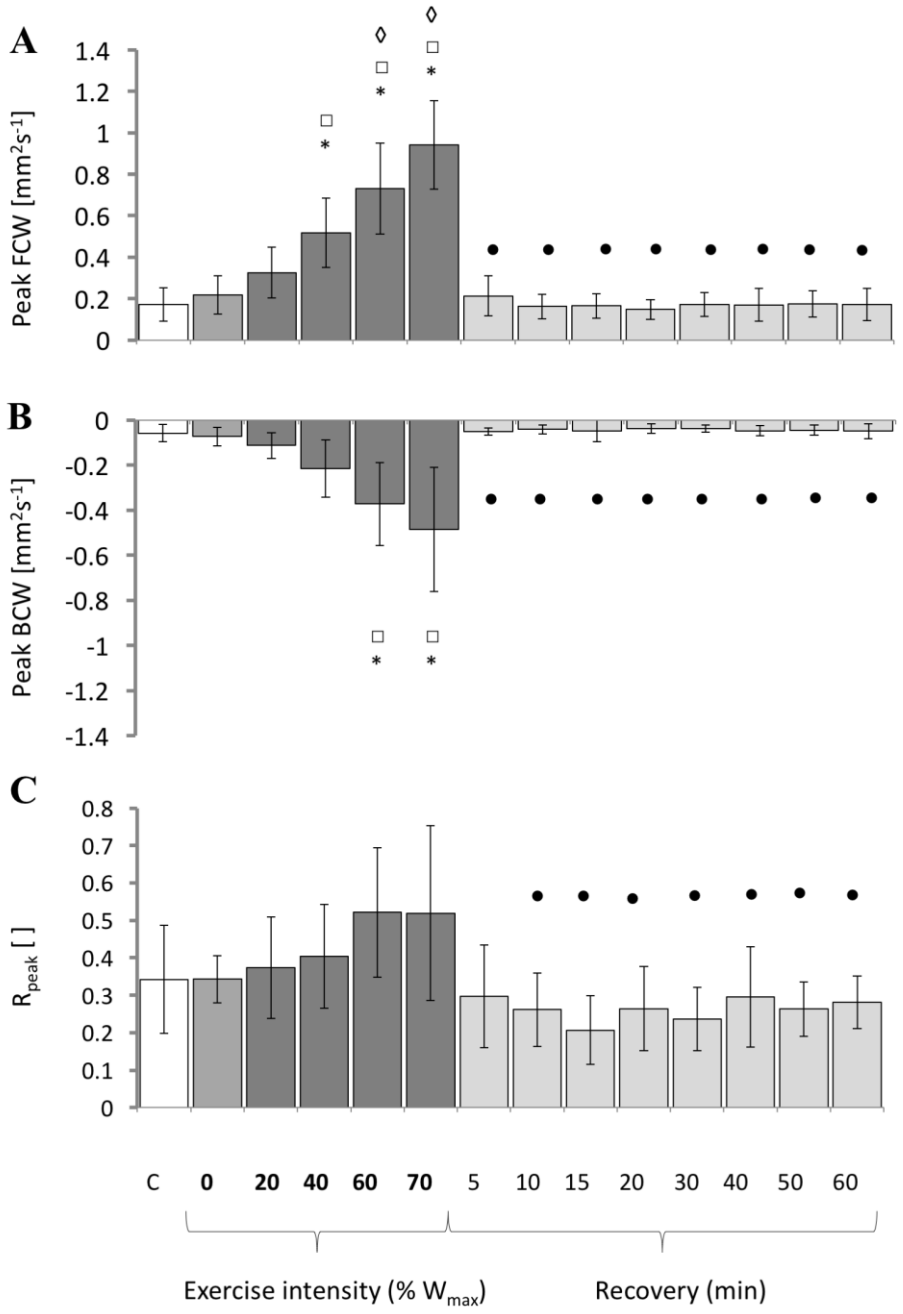

Figure 4.5: Bar chart displaying mean and standard deviation of FCW peak (A), BCW peak (B) and RI_I (C) for each working condition of the protocol (n=8). W_{max}: maximal workrate; C: control (rest); [*,●,◊,□]: ANOVA p-values. Statistical significance against the control condition was labelled with (*) and against 0% condition was labelled with (□); 40, 60, 70% maximal workrate conditions were labelled with (◊) if significantly different from the corresponding previous exercise step (20, 40, 60%, respectively); recovery conditions that were significantly different from 70% condition were labelled with (●).

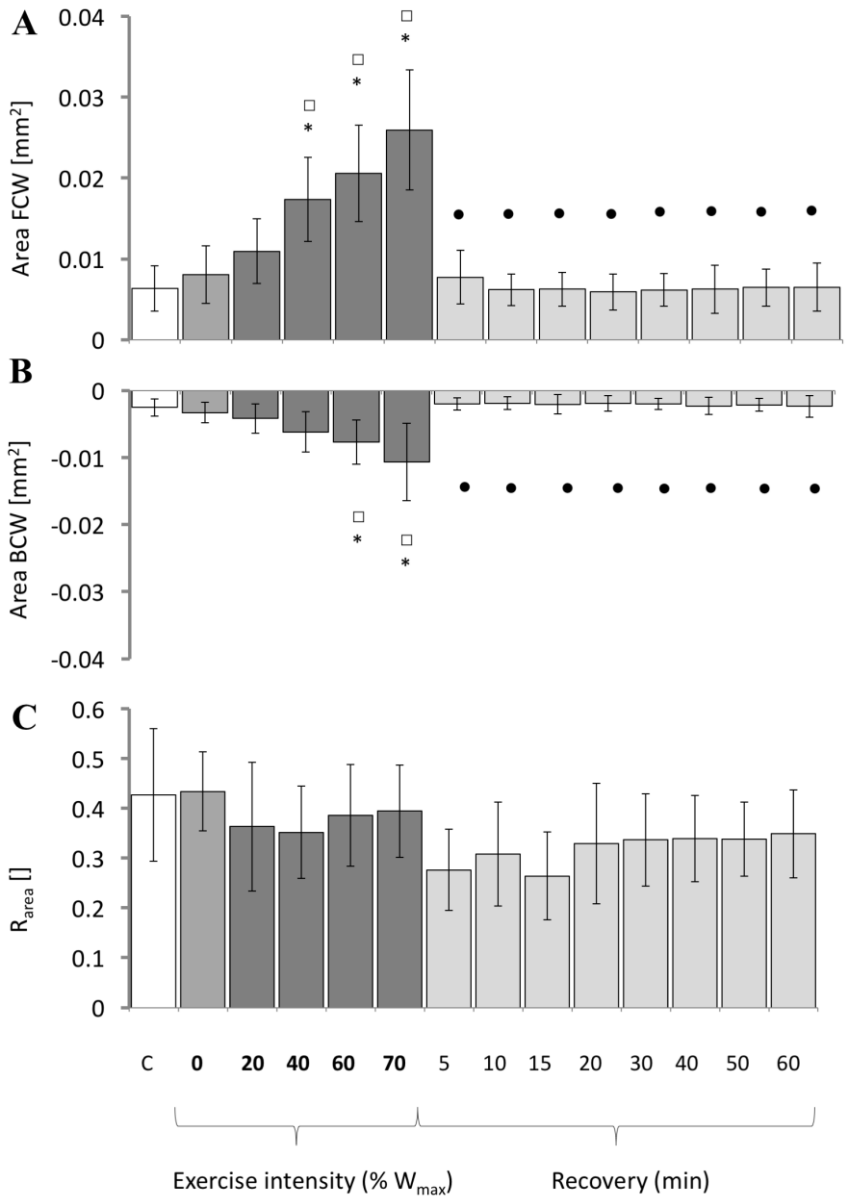

Figure 4.6: Bar chart displaying mean and standard deviation of FCW area (A), BCW area (B) and RI_E (C) for each working condition of the protocol (n=8). W_{max}: maximal workrate; C: control (rest); [*,●,◊,□]: ANOVA p-values. Statistical significance against the control condition was labelled with (*) and against 0% condition was labelled with (□); 40, 60, 70% maximal workrate conditions were labelled with (◊) if significantly different from the corresponding previous exercise step (20, 40, 60%, respectively); recovery conditions that were significantly different from 70% condition were labelled with (●).

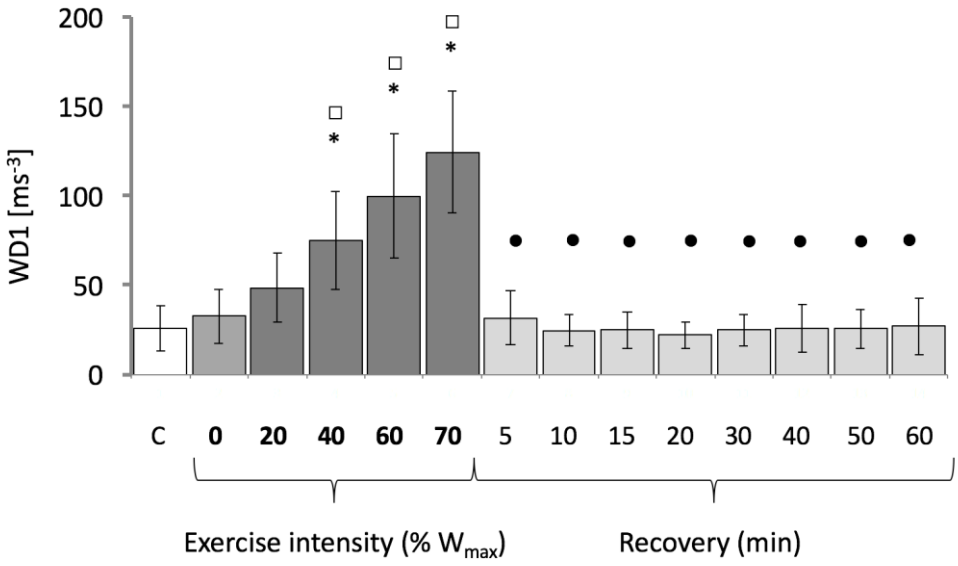

Figure 4.7: Bar chart displaying mean and standard deviation of WD1 index, for each working condition of the protocol (n=8). W_{max}: maximal workrate; C: control (rest); [*,●,◊,□]: ANOVA p-values. Statistical significance against the control condition was labelled with (*) and against 0% condition was labelled with (□); 40, 60, 70% maximal workrate conditions were labelled with (◊) if significantly different from the corresponding previous exercise step (20, 40, 60%, respectively); recovery conditions that were significantly different from 70% condition were labelled with (●).

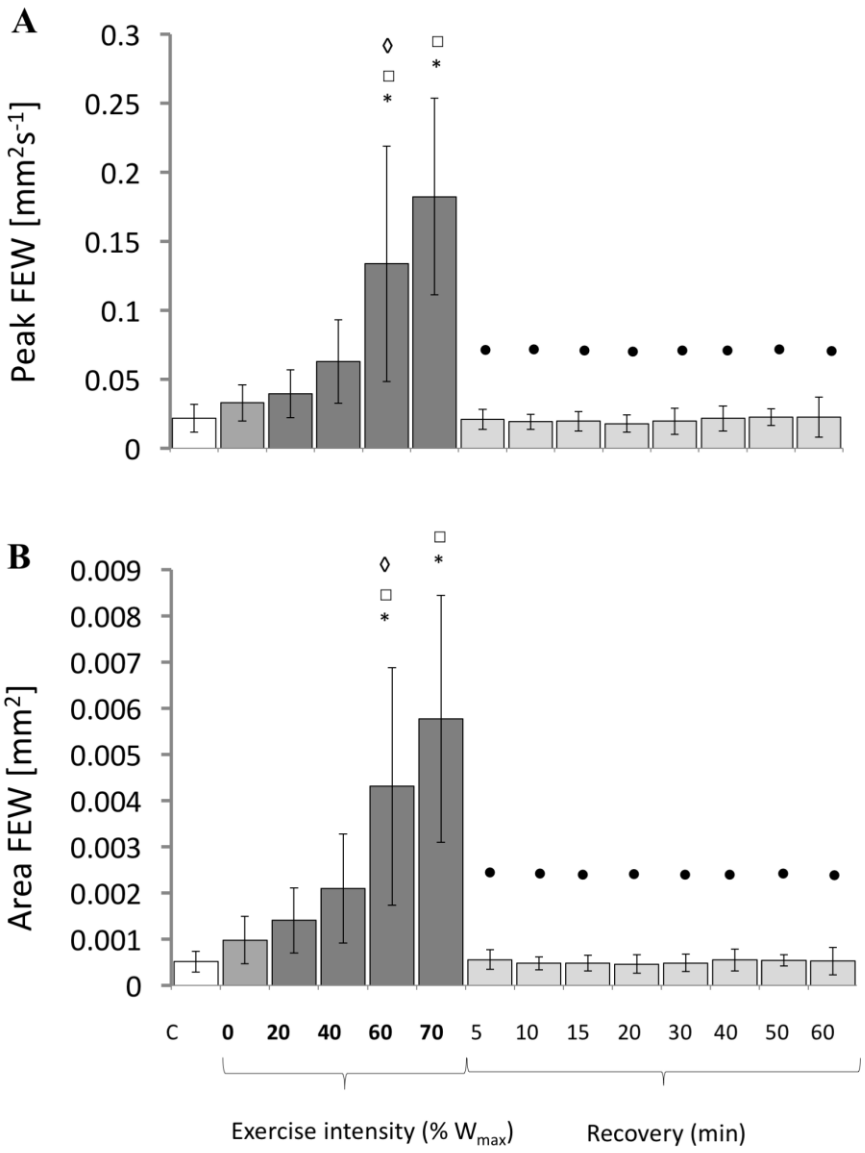

Figure 4.8: Bar chart displaying mean and standard deviation of FEW peak (A) and FEW area (B), for each working condition of the protocol (n=8). W_{max}: maximal workrate; C: control (rest); [*,●,◊,□]: ANOVA p-values. Statistical significance against the control condition was labelled with (*) and against 0% condition was labelled with (□); 40, 60, 70% maximal workrate conditions were labelled with (◊) if significantly different from the corresponding previous exercise step (20, 40, 60%, respectively); recovery conditions that were significantly different from 70% condition were labelled with (●).

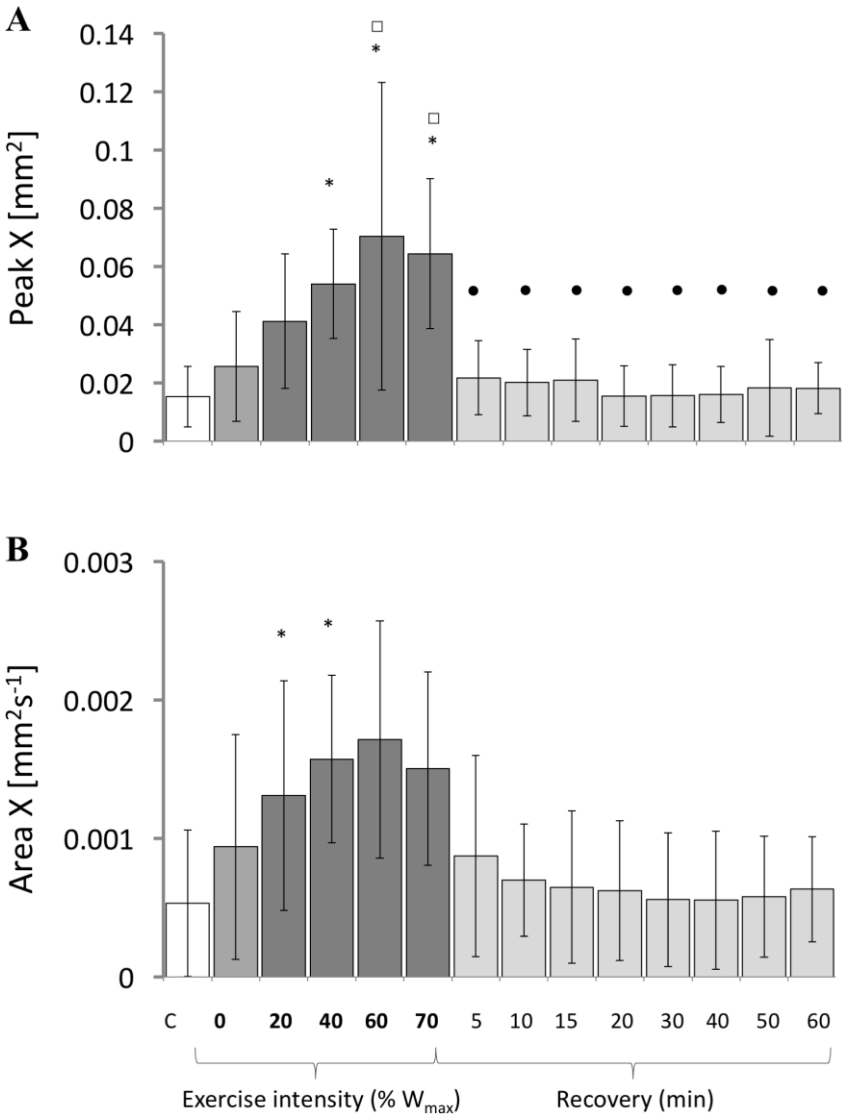

Figure 4.9: Bar chart displaying mean and standard deviation of X peak (A) and X area (B), for each working condition of the protocol (n=8). W_{max}: maximal workrate; C: control (rest); [*,●,◊,□]: ANOVA p-values. Statistical significance against the control condition was labelled with (*) and against 0% condition was labelled with (□); 40, 60, 70% maximal workrate conditions were labelled with (◊) if significantly different from the corresponding previous exercise step (20, 40, 60%, respectively); recovery conditions that were significantly different from 70% condition were labelled with (●).

4.3.4 Reflection Indices

Reflection indices are displayed in Figures 4.5-4.6 and 4.11 and related regression analysis in Table 4.2. The peak (RI_I) and energy (RI_E) reflection indices did not reach statistically significant change during the protocol, althought the former tended to continuously increase throughout incremental exercise and stabilize at 70% W_{max}, and the latter to decrease below the control condition in the moderate exercise regime (40% W_{max}) and increase again at higher workrates. CCA resistance also did not significantly change throughout the protocol (Figure 4.10). As can be seen in Figure 4.11, RI_E and RI_I were strongly correlated within and between subjects. On the contrary, the reflection indices were not correlated with the CCA resistance between subjects, whereas significantly correlated with CCA resistance within subjects.

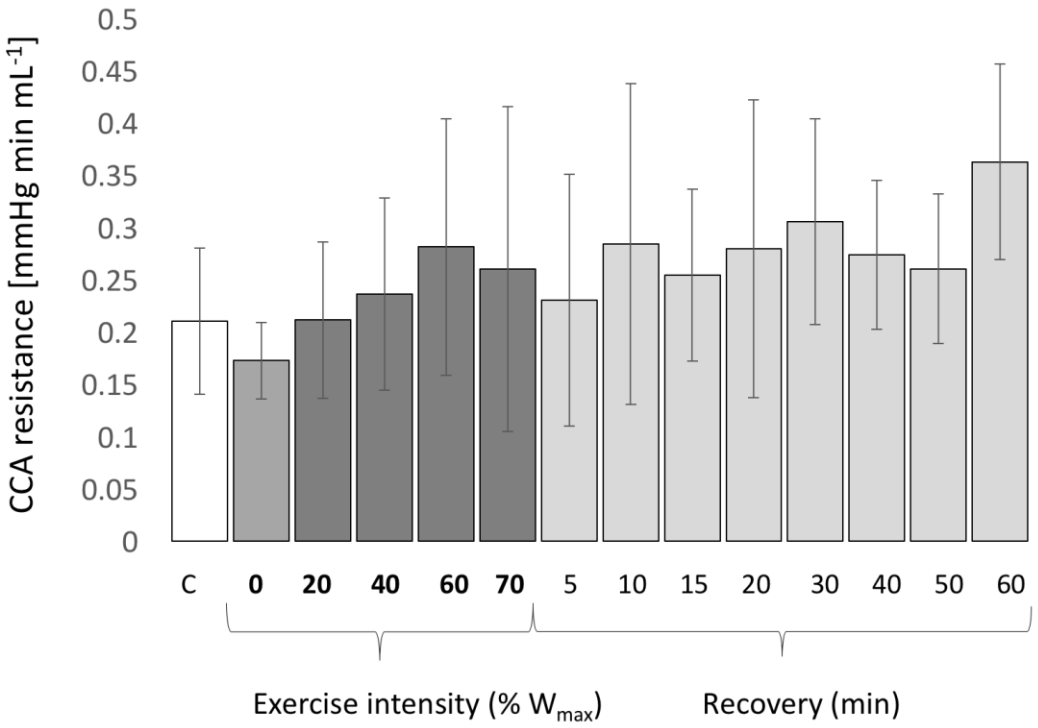

Figure 4.10: Bar chart displaying mean and standard deviation of CCA resistance for each working condition of the protocol (n=8). C: control (rest). None of the working condition was statistically significantly different from C or between each other.

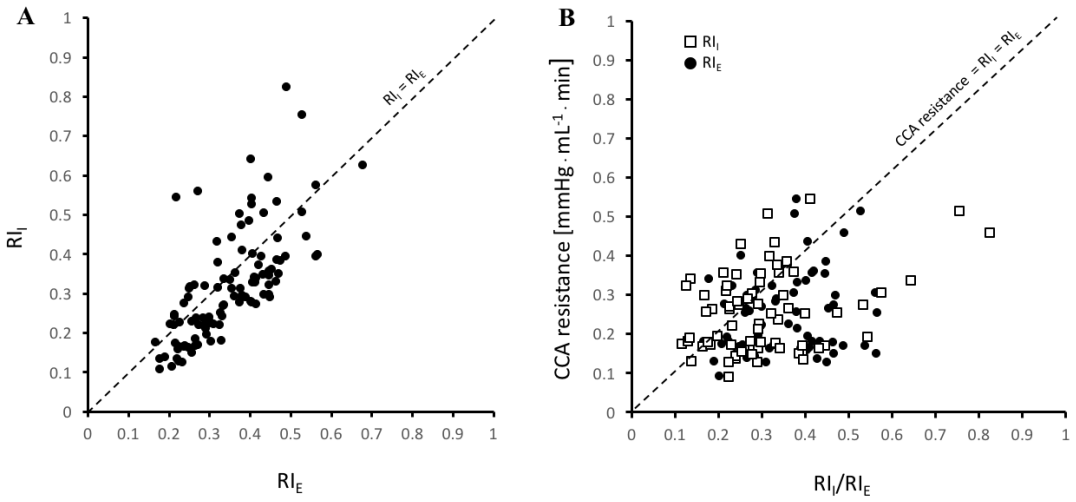

Figure 4.11: Correlation graphs for RI_I vs. RI_E (A) and for RI_I and RI_E vs. CCA resistance (B), for all working conditions (n=8). The lines with unitary slope are also displayed.

Variables	Within-subjects *r*	Between-subjects *r*
RI_I vs. RI_E	+0.95*	+0.89*
RI_I vs. CCA Res.	+0.96*	+0.68 (p=0.14)
RI_E vs. CCA Res.	+0.73*	+0.41 (p=0.42)

Table 4.2: Regression analysis for reflection indices and CCA resistance (n=8). CCA Res, common carotid artery resistance; RI_I, reflection index calculated from peaks; RI_E, reflection index calculated from areas; * Significant regression ($p<0.05$).

4.4 Discussion

In this study, local WI parameters and wave speed were non-invasively determined, to assess the cardiac and peripheral vascular alterations at the CCA, during exercise and subsequent recovery. This novel technique, that combines direct and simultaneous measurements of D and U to determine local wave speed, does not require blood pressure, which is a distinct advantage since reliable non-invasive blood pressure measurements during exercise are very difficult to obtain and often involve invasive catheterization. The main findings were that wave speed, which provides a measures of arterial stiffness, increased with workrate, yet returned to baseline values rapidly by 5 min of recovery. Also, most WI parameters (FCW, BCW, X and FEW peaks and energies, WD1)

increased during moderate and heavy exercise, again rapidly returning to baseline values by 5 min of recovery. RI_I, RI_E and CCA resistance changes during exercise were not significant. Finally, the reflection indices were not correlated with the CCA resistance between subjects, whereas significantly correlated with CCA resistance within subjects.

4.4.1 Relative contributions of diameter and velocity to blood flow

Although the absolute values for MBF were intermediate between those of Hellstrom et al. (1996) and Sato et al. (2011), continuous increases throughout exercise was observed, in agreement with both groups. In contrast with Hellstrom et al., MBF early in recovery fell below baseline where it remained. Those investigators also suggested that both D and U play an important role for MBF (as MBF $= \pi D^2 U/4$). However, there were no significant changes in the carotid diameter in Sato et al. (2011) during graded exercise. The findings in the present study suggest that increases in velocity played a more substantial role in determining MBF during incremental exercise, as shown by the peaks and pulses of D and U: increases in U_{max} and ΔU between control and heaviest workrates were 74% and 94%, respectively, while the increase in ΔD was 34% and the increase of D_{max} not significant.

4.4.2 Distensibility and wave speed with increasing exercise intensity

Distensibility of carotid arteries has wide clinical acceptance as a prognostic indicator of hypertension and cardiovascular disease (Myers et al. 2002). It represents a dynamic characteristic of the vessel, which decreases with increasing pressure and diameter, and strongly influences pulsatility (Mitchell et al. 2011). The lnDU-loop offers a tool to directly evaluate local distensibility or stiffness by first measuring diameter and blood flow velocity, then using the Bramwell-Hill equation to compute these values. In this study, distensibility over a wide range of carotid diameters was measured, and a very good agreement with previous work (Myers et al. 2002) was found at rest, for a similar, but non-trained cohort. Carotid distensibility was plotted against MAP, for all conditions, where each point is an average across all participants, in Figure 4.4. This graph suggests reduced values compared with previous work (Myers et al. 2002) at increasing mean arterial pressures (0.0015 $mmHg^{-1}$ at 100 mmHg vs. compared to 0.0030 $mmHg^{-1}$), nevertheless the distensibility values at rest (mean pressure 85 mmHg) are similar. Those reduced values, compared to the ones obtained by Myers et al., may relate to the magnitude of the sympathetic activation induced by brief isometric handgrip contractions compared to more prolonged dynamic exercise. Previous work supports the idea that the muscle mass involved

in the exercise explains part of the sympathetic response and would impact the magnitude of carotid artery smooth muscle contraction and the stiffness of the artery itself (Seals & Chase 1989). In addition, work by Victor et al. (1987) also suggests around a 2-3 fold potentiated muscle sympathetic nerve activity (MSNA) with large muscle mass dynamic exercise, compared to small muscle mass handgrip exercise. Therefore, a direct comparison between results of this study and the previous work by Myers et al. may not be straight forward.

In this study wave speed values, measured in a single vessel, increased continuously with increasing exercise workrates, and these findings agree with Sharman et al. (2005), who derived the wave speed over the whole aorta, of a young healthy but untrained cohort. As pointed out by Wilkinson et al. (2002), heart rate, per se, does not affect pulse wave velocity and mean arterial pressure, although the increase in pulse wave velocity might be secondary to an increase in mean arterial pressure. Using the lnDU-loop method and selecting the initial phase of systole to derive wave speed ensured that heart rate was not confounding the measurement directly. The apparent stiffening of the vessel likely involves the gradual recruitment of collagen fibres as the vessel distends with increasing arterial pressure and can be well characterized by changes in local wave speed (Murgo et al. 1981; Sharman et al. 2005). Interestingly, the wave speed quickly returned to values not different from baseline in recovery, which may also relate to a rapid arterial pressure drop concomitant to a reduction in sympathetic nervous system activity. Future studies involving concurrent assessments of MSNA may uncover the main contributing factor responsible for both the stiffening during exercise and the rapid return to baseline in recovery.

4.4.3 Wave intensity parameters

4.4.3.1 Forward, backward compression waves and reflection indices

As exercise intensity increased there was an obvious incremental increase in the energy delivered by the heart; effectively an enhancement of contractility, supported by both greater peaks and areas of FCW and the WD1 index. Similar to the PU-wave intensity, the DU-wave intensity indices are able to quantify the enhancement of cardiac contractility.

Those results suggest that the index of contractility WD1 is, as opposed to tissue Doppler based isovolumic acceleration, insensitive to adaptations that occur with training, since values were very similar to the untrained participants in previous studies (Tanaka et al. 2015). However, a direct comparison between athletes and sedentary individuals at the same absolute workrates would be required to fully assess the suitability of this method in this regard.

Simultaneous to the increased contractility, the energy reflected from the head microcirculation, back to the heart through the carotid arteries, increased almost proportionally. Similarly, Babcock et al. (2015) noted increases in both FCW and BCW after a brief maximal 30s exercise bout. However, isolated examination of the BCW does not provide adequate information to properly assess downstream vascular resistance, since it is also a function of the magnitude of ventricular contractility. On the contrary, WI reflection indices may estimate downstream vascular resistance and potentially CvR when measurements are taken at the carotid artery. Bleasdale et al. (2003) demonstrated reduced reflection index magnitudes using CO_2-rebreathing-induced cerebral vasodilation, suggesting reduced cerebrovascular resistance. Yet, this controlled condition may differ from exercise since microcirculatory beds in the head, including the cerebral and the skin microcirculation, cannot be differentiated by CCA WIA exclusively. The CCA bifurcates into the external carotid artery, supplying the facial tissues, among others, and the internal carotid artery, supplying the brain. The latter supplies much of the global cerebral blood flow together with the vertebral artery (Sato et al. 2011). Based on the patterns exhibited by the reflection indices in our study, there seems to be little measurable change in downstream vascular resistance within the examined exercise workrates. This could be a result of no discernible changes in cerebral and facial vascular resistances or it could be a simultaneous reduction in vascular resistance within the facial circulation, combined with increases in cerebrovascular resistance to modulate arterial inflow with enhanced perfusion pressure. Thus, results from this study demonstrated that it was not possible to assess the distinct contribution of CvR to CCA resistance.

Although the changes in reflection indices and CCA resistance were not significant, RI_I and RI_E significantly correlated with CCA resistance within subjects, with RI_I exhibiting a stronger correlation than RI_E. Thus, the increase or decrease of RI_I and RI_E values within the individual were associated with a concomitant increase or decrease in CCA resistance. On the contrary, there was no evidence that subjects with high reflection indices values also had high resistance values, due to the absence of correlation between subject means.

4.4.3.2 The X-wave

The X-wave was described for the first time by Zambanini et al. (2005) as a mid-systolic forward expansion wave, seen only in peripheral arteries (such as carotid, brachial and radial). Therefore, it is not generated by the heart, but likely by the reflection of BCW at an open-end site. Between the right CCA and the aortic valve there are two main reflection

sites, as the CCA meets the brachiocephalic artery, which in turn merges into the aortic arch. The X wave is likely generated by a combination of re-reflected waves at these sites. Hughes et al. (2013) demonstrated that the X-wave may play an important role in affecting the carotid pressure waveform morphology. The tendency of X peak and area to increase during exercise is likely due to the underlying contribution of enhanced ventricular contractility, that also increases both FCW and BCW indices.

4.4.3.3 Forward expansion wave with increasing exercise intensities

The systolic contraction and diastolic relaxation of the ventricle are controlled by the myofibril arrangement within the wall, which dictates the direction and degree of twisting and untwisting of the chamber. A FEW appears as the cardiac cycle approaches end systole and this waveform relates to the active deceleration as myofibrils no longer interact and the stored elastic potential energy is returned as ventricular untwists. Ventricular torsion is crucial for the optimal performance of the heart (Beyar et al. 1989), as it helps producing uniform stresses throughout the wall (Taber, Yang and Podszus 1996) and allows sarcomeres to shorten uniformly (Notomi 2006). Because of the twisting mechanics, major and minor axes of left ventricle reach peak shortening velocities at different times during systole. It is believed that FEW rises when the major axis, after having reached its peak velocity, begins decelerating. At this stage, the minor axis has already initiated decelerating. The FEW is then supported by the late phase of ventricular untwisting, before the aortic valve closes. The "suction" wave produced in this way acts therefore as a breaking force (Parker et al. 1988; Sugawara et al. 1997) and influences central pressure (Fok et al. 2014). Heffernan & Lefferts (2013) showed that a decrease of the FEW was associated with an increase of blood flow velocity peak.

Previous work involving prolonged high workrate cycling (Babcock et al. 2015) observed reduced FEW magnitudes in early recovery, suggesting dysfunction. In the present study, however, FEW peak and area increased during all stages of incremental exercise, suggesting that the left ventricle, while contracting with increasing force, is also able to decelerate more rapidly. It is believed that the characteristics of the exercise performed, i.e. cycling at incremental workrate in this study and high workrate cycling in Babcock's cohort, explain these disparate findings. As such, the incremental exercise may have improved deceleration mechanics, leading to more efficient relaxation which would enhance diastolic filling duration. This enhanced diastolic relaxation would reduce ventricular pressure more rapidly thus facilitating passive filling of the ventricles in early diastole.

4.4.4 Methodological considerations

As already considered, the velocity profile in the CCA at rest and during recovery could be considered parabolic whereas it became prominently flat during exercise. Also, the flow became turbulent and inertial forces more prominent during exercise whereas adjusted to control values within 5 min into recovery period. The nature of the flow can pose, therefore, real challenges to the measurements during graded exercise, because turbulence and non-parabolic velocity profile occur. In our study, the ultrasound Doppler gate was always aligned with the centre of the vessel to avoid any boundary layer effect.

Examination of the test power curve for RI_E (depicted in Figure 4.12) using t-distribution and hypothesized RI_E means found throughout the protocol showed the test power values were generally low, especially during exercise. Specifically, the power of the statistical analysis is between 0.2 and 0.4 during exercise and between 0.5 and 0.9 during recovery; therefore, the probability of error is between 0.6 and 0.8 during exercise and between 0.1 and 0.5 during recovery. This is due to the sample size, consisting of 8 subjects, therefore the interpretation of the findings needs to be treated with caution. Nonetheless, some of our results were associated with statistical significance.

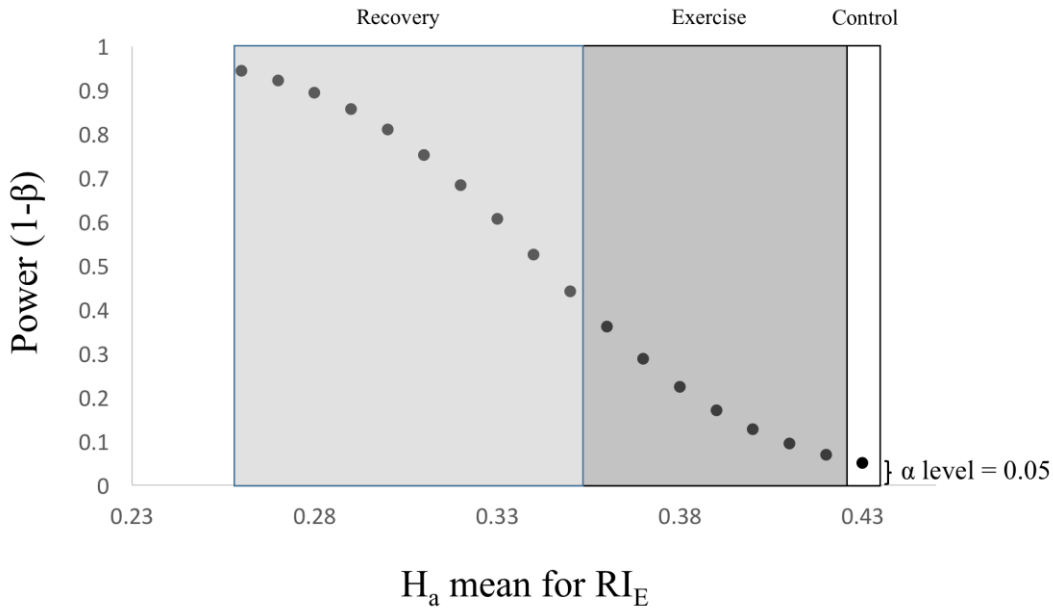

Figure 4.12: Test power curve for the reflection coefficient RI_E (n=8) at control, during exercise and recovery. Values obtained during exercise and recovery are taken as means for the alternative hypothesis. H_a, alternative hypothesis.

4.4.5 Limitations

Studies evaluating wave intensity patterns and reflection indices in the internal and external carotid arteries, to specifically assess the cerebral vascular resistance and the facial vascular resistance separately, would be a prudent next step. The calculation of MAP was based on the formula: MAP = 1/3 SBP + 2/3 DBP, which has its validity in rest condition because the systolic and diastolic time fractions within the cardiac cycle change during exercise. However, the monitoring device (based on photo-plethysmography) used in this study did not record the entire pressure waveform or the time fractions; therefore, it was impossible to assess MAP by properly integrating the curve and the aforementioned formula was used instead, bringing a slight underestimation of the MAP values at moderate-to-high exercise regime.

4.5 Conclusions

Using completely non-invasive methods involving Doppler and imaging ultrasound of the carotid artery under different exercise workrates up to 70% W_{max} and during prolonged recovery, it was possible to calculate surrogate indices of local vascular resistance, as well as WI parameters that provide insight into cardiac dynamics and the distensibility of the vessel. Wave speed significantly increases (up to +136%) and the carotid artery stiffens substantially (distensibility decreases up to 79%) as exercise intensity increases, whilst energy of the forward (FCW) and backward (BCW) compression waves also rise (up to +316% and +390%, respectively), as ventricular contractility is enhanced, leading to larger reflections from the head microcirculation. However, the reflection indices do not significantly change during exercise, highlighting that the increased magnitude of reflections is mainly due to the enhanced contractility, rather than changes in vascular resistance, at least at the carotid artery. Moreover, increases of reflection indices values within the individual are accompanied by proportional increases of CCA resistance values, whereas there is no evidence that subjects with high reflection indices also have high CCA resistance. The forward expansion wave (FEW) also increases during exercise (its energy up to +900%), as the left ventricle actively decelerates blood flow in late systole, potentially improving filling time during diastole. The X wave, attributed to the reflection of BCW, had a tendency to increase during exercise (its energy up to +240%) and to quickly decrease in recovery. Finally, in the early recovery, the magnitude of all those waves returned to baseline value promptly, suggesting no long-term effects in the investigated hemodynamic and wave intensity parameters of young healthy individuals.

Chapter 5: Implications of Varying Fitting Technique and Asymptotic Diastolic Pressure on Wave Intensity Parameters

5.1 Introduction

This Chapter discusses two types of quantitative analysis performed on blood pressure and flow velocity data of healthy humans: a) the effect of the application of different fitting techniques on the reservoir and excess components of pressure and velocity, b) the effect of varying the asymptotical pressure value (P_∞) on those same components. Corresponding hemodynamic and wave intensity parameters were then calculated and compared.

As discussed in Chapter 1, incremental changes of arterial blood pressure can be affected by forward and backward waves, as well as by the compliance of the vessel. Therefore, to properly quantify the effects of forward- or backward- travelling waves on arterial pressure (and velocity), the component due only to the increase in arterial reservoir volume should first be excluded (Tyberg et al. 2009). Hybrid reservoir-wave models assume that the measured pressure consists of two additive components: reservoir (P_r) and excess pressure (P_{ex}). The reservoir-wave approach was first applied by Wang et al. (2003) in canine aorta, considering the reasonable assumption that the blood flow is null in diastole. Consequently, the same approach was applied for the calculation of venous reservoir (Wang et al. 2006) and to any arbitrary arterial location (Aguado-Sierra, Alastruey, et al. 2008; Aguado-Sierra, Davies, et al. 2008). However, the calculation of P_r requires fitting the diastolic decay of the measured pressure waveform for calculating the parameters P_∞ (asymptotical value) and b (time constant) and there is no consensus over the value of these parameters. Some researchers prefer, instead, to not fit P_∞ and keep it fixed.

Specifically, Wang et al. (2003) fitted the diastolic decay over the last two thirds of the measured pressure, considering that waves are minimal during this period. The parameters R, C and P_∞, namely, the peripheral systemic resistance, the arterial tree compliance and the asymptotic value, were free-fitted. The value of the reservoir pressure at the onset of diastole ($\bar{P}_n = P_r(T_N)$, where T_N is the dicrotic notch) was fixed at the value of the measured pressure at the same time point (P_n). The same approach was used by Wang et al. (2006) and Wang et al. (2011), for both venous and arterial reservoir pressure in the canine cardiovascular system, although the fitting window was reduced to approximately the

last third of diastole. Davies et al. (2010) followed the approach used by Wang et al. (2003), whereas Bia et al. (2011) the later technique of Wang et al. (2011).

Aguado-Sierra, Alastruey, et al. (2008) used a free-fitting algorithm for the estimation of the diastolic time constant b and $\bar{P}_n$, starting from initial conditions of $b = 1\ s^{-1}$ and $\bar{P}_n = P_n$. The fitting window was considered to be the whole diastole. However, they fixed $P_\infty = 0$ mmHg for experimental data and $P_\infty = 3.2$ mmHg (432.6 Pa) for computational data, following Wang et al. (2006), who suggested that the asymptotical value is affected by the waterfall effect. Vermeersch et al. (2009) calculated the reservoir pressure in the Asklepios population by following Aguado-Sierra, Alastruey, et al. (2008); however, they found non-physiological values of P_∞ with free-fitting and decided to set the asymptotical value to 0 for the entire dataset. A successive study conducted by Aguado-Sierra, Davies, et al. (2008) on human subjects used the same framework but imposing $P_\infty = 25$ mmHg, based on previous work of Schipke et al. (2003), who determined the (arterial) asymptotical value in anesthetized humans under fibrillation / defibrillation sequences.

Therefore, it is hypothesised that varying the fitting method would significantly change P_∞ and b values, leading to different reservoir and excess pressure waveforms, as well as to different hemodynamic and wave intensity parameters, derived from the separated waveforms. It is also hypothesised that, using the fitting approach of keeping P_∞ fixed, different values of the asymptotical pressure value would lead to different reservoir and excess waveforms, affecting hemodynamic and wave intensity parameters.

The aims of this study were to examine the effects of a) varying fitting method and b) varying P_∞ on the calculation of reservoir and excess components of blood pressure and flow velocity measured at the common carotid artery of healthy humans. Specifically, data were drawn from the Asklepios population (see 'Material and Methods' for details). The separated components were subsequently used to determine relevant hemodynamic and wave intensity parameters. The variation of the fitting method was based on the change of the number of its free-fitted parameters (called degrees of freedom, DOF, for brevity, in the rest of the Chapter) – P_∞, b, $\bar{P}_n$ – and of the length of its fitting window (whole diastole or its two thirds). By using a reference value of P_∞ and changing it by certain percentages (from -75% to +100%), a second quantitative analysis was performed.

5.2 Material and methods

5.2.1 The Asklepios population

The Asklepios Study is a longitudinal population study focusing on the interaction between ageing, cardiovascular hemodynamics and inflammation in preclinical cardiovascular disease (Rietzschel et al. 2007). The total cohort comprised 2524 participants (1301 women, 35 – 55 years-old), free from manifest cardiovascular disease at study initiation, randomly sampled from the twinned Belgian communities of Erpe–Mere and Nieuwerkerken. All examinations were single-observer, single-device, single-site and were performed in a single 2-year consecutive timeframe (from October 2002 to September 2004) (Rietzschel et al. 2007). The procedure included measurements of basic clinical data, blood samples examination, echocardiographic examination, vascular echographic and tonometric measurements. The study protocol was approved by the ethics committee of Ghent University Hospital and all subjects gave a written informed consent.

5.2.1.1 Study Group

A study group of 1037 subjects drawn from the Asklepios database provided data for this study. Only those subjects whose common carotid blood pressure and flow velocity measurements were available were selected. Table 5.1 summarizes the physiological and hemodynamic characteristics of the study group.

5.2.2 Protocol

Subjects were asked to lay down in recumbent position, with the neck slightly hyperextended and turned approximately 30° contralateral during carotid scanning. Blood pressure and flow velocity measurements were acquired via applanation tonometry and vascular echography, respectively. The measurements were not simultaneously taken, but acquired during the same vascular examination. The signals were post-processed and subsequently aligned using the algorithm proposed by Swalen & Khir (2009).

		n	Age (years)	Height (cm)	Weight (kg)	SBP (mmHg)	DBP (mmHg)	MAP (mmHg)	HR (bpm)
1st HD	T	311	38 ± 2	171 ± 9	73 ± 13	127± 13	74 ± 10	96 ±10	63 ± 9
	F	162	38 ± 2	165 ± 6	66 ± 10	123± 12	74 ± 10	95 ± 11	65 ±10
	M	149	38 ± 2	178 ± 6	81 ± 11	132 ±12	75 ± 10	98 ± 10	61 ± 8
2ndHD	T	262	44 ± 2	170 ± 9	72 ±13	129 ± 14	77 ± 10	99 ± 11	64 ±11
	F	142	43 ± 2	165 ± 6	65 ±10	126 ± 15	75 ± 10	97 ± 12	66 ±10
	M	120	44 ± 1	176 ± 7	81 ± 11	133 ± 12	79 ± 10	101 ± 11	61±12
3rd HD	T	254	48 ± 1	170 ± 9	75 ± 14	131 ± 13	77 ± 10	100 ± 10	65 ± 9
	F	120	48 ± 1	163 ± 6	66 ± 11	128 ± 13	75 ± 9	98 ± 10	66 ± 8
	M	134	48 ± 1	175 ± 6	82 ± 11	135 ± 13	79 ± 10	102 ± 11	64 ±11
4th HD	T	210	54 ± 2	168 ± 9	73 ± 13	136 ± 16	79 ± 10	104 ± 12	64 ±10
	F	107	53 ± 2	161 ± 6	66 ± 10	136 ± 18	78 ± 11	104 ± 14	65 ± 8
	M	103	54 ± 2	175 ± 6	81± 11	137 ± 14	80 ± 9	104 ± 10	62 ±12

Table 5.1: Basic characteristics of subjects (n=1037). bpm: beats per minute, DBP: brachial diastolic blood pressure, F: female, HD: half-decade, HR: heart rate, M: male, MAP: brachial mean blood pressure, n: number of subjects, SBP: brachial systolic blood pressure, T: total. Values are reported as mean ± SD.

5.2.2.1 Blood pressure measurements

Pressure measurements were carried out via applanation tonometry. A Millar pentype tonometer was used (SPT 301, Millar Instruments, Houston, Texas, USA), recording data at a sampling rate of 200 Hz continuously for 20 s. Details of the applanation tonometry technique can be found in Rietzschel et al. (2007) and the procedure can be summarized in two steps: initially, tonometric tracings were collected from the brachial artery, divided into individual beats, using the foot of the wave as starting point, and finally ensemble-averaged. The averaged tracing was successively calibrated against oscillometrically measured brachial systolic and diastolic (DBP_b) pressure values, by scaling the peaks and troughs of the tonometric recording, respectively. Mean arterial brachial pressure (MAP_b) was then calculated, by numerically averaging the curve. In the second step, tonometry was performed on the carotid artery and the obtained tracings were ensemble-averaged and calibrated against the previously calculated tonometric brachial pressure; more precisely, assuming that diastolic and mean pressure values were fairly constant in large arteries, DBP_b and MAP_b were assigned to the trough and the mean value of the carotid recording, respectively, giving a scaled carotid pressure waveform (P).

5.2.2.2 Blood flow velocity measurements

A commercially available ultrasound system (VIVID 7, GE Vingmed Ultrasound, Horten, Norway), equipped with a linear vascular transducer (12L, 10 MHz), was used for the scans (Rietzschel et al. 2007). Blood flow velocity was measured via Pulsed Wave Doppler (with sweep speed set at 100 mm/s) and 5 to 30 ECG-gated cardiac cycles during normal breathing were recorded. The DICOM images obtained were then processed by other investigators (Borlotti et al. 2012) with home-written programs in MatLab (The MathWorks, Natick, Massachusetts, USA). Maximum and minimum velocity envelopes were subsequently detected via morphological operations and averaged to obtain the velocity profile. The velocity profile was then divided into individual cardiac cycles that were successively ensemble-averaged to obtain a single velocity contour (U).

5.2.3 Data analysis

Data analysis was performed via custom-made algorithms in Matlab (version R2010b, The MathWorks, Natick, Massachusetts, USA). The algorithm separated the P and U waveforms into their reservoir and excess components. As explained in Chapter 2, the reservoir pressure was calculated following Aguado-Sierra, Alastruey, et al. (2008):

$$P_r = \frac{b}{a+b} P_\infty + e^{-(a+b)t}\left[\int_0^t aP(t')e^{(a+b)t'}dt' + P_0 - \frac{b}{a+b}P_\infty\right] \tag{5.1}$$

where a, b and P_∞ are the systolic constant, the diastolic constant and the asymptotic pressure value, respectively. In diastole (for $T_N < t < T$, where T_N and T are the dicrotic notch time point and the duration of cardiac cycle, respectively), Eq. 5.1 reads:

$$P_r = (\bar{P}_n - P_\infty)e^{-b(t-T_N)} + P_\infty \tag{5.2}$$

where $\bar{P}_n$ is the reservoir pressure value at $t = T_N$.

After the calculation of diastolic P_r (which requires the determination of b, $\bar{P}_n$ and P_∞, as will be explained in the next section), the parameter a was calculated through the following equation, as reported in Chapter 2:

$$P_r(T_N) = \frac{b}{a+b}P_\infty + e^{-(a+b)T_N}\left[\int_0^{T_N} a\,P(t')e^{(a+b)t'}dt' + P_0 - \frac{b}{a+b}P_\infty\right] \quad (5.3)$$

The complete reservoir waveform could then be obtained via Eq. 5.1 and the excess pressure was determined as the difference between the measured pressure P and the reservoir pressure:

$$P_{ex} = P - P_r \quad (5.4)$$

Similar analysis held for the velocity components U_r and U_{ex}, where:

$$U = U_r + U_{ex} \quad (5.5)$$

$$U_r = \frac{P - P_\infty}{\bar{R}} \quad (5.6)$$

$\bar{R}$ is the averaged downstream resistance:

$$\bar{R} = (\langle P\rangle - P_\infty)/\langle U\rangle \quad (5.7)$$

and $\langle P\rangle$ and $\langle U\rangle$ are the time-averaged measured pressure and velocity, respectively, during diastole. A second approach to calculate $\bar{R}$, involving the determination of the linear part of the PU-loop in diastole and proposed by Aguado-Sierra, Alastruey, et al. (2008) was not used in this study because it was difficult to assess the linear part of the loop in diastole.

5.2.3.1 Fitting algorithm settings

The fitting parameters b, $\bar{P}_n$ and P_∞ were determined, for each subject, using the following fitting procedures (details are given in Table 5.2):

- in the so-called *DOF-Window analysis*, the value of $\bar{P}_n$ was either determined by fitting (3 DOF analysis) or fixed (2 DOF analysis), while the length of the fitting window was either set at the entire diastolic window (full diastole) or at its last two thirds (2/3 diastole, abbreviated as '23'). The combination of these settings gave four different fitting methods: 3 DOF full, 3 DOF 23, 2 DOF full, 2 DOF 23. Therefore, 3 DOF analyses had 3 degrees of freedom, because b, $\bar{P}_n$ and P_∞ were

determined by fitting, whereas in the 2 DOF analyses only b and P_∞ were calculated with the fitting algorithm and $\bar{P}_n$ was fixed to the corresponding value of measured pressure P_n. See Figures 5.1 -5.5 for examples;

- in the so-called P_∞-*Variation analysis,* the length of the fitting window was set at the entire diastolic window and $\bar{P}_n$ was fixed at P_n. The diastolic decay constant b was determined by fitting, while P_∞ was fixed at a certain percentage of the reference value, obtained in the 2 DOF full configuration. The P_∞-Variation analysis performed the following seven iterations: -25%, -50%, -75%, +25%, +50%, +75% and +100% of the reference value.

Analysis	Free-fitted parameters	Fixed paramaters	Window length
3 DOF	$\bar{P}_n$, P_∞, b	-	Full diastole
2 DOF	P_∞, b	$\bar{P}_n = P_n$	Full diastole
3 DOF 23	$\bar{P}_n$, P_∞, b	-	Last 2/3 of diastole
2 DOF 23	P_∞, b	$\bar{P}_n = P_n$	Last 2/3 of diastole
P_∞-Variation	b	$\bar{P}_n = P_n$, P_∞*	Full diastole

Table 5.2: Properties of the analyses performed. b: diastolic time constant; P_∞: asymptotical pressure value; $\bar{P}_n$: reservoir pressure value at the dicrotic notch. *: simulations are performed with different fixed P_∞ values, ranging from -75% to +100% of the reference value obtained from 2 DOF full analysis.

The fitting algorithms were implemented using the *lsqcurvefit* function, a Matlab solver optimized for non-linear least squares problems: it finds the set of parameters X that minimize $\sum_i (F(X, xdata_i) - ydata_i)^2$, where $xdata$ are the input data (time points in the current problem) and $ydata$ the observed output. X comprised P_∞, $\bar{P}_n$ and b, depending on the analysis performed (Table 5.2). The number of the iterations performed by the solver depended on the stopping criterion, i.e. a threshold, often called function tolerance, that stops the iterations if crossed. The tolerance $|f(x_i) - f(x_{i+1})|/|f(x_i)|$ was set at 10^{-6} by default. Generally the solver took less than 20 iterations to converge for each fitting analysis. P_∞ and $\bar{P}_n$ (when not fixed) and b were bound to be non-negative and the initial conditions for the solver were the following: P_∞= 60 mmHg (7999.2 Pa), $\bar{P}_n = P_n$ and b = 1 s^{-1}. The reservoir diastolic decay was calculated via Eq. 5.2. For the determination of the systolic time constant a, the same Matlab function (*lsqcurvefit*) was used to solve Eq. 5.3, with initial condition a = 10 s^{-1} (Aguado-Sierra, Alastruey, et al. 2008). Subsequently, the

separated pressure components were calculated via Eq. 5.1 and 5.4, and separated velocity components via Eq. 5.5-5.7.

In both DOF-Window and P_∞-Variation analyses the following hemodynamic parameters were calculated: the maxima of P_r and P_{ex} ($P_r\,max$ and $P_{ex}\,max$, respectively), the integral with respect to time of reservoir and excess pressure curves (PRI and PEI, respectively), the maxima of U_r and U_{ex} ($U_r\,max$ and $U_{ex}\,max$, respectively) and the index PP_r, which calculates the average squared difference, in diastole, between measured and reservoir pressure, according to the equation:

$$PP_r \text{ index} = \frac{1}{N}\sum_{i=1}^{N}(P_i - P_{r_i})^2 \tag{5.8}$$

Where N is the number of points in diastole.

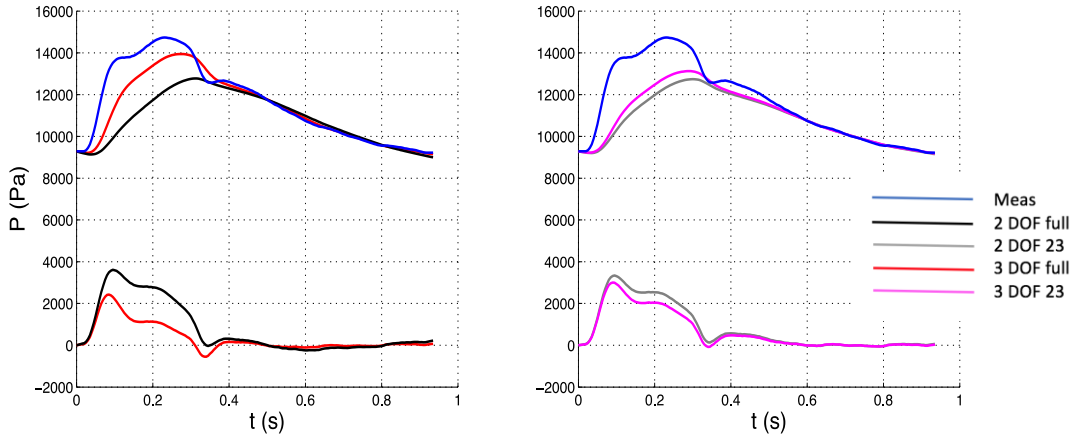

Figure 5.1: Comparison of pressure waveforms between 3 DOF and 2 DOF settings with full window (Left) and between 3 DOF and 2 DOF with 23 window (Right) for one patient. The measured pressure is depicted in blue. The top waveforms depicted along with the measured pressure represent the reservoir components, whereas the bottom waveforms the excess components. 23: 23 window, full: full window, meas: measured waveform.

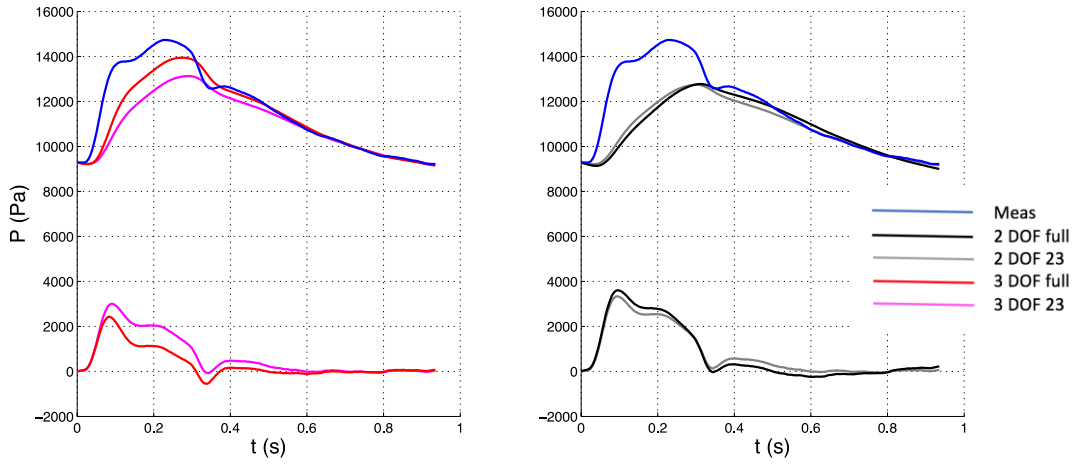

Figure 5.2: Comparison of pressure waveforms between full and 23 window with 3 DOF (Left) and between full and 23 window with 2 DOF (Right) settings for one patient. The measured pressure is depicted in blue. The top waveforms depicted along with the measured pressure represent the reservoir components, whereas the bottom waveforms the excess components. 23: 23 window, full: full window, meas: measured waveform.

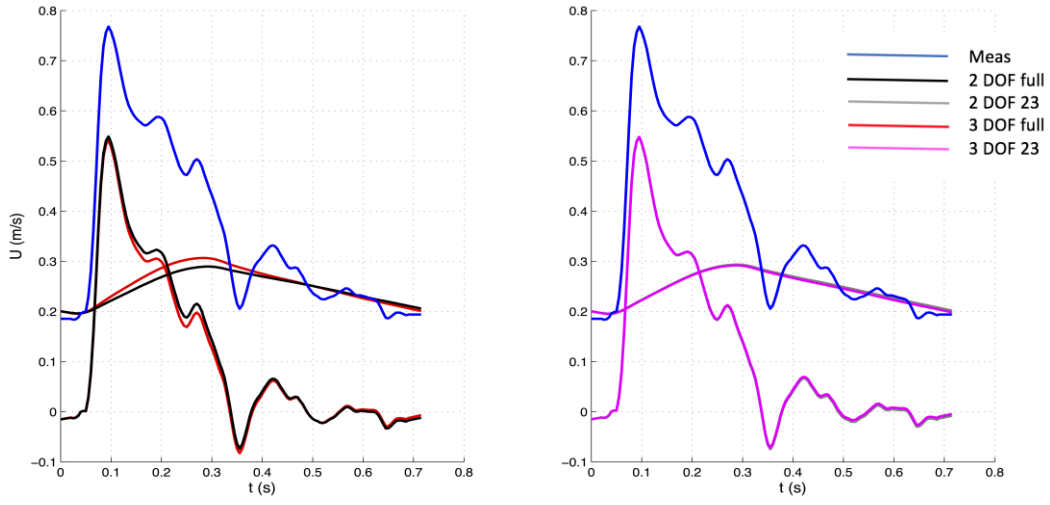

Figure 5.3: Comparison of velocity waveforms between 3 DOF and 2 DOF settings with full window (Left) and between 3 DOF and 2 DOF with 23 window (Right) for one patient. The measured velocity is depicted in blue. The top waveforms depicted along with the measured velocity represent the reservoir components, whereas the bottom waveforms the excess components. 23: 23 window, full: full window, meas: measured waveform.

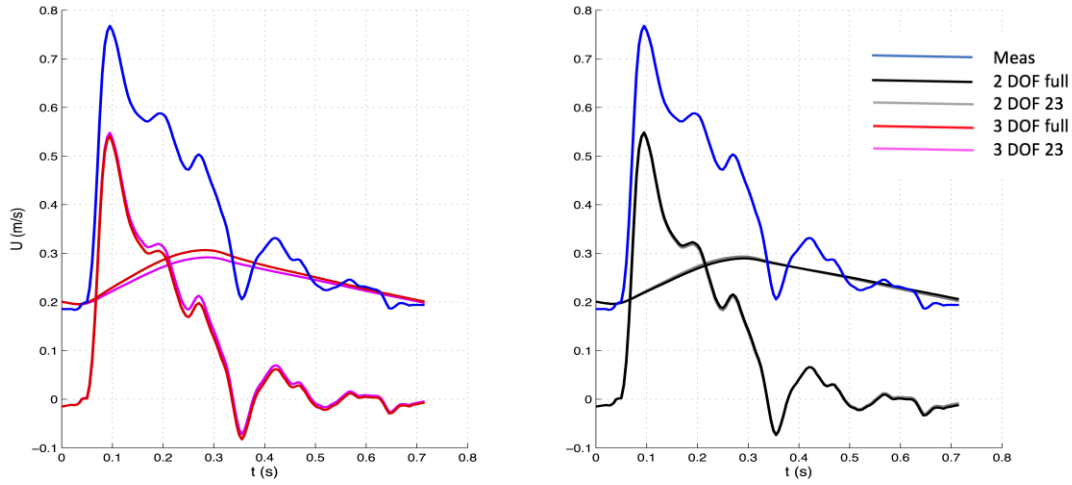

Figure 5.4: Comparison of velocity waveforms between full and 23 window with 3 DOF (Left) and between full and 23 window with 2 DOF (Right) settings for one patient. The measured velocity is depicted in blue. The top waveforms depicted along with the measured velocity represent the reservoir components, whereas the bottom waveforms the excess components. 23: 23 window, full: full window, meas: measured waveform.

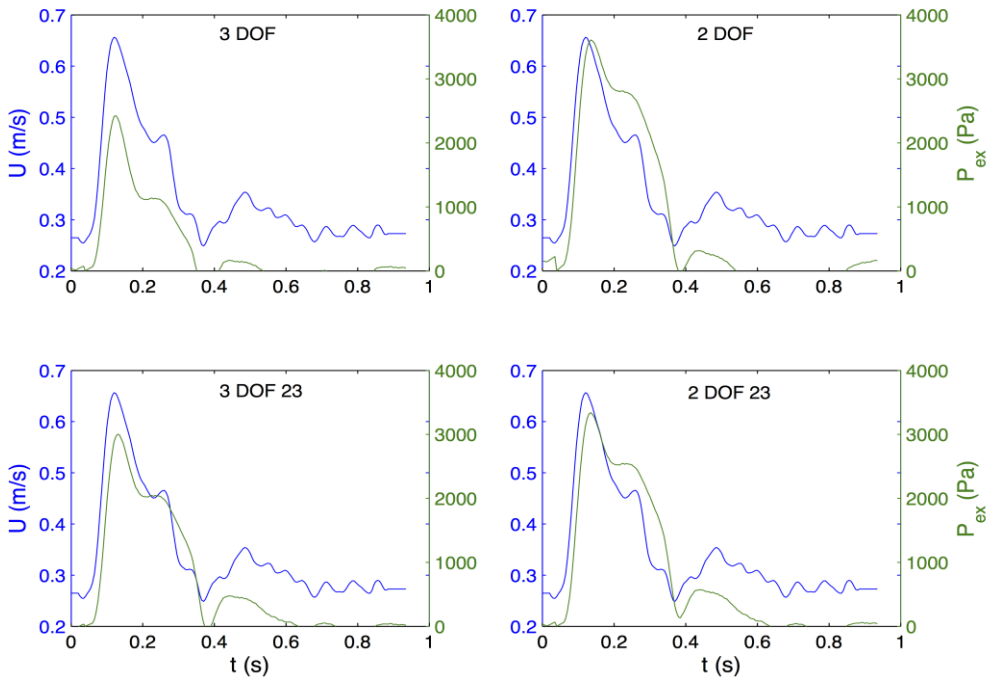

Figure 5.5: Examples of P_{ex} (green) and U (blue) waveforms for one patient. The pressure waveforms have been scaled down. Top Left: 3 DOF setting; Top Right: 2 DOF setting; Bottom Left: 3 DOF 23 setting; Bottom Left: 2 DOF 23 setting.

5.2.3.2 Wave intensity analysis

Wave intensity analysis was performed on both measured waveforms (P, U) and calculated excess waveforms (P_{ex}, U_{ex}) for each subject and in both DOF-Window and P_∞-Variation studies. Considering that reflected waves were absent during the early systolic portion of each cardiac cycle (Khir et al. 2001), the slopes of the linear part of the PU- and $P_{ex}U_{ex}$-loops were used to calculate the corresponding wave speed values (m/s) using the following equation:

$$c = \frac{1}{\rho}\frac{\Delta P_{lin}}{\Delta U_{lin}} \tag{5.9}$$

over the early systolic part of the loops (Figure 5.6), with the measured and the excess waveforms, for the PU- and the $P_{ex}U_{ex}$-loop, respectively, and blood density ρ was assumed equal to 1050 kg/m^3. Subsequently, the wave intensity $dI = dPdU$ (W/m^2) was separated into its forward-travelling and backward-travelling components (Parker & Jones 1990):

$$\begin{cases} dI_f := dP_f dU_f = +\dfrac{1}{4\rho c}(dP + \rho c dU)^2 \\ dI_b := dP_b dU_b = -\dfrac{1}{4\rho c}(dP - \rho c dU)^2 \end{cases} \tag{5.10}$$

After the calculation of wave speed and wave intensity via Eq. 5.9-5.10, relevant wave intensity parameters were extracted. The peak (W/m^2) and area (J/m^2) of the forward compression wave (FCW), which is generated by the contraction of the left ventricle, were derived from the amplitude and area, respectively, of the early-systolic peak observed in dI_+ (Figure 5.6). Similarly, the peak and area of the backward compression wave (BCW), which is attributed to reflections from the head microcirculation, if measurements are taken from the carotid artery, were determined from the amplitude and area, respectively, of the mid-systolic peak present in dI_-. Finally, the peak and the area of the forward expansion wave (FEW), which is generated by the decrease in shortening velocity of the left ventricle in the late systole, were determined from the amplitude and area of the late-systolic peak seen in dI_+ (Figure 5.6). The area parameters are associated with the energy of the waves, in comparison with similar parameters obtained with PU-WIA having units of J m^{-2}.

5.2.4 Statistical analysis

All values are reported as mean ± SD in the text, tables and figures. The statistical analyses were performed using SPSS Statistics (version 20, IBM, Armonk, New York, USA). Hemodynamic and wave intensity parameters were statistically compared via one-way analysis of variance (ANOVA) and Tukey's post-hoc test. Pearson correlation coefficients were calculated, and regression analysis was performed, in order to assess the degrees of correlation between relevant parameters and age. A paired two-tailed *t*-test was performed to assess significance of relevant parameters between genders. Statistical significance was assumed if p-value < 0.05.

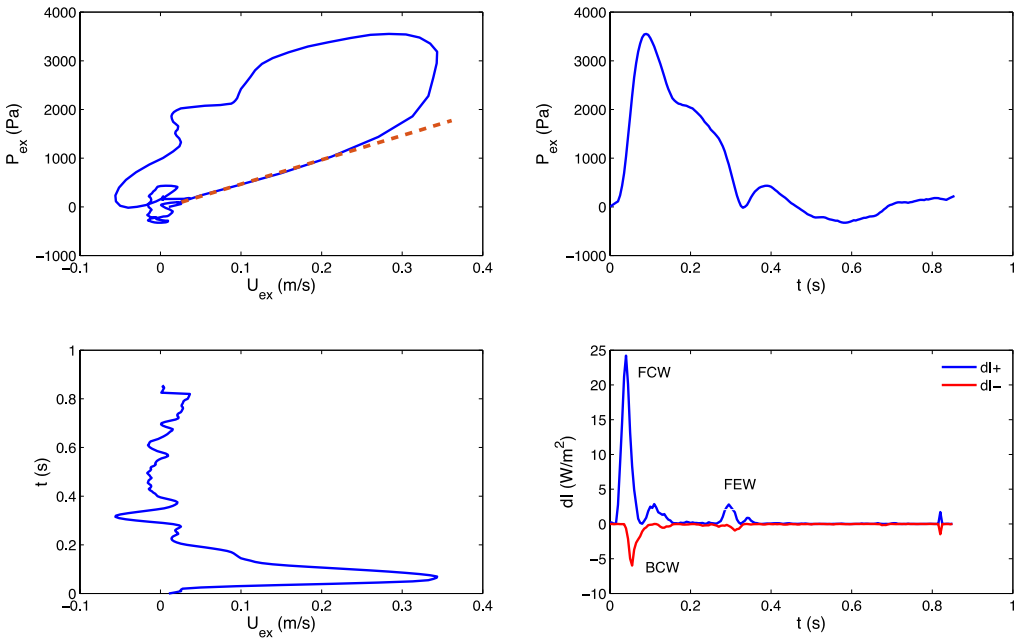

Figure 5.6: Example of $P_{ex}U_{ex}$ loop (Top Left), P_{ex} contour (Top Right), U_{ex} contour (Bottom Left) and corresponding wave intensity (Bottom Left) for one patient. A straight line highlighting the slope of the linear portion is superimposed on the $P_{ex}U_{ex}$ loop. Forward compression (FCW), backward compression (BCW) and forward expansion (FEW) waves are labelled in the wave intensity plot. dI+: forward wave intensity component, dI-: backward wave intensity component.

5.3 Results

The results are divided into four sections: a preliminary analysis of the effects of the algorithm settings on the results, the DOF-Window analysis, the P_{∞}-Variation analysis and the Age-Gender analysis. The latter section focuses on the correlation of relevant hemodynamic parameters with age and gender.

5.3.1 Effects of algorithm settings on results

5.3.1.1 Tolerance value

The effect of tolerance value is highlighted in Table 5.3. A sample of 12 subjects has been drawn from the population to perform comparisons between the results, for each parameter, with two different values of tolerance: 10^{-6} and 10^{-8}. Relevant hemoydnamic and wave intensity parameters were considered. ΔTol% in Table 5.3 is a measure of the relative difference and was averaged across the sample (of size n):

$$\Delta\text{Tol}\% = \frac{1}{n}\sum_{n}\left|\frac{Value\ at\ 10^{-6} - Value\ at\ 10^{-8}}{Value\ at\ 10^{-6}}\right| \cdot 100$$

As can be seen, the tolerance didn't play a significant role overall. However, there was a modest discrepancy, up to 8%, for wave intensity energy values (FCW, BCW and FEW areas). This may depend on the slight differences between data points located in the temporal series of that specific wave (FCW, BCW, FEW) that sum up for the calculation of the corresponding areas. Therefore, it is still important to report the tolerance value used for the fitting, in order to make the comparisons reproducible by other investigators. Finally, the number of iterations didn't change significantly: decreasing the tolerance from 10^{-6} to 10^{-8} brought an increase in the number of iterations by 6% (2 DOF) and 9% (3 DOF), meaning an increase from 11 ± 3 to 13 ± 3 iterations for 3 DOF and from 11 ± 4 to 12 ± 4 iterations for 2 DOF.

Parameter	3 DOF (ΔTol%)	2 DOF (ΔTol%)
P_∞	0	0
b	0.001	$<10^{-3}$
a	0.002	$<10^{-3}$
P_r max	$<10^{-3}$	$<10^{-3}$
P_{ex} max	$<10^{-3}$	$<10^{-3}$
PRI	$<10^{-3}$	$<10^{-3}$
PEI	0.002	$<10^{-3}$
c	$<10^{-3}$	$<10^{-3}$
FCW peak	$<10^{-3}$	$<10^{-3}$
BCW peak	0.29	$<10^{-3}$
FEW peak	$<10^{-3}$	$<10^{-3}$
FCW area	0.06	0.84
BCW area	7.3	7.1
FEW area	8.1	4.6
iterations^	+9	+6

Table 5.3: Effect of tolerance value on hemodynamic and wave intensity parameters. ΔTol%: relative difference in tolerance value; ^: the relative difference is displayed with the sign for clarity. More details in the text.

5.3.1.2 Performance of different least-squares algorithms

The standard method used by the *lsqcurvefit* function is the Trust-Region-Reflective (TRR), a subclass of trust-region algorithms that solve the minimization problem by modelling the objective function with standard functions in local regions whose size is continuously modified until convergence. Two different algorithms were compared with this standard method: the Levenberg-Marquardt (LM) and the fminsearch. LM is the alternative method associated to *lsqcurvefit* and is a combination of the gradient descent algorithm (that performs a minimization moving in the direction of the steepest descent) and the Gaussian-Newton method, that assumes the function to minimize is locally quadratic. Fminsearch is a direct search method, meaning that it doesn't compute gradients of the objective function for the minimization.

The LM method did not bring substantial differences in results, both in 3 DOF and 2 DOF, as displayed in Table 5.4. Only the area parameters showed a slight increase, up to 6%, and that can be ascribed to the process of summing up the modest differences in data

points for the calculation of the area values. The number of iterations decreased both in 3 DOF (34%) and 2 DOF (43%) using LM method over the standard TRR. The fminsearch algorithm behaved in a completely different way, bringing differences up to 300% for 3 DOF and up to 25% for 2 DOF. The number of iterations increased dramatically (+720% and +853% for 3 DOF and 2 DOF, respectively) reaching about 100 for each simulation. It is therefore important to specify the class of algorithm to make the comparisons reproducible by other investigators. Being a good compromise between simplicity and efficiency, the *lsqcurvefit* TRR was chosen over the other alternatives.

Parameter	**3 DOF LM (%)**	**2 DOF LM (%)**	**3 DOF fmin (%)**	**2 DOF fmin (%)**
P_∞	0	0	4.77	15.55
b	0.001	$<10^{-3}$	59.73	28.68
a	0.002	$<10^{-3}$	82.12	32.25
P_r max	$<10^{-3}$	$<10^{-3}$	15.38	1.17
P_{ex} max	$<10^{-3}$	$<10^{-3}$	133.78	10.86
PRI	$<10^{-3}$	$<10^{-3}$	5.98	0.65
PEI	0.002	$<10^{-3}$	309.89	12.46
c	$<10^{-3}$	$<10^{-3}$	23.09	1.33
FCW peak	$<10^{-3}$	$<10^{-3}$	106.49	4.93
BCW peak	$<10^{-3}$	$<10^{-3}$	80.38	20.88
FEW peak	$<10^{-3}$	$<10^{-3}$	173.31	25.05
FCW area	0.85	0.54	159.33	7.77
BCW area	2.02	1.48	144.49	20.15
FEW area	5.39	6.26	187.50	12.30
iterations^	-34	-43	+720	+853

Table 5.4: Effect of type of algorithm on hemodynamic and wave intensity parameters. LM: Levenberg-Marquardt; fmin: fminsearch. % refers to relative difference in value with respect to the corresponding reference algorithm "lsqcurvefit"; ^: the relative difference is displayed with the sign for clarity. More details in the text.

5.3.2 DOF-Window analysis

P_∞ (Figure 5.7) slightly decreased from 3 DOF to 2 DOF in both window settings (full and 23), non-significantly ($p>0.05$) in the former case (-4%) and significantly ($p<0.05$) for the latter case (-6%), whereas the change from full to 23 diastolic window caused bigger

variations, specifically +19% ($p<0.05$) and +15% ($p<0.05$) for 3 DOF and 2 DOF, respectively.

The diastolic constant b (Figure 5.7) significantly decreased from 3 DOF to 2 DOF in both window settings: -38% for full window and -9% for 23 window. The change in window (from full to 23) caused bigger variations: +40% ($p<0.05$) and +105% ($p<0.05$) for 3 DOF and 2 DOF, respectively. Therefore, b seemed affected by both changes in DOF and window settings, whereas P_∞ substantially changed only with changes in window. The change in window was responsible for a bigger variation than the change in DOF, for both parameters.

$P_r\ max$ (Figure 5.7) significantly decreased from 3 DOF to 2 DOF, in both window settings: -6% for full window and -5% for 23 window. The variation exhibited from full to 23 window was -4% ($p<0.05$) for 3 DOF and -3% ($p<0.05$) for 2 DOF. $U_r\ max$ (Figure 5.7) showed a slightly different pattern: a variation of -22% from 3 DOF to 2 DOF with a full window and -14% with a 23 window, while the variation exhibited from full to 23 window was +3% ($p>0.05$) for 3 DOF and +14% ($p<0.05$) for 2 DOF.

$P_{ex}\ max$ and $U_{ex}\ max$ (Figure 5.7) significantly increased from 3 DOF to 2 DOF, in both window settings: +32% and +5% with full window, and +16% and +4% with 23 window, for $P_{ex}\ max$ and $U_{ex}\ max$, respectively. The variations exhibited from full to 23 window were: +16% ($p<0.05$) and +9% ($p<0.05$) for 3 DOF, +1% ($p>0.05$) and +8% ($p<0.05$) for 2 DOF, for $P_{ex}\ max$ and $U_{ex}\ max$, respectively. Therefore, $P_{ex}\ max$ showed overall a bigger variation than $U_{ex}\ max$.

PEI (Figure 5.8) significantly increased from 3 DOF to 2 DOF, in both window settings: +64% for full window and +36% for 23 window. The change exhibited from full to 23 window was +46% ($p<0.05$) and +21% ($p>0.05$) for 3 DOF and 2 DOF, respectively.
The variation in PRI (Figure 5.8) was much less pronounced: from 3 DOF to 2 DOF, it was -3% ($p<0.05$) and -2% ($p>0.05$), for full window and 23 window, respectively, whereas the variation exhibited from full window to 23 window was not significant: -2% ($p>0.05$) and -1% ($p>0.05$) for 3 DOF and 2 DOF, respectively.

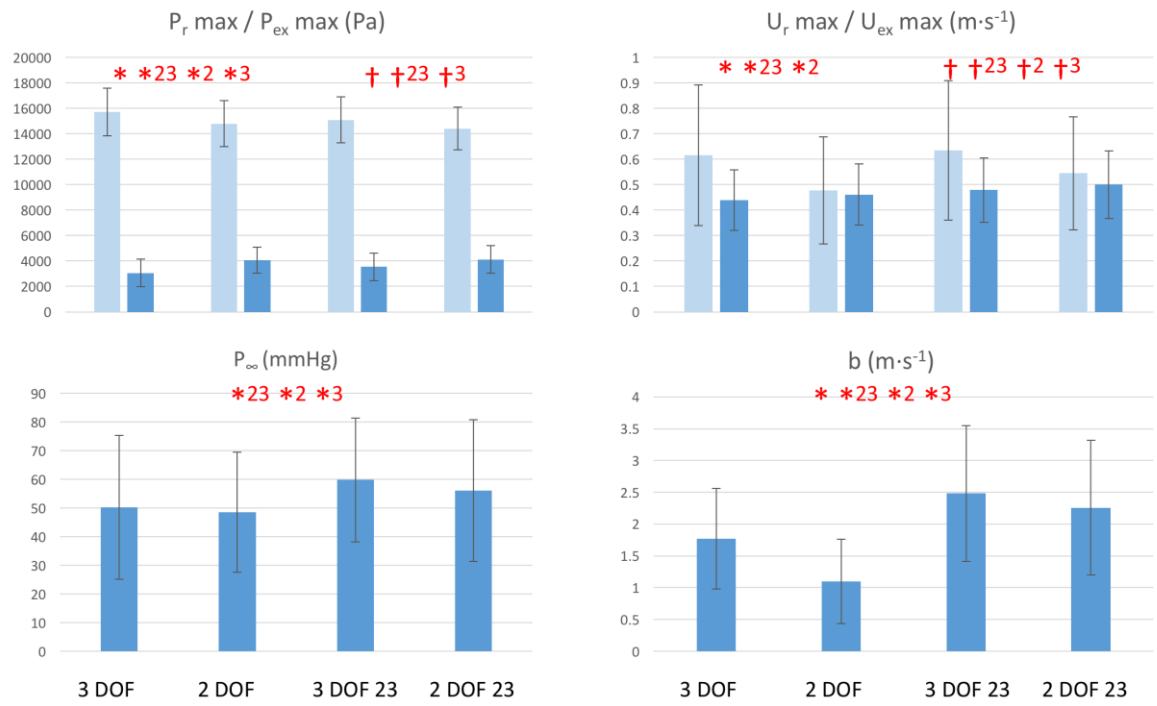

Figure 5.7: Comparisons of $P_r\ max$ and $P_{ex}\ max$ (Top Left), $U_r\ max$ and $U_{ex}\ max$ (Top Right), P_∞ (Bottom Left) and b (Bottom Right) values among all fitting settings. *: significant difference between 3 DOF and 2 DOF in full window ($p<0.05$), *23: significant difference between 3 DOF and 2 DOF in 23 window, *2: significant difference between 2 DOF and 2 DOF 23, *3: significant difference between 3 DOF and 3 DOF 23. Y-axis units are reported in each figure title. Values are reported as mean $\pm$ SD.

Index PP_r (Figure 5.9) increased from 3 to 2 DOF in both window settings: +104% and +168% in full and 23 window, respectively (both $p<0.05$). Also, it increased from full to 23 window in both DOF settings (+150% and +227% for 3 DOF and 2 DOF, respectively, $p<0.05$). This means that the lowest values for the index were found with 3 DOF-full window settings.

In the context of wave intensity analysis, variables were also compared with the ones obtained from the measured P and U signals. However, ANOVA statistical analysis was not performed on the dataset including the PU-derived parameters, but only on the $P_{ex}U_{ex}$-derived variables, to avoid masking the different effects of fitting methods on the wave intensity variables and to obtain statistical results that could be easily compared with results of hemodynamic parameters.

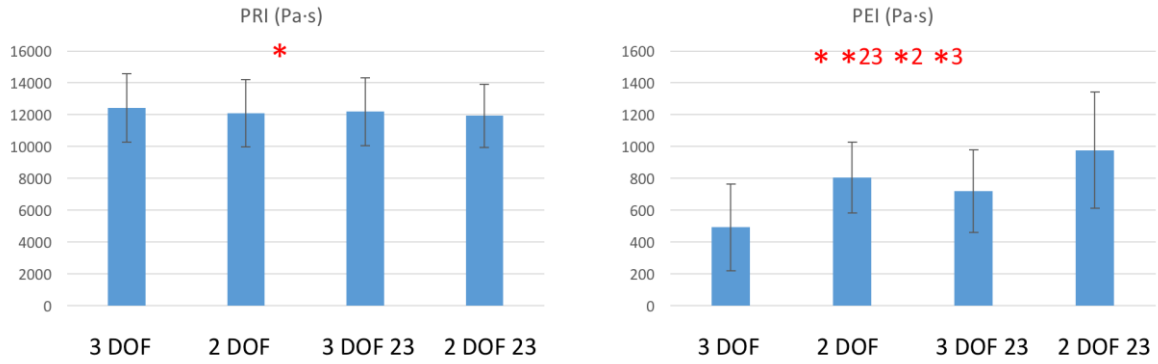

Figure 5.8: Comparisons of *PRI* (Left) and *PEI* (Right) values among all fitting settings. *: significant difference between 3 DOF and 2 DOF in full window ($p<0.05$), *23: significant difference between 3 DOF and 2 DOF in 23 window, *2: significant difference between 2 DOF and 2 DOF 23, *3: significant difference between 3 DOF and 3 DOF 23. Y-axis units are reported in each figure title. Values are reported as mean ± SD.

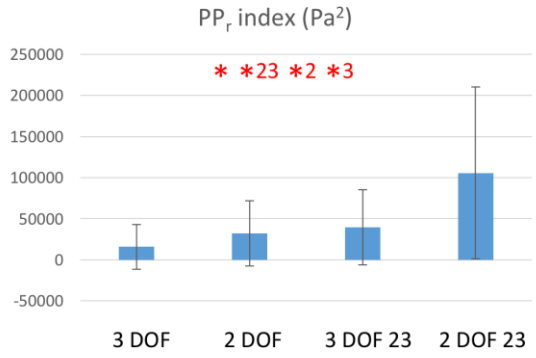

Figure 5.9: Comparisons of PP_r index values among all fitting settings. *: significant difference between 3 DOF and 2 DOF in full window ($p<0.05$), *23: significant difference between 3 DOF and 2 DOF in 23 window, *2: significant difference between 2 DOF and 2 DOF 23, *3: significant difference between 3 DOF and 3 DOF 23. Y-axis units are reported in each figure title. Values are reported as mean ± SD.

A paired two-tailed t-test was performed instead, for the comparison of PU-derived- with $P_{ex}U_{ex}$-derived parameters.

In the context of $P_{ex}U_{ex}$-derived parameters, wave speed (Figure 5.10) significantly increased (+7%, $p<0.05$) from 3 DOF to 2 DOF in full window setting and remained fairly unchanged (-1%, $p>0.05$) with 23 window. Also, it increased (+8%, $p<0.05$) in 3 DOF and

remained unchanged (-1%, $p>0.05$) in 2 DOF, from full to 23 window. Overall, wave speed values did not substantially change in-between settings.

FCW peak and area (Figure 5.10) significantly increased from 3 DOF to 2 DOF, in both window settings: +28% and +38% with full window, and +10% and +14% with 23 window, for FCW peak and area, respectively. The change exhibited from full to 23 window was +11% ($p<0.05$) and +13% ($p<0.05$) for 3 DOF, and -5% ($p>0.05$) and -6% ($p<0.05$) for 2 DOF, for FCW peak and area, respectively.

A very similar pattern was recorded for the forward expansion wave. FEW peak and area (Figure 5.10) significantly increased from 3 DOF to 2 DOF, in both window settings: +40% and +53% for full window, and +16% and +20% for 23 window, for FEW peak and area, respectively. The change exhibited from full to 23 window was +15% ($p<0.05$) and +21% ($p<0.05$) for 3 DOF, and -4% ($p>0.05$) and -5% ($p>0.05$) for 2 DOF, for FEW peak and area, respectively.

Instead, BCW peak did not show significant change in values from 3 DOF to 2 DOF (+6% and +0.1% for full and 23 window settings, respectively, $p>0.05$), whereas significantly increased from full to 23 window: +35% in 3 DOF and +28% in 2 DOF. BCW area (Figure 5.10) increased from 3 DOF to 2 DOF in both window settings: +22% ($p<0.05$) and +6% ($p>0.05$) for full and 23 window, respectively. The variation exhibited with change in window (from full to 23) was significant: +49% ($p<0.05$) and +29% ($p<0.05$) for 3 DOF and 2 DOF, respectively.

PU-derived parameters were always greater than corresponding $P_{ex}U_{ex}$-derived parameters: the biggest difference was recorded with 3 DOF full window setting (between +19.5% for wave speed and +89.5% for BCW area). Table 5.3 reports the percentage variations that PU-derived parameters exhibited with respect to corresponding $P_{ex}U_{ex}$-derived parameters and corresponding statistical significance.

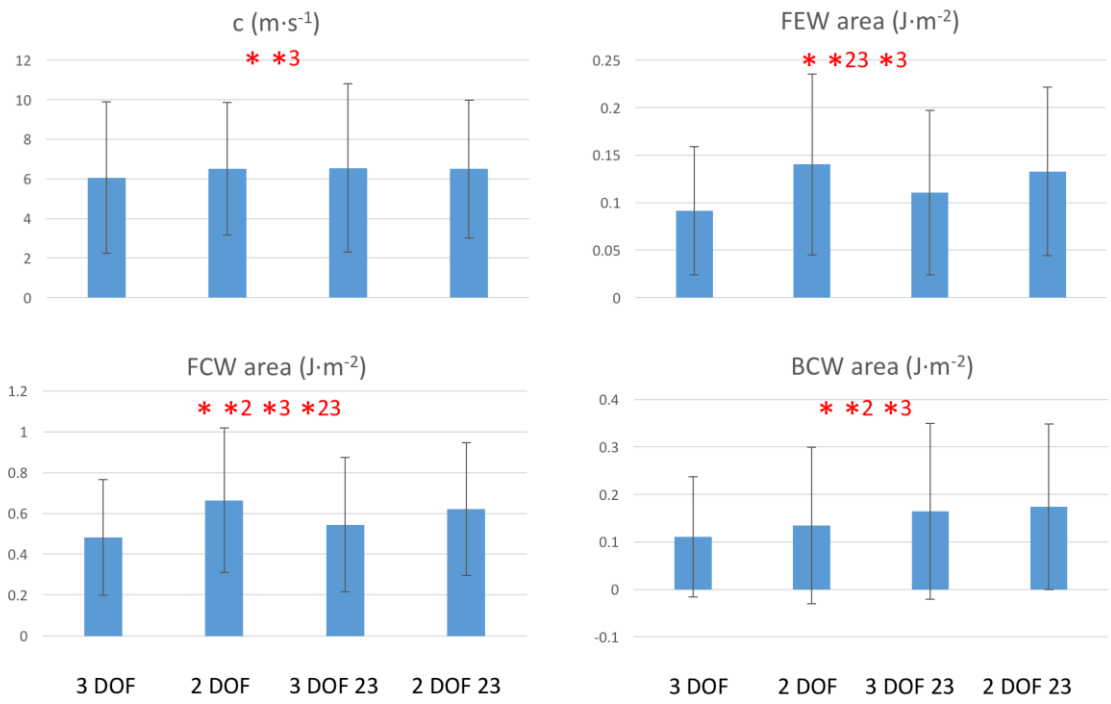

Figure 5.10: Comparisons of wave speed c (Top Left), FEW area (Top Right), FCW area (Bottom Left) and BCW area (Bottom Right) values among all fitting settings. *: significant difference between 3 DOF and 2 DOF in full window ($p<0.05$), *23: significant difference between 3 DOF and 2 DOF in 23 window, *2: significant difference between 2 DOF and 2 DOF 23, *3: significant difference between 3 DOF and 3 DOF 23. Y-axis units are reported in each figure title. Values are reported as mean $\pm$ SD.

	c	FCW peak	FEW peak	BCW peak	FCW area	FEW area	BCW area
3 DOF	+19.5	+50.1	+52.8	+50.9	+73.4	+58.8	+89.5
2 DOF	+11.3	+17.1	+9.4	+42.3	+25.8	+3.5†	+54.9
3 DOF 23	+10.5	+34.9	+32.4	+11.6	+53.5	+31.5	+27.1
2 DOF 23	+11.4	+23.2	+14.5	+11.5	+34.6	+9.1	+19.7

Table 5.5: Percentage (%) variations of wave intensity parameters obtained with PU loop (measured waveforms), with respect to corresponding parameters obtained with excess components P_{ex} and U_{ex}. †: not significant ($p>0.05$). As indicated, only one variation was not significant (FEW area in 2 DOF full setting).

5.3.3 P_∞-Variation analysis

All changes are referred to the reference value for that particular parameter (corresponding to the value obtained with 2 DOF full setting in the DOF-Window analysis, as explained in the 'Material and Methods' section). Therefore, the acronym w.r.t.R (with respect to reference) was used in the following sections.

The diastolic constant b (Figure 5.11) had a tendency to decrease (non-significantly w.r.t.R) with all negative P_∞ variations (i.e., -25%, -50%, -75%) and increased (all significantly w.r.t.R) with positive P_∞ variations, up to +75%, because at +100% b decreased again, below the value obtained at +50%. With positive P_∞ variations the standard deviation (SD) substantially increased.

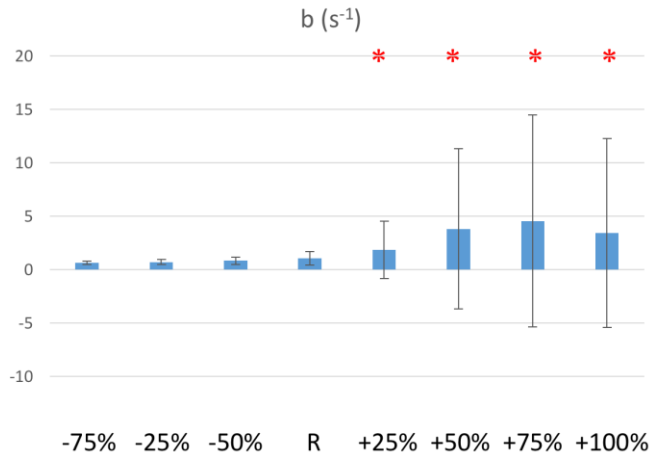

Figure 5.11: Comparison of b values among positive (+25%, +50%, +75%, +100%) and negative (-25%, -50%, -75%) variations of P_∞, with respect to the reference value (R) extracted from 2 DOF full window setting. *: significant difference with respect to R ($p<0.05$). Y-axis units are reported in each figure title. Values are reported as mean $\pm$ SD.

$P_{ex}\,max$ (Figure 5.12) increased (non-significantly w.r.t.R) with negative P_∞ variations and decreased (significantly w.r.t.R) with positive P_∞ variations, up to +50%, then increased again, reaching, at the biggest increment (+100%), the value recorded at +25%: therefore, the maximum variation w.r.t.R was at +50% and its amplitude was -12% ($p<0.05$). SD did not substantially change with P_∞ variations.

$P_r\,max$ (Figure 5.12) did not significantly change: it had a tendency to decrease w.r.t.R with negative P_∞ variations and to increase with positive P_∞ variations, up to +50%. The maximum change w.r.t.R was recorded at +50% and its amplitude was +1.6% ($p>0.05$). SD did not substantially change with P_∞ variations.

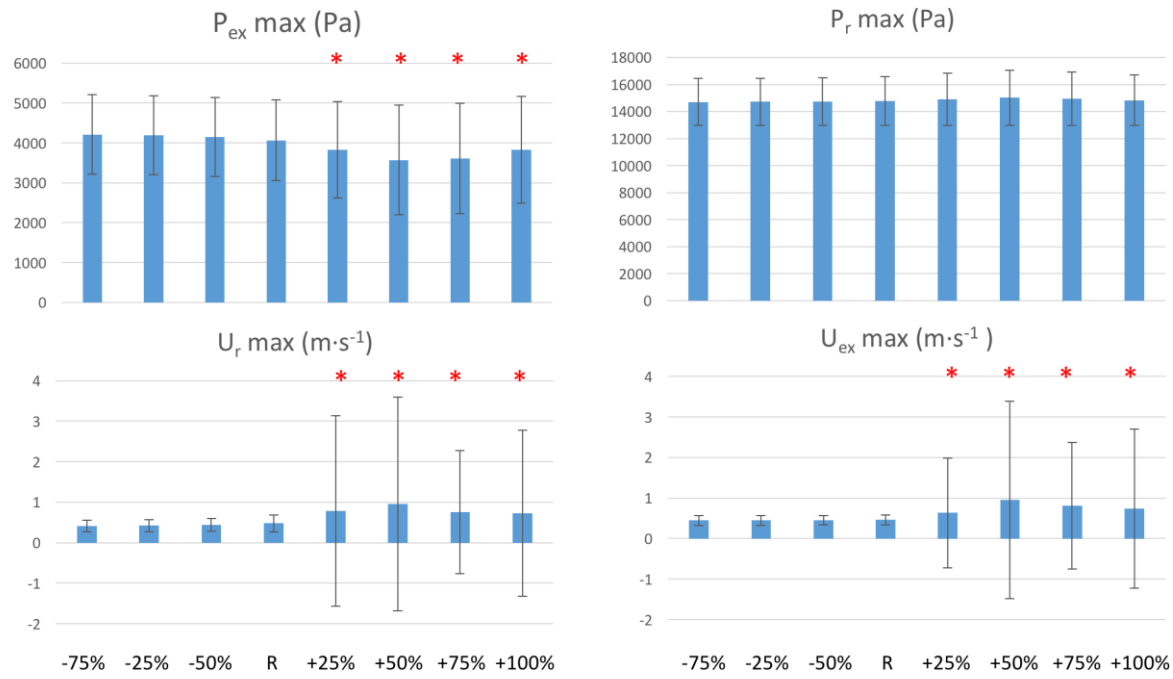

Figure 5.12: Comparisons of $P_{ex}\ max$ (Top Left), $P_r\ max$ (Top Right), $U_r\ max$ (Bottom Left) and $U_{ex}\ max$ (Bottom Right) values among positive (+25%, +50%, +75%, +100%) and negative (-25%, -50%, -75%) variations of P_∞, with respect to the reference value (R) extracted from 2 DOF full window setting. *: significant difference with respect to R ($p<0.05$). Y-axis units are reported in each figure title. Values are reported as mean $\pm$ SD.

PEI (Figure 5.13) decreased (significantly w.r.t.R) with positive P_∞variations and slightly increased (significantly w.r.t.R, except at -25%) with negative P_∞ variations. The maximum variations w.r.t.R were: -26% ($p<0.05$) at the biggest increment (+100%) and +5% ($p<0.05$) at the opposite side (-75%). *PRI* (Figure 5.13) had a tendency to decrease with negative P_∞ variations and to increase with positive variations. Overall, its value did not substantially change: the maximum increase was at +100% and its corresponding amplitude was +3% ($p<0.05$). SD did not substantially change for both *PEI* and *PRI*.

$U_r\ max$ and $U_{ex}\ max$ (Figure 5.12) had very high SD at positive P_∞ variations. $U_r\ max$ slightly decreased (non-significantly w.r.t.R) with negative P_∞ variations (maximum change: -14% at -75% variation) and increased (significantly w.r.t.R) with positive P_∞ variations (maximum change: +100% at +50% variation). At +75% and +100% iterations, it had a tendency to decrease again. The same behaviour applied to $U_{ex}\ max$: the maximum changes had amplitudes of +106% at +50% variation and -3% at -75% variation.

The increases in the positive direction were significant (except for +25%), whereas all decreases in the negative direction were non-significant.

Index PP_r (Figure 5.14) increased with positive P_∞ variations (significantly w.r.t.R, except for +25%) with a eighteen-fold maximum variation (+1790%) at +100% variation, and increased again with negative P_∞ variations (although non-significantly w.r.t.R) with a maximum variation of +22% at -75% iteration. Therefore, it seems that minimum values were recorded at the reference point. SD substantially increased with positive P_∞ variations.

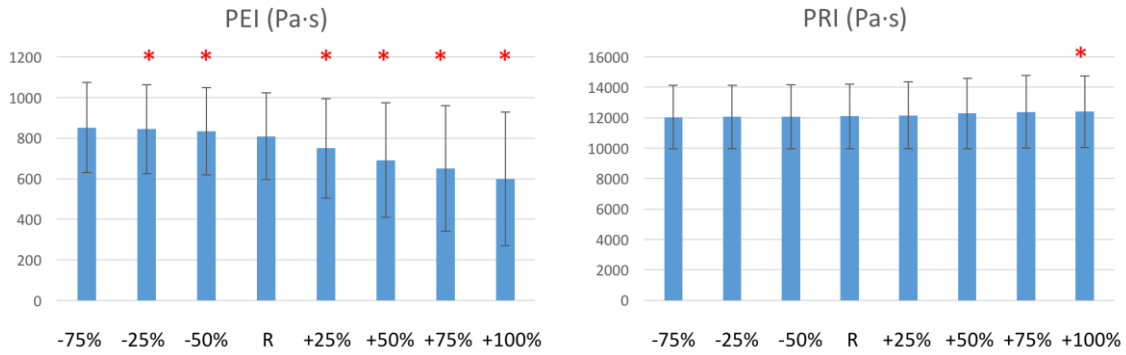

Figure 5.13: Comparisons of *PEI* (Left) and *PRI* (Right) values among positive (+25%, +50%, +75%, +100%) and negative (-25%, -50%, -75%) variations of P_∞, with respect to the reference value (R) extracted from 2 DOF full window setting. *: significant difference with respect to R ($p<0.05$). Y-axis units are reported in each figure title. Values are reported as mean $\pm$ SD.

In the context of wave intensity analysis, wave speed (Figure 5.15) did not substantially change: it slightly increased (although non-significantly w.r.t.R) with negative P_∞ variations (maximum change: +2% at -75% iteration) and tended to decrease (non-significantly w.r.t.R) with positive P_∞ variations (maximum change: -7% at +75% iteration). SD tended to remain stable.

FCW peak increased both with positive (significantly, except for +25%) and negative (non-significantly) P_∞ variations. The maximum changes were: +18% ($p<0.05$) at +75% variation in the positive direction and +3% ($p>0.05$) at -75% variation in the negative direction. The same behaviour applied to FEW peak: its increases were all significant, except at +25%, in the positive direction (maximum change: +34% at +50% iteration) and all non-significant in the negative direction (maximum change: +5% at -75% iteration). For both parameters, SD tended to increase in the positive direction and to remain stable in the negative direction.

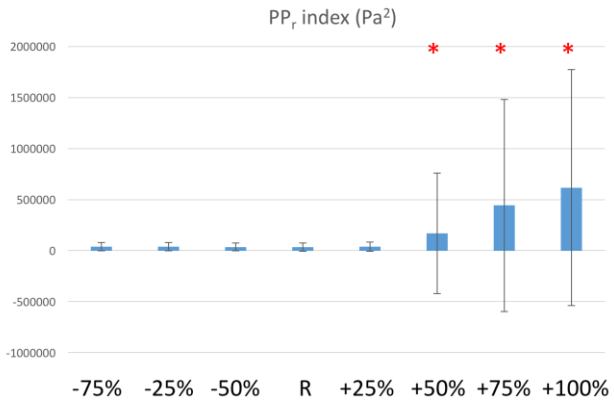

Figure 5.14: Comparisons of PP_r index values among positive (+25%, +50%, +75%, +100%) and negative (-25%, -50%, -75%) variations of P_∞, with respect to the reference value (R) extracted from 2 DOF full window setting. *: significant difference with respect to R ($p<0.05$). Y-axis units are reported in each figure title. Values are reported as mean $\pm$ SD.

FCW area (Figure 5.15) increased both with positive (significantly w.r.t.R, except for +25% iteration) and negative (non-significantly w.r.t.R) variations of P_∞. Maximum changes: +32% at +50% variation in the positive direction and +4% at -75% variation in the negative direction. The same behaviour applied to FEW area (Figure 5.15), although its increases were all non-significant, except for +50% iteration. Maximum changes were +49% at +50% iteration in the positive direction and +7% at -75% iteration in the negative direction. For both parameters, SD tended to increase in the positive direction and to remain stable in the negative direction.

Instead, the minimum values for BCW peak and area (Figure 5.15) were recorded at -50%. In particular, BCW peak slightly decreased (non-significantly wr.t.R) with negative P_∞ variations (the maximum change, recorded at -75% iteration, was -6%) and tended to increase in the positive direction (significantly w.r.t.R, except for +100% iteration). The maximum change was +31% at +50% variation. The same behaviour applied to BCW area (significant changes in the positive direction, non-significant changes in the negative direction). The max changes were: -7% at -75% variation and +103% at +50% variation.

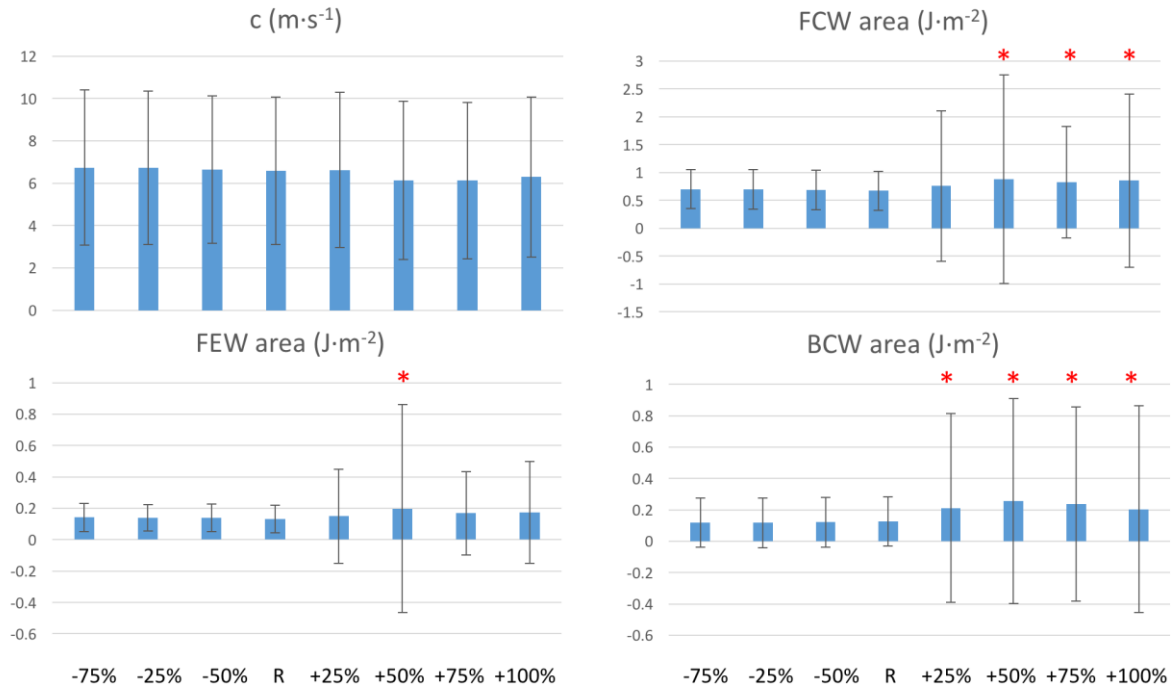

Figure 5.15: Comparisons of wave speed c (Top Left), FCW area (Top Right), FEW area (Bottom Left) and BCW area (Bottom Right) values among positive (+25%, +50%, +75%, +100%) and negative (-25%, -50%, -75%) variations of P_{∞}, with respect to the reference value (R) extracted from 2 DOF full window setting. *: significant difference with respect to R ($p<0.05$). Y-axis units are reported in each figure title. Values are reported as mean $\pm$ SD.

5.3.4 Age-gender analysis

$P_r\ max$, $P_{ex}\ max$, $U_r\ max$ and $U_{ex}\ max$ were also compared against age (Figure 5.16) and gender (Figure 5.17), among fitting methods used in the DOF-Window analysis.

Significant differences were recorded in $P_r\ max$, $P_{ex}\ max$, $U_r\ max$ and $U_{ex}\ max$ with age, among half-decades. Generally, there was an increase in values with age, except for $U_{ex}\ max$, which tended to decrease. Table 5.4 reports the percentage variations of values with respect to the 1st half-decade (1st HD) in all settings.

$P_r\ max$ exhibited significant differences in all different fitting settings, whereas $U_{ex}\ max$ lacked significance only in 3 DOF 23 setting. Overall, $P_{ex}\ max$ did not exhibit significant changes with age. There was a big variation in results among different settings, with 3 DOF 23 window showing the least degree of variability (it changed significantly only for $P_r\ max$) compared to the others.

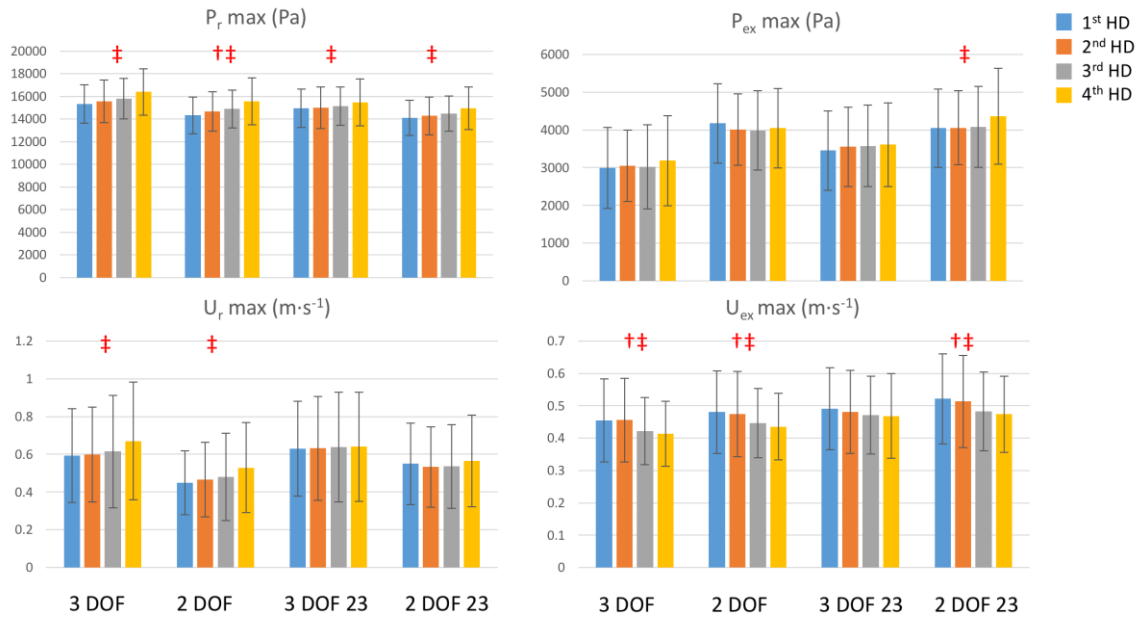

Figure 5.16: Comparison of $P_r\ max$ (Top Left), $P_{ex}\ max$ (Top Right), $U_r\ max$ (Bottom Left) and $U_{ex}\ max$ (Bottom Right), among half-decades (1st: 35-40, 2nd: 41-45, 3rd: 46-50, 4th: 51-55 yr) in all fitting settings. HD: half-decade. *: significant difference between 2nd HD and 1st HD, †: significant difference between 3rd HD and 1st HD, ‡: significant difference between 4th HD and 1st HD. Y-axis units are reported in each figure title. Values are reported as mean $\pm$ SD.

Overall, the 2nd half-decade did not record any significant difference with respect to the 1st half-decade for all parameters examined, whereas the 3rd half-decade exhibited significant changes, although mainly for $U_{ex}\ max$. As expected, the 4th half-decade showed the greatest differences with respect to the 1st half-decade.

Regression analysis was also performed to assess the degree of linearity of the parameters with age. Overall, the Pearson's correlation coefficients (R^2) were small (<0.06), suggesting a low degree of linearity, and presented a great degree of variability among parameters (especially for $P_r\ max$ and $U_r\ max$) and fitting settings, as reported in Table 5.5. Nevertheless, $P_r\ max$ and $U_{ex}\ max$ presented R^2 values an order of magnitude greater than $P_{ex}\ max$ and $U_r\ max$; however, different fitting settings led to different values of the slope, which ranged between 2.06 and 5.59 mmHg/decade for $P_r\ max$ and between -1.5 and 3.1 cm/s/decade for $U_{ex}\ max$.

		3 DOF	2 DOF	3 DOF 23	2 DOF 23
P_r max	2nd vs. 1st HD	+1.5	+2.3	+0.3	+1.3
	3rd vs. 1st HD	+2.9	+3.9	+1.2	+2.6
	4th vs. 1st HD	+6.9	+8.7	+3.5	+5.9
P_{ex} max	2nd vs. 1st HD	+1.8	-4.1	+2.8	+0.3
	3rd vs. 1st HD	+0.9	-4.6	+3.5	+0.8
	4th vs. 1st HD	+6.5	-3.2	+4.5	+7.8
U_r max	2nd vs. 1st HD	+0.9	+3.7	+0.4	-3.1
	3rd vs. 1st HD	+3.5	+7.1	+1.5	-2.6
	4th vs. 1st HD	+12.9	+17.9	+1.8	+2.7
U_{ex} max	2nd vs. 1st HD	+0.3	-1.4	-2.0	-1.5
	3rd vs. 1st HD	-7.2	-7.1	-4.1	-7.4
	4th vs. 1st HD	-9.1	-9.4	-4.7	-9.1

Table 5.6: Percentage (%) variations of 2nd, 3rd and 4th half-decade values with respect to corresponding 1st half-decade values, for $P_r\ max, P_{ex}\ max, U_r\ max$ and $U_{ex}\ max$, in all settings. Female and male values are pooled together. HD: half-decade.

		Slope (Pa/decade)	Slope (mmHg/decade)	R^2	p-value
P_r max	3 DOF	638.2	4.78	0.039	<0.01
	2 DOF	745.9	5.59	0.058	<0.01
	3 DOF 23	274.7	2.06	0.008	<0.01
	2 DOF 23	525.9	3.94	0.033	<0.01
P_{ex} max	3 DOF	113.0	0.85	0.0037	0.05
	2 DOF	-74.1	-0.56	0.0018	0.18
	3 DOF 23	115.2	0.86	0.0039	0.04
	2 DOF 23	160.3	1.20	0.0074	<0.01
		Slope (m/s/decade)	Slope (cm/s/decade)	R^2	p-value
U_r max	3 DOF	0.046	4.6	0.0092	<0.01
	2 DOF	0.048	4.8	0.0178	<0.01
	3 DOF 23	0.009	0.9	0.0003	0.55
	2 DOF 23	0.010	1.0	0.0007	0.38
U_{ex} max	3 DOF	-0.028	-2.8	0.019	<0.01
	2 DOF	-0.029	-2.9	0.020	<0.01
	3 DOF 23	-0.015	-1.5	0.005	0.02
	2 DOF 23	-0.031	-3.1	0.019	<0.01

Table 5.7: Correlation and regression analysis for $P_r\ max, P_{ex}\ max, U_r\ max$ and $U_{ex}\ max$ with age, in all fitting settings. R^2: Pearson's correlation coefficient.

Small significant differences were recorded in $P_r\ max, P_{ex}\ max, U_r\ max$ and $U_{ex}\ max$ between genders. Generally, males exhibited slightly greater values than females, although this is not true in the case of $U_r\ max$ in 2 DOF full setting. $P_r\ max$ and $U_{ex}\ max$ exhibited significant differences between males and females in all settings, whereas $P_{ex}\ max$ and $U_{ex}\ max$ did not show significant differences in all settings, except for 2 DOF full

window. Overall, the 2 DOF full setting recorded significant differences for all parameters. Unexpectedly, the greatest differences between genders were found in $U_r\ max$ and $P_{ex}\ max$ for 2 DOF full window (11.4% and 10.0%, respectively), although these parameters did not show any significant difference for the other settings. Table 5.6 reports the percentage variations of values between males and females.

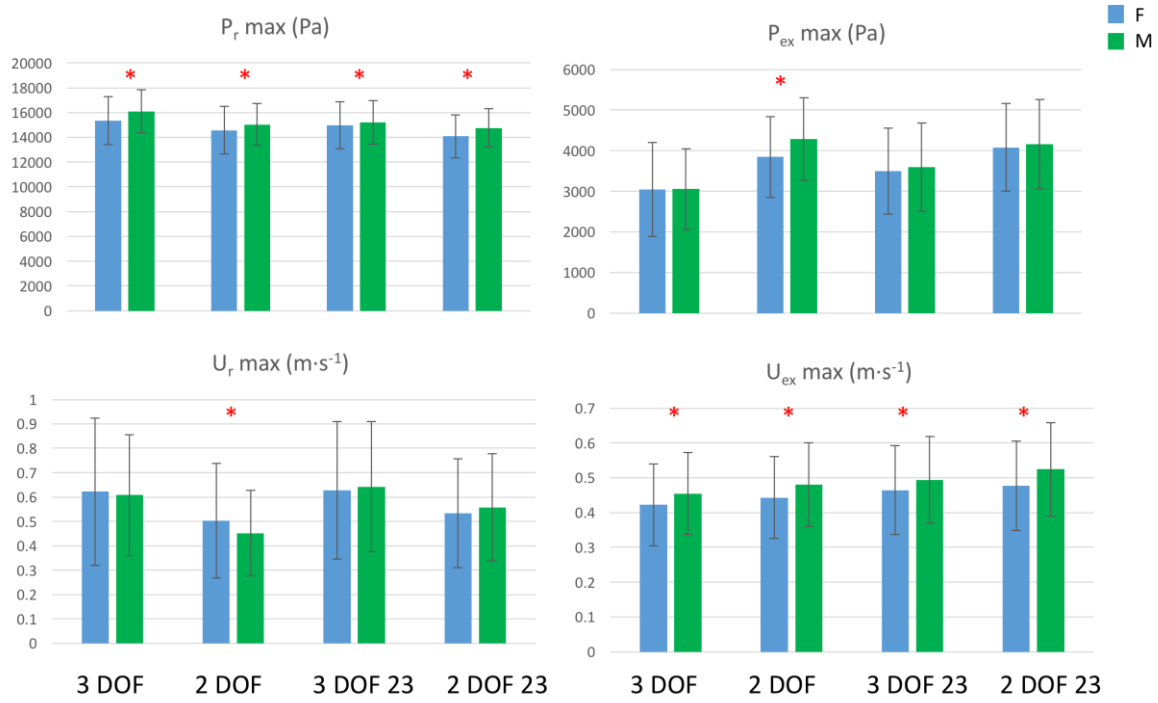

Figure 5.17: Comparisons of $P_r\ max$ (Top Left), $P_{ex}\ max$ (Top Right), $U_r\ max$ (Bottom Left) and $U_{ex}\ max$ (Bottom Right), between genders in all fitting settings. *: significant difference ($p<0.05$). Y-axis units are reported in each figure title. Values are reported as mean $\pm$ SD.

	3 DOF	2 DOF	3 DOF 23	2 DOF 23
P_r max	+4.9	+3.2	+1.6	+4.8
P_{ex} max	+0.3	+11.5	+2.7	+1.9
U_r max	-2.4	-10.0	+2.4	+4.5
U_{ex} max	+7.6	+8.5	+6.3	+9.7

Table 5.8: Percentage (%) variations of male values with respect to corresponding female values, for $P_r\ max, P_{ex}\ max, U_r\ max$ and $U_{ex}\ max$ in all settings.

5.4 Discussion

This study aimed to compare various common carotid hemodynamic and wave intensity parameters, using different fitting techniques for the calculation of the reservoir pressure and velocity waveforms. Two main quantitative analyses were carried out: a) studying the effects of varying fitting method, through the modification of the number of fixed and free-fitted parameters and of the length of the fitting window (Table 5.2); b) fixing P_∞ and studying how the specific value chosen for the analysis affected the waveforms.

The variation of fitting methods (DOF-Window analysis) brought substantial modifications to the calculated waveforms, as shown in Figures 5.1 and 5.2: for example, in a full window modality, $\bar{P}_n$ tended to significantly increase when free-fitted (+3%) with respect to the fixed (measured) value P_n, bringing a substantial negative region in P_{ex}. The change is not significant with a 23 window, because $\bar{P}_n$ tended to P_n for both DOF settings (Figure 5.1). On the contrary, $\bar{P}_n$ tended to significantly decrease when the window was shortened (-3%), although this is only true for 3 DOF, because in 2 DOF the dicrotic notch value was fixed. The differences in $\bar{P}_n$ are recapped in Figure 5.18. Nevertheless, the variation in window setting (from full to 23) brought a slight change in the shape of the reservoir waveform, even when the dicrotic notch value was fixed (Figure 5.2). These variations are mainly highlighted with the index PP_r (Eq. 5.8), because the differences between single points of corresponding waveforms are squared, then an average of those differences is calculated. In fact, the 23 window ensures an almost perfect match between measured pressure and reservoir waveform in the last two thirds of diastole, but leaves a big "gap" in the first diastolic third (Figure 5.1), compared to full diastolic window. The differences in gaps are more visible in Figure 5.2, where the 3 DOF 23 reservoir contour is closer to the dicrotic notch than the 3 DOF full reservoir contour.

The changes in the shape of both reservoir and excess waveforms affected hemodynamic and wave intensity parameters. Fixing the dicrotic notch for the reservoir pressure (2 DOF setting) generally brought a decrease in values of hemodynamic parameters directly involved with the fitting, such as $P_r\,max, P_\infty, b, PRI$ and $U_r\,max$. The variations were generally small (<10%), except for the diastolic time constant b (up to 38%) in full window and $U_r\,max$ for both window settings (up to 22%).

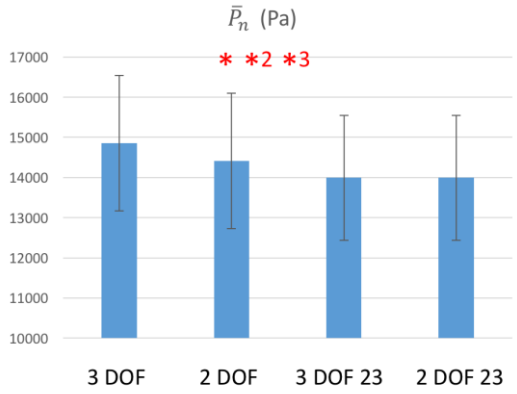

Figure 5.18: Comparison of $\bar{P}_n$ values among all fitting settings. *: significant difference between 3 DOF and 2 DOF in full window ($p<0.05$), *23: significant difference between 3 DOF and 2 DOF in 23 window, *2: significant difference between 2 DOF and 2 DOF 23, *3: significant difference between 3 DOF and 3 DOF 23. Y-axis units are reported in each figure title. Values are reported as mean $\pm$ SD.

Shortening the window length (from full to the last two thirds of diastole) caused a substantial increment of the fitting parameters (P_∞, b) up to 19% and 105%, respectively, as well as a modest increment for $U_r\,max$. $P_r\,max$ slightly decreased instead (up to 4%), whereas PRI did not significantly change. The variations brought by the change in window length were bigger, in general, than the variations occurred with a change in DOF.

Changes did not occur independently; in fact, for example, the relationship between the two diastolic fitting parameters (P_∞ and b) is a positive monotonic function, as it can be derived from the exponential decay in Eq. 5.2: for increasing P_∞ values, b has to increase [for a given data point $(\hat{P}_r, \hat{t})$]:

$$b = -\frac{1}{\hat{t} - T_N} \ln\left(\frac{\hat{P}_r - P_\infty}{\bar{P}_n - P_\infty}\right) \tag{5.11}$$

which is always positive, as $\hat{P}_r > \bar{P}_n$ when $\hat{t} > T_N$. Function (5.11) increases very slowly, except for the region in proximity of the vertical asymptote. When P_∞ is too big (for example, in the case of excessive positive variations in the P_∞-Variation analysis), b values become increasingly bigger.

The relationship between a and P_∞ is generally similar to that of b and is recapped in Figures 5.19 and 5.20: it tended to remain constant with negative variations of the asymptotical value and to significantly increase with positive variations. It also tended to significantly increase when $\bar{P}_n$ was free-fitted and to significantly decrease when the window was shortened, but only in 3 DOF.

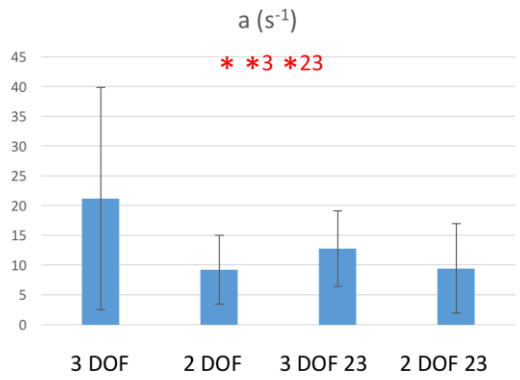

Figure 5.19: Comparison of a values among all fitting settings. *: significant difference between 3 DOF and 2 DOF in full window ($p<0.05$), *23: significant difference between 3 DOF and 2 DOF in 23 window, *2: significant difference between 2 DOF and 2 DOF 23, *3: significant difference between 3 DOF and 3 DOF 23. Y-axis units are reported in each figure title. Values are reported as mean $\pm$ SD.

Figures 5.11 – 5.15 show that an excessive increase of P_∞ is responsible for big unrealistic increases of almost all hemodynamic and wave intensity parameters, as demonstrated by the great standard deviations involved. However, this was not true for the reservoir pressure features, such as $P_r\ max$ and PRI, as well as the wave speed. Table 5.7 reports the actual P_∞ values used in the P_∞-Variation analysis. It is possible to understand from this table that asymptotical pressure values lesser than the reference R (from 12.2 $\pm$ 5.3 to 48.6 $\pm$ 21.0 mmHg), corresponding to the negative variations in the analysis, did not bring substantial changes to hemodynamic and wave intensity parameters, whereas P_∞ values greater than R (from 60.8 $\pm$ 26.2 to 97.2 $\pm$ 41.8 mmHg) brought significant changes and high standard deviations for most of the analysed parameters.

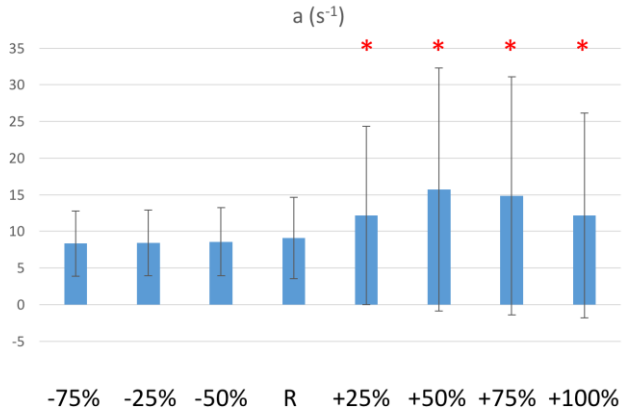

Figure 5.20: Comparison of a values among positive (+25%, +50%, +75%, +100%) and negative (-25%, -50%, -75%) variations of P_∞, with respect to the reference value (R) extracted from 2 DOF full window setting. *: significant difference with respect to R ($p<0.05$). Y-axis units are reported in each figure title. Values are reported as mean $\pm$ SD.

P_∞ Variation (w.r.t.R)	P_∞ Value (mmHg)
-75%	12.2 ± 5.3
-50%	24.4 ± 10.5
-25%	36.4 ± 15.7
0% (R)	48.6 ± 21.0
+25%	60.8 ± 26.2
+50%	72.9 ± 31.4
+75%	85.0 ± 36.6
+100%	97.2 ± 41.8

Table 5.9: Actual asymptotical pressure values corresponding to P_∞ percentage variations used in the P_∞-Variation analysis (n=1037). w.r.t.R: with respect to the reference (R). Values are reported as mean $\pm$ SD.

Wave intensity parameters calculated with the (measured) PU loop exhibited greater values than corresponding variables calculated with excess (P_{ex} and U_{ex}) components, as reported in Table 5.3. This is in agreement with Borlotti et al. (2015), who performed wave intensity analysis using excess pressure components in the canine aorta. In the present study, however, also the wave separation of U was implemented and wave intensity calculations using U_{ex} were performed. Remarkably, wave speed values did not substantially change with fitting methods and P_∞ variations, suggesting that it seems insensitive to them, whereas $P_{ex}\ max$, PEI and $U_{ex}\ max$ significantly changed in both analyses. This is not true for wave intensity parameters, that generally experienced a significant decrement when $\bar{P}_n$ was

free-fitted, rather than fixed (3 DOF vs. 2 DOF) and a significant increment when the window was shortened (from full to 23 window).

As pointed out by Borlotti et al. (2015), the wave speed should not change when measured in a specific vessel using different techniques. In fact, wave speed did change using $P_{ex}U_{ex}$ loop compared to PU loop, but did not experience any variation using alternative fitting methods, in the present study. A gold standard technique for the determination of the local wave speed has not been established yet (Borlotti et al. 2015), although it is important to consider that, if the reservoir pressure is made up of forward and backward waves produced by the reflection and re-reflection of the waves generated by the ventricle (Borlotti et al. 2015), the excess component is able to better satisfy the assumption behind the PU-loop technique, that only forward waves should be accounted. However, Mynard et al. (2012) stated that the reservoir-wave approach is able to introduce errors in the calculation of both reflected compression waves and forward expansion waves, using computational and animal data (taken from the aorta), thus likely introducing errors in the estimation of wave speed.

Bia et al. (2011) stated that, as reservoir pressure is related to systemic properties and its changes are the result of a combination of systemic variations, the excess pressure is more useful for assessing local responses. Thus, the use of excess pressure seems reasonable in the context of local studies, especially when wave intensity parameters are involved. The use of excess velocity waveform, however, is very limited in literature, but should be considered for local wave intensity analysis, especially because the reservoir component may be affected by reflected and re-reflected wavelets, masking the local effects. The only available method for the calculation of the reservoir and excess components of velocity is given by Aguado-Sierra, Alastruey, et al. (2008) and is strictly dependent upon the calculation of the pressure components. It is not possible to state, at this stage, which technique, between $P_{ex}U_{ex}$ loop or $P_{ex}U$ loop, is more reliable, and it would require a different investigation outside the scope of the present study.

The use of different fitting techniques also brought differences in correlation results between reservoir / excess components and age. Bia et al. (2011) reported a significant correlation between $P_r\ max$ and age, with a slope of +6.7 mmHg/decade in a cohort of 43 healthy subjects, aged 20-69 years. Their fitting settings were based on a window as wide as the last 1/3 of diastole and on a fixed dicrotic notch value for the reservoir pressure. Slope values were +5.6 mmHg/decade with a full window and only +3.9 mmHg/decade for the 23 window setting. This result does not agree with Davies et al. (2010) who reported a slope of +9.9 mmHg/decade in a cohort of 15 healthy subjects (53 ± 10 yr). They calculated the reservoir components in the same way as Wang et al. (2003), with the last two thirds of diastole used as fitting window and a fixed dicrotic notch for P_r.

Because of the differences in hemodynamic parameters, with age and between genders, brought by different fitting techniques on the same population, it is important to specify the fitting method used in a study, in order to make meaningful and coherent comparisons of clinical relevance. Generally, the 2 DOF full setting brought the greatest differences, with respect to the other techniques (Figures 5.16 and 5.17).

5.4.1 Limitations

As highlighted in the 'Material and Methods' section, pressure and velocity measurements were not taken simultaneously, but sequentially. However, rapid physiological perturbations were not involved in this study and the time interval between recordings was short (Borlotti et al. 2012); therefore, it can be assumed that the hemodynamic parameters did not change significantly between recordings.

Although in literature another window size is used for the fitting of the reservoir pressure waveform, namely the last third (1/3) of diastole (as specified in the 'Introduction'), it was not considered in this work, as it was believed that a further comparison, between 2/3 and 1/3 of diastole, was not necessary at this stage. Further studies would be able to highlight the differences in hemodynamic and wave intensity parameters between those two settings.

5.5 Conclusions

This quantitative study of hemodynamic and wave intensity parameters, under different fitting techniques for the reservoir pressure and velocity, demonstrated that the fitting method could bring significant variations in values and trends. Despite the changes in the shape of the reservoir waveform, its peak and time integral tended to remain constant in this study. This is an important feature, because both $P_r.max$ and PRI can be used in clinical settings for the calculation of diagnostic indicators, such as the aortic augmentation index. The reservoir and excess velocity peaks, instead, changed more significantly. This outcome, together with the concomitant substantial change in excess pressure peak and integral, may greatly affect wave intensity parameters. Wave intensity analysis, in fact, was significantly more sensitive to fitting techniques than pressure parameters. On the contrary, the wave speed did not substantially change and seemed to be insensitive to fitting techniques.

The P_∞-Variation Analysis revealed that the underestimation (up to -75%) of the asymptotical value (with respect to a reference obtained with 2 DOF full fitting and corresponding to 48.6 $\pm$ 21 mmHg) did not bring any substantial change in both

hemodynamic and wave intensity parameters, whereas its overestimation (from +25% to +100%) brought unrealistic increases of relevant parameters, as well as big standard deviations. Nevertheless, reservoir pressure features and wave speed seemed insensitive to this analysis.

Chapter 6: General Discussions and Conclusions

The work presented in this thesis deals with important issues related to the non-invasive determination of wave intensity parameters. Sugawara et al. (2000) found a linear relationship between common carotid pressure and diameter in patients, introducing the possibility to scale the measured diameter waveform against distally-recorded pressure values. Niki et al. (2002) applied this technique to perform carotid wave intensity analysis. In the same year, Zambanini et al. (2002) used applanation tonometry to perform the same type of investigation. However, the development of the DU approach by Feng & Khir (2010) unfolded the possibility to calculate wave intensity parameters from direct and simultaneous diameter and velocity waveforms. The pressure waveform was then replaced by the diameter and wave intensity was expressed as product of dD and dU, instead of dP and dU.

Therefore, the DU approach is suitable for the investigation of rapid physiological perturbations and for the measurement of wave intensity under rapidly-varying exercise workrates. Although the DU approach has been tested both in vitro and in vivo (Feng & Khir 2010; Li & Khir 2011; Borlotti et al. 2012), a reproducibility analysis of this technique under physiological perturbations was lacking.

The aim of the study in Chapter 3 was to assess the reproducibility of common carotid hemodynamic and wave intensity parameters using the DU approach, on a cohort of young healthy subjects, at rest and during exercise. Diameter variables exhibited higher intra-class correlation coefficients (ICCs) and lower dispersion than corresponding velocity variables, whereas local wave speed was overall reproducible. Among wave intensity parameters, energy variables exhibited higher ICCs and lower dispersion than corresponding peak variables. Finally, the majority of variables exhibited higher ICCs and lower dispersion during exercise compared to rest. Therefore, measurements of common carotid diameter and blood flow velocity, as well as DU-derived wave intensity parameters, are fairly reproducible, both at rest and during submaximal semi-recumbent exercise, for a cohort of young healthy participants. This outcome opens up new possibilities for non-invasive studies of cardiovascular properties.

For this reason, the DU approach was used in Chapter 4 to investigate physiological changes in carotid wave intensity in healthy humans, under different exercise workrates and subsequent recovery. It was possible to calculate surrogate indices of local vascular resistance, of the distensibility of the vessel, as well as wave intensity parameters that provided insight into cardiac dynamics under different conditions. It was found that the carotid artery substantially stiffened as exercise workrates increased, whilst peak and energy

of the forward (FCW) and backward (BCW) compression waves also increased, as ventricular contractility was enhanced, leading to larger reflections from the head microcirculation. However, the reflection indices remained unchanged from rest to exercise, highlighting that the increased magnitude of reflections was mainly due to the enhanced contractility, rather than changes in vascular resistance, at least at the common carotid artery. The forward expansion wave (FEW) also increased during exercise, as the left ventricle actively decelerated blood flow in late systole, potentially improving filling time during diastole. In the early recovery, the magnitude of all those waves returned to baseline value. Finally, the X wave, attributed to the reflection of BCW, had a tendency to increase during exercise and to decrease to baseline value in early recovery. For the first time, the main wave intensity peaks (FCW, BCW, FEW), as well as the mid-systolic X wave, were measured under different exercise workrates using only measured diameter and velocity waveforms at the carotid artery, enabling the non-invasive evaluation of cardiac performance and local vascular changes at sub-beat temporal resolution.

The reservoir-wave approach was first developed by Wang et al. (2003) to separate, from the pressure waveform, the component solely due to the reservoir volume, for the correct evaluation of backward- and forward-travelling waves. This theoretical framework, developed for the aorta, was later expanded to the central arteries by Aguado-Sierra, Alastruey, et al. (2008), who also introduced the reservoir-wave approach for the velocity waveform. A number of issues, however, still remains, involving specifically the lack of consensus over the fitting technique and the asymptotic pressure value (P_∞) used for the determination of the reservoir waveform; therefore, in the pursuit of future development of a hybrid reservoir-wave approach for the diameter, a study aimed to compare various common carotid hemodynamic and wave intensity parameters using different fitting techniques and P_∞ values, for the calculation of the reservoir pressure and velocity waveforms, was performed and described in Chapter 5 of this thesis.

Two quantitative analyses are presented in Chapter 5: a) the effects of varying fitting method, through the modification of both the number of free-fitted parameters and of the length of the fitting window; b) the effect of varying P_∞ by specific percentages for the determination of the reservoir waveform.

This study demonstrated that the fitting method could bring significant variations in values and trends of hemodynamic and wave intensity parameters. However, despite the changes in the shape of the reservoir pressure waveform, its peak and time integral tended to remain constant in this study. This is an important feature, because both reservoir pressure peak and integral have been used in clinical settings for the calculation of diagnostic indicators, such as the aortic augmentation index. The reservoir and excess velocity peaks, instead, changed more significantly. This outcome, together with the concomitant substantial

change in excess pressure peak and integral, may greatly affect wave intensity parameters. Wave intensity analysis, in fact, was significantly more sensitive to fitting techniques than pressure parameters. Finally, the wave speed did not substantially change with fitting methods. This outcome is also important, because the calculation of local vessel distensibility and/or compliance relies upon the wave speed measurement and seems insensitive to fitting techniques.

The second analysis, on the effects of varying P_{∞}, revealed that the underestimation (up to -75%) of the asymptotical value (with respect to a reference corresponding to 48.6 $\pm$ 21 mmHg; details in Chapter 5) did not bring any substantial change in both hemodynamic and wave intensity parameters, whereas its overestimation (from +25% to +100% of the reference) brought unrealistic increases of relevant parameters, as well as big standard deviations. Nevertheless, reservoir pressure features (its peak and time integral) and wave speed seemed insensitive to this analysis.

6.1 Advantages and limitations of the DU approach

As explained in Chapter 1, wave intensity analysis is a mathematical tool able to decompose arterial waves in the time domain. It is easy and fast to compute, especially with modern digitally acquired data. It only needs measurements at a single site and can be performed non-invasively. Wave intensity analysis requires recordings of P and U, or D and U. The DU approach does not account for the pressure waveform and it relies only upon D and U measurements. Although the forward components always make a positive contribution to wave intensity, and backward components a negative contribution, it may be difficult to assess both by only analysing the net wave intensity, especially if the two components have similar magnitude and cancel each other out during a specific time interval. The assumption of linearity allows further investigation and a complete separation of the forward and backward waves. In order to perform wave intensity separation in forward and backward components, local wave speed c must be known, whereas in order to perform reservoir-wave separation, a specific fitting technique must be chosen, giving that it is not possible to apply this separation to the diameter waveform yet.

The clinical usefulness of WIA has been proved by many studies, highlighted in Chapter 1 [such as Sugawara et al. (2009)] but still a lot of research needs to be done. As pointed out by Cameron (2009): *"rather than making excessive inference from small underpowered sub-studies of larger trials which were designed to test different hypotheses, we must await properly designed randomized, prospective, and longitudinal trials (having*

baseline data) with entry criteria determined on the basis of hemodynamic parameters and with appropriately chosen end points".

Below is a more detailed list of the advantages and disadvantages of the DU approach, most of them shared by the standard (PU) wave intensity analysis.

6.1.1 Advantages

- Because the DU approach, and the wave intensity analysis in general, are carried out in the time domain, information about single events brought by each individual wavelet can be immediately extracted from the time series;
- It is very easy and fast to perform wave intensity analysis on digitally acquired data off-line, or on-line on some specific machines;
- Due to the possibility to be performed in several locations of the body, the DU approach, and the wave intensity analysis in general, can be virtually measured in all different types of patients, which open the doors of a future clinical setting;
- The DU analysis can be easily performed non-invasively with ultrasound machines, which is widely available in the clinic. It can also be performed using MRI (Li et al. 2010; Biglino et al. 2012);
- The DU approach does not require additional equipment, such as cuff-type manometers or tonometers, and can be performed entirely independent of pressure measurements.

6.1.2 Limitations

- Measurements of local wave speed, essential for the wave separation, are challenging, but several one-point (local) methods were developed in the research environment, which assume an early systolic, reflection-free period to exist in the cardiac cycle. This is a reasonable assumption in large and central arteries, but it becomes inaccurate in small and peripheral vessels such as coronaries (Davies et al. 2006). Furthermore, the presence of bifurcations or change of geometric and/or elastic properties across the vessels could bring inaccuracies on the estimation of wave speed (Li et al. 2011; Borlotti et al. 2014) and the simultaneous measurements of P, D, U at the same location, which is challenging in the clinical settings, may be needed to overcome this problem (Segers et al. 2014);

- The one-dimensional approximation that characterizes wave intensity analysis in general ignores the distribution of pressure and velocity over the cross-sectional area of the vessel and only takes account of their axial behaviour;
- The wave separation into forward and backward components requires the assumption of linearity. However, the context of arterial hemodynamics (with very low Mach number) and the possibility to acquire data at high sampling rate make the linearized theory accurate and not significantly different from the non-linearized theory (Parker 2009);
- The calculation of dI from incremental differences dD (or dP) and dU makes the quantity sensitive to noise. Proper filter settings have to be applied to the measured waveforms before taking the simple differences;
- The calculation of dI depends upon the sampling time: by doubling the sampling time, for example, the differences dD (or dP) and dU double, increasing the magnitude of dI four-fold. To take account of this effect, wave intensity values can be only compared when the same sampling time is taken, or by considering, for the PU case, the alternative definition $dI' = \frac{dP}{dt}\frac{dU}{dt}$.

6.2 Conclusions

The work presented in this thesis demonstrated that the DU approach is qualified for the investigation of rapid physiological changes through wave intensity analysis, as it is a reproducible technique in healthy humans and is able to track changes in hemodynamic and wave intensity parameters during different exercise workrates and recovery. In particular, the effects of incremental exercise upon the main wave intensity peaks and reflection indices were studied in this thesis. In the context of reservoir-wave separation of pressure and velocity waveforms, wave intensity parameters seem to be affected by the specific fitting technique used. It is reasonable to believe that also the DU-derived wave intensity parameters would be affected by the fitting method; therefore, further studies are needed to set up a standard for the reservoir-wave separation.

6.3 Limitations of the Thesis

In the context of the studies involving reproducibility of WI parameters (Chapter 3) and CCA WIA under incremental exercise (Chapter 4), the ensemble averaging process was

not used, although is more common in the analysis of ultrasound measurements. It is believed it could lead to miscalculations of wave speed values, which are strictly dependent on the early upstroke of the waveforms; consequently, it can lead to erroneous estimates of WI parameters. Therefore, it was chosen to calculate all the parameters from individual cardiac cycles and then average the results. This method may have contributed to lower theoretical reproducibility values. On the other hand, the wave speed derived from the lnDU loop has been derived visually from the optimal linear fit over the early systolic part of the loop. Although repeating the calculations manually gave very similar results, the possibility exists that the use of an automatic linear regression algorithm would reduce the inter-observer variability. However, as highlighted in Chapter 3, a drawback associated with the use of an automatic linear regression algorithm could be the assessment of a proper "linearity threshold", which may in turn be dataset dependent (Khir et al. 2007). Furthermore, the limited number of participants (12 in the reproducibility study and 8 in the exercise WIA) could have affected the outcome of the statistical analysis. Nevertheless, it is believed that even such a small cohort was representative of the main physiological features presented here. Finally, the calculation of MAP in Chapter 4 was based on the formula: MAP = 1/3 SBP + 2/3 DBP, which has its validity in rest condition, whereas the systolic and diastolic time fractions within the cardiac cycle change during exercise. However, the monitoring device (based on photo-plethysmography) used in this study did not record the entire pressure waveform or the time fractions; therefore, it was impossible to assess MAP by properly integrating the curve and the aforementioned formula was used instead, bringing a slight underestimation of the MAP values at moderate-to-high exercise regime.

In the context of reservoir-wave approach (Chapter 5), pressure and velocity measurements were not taken simultaneously, but sequentially. However, rapid physiological perturbations were not involved and the time interval between recordings was short (Borlotti et al. 2012); therefore, it can be assumed that the hemodynamic parameters did not change significantly between recordings. Although in literature another window size is used for the fitting of the reservoir pressure waveform, namely the last third (1/3) of diastole, it was not considered in this work, because believed unnecessary at this stage. Further studies would be able to highlight the differences in hemodynamic and wave intensity parameters between 1/3 and 2/3 diastole settings.

6.4 Future Perspective

Possible future works, that are direct continuations of the studies presented in this thesis, are described in the following list:

- In this thesis, the DU approach was used to evaluate common carotid wave intensity parameters. However, to properly assess changes in the cerebral microvasculature with physiological perturbations, measurements at the internal carotid artery during exercise are needed. Therefore, a future study can involve the comparison of hemodynamic and wave intensity parameters between common and internal carotid artery, and it will be able to shed more light on the interaction of cardiac performance, cerebrovascular changes and wave intensity;

- The work presented in this thesis dealt with cardiovascular alterations to common carotid wave intensity parameters brought by incremental exercise performed by lower limbs; future studies can focus on the effects of exercise performed by upper limbs, that triggers different cardiovascular responses (Clausen 1977);

- In the context of the reservoir-wave approach, a diameter reservoir theory is needed, to properly quantify the reservoir volume contribution and the "excess" components when the DU approach is used. A comparison between PU-reservoir and DU-reservoir parameters for a similar cohort would follow.

List of references

Aguado-Sierra, J., Alastruey, J., Wang, J.-J., Hadjiloizou, N., Davies, J. and Parker, K. H. (2008) 'Separation of the reservoir and wave pressure and velocity from measurements at an arbitrary location in arteries.', *Proceedings of the Institution of Mechanical Engineers. Part H, Journal of engineering in medicine*, 222(August), pp. 403–416. doi: 10.1243/09544119JEIM315.

Aguado-Sierra, J., Davies, J., Hadjiloizou, N., Francis, D., Mayet, J., Hughes, A. and Parker, K. (2008) 'Reservoir-wave separation and wave intensity analysis applied to carotid arteries: a hybrid 1D model to understand haemodynamics.', *30th Annual International IEEE EMBS Conference*, (March), pp. 1381–1384. doi: 10.1109/IEMBS.2008.4649422.

Alastruey, J., Khir, A. W., Matthys, K. S., Segers, P., Sherwin, S. J., Verdonck, P. R., Parker, K. H. and Peiró, J. (2011) 'Pulse wave propagation in a model human arterial network: Assessment of 1-D visco-elastic simulations against in vitro measurements', *Journal of Biomechanics*, 44(12), pp. 2250–2258. doi: 10.1016/j.jbiomech.2011.05.041.

Allen J. (2007) 'Photoplethysmography and its application in clinical physiological measurement'. *Physiol Meas* 28(3): R1.

Anliker, M., Rockwell, R. L. and Ogden, E. (1971) 'Nonlinear analysis of flow pulses and shock waves in arteries', *Zeitschrift für angewandte Mathematik und Physik ZAMP*, 22(2), pp. 217–246. doi: 10.1007/BF01591407.

Arnett, D. K., Boland, L. L., Evans, G. W., Riley, W., Barnes, R., Tyroler, H. A. and Heiss, G. (2000) 'Hypertension and arterial stiffness: The atherosclerosis risk in communities study*', *American Journal of Hypertension*, 13(4), pp. 317–323. Available at: http://dx.doi.org/10.1016/S0895-7061(99)00281-2.

Babcock, M. C., Lefferts, W. K., Hughes, W. E., Fitzgerald, K. L., Leyer, B. K., Redmond, J. G. and Heffernan, K. S. (2015) 'Acute effect of high-intensity cycling exercise on carotid artery hemodynamic pulsatility', *European Journal of Applied Physiology*, 115(5), pp. 1037–1045. doi: 10.1007/s00421-014-3084-6.

Barnett, G. O., Mallos, A. J. and Shapiro, A. (1961) 'Relationship of aortic pressure and diameter in the dog', *Journal of Applied Physiology*, 16(3), p. 545 LP-548. Available at: http://jap.physiology.org/content/16/3/545.abstract.

Beales, L., Wolstenhulme, S., Evans, J. A., West, R. and Scott, D. J. A. (2011) 'Reproducibility of ultrasound measurement of the abdominal aorta', *British Journal of Surgery*, 98(11), pp. 1517–1525. doi: 10.1002/bjs.7628.

Benetos, A., Safar, M., Rudnichi, A., Smulyan, H., Richard, J.-L., Ducimetière, P. and Guize, L. (1997) 'Pulse Pressure', *Hypertension*, 30(6), p. 1410 LP-1415. Available at: http://hyper.ahajournals.org/content/30/6/1410.abstract.

Bergel, D. (1960) 'The visco-elastic properties of the arterial wall', *Doctoral dissertation*.

Bergel, D. (1961a) 'The dynamic elastic properties of the arterial wall', *The Journal of physiology*, 156(3), p. 458.

Bergel, D. (1961b) 'The static elastic properties of the arterial wall', *The Journal of physiology*, 156(3), p. 445.

Beyar, R., Yin, F. C., Hausknecht, M., Weisfeldt, M. L. and Kass, D. a (1989) 'Dependence of left ventricular twist-radial shortening relations on cardiac cycle phase.', *The American journal of physiology*, 257, pp. H1119–H1126.

Bia, D., Cymberknop, L., Zócalo, Y., Farro, I., Torrado, J., Farro, F., Pessana, F. and Armentano, R. L. (2011) 'Age-related changes in reservoir and excess components of central aortic pressure in asymptomatic adults', *Proceedings of the Annual International Conference of the IEEE Engineering in Medicine and Biology Society, EMBS*, 2, pp. 6454–6457. doi: 10.1109/IEMBS.2011.6091593.

Biglino, G., Schievano, S., Steeden, J. A., Ntsinjana, H., Baker, C., Khambadkone, S., De Leval, M. R., Hsia, T. Y., Taylor, A. M. and Giardini, A. (2012) 'Reduced ascending aorta distensibility relates to adverse ventricular mechanics in patients with hypoplastic left heart syndrome: Noninvasive study using wave intensity analysis', *Journal of Thoracic and Cardiovascular Surgery*. The American Association for Thoracic Surgery, 144(6), pp. 1307–1314. doi: 10.1016/j.jtcvs.2012.08.028.

Bland, J. M. and Altman, D. (1986) 'Statistical methods for assessing agreement between two methods of clinical measurement', *The lancet*. Elsevier, 327(8476), pp. 307–310.

Bland JM, Altman DG. (1995) 'Statistics Notes: Calculating correlation coefficients with repeated observations: Part 1 - correlation within subjects'. BMJ 310 (6977): 446.

Bland JM, Altman DG. (1995) 'Calculating correlation coefficients with repeated observations: Part 2 – correlation between subjects'. BMJ 310(6980): 633.

Bleasdale, R. a., Mumford, C. E., Campbell, R. I., Fraser, A. G., Jones, C. J. H. and Frenneaux, M. P. (2003) 'Wave intensity analysis from the common carotid artery: A new noninvasive index of cerebral vasomotor tone', *Heart and Vessels*, 18(4), pp. 202–206. doi: 10.1007/s00380-003-0711-2.

Borelli, G. (1680) *De Motu Animalium (translated as On the Movement of Animals, translated by Paul Maquet. Springer, Berlin, 1989)*.

Borlotti, A., Khir, A. W., Rietzschel, E. R., De Buyzere, M. L., Vermeersch, S. and Segers, P. (2012) 'Noninvasive determination of local pulse wave velocity and wave intensity: changes with age and gender in the carotid and femoral arteries of healthy human.', *Journal of applied physiology (Bethesda, Md. : 1985)*, 113(5), pp. 727–35. doi: 10.1152/japplphysiol.00164.2012.

Borlotti, A., Li, Y., Parker, K. H. and Khir, A. W. (2014) 'Experimental evaluation of local wave speed in the presence of reflected waves', *Journal of Biomechanics*, 47(1), pp. 87–95. doi: 10.1016/j.jbiomech.2013.10.007.

Borlotti, A., Park, C., Parker, K. H. and Khir, A. W. (2015) 'Reservoir and reservoir-less pressure effects on arterial waves in the canine aorta', *Journal of Hypertension*, 33(3), pp. 564–574. doi: 10.1097/HJH.0000000000000425.

Van Bortel, L. M., Balkestein, E. J., van der Heijden-Spek, J. J., Vanmolkot, F. H., Staessen, J. A., Kragten, J. A., Vredeveld, J. W., Safar, M. E., Boudier, H. A. S. and Hoeks, A. P. (2001) 'Non-invasive assessment of local arterial pulse pressure: comparison of applanation tonometry and echo-tracking', *Journal of hypertension*. LWW, 19(6), pp. 1037–1044.

Bramwell, J. C. and Hill, A. V. (1922) 'The velocity of the pulse wave in man', *Proceedings of the Royal Society of London*, 93(652), pp. 298–306.

Burattini, R. and Gnudi, G. (1982) 'Computer identification of models for the arterial tree

input impedance: Comparison between two new simple models and first experimental results', *Medical and Biological Engineering and Computing*, 20(2), pp. 134–144. doi: 10.1007/BF02441348.

Cameron, J. D. (2009) 'Wave intensity analysis and central blood pressure', *Hypertension*, 54(5), pp. 958–959. doi: 10.1161/HYPERTENSIONAHA.109.137638.

Carbone, G., Nakadate, R., Solis, J., Ceccarelli, M., Takanishi, A., Minagawa, E., Sugawara, M. and Niki, K. (2010) 'Workspace analysis and design improvement of a carotid flow measurement system', *Proceedings of the Institution of Mechanical Engineers, Part H: Journal of Engineering in Medicine*. SAGE Publications Sage UK: London, England, 224(11), pp. 1311–1323.

Clausen, J. P. (1977) 'Effect of physical training on cardiovascular adjustments to exercise in man.', *Physiological reviews*, 57(4), pp. 779–815. Available at: http://www.ncbi.nlm.nih.gov/pubmed/333481.

Connes P, Bouix D, Durand F, Kippelen P, Mercier J, Prefaut C, Caillaud C. (2004) 'Is hemoglobin desaturation related to blood viscosity in athletes during exercise? '. *Int J Sports Med* 25(08): 569-574.

Curtis, S. L., Zambanini, A., Mayet, J., McG Thom, S. a, Foale, R., Parker, K. H. and Hughes, A. D. (2007) 'Reduced systolic wave generation and increased peripheral wave reflection in chronic heart failure.', *American journal of physiology. Heart and circulatory physiology*, 293(1), pp. H557-62. doi: 10.1152/ajpheart.01095.2006.

Davies, J. E., Baksi, J., Francis, D. P., Hadjiloizou, N., Whinnett, Z. I., Manisty, C. H., Aguado-Sierra, J., Foale, R. a, Malik, I. S., Tyberg, J. V, Parker, K. H., Mayet, J. and Hughes, A. D. (2010) 'The arterial reservoir pressure increases with aging and is the major determinant of the aortic augmentation index.', *American journal of physiology. Heart and circulatory physiology*, 298(2), pp. H580–H586. doi: 10.1152/ajpheart.00875.2009.

Davies, J. E., Hadjiloizou, N., Leibovich, D., Malaweera, A., Alastruey-Arimon, J., Whinnett, Z. I., Manisty, C. H., Francis, D. P., Aguado-Sierra, J., Foale, R. A., Malik, I. S., Parker, K. H., Mayet, J. and Hughes, A. D. (2007) 'Importance of the aortic reservoir in determining the shape of the arterial pressure waveform - The forgotten lessons of Frank', *Artery Research*, 1(2), pp. 40–45. doi: 10.1016/j.artres.2007.08.001.

Davies, J. E., Whinnett, Z. I., Francis, D. P., Manisty, C. H., Aguado-Sierra, J., Willson, K., Foale, R. A., Malik, I. S., Hughes, A. D., Parker, K. H. and Mayet, J. (2006) 'Evidence of a dominant backward-propagating "suction" wave responsible for diastolic coronary filling in humans, attenuated in left ventricular hypertrophy', *Circulation*, 113(14), pp. 1768–1778. doi: 10.1161/CIRCULATIONAHA.105.603050.

Davies, J. E., Whinnett, Z. I., Francis, D. P., Willson, K., Foale, R. a, Malik, I. S., Hughes, A. D., Parker, K. H. and Mayet, J. (2006) 'Use of simultaneous pressure and velocity measurements to estimate arterial wave speed at a single site in humans.', *American journal of physiology. Heart and circulatory physiology*, 290(2), pp. H878-85. doi: 10.1152/ajpheart.00751.2005.

Deane, C. R. and Markus, H. S. (1997) 'Colour velocity flow measurement: in vitro validation and application to human carotid arteries', *Ultrasound in medicine & biology*. Elsevier, 23(3), pp. 447–452.

Drzewiecki, G. M., Melbin, J. and Noordergraaf, A. (1983) 'Arterial tonometry: Review and analysis', *Journal of Biomechanics*, 16(2), pp. 141–152. doi: 10.1016/0021-9290(83)90037-4.

Esper, S. A., Pinsky, M. R. and Care, C. (2014) 'Best Practice & Research Clinical Anaesthesiology Arterial waveform analysis', 28, pp. 363–380.

Euler, L. (1775) 'Principia pro motu sanguinis per arterias determinando', *Opera posthuma mathematica et physica anno 1844 detecta*.

Feng, J. and Khir, A. (2010) 'Determination of wave speed and wave separation in the arteries using diameter and velocity', *Journal of Biomechanics*, 43, pp. 455–462.

Feng, J. and Khir, A. W. (2010) 'Determination of wave speed and wave separation in the arteries using diameter and velocity', *Journal of Biomechanics*, 43(3), pp. 455–462. doi: 10.1016/j.jbiomech.2009.09.046.

Fletcher, G. F., Ades, P. A., Kligfield, P., Arena, R., Balady, G. J., Bittner, V. A., Coke, L. A., Fleg, J. L., Forman, D. E. and Gerber, T. C. (2013) 'Exercise standards for testing and training', *Circulation*. Am Heart Assoc, 128(8), pp. 873–934.

Flewitt, J. A., Hobson, T. N., Wang Jr., J., Johnston, C. R., Shrive, N. G., Belenkie, I., Parker, K. H. and Tyberg, J. V (2007) 'Wave intensity analysis of left ventricular filling: application of windkessel theory', *Am J Physiol Heart Circ Physiol*, 292(6), pp. H2817-23. doi: 10.1152/ajpheart.00936.2006.

Fok, H., Guilcher, A., Li, Y., Brett, S., Shah, A., Clapp, B. and Chowienczyk, P. (2014) 'Augmentation pressure is influenced by ventricular contractility/relaxation dynamics novel mechanism of reduction of pulse pressure by nitrates', *Hypertension*, 63(5), pp. 1050–1055. doi: 10.1161/HYPERTENSIONAHA.113.02955.

Frank, O. (1899) 'Die Grundform des Arteriellen Pulses', *Z Biol*, 37, pp. 483–526.

Frank, O. (1920) 'Die Elastizita¨t der Blutegefa¨sse', *Z Biol*, 71, pp. 255–272.

Franklin, S. S., Jacobs, M. J., Wong, N. D., L'Italien, G. J. and Lapuerta, P. (2001) 'Predominance of Isolated Systolic Hypertension Among Middle-Aged and Elderly US Hypertensives', *Hypertension*, 37(3), p. 869 LP-874. Available at: http://hyper.ahajournals.org/content/37/3/869.abstract.

Franklin, S. S., Pio, J. R., Wong, N. D., Larson, M. G., Leip, E. P., Vasan, R. S. and Levy, D. (2005) 'Predictors of new-onset diastolic and systolic hypertension: The framingham heart study', *Circulation*, 111(9), pp. 1121–1127. doi: 10.1161/01.CIR.0000157159.39889.EC.

Fujimoto, S., Mizuno, R., Saito, Y. and Nakamura, S. (2004) 'Clinical application of wave intensity for the treatment of essential hypertension', *Heart and Vessels*, 19(1), pp. 19–22. doi: 10.1007/s00380-003-0725-9.

Hagen, G. (1839) 'On the motion of water in narrow cylindrical tubes', *Pogg. Ann.*, 46, pp. 423–442.

Hagenbach, E. (1860) 'Ueber die Bestimmung der Zähigkeit einer Flüssigkeit durch den Ausfluss aus Röhren', *Annalen der Physik*, 185(3), pp. 385–426.

Hales, S. (1733) *Statical Essays: contining Haemastaticks*.

Hall, J. E. (2015) *Guyton and Hall textbook of medical physiology*. Elsevier Health Sciences.

Harms MP, Wesseling KH, Pott F, Jenstrup M, Van Goudoever J, Secher NH, Van Lieshout JJ. (1999) 'Continuous stroke volume monitoring by modelling flow from non-invasive measurement of arterial pressure in humans under orthostatic stress'. *Clin Sci* 97: 291-301.

Harvey, W. (1628) *Exercitatio Anatomica De Motu Cordis et Sanguinis in Animalibus (translated as movement of the heart and blood in animals by K.J. Franklin, Blackwell, Oxford, 1957)*. 1628th edn. Frankfurt am Main. doi: 10.1017/CBO9781107415324.004.

Hatano, S., Nobuoka, S., Aono, J., Nagashima, J., Tokuoka, S., Ozawa, Y., Mitsuya, N. and Miyake, F. (2002) 'Influence of Hot Water Bathing on Reflection Pressure Wave. Analysis by noninvasive measurement of wave intensity', *J Jpn Soc Balneol Climatol Phys Med*, 65(2), pp. 83–88.

Heffernan, K. S. and Lefferts, W. K. (2013) 'A New Exercise Central Hemodynamics Paradigm', *Hypertension*. Am Heart Assoc, 62(5), pp. e35–e35.

Hellstrom, G., Fischer-Colbrie, W., Wahlgren, N. G. and Jogestrand, T. (1996) 'Carotid artery blood flow and middle cerebral artery blood flow velocity during physical exercise', *Journal of applied physiology*, 81, pp. 413–418.

Hess, W. R. (1917) 'Über die periphere Regulierung der Blutzirkulation', *Pflüger's Archiv für die gesamte Physiologie des Menschen und der Tiere*. Springer, 168(9–12), pp. 439–490.

Hoaglin, D. C. and Iglewicz, B. (1987) 'Fine-tuning some resistant rules for outlier labeling', *Journal of the American Statistical Association*. Taylor & Francis, 82(400), pp. 1147–1149.

Hoaglin, D. C., Iglewicz, B. and Tukey, J. W. (1986) 'Performance of some resistant rules for outlier labeling', *Journal of the American Statistical Association*. Taylor & Francis Group, 81(396), pp. 991–999.

Hollander, E. H., Wang, J. J., Dobson, G. M., Parker, K. H. and Tyberg, J. V (2001) 'Negative wave reflections in pulmonary arteries.', *American journal of physiology. Heart and circulatory physiology*, 281(2), pp. H895-902. Available at: http://www.ncbi.nlm.nih.gov/pubmed/11454596.

Hughes, A. D., Park, C., Davies, J., Francis, D., McG Thom, S. A., Mayet, J. and Parker, K. H. (2013) 'Limitations of Augmentation Index in the Assessment of Wave Reflection in Normotensive Healthy Individuals', *PLoS ONE*, 8(3), pp. 1–8. doi: 10.1371/journal.pone.0059371.

Hughes, D. J., Babbs, C. F., Geddes, L. A. and Bourland, J. D. (1979) 'Measurements of Young's modulus of elasticity of the canine aorta with ultrasound', *Ultrasonic Imaging*, 1(4), pp. 356–367. doi: 10.1016/0161-7346(79)90028-2.

Ide, K. and Secher, N. H. (2000) 'Cerebral blood flow and metabolism during exercise.', *Progress in neurobiology*, 61(4), pp. 397–414. doi: 10.1152/japplphysiol.00853.2007.

Jcgm, J. C. F. G. I. M. (2008) 'Evaluation of measurement data — Guide to the expression of uncertainty in measurement', *International Organization for Standardization Geneva ISBN*, 50(September), p. 134. doi: 10.1373/clinchem.2003.030528.

Jones, C. J. H., Sugawara, M., Kondoh, Y., Uchida, K. and Parker, K. H. (2002) 'Compression and expansion wavefront travel in canine ascending aortic flow: Wave intensity analysis', *Heart and Vessels*, 16(3), pp. 91–98. doi: 10.1007/s003800200002.

Jones, C. J., Parker, K. H., Hughes, R. and Sheridan, D. J. (1992) 'Nonlinearity of human arterial pulse wave transmission.', *Journal of biomechanical engineering*, 114(1), pp. 10–14.

Karamanou, M., Stefanadis, C., Tsoucalas, G., Laios, K. and Androutsos, G. (2015)

‘Historical Perspective Galen’s (130-201 AD) Conceptions of the Heart’, *Hellenic J Cardiol*, 56, pp. 197–200.

Khir, A. W., O’Brien, A., Gibbs, J. S. R. and Parker, K. H. (2001) ‘Determination of wave speed and wave separation in the arteries using diameter and velocity’, *Journal of Biomechanics*, 34, pp. 1145–1155. doi: 10.1016/j.jbiomech.2009.09.046.

Khir, A. W., Swalen, M. J. P., Feng, J. and Parker, K. H. (2007) ‘Simultaneous determination of wave speed and arrival time of reflected waves using the pressure-velocity loop’, *Medical and Biological Engineering and Computing*, 45(12), pp. 1201–1210. doi: 10.1007/s11517-007-0241-7.

Korteweg, D. (1878) ‘Ueber die Fortpflanzungsgeschwindigkeit des Schalles in elastischen Röhren’, *Annalen der Physik*, 241(12), pp. 525–42.

Laurent, S., Boutouyrie, P., Asmar, R., Gautier, I., Laloux, B., Guize, L., Ducimetiere, P. and Benetos, A. (2001) ‘Aortic stiffness is an independent predictor of all-cause and cardiovascular mortality in hypertensive patients.’, *Hypertension (Dallas, Tex. : 1979)*, 37(5), pp. 1236–1241. doi: 10.1161/01.HYP.37.5.1236.

Laurent, S., Katsahian, S., Fassot, C., Tropeano, A. I., Gautier, I., Laloux, B. and Boutouyrie, P. (2003) ‘Aortic stiffness is an independent predictor of fatal stroke in essential hypertension’, *Stroke*, 34(5), pp. 1203–1206. doi: 10.1161/01.STR.0000065428.03209.64.

Li, Y., Borlotti, A., Hickson, S. S., McEniery, C. M., Wilkinson, I. B. and Khir, A. W. (2010) ‘Using magnetic resonance imaging measurements for the determination of local wave speed and arrival time of reflected waves in human ascending aorta’, *2010 Annual International Conference of the IEEE Engineering in Medicine and Biology Society, EMBC’10*, pp. 5153–5156. doi: 10.1109/IEMBS.2010.5626183.

Li, Y., Borlotti, A., Parker, K. H. and Khir, A. W. (2011) ‘Variation of wave speed determined by the PU-loop with proximity to a reflection site’, *Proceedings of the Annual International Conference of the IEEE Engineering in Medicine and Biology Society, EMBS*, (1), pp. 199–202. doi: 10.1109/IEMBS.2011.6090032.

Li, Y. and Guo, L. (2013) ‘Clinical value of carotid wave intensity analysis for differentiating nonobstructive hypertrophic cardiomyopathy from left ventricular hypertrophy secondary to systemic hypertension’, *Journal of Clinical Ultrasound*, 41(3), pp. 151–157. doi: 10.1002/jcu.22012.

Li, Y. and Khir, A. W. (2011) ‘Experimental validation of non-invasive and fluid density independent methods for the determination of local wave speed and arrival time of reflected wave’, *Journal of Biomechanics*, 44(7), pp. 1393–1399. doi: 10.1016/j.jbiomech.2010.12.019.

Lighthill, M. (1978) *Waves in fluids*. Cambridge, Cambridge.

Manisty, C. H., Zambanini, A., Parker, K. H., Davies, J. E., Francis, D. P., Mayet, J., McG Thom, S. A. and Hughes, A. D. (2009) ‘Differences in the magnitude of wave reflection account for differential effects of amlodipine- versus atenolol-based regimens on central blood pressure: An anglo-scandinavian cardiac outcome trial substudy’, *Hypertension*, 54(4), pp. 724–730. doi: 10.1161/HYPERTENSIONAHA.108.125740.

Manisty, C., Mayet, J., Tapp, R. J., Parker, K. H., Sever, P., Poulter, N. H., Thom, S. A. M. and Hughes, A. D. (2010) ‘Wave Reflection Predicts Cardiovascular Events in Hypertensive Individuals Independent of Blood Pressure and Other Cardiovascular Risk Factors. An ASCOT (Anglo-Scandinavian Cardiac Outcome Trial) Substudy’, *Journal of the American*

College of Cardiology. Elsevier Inc., 56(1), pp. 24–30. doi: 10.1016/j.jacc.2010.03.030.

Manisty, C., Mayet, J., Tapp, R. J., Sever, P. S., Poulter, N., Simon, S. A. and Hughes, A. D. (2009) 'Atorvastatin treatment is associated with less augmentation of the carotid pressure waveform in hypertension: A substudy of the anglo-scandinavian cardiac outcome trial (ASCOT)', *Hypertension*, 54(5), pp. 1009–1013. doi: 10.1161/HYPERTENSIONAHA.109.130914.

Matthys, K., Vanhercke, D., Van Aken, S., De Groote, K., Coomans, I. and Verdonck, P. (2002) 'Non-invasive Assessment of Hemodynamics in Adolescents with Arterial Tonometry and Doppler Ultrasound during a Conventional Stress Test', *Computers in Cardiology*, IEEE, pp. 517–520.

Matthys, K. and Verdonck, P. (2002) 'Development and modelling of arterial applanation tonometry: a review', *Technology and Health Care*, 10(1), pp. 65–76.

Mcdonald, D. (1952) 'The occurrence of turbulent flow in the rabbit aorta', *J Physiol*, 118, pp. 340–347.

Mcdonald, D. A. (1955) 'the Relation of Pulsatile Pressure To Flow in Arteries', *J. Physiol.*, I27, pp. 533–552. doi: 10.1113/jphysiol.1955.sp005275.

Meinders, J. M. and Hoeks, A. P. G. (2004) 'Simultaneous assessment of diameter and pressure waveforms in the carotid artery', *Ultrasound in Medicine and Biology*, 30(2), pp. 147–154. doi: 10.1016/j.ultrasmedbio.2003.10.014.

Miao, D. M., Ye, P., Zhang, J. Y., Gao, P. and Xiao, W. K. (2011) 'Clinical usefulness of carotid arterial wave intensity in noninvasively assessing left ventricular performance in different hypertensive remodeling hearts', *Zhongguo ying yong sheng li xue za zhi= Zhongguo yingyong shenglixue zazhi= Chinese journal of applied physiology*, 27(2), pp. 136–139.

Mitchell, G. F., van Buchem, M. A., Sigurdsson, S., Gotal, J. D., Jonsdottir, M. K., Kjartansson, Ó., Garcia, M., Aspelund, T., Harris, T. B. and Gudnason, V. (2011) 'Arterial stiffness, pressure and flow pulsatility and brain structure and function: the Age, Gene/Environment Susceptibility–Reykjavik study', *Brain*. Oxford Univ Press, 134(11), pp. 3398–3407.

Moens, A. (1877) 'Over de voortplantingssnelheid von den pols (On the speed of propagation of the pulse)', *Acad. Profsch.*, 1, pp. 1–72.

Mortensen, S. P., Damsgaard, R., Dawson, E. A., Secher, N. H. and González-Alonso, J. (2008) 'Restrictions in systemic and locomotor skeletal muscle perfusion, oxygen supply and VO2 during high-intensity whole-body exercise in humans.', *The Journal of Physiology*, 586(Pt 10), pp. 2621–35. doi: 10.1113/jphysiol.2007.149401.

Motoaki Sugawara, Keisuke Uchida and Yukiyoshi Kondoh (1997) 'Aortic Blood Momentum - the more better for the ejection heart in vigo', *Cardiovascular Research*, (33), pp. 433–466.

Munch, G. D. W., Svendsen, J. H., Damsgaard, R., Secher, N. H., González-Alonso, J. and Mortensen, S. P. (2014) 'Maximal heart rate does not limit cardiovascular capacity in healthy humans: insight from right atrial pacing during maximal exercise', *The Journal of physiology*. Wiley Online Library, 592(2), pp. 377–390.

Murgo, J. P., Westerhof, N., Giolma, J. P. and Altobelli, S. A. (1981) 'Effects of exercise on aortic input impedance and pressure wave forms in normal humans.', *Circulation Research*.

Am Heart Assoc, 48(3), pp. 334–343.

Myers, C. W., Farquhar, W. B., Forman, D. E., Williams, T. D., Dierks, D. L. and Taylor, J. A. (2002) 'Carotid distensibility characterized via the isometric exercise pressor response.', *American journal of physiology. Heart and circulatory physiology*, 283, pp. H2592–H2598. doi: 10.1152/ajpheart.00309.2002.

Mynard, J. P., Penny, D. J., Davidson, M. R. and Smolich, J. J. (2012) 'The reservoir-wave paradigm introduces error into arterial wave analysis: a computer modelling and in-vivo study', *Journal of hypertension*. LWW, 30(4), pp. 734–743.

Niki, K., Sugawara, M., Chang, D., Harada, A., Okada, T., Sakai, R., Uchida, K., Tanaka, R. and Mumford, C. E. (2002) 'A new noninvasive measurement system for wave intensity: Evaluation of carotid arterial wave intensity and reproducibility', *Heart and Vessels*, 17(1), pp. 12–21. doi: 10.1007/s003800200037.

Niki, K., Sugawara, M., Uchida, K., Tanaka, R., Tanimoto, K., Imamura, H., Sakomura, Y., Ishizuka, N., Koyanagi, H. and Kasanuki, H. (1999) 'A noninvasive method of measuring wave intensity, a new hemodynamic index: application to the carotid artery in patients with mitral regurgitation before and after surgery.', *Heart and vessels*, 14(6), pp. 263–271.

Notomi, Y. (2006) 'Enhanced Ventricular Untwisting During Exercise: A Mechanistic Manifestation of Elastic Recoil Described by Doppler Tissue Imaging', *Circulation*, 113(21), pp. 2524–2533. doi: 10.1161/CIRCULATIONAHA.105.596502.

O'Rourke, M. F. and Taylor, M. G. (1967) 'Input Impedance of the Systemic Circulation', *Circulation Research*, 20(4), pp. 365–380. doi: 10.1161/01.RES.20.4.365.

O'Rourke, M. F. (1982) 'Vascular impedance in studies of arterial and cardiac function.', *Physiological Reviews*, 62(2), p. 570 LP-623. Available at: http://physrev.physiology.org/content/62/2/570.abstract.

Ohte, N., Narita, H., Sugawara, M., Niki, K., Okada, T., Harada, A., Hayano, J. and Kimura, G. (2003) 'Clinical usefulness of carotid arterial wave intensity in assessing left ventricular systolic and early diastolic performance', *Heart and Vessels*, 18(3), pp. 107–111. doi: 10.1007/s00380-003-0700-5.

Palombo, C., Malshi, E., Morizzo, C., Rakebrandt, F., Corretti, V., Santini, F., Fraser, A. G. and Kozakova, M. (2009) 'Arterial wave reflection during antihypertensive therapy with barnidipine: A 6-month, open-label study using an integrated cardiovascular ultrasound approach in patients with newly diagnosed hypertension', *Clinical Therapeutics*. Excerpta Medica Inc., 31(12), pp. 2873–2885. doi: 10.1016/j.clinthera.2009.12.011.

Parker, K. H. (2009a) 'A brief history of arterial wave mechanics', *Medical and Biological Engineering and Computing*, 47(2), pp. 111–118. doi: 10.1007/s11517-009-0440-5.

Parker, K. H. (2009b) 'An introduction to wave intensity analysis', *Medical and Biological Engineering and Computing*, 47(2), pp. 175–188. doi: 10.1007/s11517-009-0439-y.

Parker, K. H. and Jones, C. J. H. (1990) 'Forward and backward running waves in the arteries: analysis using the method of characteristics', *ASME J Biomech Eng*, 112, pp. 322–326.

Parker, K. H., Jones, C. J. H., Dawson, J. R. and Gibson, D. G. (1988) 'What stops the flow of blood from the heart?', *Heart and Vessels*, 4, pp. 241–245.

Patel, D. J., De Freitas, F. M., Greenfield, J. C. and Fry, D. L. (1963) 'Relationship of radius to pressure along the aorta in living dogs', *Journal of Applied Physiology*, 18(6), p. 1111 LP-

1117. Available at: http://jap.physiology.org/content/18/6/1111.abstract.

Pedley, T. J. (1980) *The fluid mechanics of large blood vessels*. Cambridge University Press Cambridge.

Peters, H. P. F., de Leeuw, D., Lapham, R. C., Bol, E., Mosterd, W. L. and de Vries, W. R. (2001) 'Reproducibility of ultrasound blood flow measurement of the superior mesenteric artery before and after exercise. / Reproductibilite des mesures par ultrasons du flux sanguin de l'artere superieure mesenterique avant et apres l'effort.', *International Journal of Sports Medicine*, 22(4), pp. 245–249. Available at: http://articles.sirc.ca/search.cfm?id=S-781630%5Cnhttp://search.ebscohost.com/login.aspx?direct=true&db=sph&AN=SPHS-781630&site=ehost-live%5Cnhttp://www.thieme.com.

Poiseuille, J. (1846) 'Experimental research on the movement of liquids in tubes of very small diameters. Mémoires presentés par divers savants a l'Académie Royale des Sciences de l'Institut de France', 9.

Portney, L. G. and Watkins, M. P. (2000) *Foundations of clinical research: applications to practice*. Prentice Hall Upper Saddle River, NJ.

Pressman, G. L. (no date) 'A Transducer for the Continuous External Measurement of Arterial Blood Pressure', *IRE transactions on bio-medical electronics*. Professional Group on Bio-medical Electronics, Institute of Radio Engineers, 10(2), pp. 73–81. doi: 10.1109/TBMEL.1963.4322794.

Rabben, S. I., Stergiopulos, N., Hellevik, L. R., Smiseth, O. A., Slørdahl, S., Urheim, S. and Angelsen, B. (2004) 'An ultrasound-based method for determining pulse wave velocity in superficial arteries', *Journal of Biomechanics*, 37(10), pp. 1615–1622. doi: 10.1016/j.jbiomech.2003.12.031.

Rakebrandt, F., Palombo, C., Swampillai, J., Schön, F., Donald, A., Kozàkovà, M., Kato, K. and Fraser, A. G. (2009) 'Arterial wave intensity and ventricular-arterial coupling by vascular ultrasound: rationale and methods for the automated analysis of forwards and backwards running waves', *Ultrasound in medicine & biology*. Elsevier, 35(2), pp. 266–277.

Ralston, H. J., Taylor, A. N. and Elliott, H. W. (1947) 'Further studies on streamline blood flow in the arteries of the cat', *American Journal of Physiology--Legacy Content*. Am Physiological Soc, 150(1), pp. 52–57.

Ramsey, M. W. and Sugawara, M. (1997) 'Arterial wave intensity and ventriculoarterial interaction.', *Heart and vessels*. Japan, Suppl 12, pp. 128–134.

Riemann, B. (1860) 'Uber die Fortpflanzung ebener Luftwellen von endlicher Schwingungswei', *Abhandlungen der Gesellsehaft der Wissenschaften zu Gottingen, Math.-physikal.*, 8(April), pp. 43–65.

Rietzschel, E.-R., De Buyzere, M. L., Bekaert, S., Segers, P., De Bacquer, D., Cooman, L., Van Damme, P., Cassiman, P., Langlois, M., van Oostveldt, P., Verdonck, P., De Backer, G., Gillebert, T. C. and investigators, on behalf of the A. (2007) 'Rationale, design, methods and baseline characteristics of the Asklepios Study', *European Journal of Cardiovascular Prevention & Rehabilitation*, 14(2), pp. 179–191. doi: 10.1097/HJR.0b013e328012c380.

Rivolo, S., Asrress, K. N., Chiribiri, A., Sammut, E., Wesolowski, R., Bloch, L. Ø., Grøndal, A. K., Hønge, J. L., Kim, W. Y. and Marber, M. (2014) 'Enhancing coronary wave intensity analysis robustness by high order central finite differences', *Artery research*. Elsevier, 8(3), pp. 98–109.

Rossiter, H. B., Kowalchuk, J. M. and Whipp, B. J. (2006) ‘A test to establish maximum O2 uptake despite no plateau in the O2 uptake response to ramp incremental exercise.’, *Journal of applied physiology (Bethesda, Md. : 1985)*, 100(3), pp. 764–70. doi: 10.1152/japplphysiol.00932.2005.

Saiki, H., Kurishima, C., Masutani, S. and Senzaki, H. (2014) ‘Cerebral circulation in patients with fontan circulation: Assessment by carotid arterial wave intensity and stiffness’, *Annals of Thoracic Surgery*. Elsevier Inc, 97(4), pp. 1394–1399. doi: 10.1016/j.athoracsur.2013.10.079.

Saladin, K. S. (2007) *Human Anatomy*. Springer.

Sallis, J. F., Haskell, W. L., Wood, P. D., Fortmann, S. P., Rogers, T., Blair, S. N. and Paffenbarger, R. S. (1985) ‘Physical activity assessment methodology in the Five-City Project’, *American journal of epidemiology*. Oxford Univ Press, 121(1), pp. 91–106.

Saltin, B., Rådegran, G., Koskolou, M. D. and Roach, R. C. (1998) ‘Skeletal muscle blood flow in humans and its regulation during exercise’, *Acta Physiologica Scandinavica*, 162, pp. 421–436. doi: 10.1046/j.1365-201X.1998.0293e.x.

Sato, K., Ogoh, S., Hirasawa, A., Oue, A. and Sadamoto, T. (2011) ‘The distribution of blood flow in the carotid and vertebral arteries during dynamic exercise in humans’, *J Physiol*, 589(Pt 11), pp. 2847–2856. doi: 10.1113/jphysiol.2010.204461.

Savitzky, A. and Golay, M. J. E. (1964) ‘Smoothing and Differentiation of Data by Simplified Least Squares Procedures’, *Analytical Chemistry*, 36(8), pp. 1627–1639. doi: 10.1021/ac60214a047.

Schipke, J. D., Heusch, G., Sanii, A. P., Gams, E. and Winter, J. (2003) ‘Static filling pressure in patients during induced ventricular fibrillation’, *American Journal of Physiology-Heart and Circulatory Physiology*. Am Physiological Soc, 285(6), pp. H2510–H2515.

Seals, D. R. and Chase, P. B. (1989) ‘Influence of physical training on heart rate variability and baroreflex circulatory control’, *Journal of Applied Physiology*. Am Physiological Soc, 66(4), pp. 1886–1895.

Segers, P., Swillens, A., Taelman, L. and Vierendeels, J. (2014) ‘Wave reflection leads to over- and underestimation of local wave speed by the PU- and QA-loop methods: theoretical basis and solution to the problem.’, *Physiological measurement*, 35(5), pp. 847–61. doi: 10.1088/0967-3334/35/5/847.

Shapiro, S. S. and Wilk, M. B. (1965) ‘An analysis of variance test for normality (complete samples)’, *Biometrika*. Biometrika Trust, 52(3–4), pp. 591–611.

Sharman, J. E., McEniery, C. M., Campbell, R. I., Coombes, J. S., Wilkinson, I. B. and Cockcroft, J. R. (2005) ‘The effect of exercise on large artery haemodynamics in healthy young men’, *Eur J Clin Invest*, 35(12), pp. 738–744. doi: 10.1111/j.1365-2362.2005.01578.x.

Siniawski, H., Unbehaun, A., Lehmkuhl, H., Susanne, K., Schoen, F. and Hetzer, R. (2002) ‘Clinical and echocardiographic features in patients with dilated cardiomyopathy: wave intensity and diastolic abnormality analysis’, *Przeglad lekarski*. Department of Cardiothoracic and Vascular Surgery, Deutsches Herzzentrum Berlin, Augustenburger Platz 1, 13353 Germany. siniawski@dhzb.de, 59(8), pp. 562–567. Available at: http://europepmc.org/abstract/MED/12638320.

Spaan, J. a., Breuls, N. P. and Laird, J. D. (1981) ‘Diastolic-systolic coronary flow

differences are caused by intramyocardial pump action in the anesthetized dog', *Circulation Research*, 49(3), pp. 584–593. doi: 10.1161/01.RES.49.3.584.

Stergiopulos, N., Segers, P. and Westerhof, N. (1999) 'Use of pulse pressure method for estimating total arterial compliance in vivo.', *The American journal of physiology*, 276(2 Pt 2), pp. H424–H428.

Stergiopulos, N., Westerhof, B. E. and Westerhof, N. (1999) 'Total arterial inertance as the fourth element of the windkessel model', *Am J Physiol Heart Circ Physiol*, 276, pp. H81–H88.

Stöhr, E. J., González-Alonso, J. and Shave, R. (2011) 'Left ventricular mechanical limitations to stroke', *Am J Physiol Heart Circ Physiol*, 301, pp. H478–H487.

Studinger, P., Lénárd, Z., Kováts, Z., Kocsis, L. and Kollai, M. (2003) 'Static and dynamic changes in carotid artery diameter in humans during and after strenuous exercise.', *The Journal of physiology*, 550, pp. 575–583. doi: 10.1113/jphysiol.2003.040147.

Sugawara, M., Niki, K., Furuhata, H., Ohnishi, S. and Suzuki, S. (2000) 'Relationship between the pressure and diameter of the carotid artery in humans.', *Heart and vessels*, 15(1), pp. 49–51. doi: 10.1007/PL00007261.

Sugawara, M., Niki, K., Ohte, N., Okada, T. and Harada, A. (2009) 'Clinical usefulness of wave intensity analysis', *Medical and Biological Engineering and Computing*, 47(2), pp. 197–206. doi: 10.1007/s11517-008-0388-x.

Sun, Y., Anderson, T. J., Parker, K. I. M. H. and Tyberg, J. V (2000) 'cutting-edge report', *J Appl Physiol*, 89, pp. 1636–1644.

Sutera, S. P. and Skalak, R. (1993) 'The History of Poiseuille Law', *Annual Review of Fluid Mechanics*, 25, p. 1. doi: 10.1146/annurev.fl.25.010193.000245.

Swalen, M. J. P. and Khir, A. W. (2009) 'Resolving the time lag between pressure and flow for the determination of local wave speed in elastic tubes and arteries', *Journal of Biomechanics*, 42(10), pp. 1574–1577. doi: 10.1016/j.jbiomech.2009.03.038.

Swampillai, J., Rakebrandt, F., Morris, K., Jones, C. J. H. and Fraser, A. G. (2006) 'Acute effects of caffeine and tobacco on arterial function and wave travel', *European Journal of Clinical Investigation*, 36(12), pp. 844–849. doi: 10.1111/j.1365-2362.2006.01738.x.

Swillens, A., Taelman, L., Degroote, J., Vierendeels, J. and Segers, P. (2013) 'Comparison of non-invasive methods for measurement of local pulse wave velocity using fsi-simulations and in vivo data', *Annals of Biomedical Engineering*, 41(7), pp. 1567–1578. doi: 10.1007/s10439-012-0688-z.

Taber, L. a., Yang, M. and Podszus, W. W. (1996) 'Mechanics of ventricular torsion', *Journal of Biomechanics*, 29(6), pp. 745–752. doi: 10.1016/0021-9290(95)00129-8.

Tanaka, M., Sugawara, M., Ogasawara, Y., Suminoe, I., Izumi, T., Niki, K. and Kajiya, F. (2015) 'Noninvasive evaluation of left ventricular force− frequency relationships by measuring carotid arterial wave intensity during exercise stress', *Journal of Medical Ultrasonics*. Springer, 42(1), pp. 65–70.

Taylor, M. G. (1966a) 'Use of Random Excitation and Spectral Analysis in the Study of Frequency-Dependent Parameters of the Cardiovascular System', *Circulation Research*, 18(5), pp. 585–595. doi: 10.1161/01.RES.18.5.585.

Taylor, M. G. (1966b) 'Wave Transmission through an Assembly of Randomly Branching

Elastic Tubes', *Biophysical Journal*. Elsevier, 6(6), pp. 697–716. doi: 10.1016/S0006-3495(66)86689-4.

Tokaty, G. A. (1971) 'A History and Philosophy of Fluid Mechanics GT Foulis & Co', *Ltd., Oxfordshire*.

Trangmar, S. J., Chiesa, S. T., Stock, C. G., Kalsi, K. K., Secher, N. H. and González-Alonso, J. (2014) 'Dehydration affects cerebral blood flow but not its metabolic rate for oxygen during maximal exercise in trained humans.', *The Journal of physiology*, 592(Pt 14), pp. 3143–60. doi: 10.1113/jphysiol.2014.272104.

Tukey, J. W. (1977) 'Exploratory data analysis'. Reading, Mass.

Tyberg, J. V., Davies, J. E., Wang, Z., Whitelaw, W. A., Flewitt, J. A., Shrive, N. G., Francis, D. P., Hughes, A. D., Parker, K. H. and Wang, J. J. (2009) 'Wave intensity analysis and the development of the reservoir-wave approach', *Medical and Biological Engineering and Computing*, 47(2), pp. 221–232. doi: 10.1007/s11517-008-0430-z.

Vandewalle H, Lacombe C, Lelievre JC, Poirot C. (1988) 'Blood viscosity after a 1-h submaximal exercise with and without drinking'. *Inter J Sports Med* 9(02): 104-107.

Vermeersch, S. J., Rietzschel, E. R., Buyzere, M. L., Bortel, L. M., Gillebert, T. C., Verdonck, P. R. and Segers, P. (2009) 'The reservoir pressure concept: The 3-element windkessel model revisited? Application to the Asklepios population study', *Journal of Engineering Mathematics*, 64(4), pp. 417–428. doi: 10.1007/s10665-009-9286-y.

Victor, R. G., Seals, D. R. and Mark, A. L. (1987) 'Differential control of heart rate and sympathetic nerve activity during dynamic exercise. Insight from intraneural recordings in humans.', *Journal of Clinical Investigation*. American Society for Clinical Investigation, 79(2), p. 508.

Vriz, O., Pellegrinet, M., Zito, C., di Bello, V., Bettio, M., Carerj, S., Cittadini, A., Bossone, E. and Antonini-Canterin, F. (2015) 'One-point carotid wave intensity predicts cardiac mortality in patients with congestive heart failure and reduced ejection fraction.', *The international journal of cardiovascular imaging*. Springer Netherlands, 31(7), pp. 1369–1378. doi: 10.1007/s10554-015-0696-9.

Wang, J.-J., Flewitt, J. a, Shrive, N. G., Parker, K. H. and Tyberg, J. V (2006) 'Systemic venous circulation. Waves propagating on a windkessel: relation of arterial and venous windkessels to systemic vascular resistance.', *American journal of physiology. Heart and circulatory physiology*, 290(1), pp. H154–H162. doi: 10.1152/ajpheart.00494.2005.

Wang, J.-J., O'Brien, A. B., Shrive, N. G., Parker, K. H. and Tyberg, J. V (2003) 'Time-domain representation of ventricular-arterial coupling as a windkessel and wave system.', *American journal of physiology. Heart and circulatory physiology*, 284(4), pp. H1358–H1368. doi: 10.1152/ajpheart.00175.2002.

Wang, J. J., Shrive, N. G., Parker, K. H., Hughes, A. D. and Tyberg, J. V. (2011) 'Wave propagation and reflection in the canine aorta: Analysis using a reservoir-wave approach', *Canadian Journal of Cardiology*. Elsevier Inc., 27(3), p. 389.e1-389.e10. doi: 10.1016/j.cjca.2010.12.072.

Webb, H. E., McMinn, D. R., Garten, R. S., Beckman, J. L., Kamimori, G. H. and Acevedo, E. O. (2010) 'Cardiorespiratory responses of firefighters to a computerized fire strategies and tactics drill during physical activity', *Applied Ergonomics*. Elsevier Ltd, 41(3), pp. 376–381. doi: 10.1016/j.apergo.2009.08.003.

Weber, E. and Weber, W. (1825) *Wellenlehre auf Experimente gegru¨ndet, oder u¨ber die Wellen tropbarer Flu¨ssigkeiten mit Andwendung auf die Schall- und Lichtwellen*. Leipzig, East Germany: Fleischer.

Weber, W. (1866) 'Theorie der durch Wasser oder andere in- compressibele Flu¨ssigkeiten in elastischen Ro¨hren fortgeplanzten Wellen', *Berichte der Gesellschaft der Wissenschaften zu Leipzig: Math phys Kl*, 18, pp. 353–357.

Wen, H., Tang, H., Li, H., Kang, Y., Peng, Y. and Zhou, W. (2010) 'Carotid arterial wave intensity in assessing the hemodynamic change in patients with chronic heart failure', *Sheng wu yi xue gong cheng xue za zhi= Journal of biomedical engineering= Shengwu yixue gongchengxue zazhi*, 27(3), pp. 578–582.

Westerhof, N., Bosman, F., De Vries, C. J. and Noordergraaf, A. (1969) 'Analog studies of the human systemic arterial tree', *J. Biomech.*, 2(2), pp. 121–43. doi: 10.1016/0021-9290(69)90024-4.

Westerhof, N., Elzinga, G. and Sipkema, P. (1971) 'An artificial arterial system for pumping hearts.', *Journal of applied physiology*, 31(5), pp. 776–81. Available at: http://www.ncbi.nlm.nih.gov/pubmed/5117196.

Westerhof, N., Lankhaar, J. W. and Westerhof, B. E. (2009) 'The arterial windkessel', *Medical and Biological Engineering and Computing*, 47(2), pp. 131–141. doi: 10.1007/s11517-008-0359-2.

Westerhof, N., Sipkema, P., Bos, G. C. Van Den and Elzinga, G. (1972) 'Forward and backward waves in the arterial system', *Cardiovascular Research*, 6(6), pp. 648–656. doi: 10.1093/cvrese/6.6.648.

WHO (2014) 'Global status report on noncommunicable diseases 2014', *World Health*, p. 176. doi: ISBN 9789241564854.

Wilkinson, I. B., Mohammad, N. H., Tyrrell, S., Hall, I. R., Webb, D. J., Paul, V. E., Levy, T. and Cockcroft, J. R. (2002) 'Heart rate dependency of pulse pressure amplification and arterial stiffness', *American journal of hypertension*. Oxford University Press, 15(1), pp. 24–30.

Womersley, J. R. (1955) 'Oscillatory flow in arteries: effect of radial variation in viscosity on rate of flow.', *The Journal of physiology*. Wiley Blackwell (Blackwell Publishing), 127(2).

Womersley, J. R. (1958) 'Oscillatory flow in arteries. II. The reflection of the pulse wave at junctions and rigid inserts in the arterial system.', *Physics in medicine and biology*, 2(4), pp. 313–323. doi: 10.1088/0031-9155/2/4/301.

Yan, H., Fahs, C. A., Ranadive, S., Rossow, L. M., Lane, A. D., Agiovlasitis, S., Echols, G., Smith, D., Horn, G. P., Rowland, T. and Fernhall, B. (2012) 'Evaluation of carotid wave intensity in firefighters following firefighting', *European Journal of Applied Physiology*, 112(7), pp. 2385–2391. doi: 10.1007/s00421-011-2188-5.

Young, T. (1808) 'Hydraulic Investigations, Subservient to an Intended Croonian Lecture on the Motion of the Blood', *Philosophical Transactions of the Royal Society of London*. The Royal Society, 98, pp. 164–186. Available at: http://www.jstor.org/stable/107293.

Zambanini, a., Khir, a. W., Byrd, S. M., Parker, K. H., Thom, S. a. M. and Hughes, a. D. (2002) 'Wave intensity analysis: a novel non-invasive method for determining arterial wave transmission', *Computers in Cardiology*, pp. 717–720. doi: 10.1109/CIC.2002.1166873.

Zambanini, a, Cunningham, S. L., Parker, K. H., Khir, a W., McG Thom, S. a and Hughes, a D. (2005) 'Wave-energy patterns in carotid, brachial, and radial arteries: a noninvasive approach using wave-intensity analysis.', *American journal of physiology. Heart and circulatory physiology*, 289(1), pp. H270–H276. doi: 10.1152/ajpheart.00636.2003.

Zhang, Y., Liu, M., Wang, M., Zhang, L., Lv, Q., Xie, M., Xiang, F., Fu, Q., Yin, Y., Lu, C., Yan, T. and Huang, Y. (2010) 'Wave intensity analysis of carotid artery: A noninvasive technique for assessing hemodynamic changes of hyperthyroid patients', *Journal of Huazhong University of Science and Technology - Medical Science*, 30(5), pp. 672–677. doi: 10.1007/s11596-010-0563-9.

List of publications related to this thesis

Peer-reviewed journal publications

Pomella N, Wilhelm EN, Kolyva C, González-Alonso J, Rakobowchuk M, Khir AW. Common Carotid Artery Diameter, Blood Flow Velocity and Wave Intensity Responses at Rest and during Exercise in Young Healthy Humans: A Reproducibility Study. *Ultrasound in Medicine & Biology*. 2017 May 1; 43(5): 943-57.

Pomella N, Rakobowchuk M, Kolyva C, Khir AW. Changes in non-invasive wave intensity parameters with variations of Savitzky-Golay filter settings. In *Computing in Cardiology Conference (CinC)*, 2016 Sep 11 (pp. 1041-1044), IEEE.

Conference proceedings

Pomella N, Kolyva C, Negoita M, Rietzschel E, Segers P, Khir AW. Variation of the asymptotic diastolic pressure with different techniques in healthy humans. Artery Research 2016, 16:70.

Pomella N, Kolyva C, Khir AW. Common carotid artery wave intensity analysis in healthy humans with increasing exercise intensities. Artery Research 2015, 12:37.

Pomella N, Kolyva C, Khir AW. Correction of wave speed measurement techniques in close proximity to a reflection site in elastic tubes. MEC Annual Meeting and Bioengineering 2014, London, UK.